

THE UNIVERSITY OF NEW SOUTH WALES
GRADUATE SCHOOL OF BIOMEDICAL ENGINEERING

Non-linear transient stability
analysis of the VentrAssist
hydrodynamically suspended
impeller



by
MICHAEL C. HOGG

Supervisor: Geoff Tansley

January 2002

Abstract

VentrAssist is currently developing a unique implantable rotary blood pump (IRBP) to treat patients suffering from end-stage heart failure. Mechanical support by means of ventricular assist devices (VADs) is at present the most promising alternative to present methods of treatment. In particular, VADs based on rotary blood pump technology are relatively inexpensive, small, extremely reliable and efficient.

The VentrAssist IRBP features a hydrodynamically suspended impeller that reduces complications associated with conventional means of impeller suspension. The issue of stability arises, as the impeller is now free to move in the five degrees of freedom that were previously constrained by the shaft in such pumps. A displacement (or rotation) of the impeller towards the pump housing is accompanied by an increase in the pressure at that location, which produces a force (or moment) that restores the impeller to its initial position. If the force on the impeller, which causes such a displacement, exceeds the load capacity of the passive suspension system then contact between the impeller and pump housing will occur. Additionally, self-excited oscillations known as “whirl” may also result in such a “touchdown”.

A numerical tool called *Orbit3D* was developed in order to assess the stability of the impeller. A non-linear method of analysis was employed where the trajectory of the impeller was marched out in a number of finite time steps. More specifically, the Reynolds equation was solved to determine the pressure distribution over the thrust bearing and conical journal bearing surfaces of the impeller at the initial position specified by the user. The forces and moments on the impeller derived from this pressure field were calculated by numerical integration using the trapezoidal rule, and the five equations of motion were then solved simultaneously using the classical fourth-order Runge-Kutta method to calculate the position of the impeller at the next step.

This process was continued until touchdown occurred, the impeller settled to a stable point / limit cycle, or until the number of time steps specified by the user was reached. Stability was assessed by observation of the impeller trajectory.

The trajectory of the impeller was determined under a number of conditions including various pump speeds and orientations of the pump housing, and various simulated disturbances including an unbalance force and “shaking” of the pump housing. In all cases, the corresponding trajectory indicated stable operation except when the rotational speed was dropped to 500 RPM.

Orbit3D is a powerful tool which not only helps the designer to build an understanding of the behaviour of the VentrAssist IRBP, but additionally allows the user to observe the shape of the pressure distribution over the bearing surfaces of each impeller blade such that the shape of the bearing surfaces may be optimised to minimise pressure gradients and therefore lower the incidence of blood damage.

Acknowledgements

I would like to thank the following people for their aid in writing this thesis:

To my supervisor Geoff Tansley for giving me a very challenging but interesting topic, providing me technical support, looking out for my interests and just making the year enjoyable.

To Martin Cook of VentrAssist for always being interested in my work and providing very helpful advice, criticism and encouragement. Thankyou for making me feel both welcome and comfortable at VentrAssist.

To my friends and family, for your most grateful help, support and, most importantly, understanding.

To my friends at St. Philip's Anglican Church Eastwood, thankyou for your prayers and your encouragement throughout the year – without God's help, this paper may never have been finished.

To my "biomed buddies", thanks for your friendship, support and encouragement over the last year. It was always great to grab a coffee at James's and to chat about our work, life and whether or not we were going to graduate. That seems behind us now, but as we all (well, most of us) venture out into the "real" world, I wish you all the best and will remember fondly the times we shared over our time together at UNSW.

Thankyou to Michelle, my future wife (!), who is there for me always. Thankyou for helping me to get myself organised so that I was not still writing this paper on our honeymoon, but more importantly just for being yourself. Love you.

Table of Contents

Abstract	i
Acknowledgements	iii
Table of contents	iv
Nomenclature	vii
Chapter 1 – Introduction	1
Chapter 2 – Background	4
2.1. The impeller	4
2.2. The VentrAssist hydrodynamically suspended impeller	6
2.3. Stability	9
2.3.1. <i>The linearised (perturbation) method</i>	10
2.3.2. <i>Non-linear transient analysis</i>	15
Chapter 3 – Theoretical methodology	21
3.1. Reynolds equation	21
3.1.1. <i>Assumptions for hydrodynamic theory</i>	21
3.1.2. <i>Derivation of Reynolds equation</i>	23
3.1.2.1. Equilibrium of an element of fluid	23
3.1.2.2. Equilibrium of a fluid column	26
3.1.3. <i>Reynolds equation in Cartesian coordinates</i>	32
3.1.4. <i>Reynolds equation in cylindrical coordinates</i>	33
3.1.5. <i>Reynolds equation in spherical coordinates</i>	37
3.2. Geometry and properties	41
3.3. Film thickness	45
3.3.1. <i>Thrust bearing</i>	47
3.3.1.1. Spatial and temporal derivatives of the film thickness	52
3.3.2. <i>Conical journal bearing</i>	53
3.3.2.1. Spatial and temporal derivatives of the film thickness	58

3.4. Solution of Reynolds equation	60
3.4.1. <i>Discretisation</i>	60
3.4.1.1. Thrust bearing	60
3.4.1.2. Conical journal bearing	62
3.4.2. <i>Solving of discretised equations</i>	64
3.4.2.1. The Thomas algorithm in 2D	65
3.4.2.2. Thrust bearing	67
3.4.2.3. Conical journal bearing	68
3.4.2.4. Iterative procedure	70
3.4.3. <i>Verification of solution method</i>	72
3.4.4. <i>Refinement of the numerical grid</i>	72
3.5. Calculation of fluid film forces	74
3.5.1. <i>Thrust bearing</i>	74
3.5.2. <i>Conical journal bearing</i>	79
3.5.3. <i>Total forces and moments on the impeller</i>	84
3.6. Dynamic motion of the impeller	85
3.6.1. <i>Forces and moments on the impeller</i>	85
3.6.2. <i>Equations of motion</i>	90
3.6.3. <i>Solution of the equations of motion</i>	94
3.6.4. <i>Computational procedure</i>	97
3.7. Test cases	99
3.8. Orbit3D	103
Chapter 4 – Results and discussion	104
4.1. Pressure distribution	104
4.1.1. <i>Thrust bearing</i>	104
4.1.2. <i>Conical journal bearing</i>	106
4.2. Impeller trajectory	110
Chapter 5 – Conclusion	131
Chapter 6 – Future directions	133
Reference	135

Appendix A – The Thomas Algorithm

Appendix B – The Thomas Algorithm FORTRAN subroutine

Appendix C – Analysis of a rectangular tilting thrust bearing

Appendix D – Grid independence study

Appendix E – FORTRAN program “tb2d.f”

Appendix F – Double integration with the trapezoidal rule

Appendix G – FORTRAN program *Orbit3D*

Appendix H – Matlab script file “Orb3Dvis.m”

Nomenclature

Symbols

a, b, c, d	Coefficient of nodal pressure values in the Thomas algorithm
c	Axial (vertical) clearance of both thrust bearing and conical journal bearing, $c = h_{0,TB} = h_{vc}$
d_m	Average film thickness
e_x, e_y, e_z	Eccentricity of the impeller in the x, y, z direction
e_X, e_Y, e_Z	Eccentricity of the impeller in the X, Y, Z direction
\dot{e}_x	Relative velocity of the impeller in the X direction with respect to the pump housing, $\dot{e}_x = de_x/dt$
\dot{e}_y	Relative velocity of the impeller in the Y direction with respect to the pump housing, $\dot{e}_y = de_y/dt$
\dot{e}_z	Relative velocity of the impeller in the Z direction with respect to the pump housing, $\dot{e}_z = de_z/dt$
$\hat{\mathbf{e}}_r, \hat{\mathbf{e}}_\rho, \hat{\mathbf{e}}_\theta, \hat{\mathbf{e}}_\alpha$	Unit vectors in the r, ρ, θ, α direction
f	An arbitrary scalar function
F	Applied constant load, $F = Mg = W$
\mathbf{F}	An arbitrary vector
F_L	Lift force
F_D	Drag force
F_x, F_y, F_z	Total force in the X, Y, Z direction resulting from the hydrodynamic pressure distribution
$F_{unbalance}$	Force on the impeller due to unbalance
g	Acceleration due to gravity, $g = 9.81 \text{ m/s}^2$
h	Thickness of lubricating fluid film
h_0	Entry film thickness
h_1	Exit film thickness
h_{hc}	Radial (horizontal) clearance when $e_z = 0$, $h_{hc} = h_{0,CJB}/\cos\alpha$
h'_{hc}	Corrected radial clearance of the conical journal bearing,

h'_{hc}	$h_{hc} - e_Z \tan \alpha$
h_{vc}	Axial (vertical) clearance of the conical journal bearing when $e_X = e_Y = 0, h_{vc} = h_{0,CJB}/\sin \alpha$
i	Index of grid points in the θ direction over each impeller blade, $i = 1, 2, \dots, I$
$\hat{\mathbf{i}}, \hat{\mathbf{j}}$	Unit vector in x, y direction
I_T	Transverse moment of inertia of the impeller, $I_T = I_{xx} = I_{yy}$
I_P	Polar moment of inertia of the impeller, $I_P = I_{zz}$
j	Index of grid points in the radial (r or ρ) direction over each impeller blade, $j = 1, 2, \dots, J$
k	Time step index, $k = 1, 2, \dots, K$
k_1, k_2, k_3, k_4	Variables used in the classical Runge-Kutta method
K	(i) Total number of time steps (ii) Inclination of pad, $K = h_1/h_0 - 1$
L	Radial length of bearing in r direction, $L = r_2 - r_1$
L_ρ	Radial length of bearing in ρ direction, $L_\rho = \rho_2 - \rho_1$
m	(i) Index of impeller blades, $m = 1, 2, \dots, N_p$ (ii) Unbalance mass
M	Mass of the impeller
M_x, M_y	Total moment about the X, Y axis on the impeller resulting from the hydrodynamic pressure distribution
N_p	Number of impeller blades
p	Pressure
q_x	Lubricant flow per unit width in the x direction
q_y	Lubricant flow per unit width in the y direction
r	Eccentricity of unbalance mass
r, θ, z	Cylindrical coordinates
r_1, r_2	Inner, outer radius of thrust bearing
S_0	Stability parameter, $S_0 = F/Mc\omega^2 = 1/M^*$
t	Time
u, v	Particle velocity in x, y direction

U_x, U_y	Surface velocity in the x, y coordinate direction
U_X, U_Y	Surface velocity in the X, Y coordinate direction
U_r, U_ρ, U_θ	Surface velocity in the r, ρ, θ coordinate direction
U	Velocity vector
w	Particle or surface velocity in the z direction
W	Weight of impeller
W_X, W_Y, W_Z	Component of impeller weight in X, Y, Z direction
x, y, z	Cartesian coordinates
x_H, y_H, z_H	Absolute displacement of the pump housing in the X, Y, Z direction
X_H, Y_H, Z_H	Amplitude of absolute displacement of the pump housing in the X, Y, Z direction
z_G	Position of the centre of mass in the z direction measured from the trailing edge of the thrust bearing

Greek symbols

α	Half-cone angle
β_1	Phase angle of “shaking” of pump housing in the X, Y, Z direction
Δh	Change in film thickness
$\Delta r, \Delta \rho, \Delta \theta$	Uniform grid spacing in the r, ρ, θ direction
Δt	Time increment
γ_x, γ_y	Rotation of impeller about the x, y axis
γ_X, γ_Y	Rotation of impeller about the X, Y axis
η	Dynamic (absolute) viscosity
ρ	Density
ρ, θ, α	Spherical coordinates
ρ_1, ρ_2	Inner, outer radius of conical journal bearing in the ρ direction
ρ_G	Position of the centre of mass G in spherical coordinates
τ	Shear stress on any layer of fluid
ω	(i) Angular velocity (ii) Over-relaxation factor
ω_0	Optimum value of the over-relaxation factor

ψ_1, ψ_2	Angles used in the specification of direction of the gravitational force
Ω_1	Frequency of “shaking” of the pump housing in the X, Y, Z direction
Ω_2	Frequency of rotating unbalance
θ_0	Angular span of impeller blade
θ_{0a}	Angular span of untapered land section of impeller blade
θ_{0b}	Angular span of tapered section of impeller blade
θ_1	Angular distance between the trailing (or leading) edge of consecutive impeller blades, $\theta_1 = 2\pi/N_p$
ξ	Angular location of the trailing edge of each blade m , $\xi = (m-1)\theta_1$

Superscripts

$*$	Non-dimensional quantity
k	Time step index, $k = 0, 1, \dots, K-1$
n	Iteration level

Subscripts

1	Refers to the top surface, e.g. $U_{x,1}, U_{y,1}$ (exceptions: $r_1, h_1, \psi_1, k_1, \theta_1, \Omega_1, \beta_1$)
2	Refers to the lower surface, e.g. $U_{x,2}, U_{y,2}$ (exceptions: $r_2, \psi_2, k_2, \Omega_2$)
0	Refers to where $z = 0$, e.g. w_0, τ_0 (exceptions: $h_0, S_0, \omega_0, \theta_0$)
<i>CJB</i>	Refers to the conical journal bearing, e.g. $h_{0,CJB}, K_{CJB}, F_{X,CJB}, M_{X,CJB}$
<i>G</i>	Refers to the centre of mass, e.g. z_G, ρ_G
<i>h</i>	Refers to where $z = h$, e.g. w_h, τ_h
<i>i</i>	Index of grid points in the θ direction over each impeller blade, $i = 1, 2, \dots, I$
<i>j</i>	Index of grid points in the radial (r or ρ) direction over each impeller blade, $j = 1, 2, \dots, J$
<i>m</i>	Index of impeller blades, $m = 1, 2, \dots, N_p$

<i>TB</i>	Refers to the thrust bearing, e.g. $h_{TB}, F_{Z,TB}, M_{X,TB}, M_{Y,TB}$
-----------	---------------------------------------------------------------------------

Groups

ε_x	$= e_x / h_{hc}$	Eccentricity ratio in the <i>X</i> direction when $e_z = 0$
ε_y	$= e_y / h_{hc}$	Eccentricity ratio in the <i>Y</i> direction when $e_z = 0$
ε_z	$= e_z / c$	Eccentricity ratio in the <i>Z</i> direction
ε'_x	$= e_x / h'_{hc} = \varepsilon_x / (1 - \varepsilon_z)$	Corrected eccentricity ratio in the <i>X</i> direction
ε'_y	$= e_y / h'_{hc} = \varepsilon_y / (1 - \varepsilon_z)$	Corrected eccentricity ratio in the <i>Y</i> direction
$\dot{\varepsilon}_x$	$= d\varepsilon_x / dt^*$	Velocity of impeller in the <i>X</i> direction
$\dot{\varepsilon}_y$	$= d\varepsilon_y / dt^*$	Velocity of impeller in the <i>Y</i> direction
$\dot{\varepsilon}_z$	$= d\varepsilon_z / dt^*$	Velocity of impeller in the <i>Z</i> direction
F_x^*	$= \frac{c^2}{6\eta\omega L^2 r_2^2} F_x = \frac{F_x}{\Lambda F}$	Non-dimensional force in the <i>X</i> direction
F_y^*	$= \frac{c^2}{6\eta\omega L^2 r_2^2} F_y = \frac{F_y}{\Lambda F}$	Non-dimensional force in the <i>Y</i> direction
F_z^*	$= \frac{c^2}{6\eta\omega L^2 r_2^2} F_z = \frac{F_z}{\Lambda F}$	Non-dimensional force in the <i>Z</i> direction
g^*	$= g / c\omega^2 = 1/M^* = S_0$	Non-dimensional gravitational constant
γ_x^*	$= \gamma_x r_2 / c$	Non-dimensional rotation about the <i>X</i> axis
γ_y^*	$= \gamma_y r_2 / c$	Non-dimensional rotation about the <i>Y</i> axis
h^*	$= h / c$	Non-dimensional film thickness
I_T^*	$= \frac{c^2 \omega}{6\eta L^2 r_2^3} I_T$	Non-dimensional transverse moment of inertia
J_P^*	$= I_P / I_T$	Non-dimensional polar moment of inertia
m^*	$= mr\omega^2 / F$	Non-dimensional unbalance mass
M^*	$= Mc\omega^2 / F = 1/S_0$	Non-dimensional impeller mass (inverse of the stability parameter)
M_x^*	$= \frac{c^2}{6\eta\omega L^2 r_2^3} M_x$	Non-dimensional total moment about the <i>X</i> axis

M_Y^*	$= \frac{c^2}{6\eta\omega L^2 r_2^3} M_Y$	Non-dimensional total moment about the Y axis
p^*	$= \frac{p}{6\eta\omega} \left(\frac{c}{L} \right)^2$	Non-dimensional pressure
r^*	$= r/r_2$	Non-dimensional radius
R^*	$= (r_2/L)^2 = (\rho_2/L_p)^2$	Ratio of outer radius to radial length of bearing
ρ^*	$= \rho/(\rho_2 \sin \alpha) = \rho/r_2$	Non-dimensional ρ coordinate
ρ_G^*	$= \rho_G/(\rho_2 \sin \alpha) = \rho_G/r_2$	Non-dimensional location of the centre of mass in the ρ coordinate direction
t^*	$= \omega t$	Non-dimensional time
V_1^*	$= \Omega_1/\omega$	Non-dimensional frequency of "shaking" of the pump housing in the X, Y, Z direction
V_2^*	$= \Omega_2/\omega$	Non-dimensional frequency of unbalance
X_H^*	$= X_H/c$	Non-dimensional amplitude of "shaking" in the X direction
Y_H^*	$= Y_H/c$	Non-dimensional amplitude of "shaking" in the Y direction
Z_H^*	$= Z_H/c$	Non-dimensional amplitude of "shaking" in the Z direction
Λ	$= \frac{6\eta\omega L^2}{F} \left(\frac{r_2}{c} \right)^2$	Load parameter
Δt^*	$= \omega \Delta t$	Non-dimensional time increment

Chapter 1 – Introduction

VentrAssist is currently developing a unique implantable rotary blood pump (IRBP) to treat patients suffering from heart failure. Currently, heart transplantation is the only definitive treatment of this condition. A shortage of donor hearts indicates the need for an alternative to transplantation. Mechanical support by means of ventricular assist devices (VADs) is at present the most promising alternative.

Current generation pulsatile VADs have demonstrated the feasibility of long term mechanical support as a bridge and an alternative to transplantation. Successfully rehabilitated patients have returned to a relatively normal lifestyle, in some cases warranting removal of the artificial device. However, the cost and size of pulsatile devices have limited their uptake in a large proportion of the population.

Artificial hearts based on rotary pump design offer a less expensive, very small, extremely reliable and more energy efficient alternative. However, the traditional means of suspending the rotating impeller using mechanical shafts, bearings and seals has been linked to blood damage, clotting and pump failure. This has severely limited the use of rotary blood pumps in permanent applications.

The VentrAssist IRBP employs an alternative and distinct means of impeller suspension which eliminates complications associated with such conventional means of suspension. This method involves supporting the impeller completely with fluid forces, termed “hydrodynamic suspension”. The impeller consists of four blades, each of which contain permanent rare-earth magnets, and is rotated about the pump axis by means of electromagnetic interaction between these magnets and the rotating magnetic field produced by the motor stator.

Having eliminated the shaft, the issue of impeller “stability” arises. Instability introduces a risk to the patient in the event that contact occurs between the impeller and pump housing. Such a “touchdown” could result in damage to the impeller, damage to the blood contacting surfaces which may increase thrombogenicity, or the constriction of secondary flow paths, in turn causing haemolysis and possible pump failure. Severe “whirl”, characterised by large amplitude oscillation of the impeller occurring at about half the rotational frequency, may be the cause of any touchowns that do occur.

The aim of this study was to develop a numerical design tool, which was named *Orbit3D*, in order to analyse the VentrAssist IRBP as a “system” and ultimately optimise the design by starting to develop an understanding of the interaction between the individual surfaces of the thrust bearing and the conical journal bearing of the impeller. A non-linear method of analysis was employed, making no assumptions of linearity, where the trajectory of the centre of mass of the impeller was obtained in response to an initial disturbance, unbalance force, and “shaking” of the pump body. This involved solution of the Reynolds equation over the bearing surfaces of the impeller, numerical integration of the resulting pressure field, and solution of the five second-order non-linear differential equations of motion using numerical methods. The stability of the system was assessed by observation of each trajectory.

It is intended that this initial analysis be extended in a future study by employing *Orbit3D* to obtain a “stability map” to indicate regions of stability and instability of the impeller, thereby identifying the range of operating conditions that correspond to each zone. Further, optimisation of the pump design will involve using an iterative approach such that, amongst other requirements, the final impeller design should exhibit both the greatest achievable film thickness for any given set of loading conditions and also the

greatest “stability reserve”, acting as a factor of safety against the occurrence of touchdown.

Program *Orbit3D*, written in the FORTRAN 77 programming language, was used to calculate the coordinates of the impeller trajectory and all minor calculations inherent to this task. Matlab 5.3 Release 11 (The Mathworks Inc., 1984-1999) was used to visualise the pressure distribution over each bearing surface and to plot the impeller trajectories.

Chapter 2 – Background

This chapter seeks to outline the history of IRBPs and the failure of shafted devices to meet the requirements of a successful means of chronic mechanical support, which subsequently lead to the evolutionary development of the hydrodynamically suspended VentrAssist IRBP. By elimination of the shaft, the rotating impeller is no longer mechanically constrained in the remaining five degrees of freedom (DOF). Consequently, the “stability” of the impeller must be evaluated. Two methods, namely the linearised (perturbation) method and the method of non-linear transient analysis, are commonly used as the basis of this evaluation. The underlying theory and the advantages / limitations of each method are briefly explained herein.

2.1. The impeller

The design of IRBPs has altered considerably from the time the concept was first envisaged. The original Medtronic centrifugal blood pump consisted of a small impeller supported by a shaft inside the pump head rotated by a DC micromotor [1].

In recent years, the power driven shaft was replaced with a shaft supported impeller driven through magnetic coupling by an extracorporeal motor and console as used in the Biomedicus centrifugal pump [2]. The shaft was attached to the pump housing by mechanical bearings and a shaft seal was used to isolate the bearings from the blood. This allowed the impeller to freely spin about the pump axis, but rigidly constrained the remaining five DOF [3, 4]. In this case, therefore, stability was not an issue.

Clinical studies evaluating various pump models have identified contact sites between moving parts as stagnation points and local heat sources [8, 12]. Consequently contact sites are potential sources of thromboembolic build up and may cause blood damage. The use of a chronic implantable VAD based on rotary blood pump technology is not a feasible option until a simple, durable alternative to the shaft seal is developed. Many approaches have been suggested to solve these problems, primarily involving minimising the contact area between moving parts and maximising “washing” [5, 6].

Other suggestions involved the elimination of all sites of mechanical contact. In such pumps the impeller is rotated about the pump axis by means of electromagnetic interaction between permanent magnets embedded within each blade and the rotating magnetic field produced by the motor stator. Such designs involve the use of magnetic, hydrostatic and hydrodynamic forces for support of the rotating assembly, where each suspension method has its own advantages and disadvantages.

For example, a disadvantage of current active magnetically suspension systems is the large power requirement, typically in the range of 5-16 W in addition to the power required to actuate the pump rotor [7]. Furthermore, the extra hardware, including proximity sensors and electromagnets, add bulk and extra weight whereas increased complexity of the control circuitry may compromise reliability. These problems can be partially solved through the exclusive or combined use of bearings such as permanent magnets, hydrostatic and hydrodynamic pressure bearings [8] which are passive and therefore require no power. Conversely, the advantage of pumps utilising active magnetic suspension systems is that impeller stability is adequately maintained as enough (i.e. excess) power is readily available to provide a restoring force of appropriate magnitude in response to a large disturbance [4, 9]. However, this is not the case for passive suspension systems. For example, in regards to a hydrodynamic

suspension system, increasing the restoring force involves either altering the geometry of the impeller blades, increasing the rotational speed, or decreasing the clearance gap between the impeller and the pump housing [10]. If disturbances applied to the pump exceed the pre-existing load capacity of a passive suspension system then touchdown will undoubtedly occur. As a conservative guide, the load capacity of such a suspension system must be in excess of approximately 1,150g, resulting from the combination of up to 1,000g due to a pressure increase across the pump from changes in the incoming blood or aortic pressure [8], approximately 35-45g due to the weight of the impeller, up to 100-200g due to imbalances in the rotor drive magnets [11], approximately 10-20g due to the asymmetric structure of any centrifugal pump [8], and additional loads caused by movement of the patient [12].

2.2. *The VentrAssist hydrodynamically suspended impeller*

The VentrAssist impeller consists of four thick blades connected by rigid struts. Blood enters the impeller axially where it is accelerated by the exertion of a force via the rotating impeller and subsequently passes radially either above or below the struts as indicated in Figure 2.1. The front and back faces the impeller blades are each tapered such that the small gaps between themselves and the appropriate half of the pump housing are larger at the leading edge of each blade than at the trailing edge. When rotating the impeller is suspended hydrodynamically as blood from within the pump volume is drawn into the these gaps which, as a result of the taper, will be subject to increasing constriction and generate a pressure which acts to increase the thickness of the lubricating film of blood. By this means the top and bottom bearings together produce a net force that maintains separation of the impeller from both the top and bottom of the pump housing such that ideally the impeller “floats” within the pump volume without contacting the pump housing. To go one step further, the film thickness

should be kept as large as possible and must not be allowed to drop below $8\mu\text{m}$, the diameter of red blood cells.

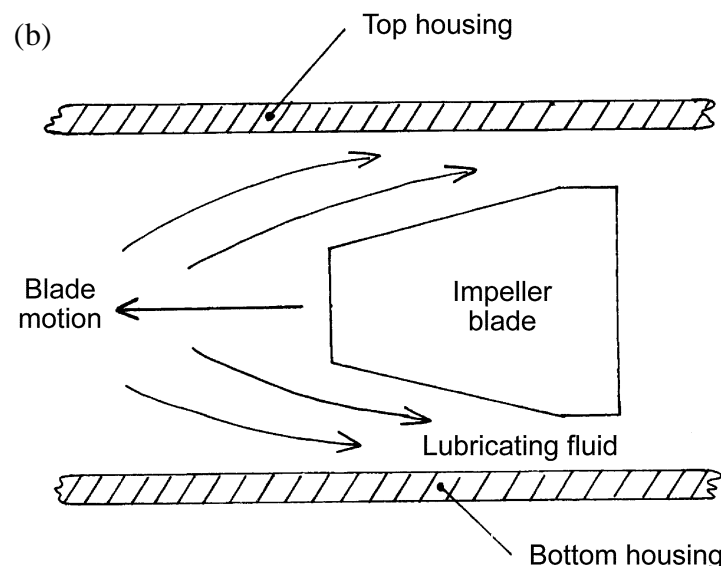
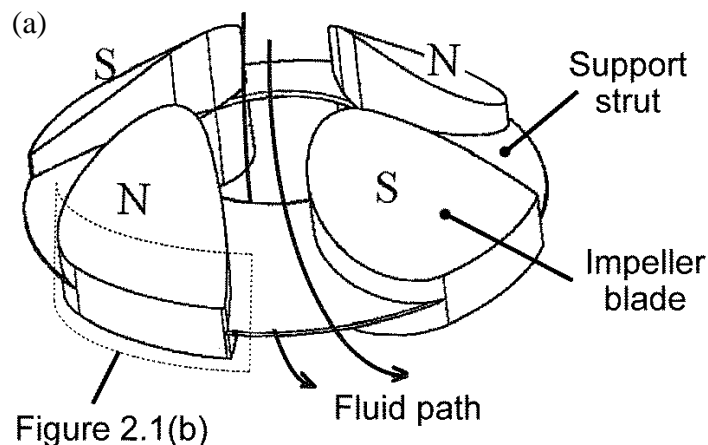


Figure 2.1. (a) The schematic drawing shows the VentrAssist impeller, Tear Drop rotor 2.4, indicating fluid flow paths and magnet polarities (Source: Watterson *et al.* [10]); (b) This diagram shows an idealised constant radius section through a blade, dashed in (a). Note the tapered and untapered land sections (Source: Modified from Watterson *et al.* [10])

The shape of the VentrAssist impeller has evolved significantly from the initial concept design known as the Block rotor 1.1, pictured in Figure 2.2(a), where the leading and trailing edges of the bearing surfaces are parallel. More recent designs, the Sector rotor 2.2, the Shark Fin rotor 2.8 and the Tear Drop rotor 2.9, are pictured in Figures 2.2(b), 2.2(c) and 2.2(d) respectively. Furthermore, the profile of the taper on each bearing surface of early impeller models was a $50\mu\text{m}$ linear taper, whereas recent designs take advantage of the higher load capacity of a tapered land configuration. See section 3.2. for details.

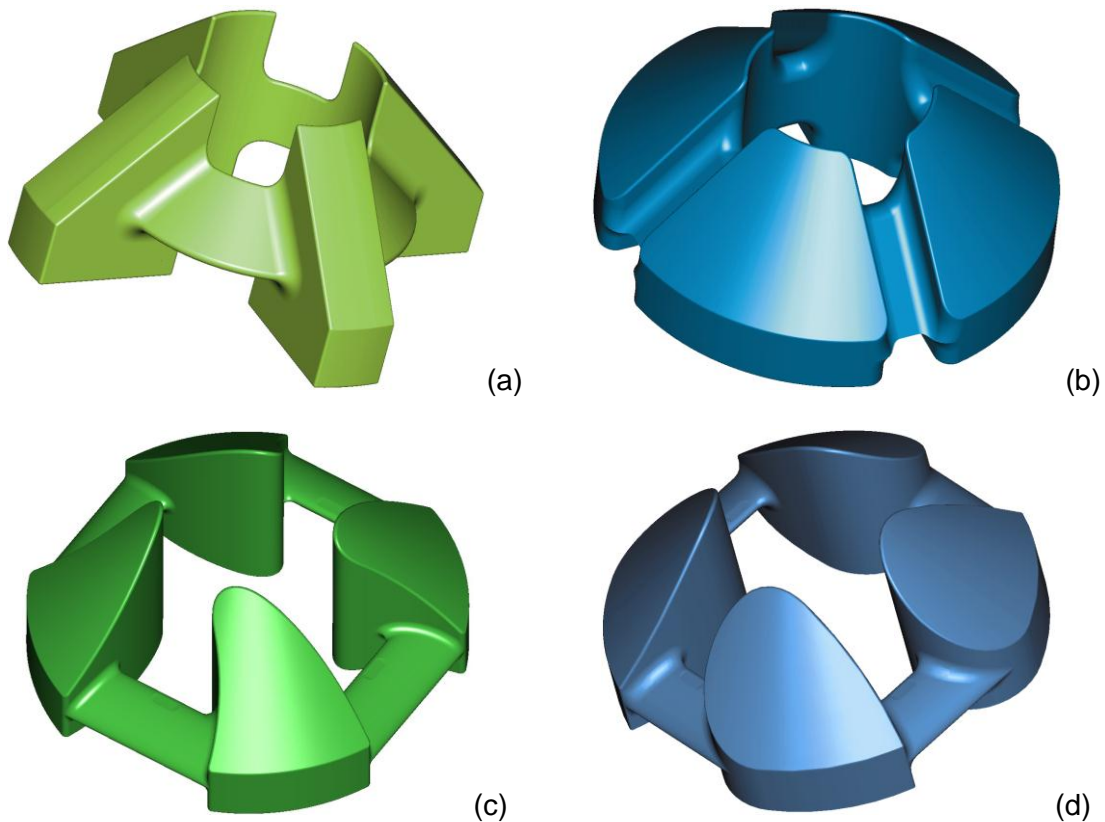


Figure 2.2. The impellers used in the VentrAssist IRBP are the (a) Block rotor 1.3, (b) Sector rotor 2.2, (c) Shark Fin rotor 2.8, and (d) Tear Drop rotor 2.9.

2.3. Stability

The mechanical properties of the lubricating film combined with the mass of the rotating shaft constitute a damped spring-mass system. When placed into motion, oscillation will take place at the natural frequency of the system or, if subjected to a forcing function will vibrate at the same frequency as that of the excitation. As for any mechanical system the natural frequency is primarily a function of the mass and stiffness of the system. To some small extent, damping lowers the natural frequency, although plays a large part in reducing the amplitude of vibration with time.

Depending on the operating conditions, the vibration in a bearing-rotor system usually occurs at a frequency just under half the rotational speed of the shaft. Such vibration is commonly known as “whirl”, “half-synchronous whirl”, or “half-frequency whirl”. There are two types of whirl, cylindrical (translatory) and conical, both named for the shape traced by the shaft centre during the vibration. Whirl in high speed turbo-machinery often leads to instability, characterised by large amplitude motion and in severe cases contact may occur between the journal and bush. Before proceeding further, a definition of stability is required.

A bearing-rotor system can be considered stable if the rotor, once disturbed, returns to its initial position or equilibrium state i.e. if the oscillations decay in time. The system may be considered critically stable, or on the threshold of stability, if the oscillations of vibration continue forever without a change in the vibration amplitude. Furthermore, such a system is unstable if the oscillations increase without bound, with possibly disastrous results if the amplitude becomes equal to the bearing clearance.

There are two basic approaches in assessing the stability of a bearing-rotor system – the linearised (perturbation) method and the method of non-linear transient analysis.

2.3.1. The linearised (perturbation) method

The linearised (perturbation) method is best explained by the example of a stiff symmetric rotor running in two identical bearings. Such a system has two DOF, x and y. The following details are modified from Cameron *et al.* [13], Agrawal [14] and Akkök *et al.* [15].

The linearised equations of motion about the equilibrium position may be written

$$\begin{aligned} M\ddot{x} + a_{xx}x + a_{xy}y + b_{xx}\dot{x} + b_{xy}\dot{y} &= 0 \\ M\ddot{y} + a_{yy}y + a_{yx}x + b_{yy}\dot{y} + b_{yx}\dot{x} &= 0 \end{aligned} \quad (2.1)$$

where $2M$ is the mass of the rotor, a_{xx} is the direct stiffness coefficient corresponding to the restoring force in the x-direction following a displacement perturbation in that same direction, and a_{xy} is the cross stiffness coefficient corresponding to the restoring force in the x-direction following a displacement in the y-direction. Further, b_{xx} is the direct damping coefficient corresponding to the restoring force in the x-direction consequent on a velocity perturbation in the same direction, and b_{xy} is the cross damping coefficient corresponding to the restoring force in the x-direction following a velocity perturbation in the y-direction. Remaining coefficients a_{yy} , a_{yx} , b_{yy} , and b_{yx} can be similarly defined. The presence of cross stiffness and damping terms indicate that a load applied in a single coordinate direction is accompanied by displacements in both coordinate directions.

These linearised stiffness and damping coefficients are basically the slope of the force-displacement and force-velocity curves at zero displacement and velocity respectively and can be found as follows. To begin with, the loads W_x and W_y on the shaft in the equilibrium position (x_0, y_0) are found. In order to find the spring constants the

velocities are set to zero, i.e. $\dot{x} = \dot{y} = 0$, and the shaft is given a small displacement Δx in the x-direction from the equilibrium position to new shaft position (x, y_0) where $\Delta x = (x - x_0)$. The resultant loads W_{xx} and W_{yx} in the x- and y-directions, respectively, are computed. The first two stiffness coefficients are then

$$a_{xx} = (W_{xx} - W_x)/\Delta x \text{ and } a_{yx} = (W_{yx} - W_y)/\Delta x \quad (2.2)$$

Furthermore, the shaft is given a small displacement Δy in the y-direction from the equilibrium position to new shaft position (x_0, y) where $\Delta y = (y - y_0)$ and resultant loads W_{yy} and W_{xy} in the y- and x-directions, respectively, are subsequently computed.

Then the remaining stiffness coefficients are given by

$$a_{yy} = (W_{yy} - W_y)/\Delta y \text{ and } a_{xy} = (W_{xy} - W_x)/\Delta y \quad (2.3)$$

In a similar manner the damping coefficients are found by first giving the shaft a small velocity perturbation \dot{x} in the x-direction about the equilibrium position of the shaft whilst keeping $\dot{y} = 0$. The resultant loads W'_{xx} and W'_{yx} in the x- and y-directions, respectively, are computed. The first two damping coefficients are given by

$$b_{xx} = (W'_{xx} - W_x)/\dot{x} \text{ and } b_{yx} = (W'_{yx} - W_y)/\dot{x} \quad (2.4)$$

Furthermore, a small velocity \dot{y} in the y-direction is then applied to the shaft about the equilibrium position whilst setting $\dot{x} = 0$. The resultant loads W'_{yy} and W'_{xy} in the y- and x-directions, respectively, are then computed and the remaining damping coefficients are found from

$$b_{yy} = (W'_{yy} - W_y)/\dot{y} \text{ and } b_{xy} = (W'_{xy} - W_x)/\dot{y} \quad (2.5)$$

Substituting the following non-dimensional variables

$$X = x/c; Y = y/c; A = ac/F; B = bc\omega/F; T = \omega t$$

where c is the bearing clearance, F is the force on the bearing, and ω is the angular velocity of the bearing, equation (2.1) can be written in the following non-dimensional form

$$\begin{aligned}\ddot{X}/S_0 + A_{xx}X + A_{xy}Y + B_{xx}\dot{X} + B_{xy}\dot{Y} &= 0 \\ \ddot{Y}/S_0 + A_{yy}Y + A_{yx}X + B_{yy}\dot{Y} + B_{yx}\dot{X} &= 0\end{aligned}\quad (2.6)$$

where $S_0 = F/Mc\omega^2$ is the stability parameter.

The standard method of solution is to assume the motion given by

$$X = K_1 e^{\lambda T} \text{ and } Y = K_2 e^{\lambda T} \quad (2.7)$$

and furthermore

$$\begin{aligned}\dot{X} &= \lambda K_1 e^{\lambda T} = \lambda X \text{ and } \ddot{X} = \lambda^2 K_1 e^{\lambda T} = \lambda^2 X \\ \dot{Y} &= \lambda K_2 e^{\lambda T} = \lambda Y \text{ and } \ddot{Y} = \lambda^2 K_2 e^{\lambda T} = \lambda^2 Y\end{aligned}\quad (2.8)$$

Upon substitution of equation sets (2.7) and (2.8), equation (2.6) becomes

$$\begin{bmatrix} \lambda^2/S_0 + A_{xx} + B_{xx}\lambda & A_{xy} + B_{xy}\lambda \\ A_{yx} + B_{yx}\lambda & \lambda^2/S_0 + A_{yy} + B_{yy}\lambda \end{bmatrix} \begin{bmatrix} X \\ Y \end{bmatrix} = 0 \quad (2.9)$$

For a non-trivial solution the determinant must be zero. That is,

$$\det \begin{bmatrix} \lambda^2/S_0 + A_{xx} + B_{xx}\lambda & A_{xy} + B_{xy}\lambda \\ A_{yx} + B_{yx}\lambda & \lambda^2/S_0 + A_{yy} + B_{yy}\lambda \end{bmatrix} = 0 \quad (2.10)$$

Expansion of equation (2.10) yields a fourth-order polynomial in λ known as the characteristic equation. The characteristic equation has four roots, which are usually complex and occur in conjugate pairs,

$$\lambda_{1,2} = \alpha_1 \pm i\beta_1 \text{ and } \lambda_{3,4} = \alpha_2 \pm i\beta_2 \quad (2.11)$$

where the real part of the complex eigenvalues, the α terms, represent damping and determine whether the vibration, once initiated, will grow, continue unaltered or decay. The imaginary part of the complex eigenvalues, the β terms, represent the corresponding frequency of this motion. More specifically, the system stability depends on the largest value of α_1 and α_2 . For example, under the condition that $\alpha_1 > \alpha_2$, if $\alpha_1 > 0$ then the system is unstable and the motion will grow. If $\alpha_1 = 0$ the system lies on the threshold of instability and the motion will continue forever. If $\alpha_1 < 0$ the system is stable and the vibration will decay. In fact, if $\alpha_1 \ll 0$ then the damping is strong and the shaft, when disturbed, will return more quickly to the equilibrium position. Based on how close α_1 is to zero, the linearised method gives a measure of the reserve of stability.

Once the eight linearised coefficients have been evaluated, the numerical values of the real and imaginary parts of the roots can be found by assuming a value of S_0 . In this way, the values of S_0 corresponding to the threshold of stability (i.e. when $\alpha_1 = 0$) are plotted over a range of eccentricity ratios $\varepsilon \approx 0.0 - 1.0$ thereby indicating regions of stability and instability. Typically, the region of stability is situated above this curve, and the region of instability below.

Stachowiak *et al.* [16] details a computer program which calculates the eight linearised stiffness and damping coefficients for a partial arc journal bearing using the linearised (perturbation) method and, by subsequently calculating the threshold speed at the onset of vibration using the Routh-Hurwitz criterion of stability, plotted a stability map.

The response of the journal is highly non-linear and the solution obtained through the use of constant coefficients A and B is only valid for small displacements about the

equilibrium position. Makdissi [17] suggested that the hydrodynamic fluid film forces can be considered to be linear for running eccentricity ratios up to 0.8 provided that the peak-to-peak amplitude of vibration of the journal does not exceed 0.4 times the radial clearance. Therefore, under these conditions, the dynamic properties of the lubricating film may be represented by eight linear stiffness and damping coefficients. On the other hand, Holms [18] concluded that, up to an eccentricity ratio of 0.7, the non-linearity of the system should only be taken to account for vibrations larger than about one third of the radial clearance. Akk  k et al. [15] measured the stiffness coefficients where small increments of load were applied in the x- and y-directions. The forces were large enough such the resulting displacements could be accurately measured but kept below 0.3 of the radial clearance so as to not deviate outside the “linear” range. Good agreement was found between these measured values and the theoretical coefficients, justifying use of the linearised perturbation method under such conditions. However, if suspected that severe whirl and therefore large amplitude oscillations may occur, the linearised method is insufficient and non-linear methods should be employed.

Agrawal [14] and Akk  k et al. [15] each investigated the stability of a rigid shaft supported by two hydrodynamic journal bearings using the linearised (perturbation) method. To simplify the problem, both assumed the rotor to have only two DOF and considered the supporting bearings to be identical. As a result, only two equations of motion were required and eight linearised stiffness and damping coefficients needed to be found in order to determine system stability. However, the complexity of the linearised method drastically increases as the number of DOF increases. That is, with regards to the VentrAssist impeller, which has 5 (3 translational, 2 rotational) DOF, five equations of motion are involved and the linearised method would require the evaluation of 25 stiffness coefficients and 25 damping coefficients. Furthermore, the characteristic equation would be a tenth-order polynomial in λ with 5 pairs of complex

roots. Such a task is unrealistic and upon consideration of the limitations of the linearised method previously discussed and to be discussed in the following section, it was deemed more practical to perform a non-linear transient analysis.

2.3.2. Non-linear transient analysis

In this method, the position of the shaft centre is traced from some arbitrary starting point using a step-wise progression technique. By observing the subsequent motion, known as the shaft “trajectory”, “locus” or “orbit”, the stability of the system can be deduced. If stable, in the presence of forcing (i.e. from unbalance) the motion will settle into a repetitive orbit known as a “limit cycle”. In the absence of forcing the motion will decay inwards to a point. The rate of decay gives a measure the level of damping and therefore of the “stability reserve”. That is, if the decay is rapid the system damping is high and the system is far from critical. However, if the decay is slow, the damping is low and the system is close to the stability threshold. If unstable, the trajectory will spiral outwards until contact between the journal and bush occurs. However, in many cases it is found that a touch does not occur despite indications of instability from the linearised method.

Akkök *et al.* [15] experimentally obtained the critical value of the stability parameter $S_0 = F/Mc\omega^2$ by running the shaft at a certain speed ω and then by gradually reducing the applied load F until whirl was initiated. Upon comparison, it was shown that the threshold speeds obtained experimentally were typically 50 percent higher than the threshold speeds given by linear theory. Akkök *et al.* termed this phenomenon “spread”. Makdissi [17] explained and experimentally verified that rotors pass through a “transitional zone” when shifting from stable to unstable operating conditions, and altered the traditional form of the stability map such that the stable and unstable

regions were separated by a transitional zone rather than a single line. Makdissi concluded that while the journal is operating in this transitional zone, the non-linearity of the fluid film is present even for infinitesimal movements of the journal centre which can be offered as a possible explanation for the occurrence of spread. A further advantage of the non-linear transient analysis method is that a Fourier Transform can be performed such that the frequency spectra of the orbit can be determined and analysed.

As an example of how stability is assessed by observation of the journal trajectory, the work of Crosby [19] is briefly repeated herein. Crosby performed a non-linear stability analysis of a rigid rotor supported in fluid film journal bearings subjected to a unidirectional steady load and unbalance load. The rotor was restricted to plane motion (i.e. 2 translational DOF) and therefore cylindrical whirl only was considered. The two non-linear second-order differential equations of motion were solved simultaneously to predict the transient behaviour of the journal centre using a fourth-order Runge-Kutta method where the position (ε, ϕ) and velocities $\dot{\varepsilon}$ and $\dot{\phi}$ of the journal centre were calculated at each discrete time step starting from initial position (ε_0, ϕ_0) . The initial values of the velocities $\dot{\varepsilon}_0$ and $\dot{\phi}_0$ were set to zero, thereby simulating an initial position disturbance. Journal centre trajectories were plotted for various external loads F_e and unbalance force F_u . A stability map was created by observation of the trajectories corresponding to the balanced rotors. This map is shown in Figure 2.3 and consists of the normalised rotational speed $\bar{\omega} = \omega(cm/F_e)^{1/2}$ plotted on the abscissa and the eccentricity ratio ε on the ordinate. The numerals refer to the figure numbers of the corresponding trajectory plots.

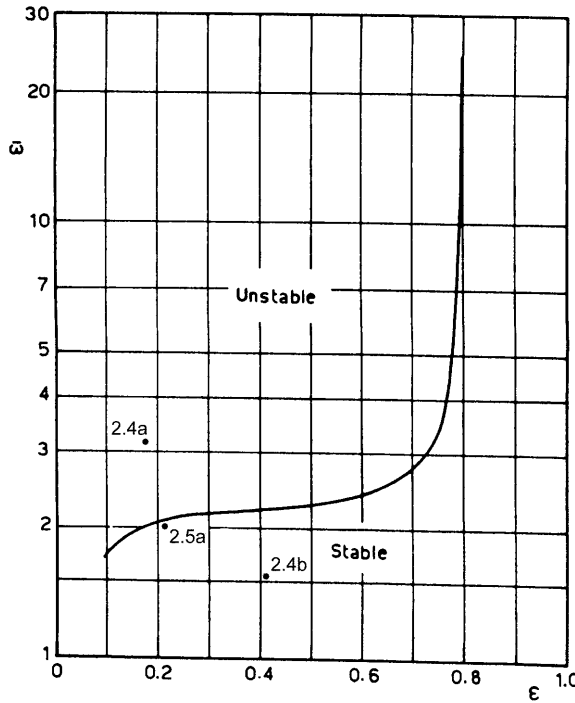


Figure 2.3. Stability curve for a loaded balanced journal bearing ($L/D = 1$) (Source: Crosby [19]).

Figure 2.4a shows the orbit of the journal centre running at $\omega = 500\text{Hz}$ ($\bar{\omega} = 3.14$) and carrying an external load of $F_e = 5\text{kN}$ with an equilibrium eccentricity ratio of $\epsilon = 0.18$. The trajectory is started at an eccentricity ratio of $\epsilon_0 = 0.25$ and is seen to spiral outwards towards the clearance circle, indicating an unstable performance. In Figure 2.4b the load is kept constant and the speed is decreased to 250Hz ($\bar{\omega} = 1.57$). Starting at $\epsilon_0 = 0.55$, the orbit spirals inwards with decreasing radius and approaches the equilibrium point of $\epsilon = 0.405$, indicating that the system is stable. In Figure 2.5a the speed remains at $\omega = 250\text{Hz}$ but the load is decreased to $F_e = 3\text{kN}$, giving a normalised rotational speed of $\bar{\omega} = 2.02$ and equilibrium eccentricity ratio of 0.214. Starting at $\epsilon_0 = 0.25$, the trajectory slowly spirals outwards reaching a limit cycle, indicating that that bearing is stable but close to threshold. From the stability map of Figure 2.3, it is clear that the bearing is stable for all speeds for equilibrium eccentricity ratios above 0.8.

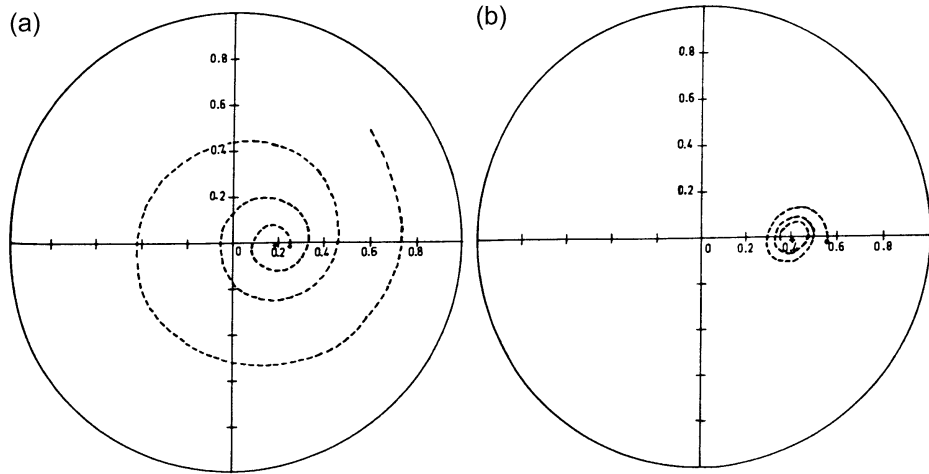


Figure 2.4. Journal trajectory for a balanced horizontal rotor (a) $L/D = 1$; $F_e = 5\text{kN}$; $\omega = 500\text{Hz}$, and (b) $L/D = 1$; $F_e = 5\text{kN}$; $\omega = 250\text{Hz}$ (Source: Crosby [19]).

By introducing an unbalance force of $F_u = 1\text{kN}$ the journal became unstable, as shown by the trajectory of Figure 2.5b. However, if F_u is further increased to $F_u = 11.25\text{kN}$, the trajectory of Figure 2.6 reaches a limit cycle, indicating that the system is now stable. These observations agree with the results of Akkök *et al.* [15] and Pai *et al.* [20] who each concluded that a stable journal with a constant load may be made unstable by superimposing a transient or periodic load on the system such as a pulse or unbalance force respectively. However, Makdissi [17] found that an unbalance force reduces the transient time for the journal to reach a stationary response in both stable and unstable zones of operation and additionally that the larger the unbalance force, the more stable the fluid film behaves.

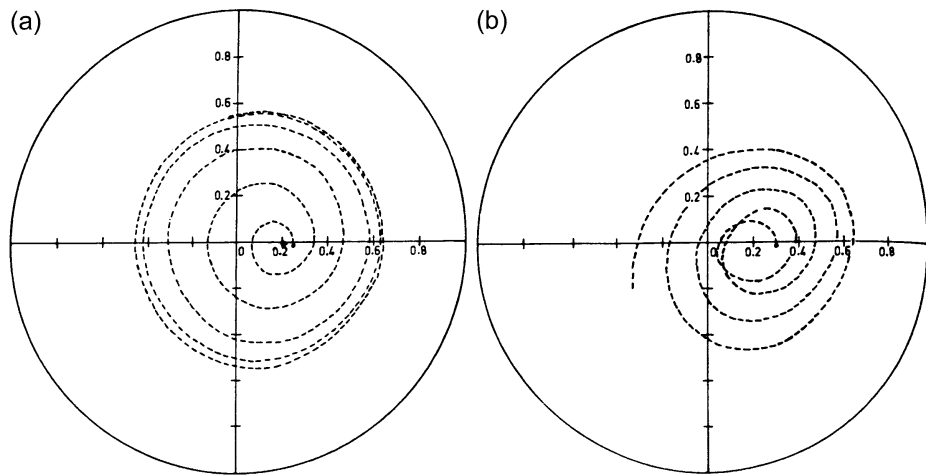


Figure 2.5. (a) Journal trajectory for a balanced rotor ($L/D = 1$; $F_e = 3\text{kN}$; $\omega = 250\text{Hz}$); (b) Journal trajectory for an unbalanced horizontal rotor ($L/D = 1$; $F_e = 3\text{kN}$; $F_u = 1\text{kN}$; $\omega = 250\text{Hz}$) (Source: Crosby [19]).

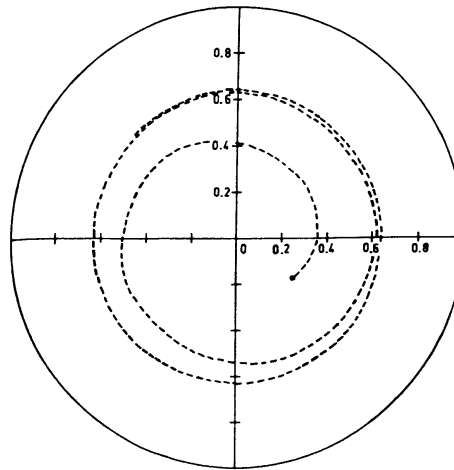


Figure 2.6. Journal trajectory for an unbalanced horizontal rotor
($L/D = 1$; $F_e = 3\text{kN}$; $F_u = 11.25\text{kN}$; $\omega = 250\text{Hz}$) (Source: Crosby [19]).

Pai *et al.* [21] performed a non-linear transient analysis of unloaded submerged oil journal bearings to investigate conical whirl instability. The bearing was assumed to have two rotational degrees of freedom, rotations about the x - and y - axes denoted by ψ_x and ψ_y respectively. Special consideration was given to the specification of pressure boundary conditions with the reason that the instability threshold is sensitive

to the oil film extent. The non-dimensional moments on the journal about the x- and y-directions, \bar{M}_x and \bar{M}_y respectively, were calculated by integration of the pressure field over the journal surface. Using these moment components the equations of motion were solved by a fourth-order Runge-Kutta method to get the non-dimensional angular rotations $\bar{\psi}_x$, $\bar{\psi}_y$ and their derivatives $\dot{\bar{\psi}}_x$ and $\dot{\bar{\psi}}_y$ at each discrete time step. Several plots of the journal centre trajectory on a plane at the edge of the bearing are given and observed to assess the system stability. Defining $\bar{J} = \bar{I}_P / \bar{I}_T$, where \bar{I}_P and \bar{I}_T are the non-dimensional polar and transverse moments of inertia of the journal respectively, Pai *et al.* found that an increase in \bar{J} makes the journal more stable in regards to conical whirl. Interestingly, it was also concluded that an increase in \bar{I}_T with L/D and \bar{J} kept constant makes the journal reach its stability point faster, whereas an increase in L/D with \bar{J} and \bar{I}_T kept constant makes the journal reach its stability point more slowly.

Chapter 3 – Theoretical methodology

This chapter details the theory behind the non-linear transient analysis employed by this study to evaluate the stability of the VentrAssist impeller. More specifically, this includes the hydrodynamic theory used to obtain the pressure distribution over the thrust bearing and conical journal bearing surfaces of the impeller. The trapezoidal rule of integration is used to calculate the resulting forces (and/or moments) acting to translate (and/or tilt) the impeller which are used as input to the equations of motion. These five equations are solved by the classical Runge-Kutta method, where the position of the impeller is “marched-out” in a series of time steps to obtain the impeller “trajectory”. The “stability” of the impeller at the particular running conditions may be determined by observation of the trajectory.

3.1. Reynolds equation

In order to study the dynamic properties of the VentrAssist impeller, it is necessary to compute the pressures which are generated within the fluid film due to the hydrodynamic action. These pressures, from which the forces on the impeller are derived, can be obtained by solving the Reynolds equation over the lubricated bearing surfaces of the impeller blades.

3.1.1. Assumptions for hydrodynamic theory

The assumptions for hydrodynamic theory are [22]:

- 1) Body forces are neglected. This means that there is no outside field of force, such as a gravitational or magnetic force, acting on the lubricant. The validity of

this assumption is not certain considering that the lubricant, blood, is a conducting fluid and magneto hydrodynamics are involved;

- 2) The pressure is constant through the thickness of the film. This assumption is valid as the fluid film is typically very thin (in the order of a few microns);
- 3) The curvatures of the bearing surfaces are large in comparison with the thickness of the fluid film;
- 4) There is no slip at the bounding surfaces. This means that the velocities of the outer layers of the lubricant film are the same as the surfaces to which they are adjacent;
- 5) The lubricant is Newtonian;
- 6) The flow is laminar. This means that no vortex flow or turbulence occur at any point in the bearing. The validity of this assumption depends on the dimensions and speed of the bearing. Qian *et al.* [23] note that turbulent flow occurs in tapered bearings when the mean-gap Reynolds number exceeds 1000. That is, when $\rho d_m U / \eta > 1000$, where d_m is taken as the average of the film thicknesses at the leading and trailing edge of the bearing. Considering a minimum film thickness of $180\mu\text{m}$ (note that the total axial impeller travel is typically $200\mu\text{m}$) which corresponds to a mean gap of $d_m = 205\mu\text{m}$ with a $50\mu\text{m}$ taper, the maximum Reynolds number was 943;
- 7) The inertia of the fluid can be neglected if the flow is laminar i.e. if $\rho d_m U / \eta < 1000$. See assumption 6 for details;
- 8) The viscosity is constant through the thickness of the film;
- 9) Compared with the rotational velocity of the bearing, all translational velocities are negligible (an additional assumption made by the author – not formally an assumption of hydrodynamic theory).

Reynolds originally derived the Reynolds equation from the Navier-Stokes equations. The following is a much simpler derivation, although arrives at the same equation as the Navier-Stokes equations under the same assumptions.

It is necessary to consider first the equilibrium of a small fluid element under the action of both viscous shear stresses and fluid pressure, followed by satisfying the continuity of flow of a fluid column.

3.1.2. *Derivation of Reynolds equation*

The Reynolds equation was originally derived in Cartesian coordinates although may be subsequently transformed into other coordinate systems which are more appropriate to the respective geometry. For the VentrAssist impeller, cylindrical coordinates are convenient for describing the thrust bearing of the impeller, whereas spherical coordinates are convenient for describing the conical journal bearing. Thus, Reynolds equation will be initially derived in Cartesian coordinates and then transformed into cylindrical and spherical coordinates using vector analysis. The following derivation has been adapted from Cameron [22].

3.1.2.1. *Equilibrium of an element of fluid*

Consider the equilibrium of a small element of fluid from a hydrodynamic film as shown in Figure 3.1. The element has sides of length dx , dy and dz where initially the forces in the x-direction only are considered.

Acting on the left face, of area $dydz$, is a pressure p and corresponding force $pdydz$, which acts to the right. On the right face the pressure is

$$p + \left(\frac{\partial p}{\partial x} \right) dx$$

and the corresponding force on this face, which acts to the left, is

$$\left[p + \left(\frac{\partial p}{\partial x} \right) dx \right] dy dz$$

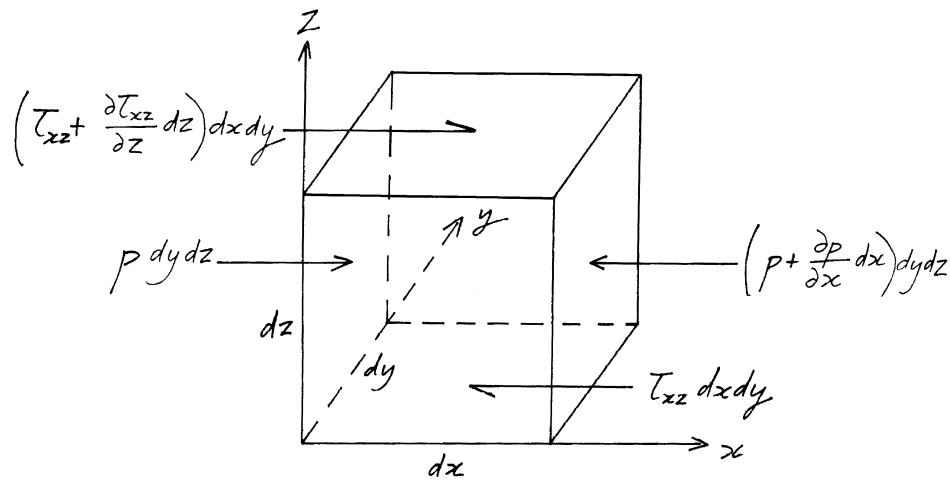


Figure 3.1. Equilibrium of an element of lubricating fluid

On the bottom face, of area $dx dy$, there is a shear stress τ_{xz} (where τ_{ij} refers to a shear acting on the j face and in the i direction) and a corresponding force $\tau_{xz} dx dy$ acting to the left. On the top face the shear stress is

$$\tau_{xz} + \left(\frac{\partial \tau_{xz}}{\partial z} \right) dz$$

and the shear force is

$$\left[\tau_{xz} + \left(\frac{\partial \tau_{xz}}{\partial z} \right) dz \right] dx dy$$

which acts to the right.

For equilibrium, the forces acting to the left must balance the forces acting to the right, so

$$pdydz + \left[\tau_{xz} + \left(\frac{\partial \tau_{xz}}{\partial z} \right) dz \right] dxdy = \left[p + \left(\frac{\partial p}{\partial x} \right) dx \right] dydz + \tau_{xz} dxdy$$

which yields

$$\frac{\partial \tau_{xz}}{\partial z} dxdydz = \frac{\partial p}{\partial x} dxdydz$$

which, since $dxdydz$ is an arbitrary non-zero volume, can be simplified to give

$$\frac{\partial \tau_{xz}}{\partial z} = \frac{\partial p}{\partial x} \quad (3.1a)$$

Following a similar procedure for forces in the y-direction, it can be shown that

$$\frac{\partial \tau_{yz}}{\partial z} = \frac{\partial p}{\partial y} \quad (3.1b)$$

The pressure gradient in the z-direction is equal to zero since the pressure is constant throughout the film thickness (assumption 2), so $\partial p / \partial z = 0$.

For a Newtonian fluid (assumption 5), Newton's law of viscous flow is used to relate shear stress to the shear rate via dynamic viscosity η , which states:

$$\tau_{xz} = \eta \frac{\partial u}{\partial z} \quad (3.2a)$$

and

$$\tau_{yz} = \eta \frac{\partial v}{\partial z} \quad (3.2b)$$

where u and v are the particle velocities in the x- and y- directions. If these expressions are substituted into equations (3.1a) and (3.1b), and assuming constant

viscosity through the thickness of the film ($\partial\eta/\partial z = 0$ - assumption 8), then the statement of equilibrium can be written, with respect to the x-direction,

$$\frac{\partial p}{\partial x} = \eta \frac{\partial^2 u}{\partial z^2} \quad (3.3a)$$

and, with respect to the y-direction,

$$\frac{\partial p}{\partial y} = \eta \frac{\partial^2 v}{\partial z^2} \quad (3.3b)$$

Equation (3.3a) and (3.3b) can be integrated to give the pressure gradient in terms of the respective velocity at either surface. That is, considering the x-direction only, and remembering that p and η are independent of z , then

$$\frac{\partial u}{\partial z} = \frac{1}{\eta} \cdot \frac{\partial p}{\partial x} z + C_1 \quad (3.4)$$

which, upon further integration yields

$$u = \frac{1}{\eta} \cdot \frac{\partial p}{\partial x} \cdot \frac{z^2}{2} + C_1 z + C_2 \quad (3.5)$$

where C_1 and C_2 are constants of integration that need two boundary conditions for their evaluation that are found upon consideration of a fluid column.

3.1.2.2. Equilibrium of a fluid column

Consider a column of lubricant of height h , the local film thickness, and cross-sectional area $dxdy$ as shown in Figure 3.2. The top surface at $z = h$ moves at velocity in the x-direction of $U_{x,1}$, and the bottom bounding surface at $z = 0$ moves at a velocity $U_{x,2}$ in the x-direction. Assuming that the fluid in contact with the bounding surfaces has the same velocity as that surface (no slip condition – assumption 4), then the boundary conditions are

$$u = U_{x,1} \text{ at } z = h$$

$$u = U_{x,2} \text{ at } z = 0$$

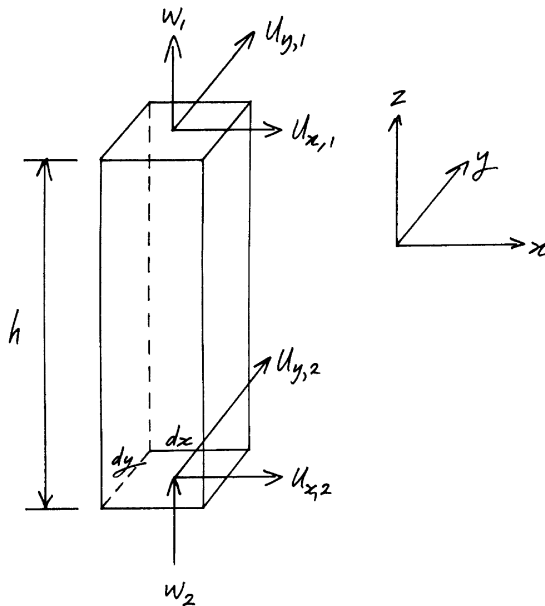


Figure 3.2. Column of lubricant

On substitution of these boundary conditions into equations (3.4) and (3.5) gives

$$C_1 = \left(\frac{U_{x,1} - U_{x,2}}{h} \right) - \frac{1}{\eta} \cdot \frac{\partial p}{\partial x} \cdot \frac{h}{2} \text{ and } C_2 = U_{x,2}$$

Upon back substitution of these constants, equations (3.4) and (3.5) become

$$\frac{\partial u}{\partial z} = \frac{1}{\eta} \cdot \frac{\partial p}{\partial x} \left(z - \frac{h}{2} \right) + \left(\frac{U_{x,1} - U_{x,2}}{h} \right) \quad (3.6)$$

and

$$u = \frac{1}{2\eta} \cdot \frac{\partial p}{\partial x} \left(z^2 - zh \right) + \left(U_{x,1} - U_{x,2} \right) \frac{z}{h} + U_{x,2} \quad (3.7)$$

If the upper bounding surface has velocity $U_{y,1}$ in the y -direction, and the lower boundary has velocity $U_{y,2}$ then, following the same procedure, it can be shown that

$$\frac{\partial v}{\partial z} = \frac{1}{\eta} \cdot \frac{\partial p}{\partial y} \left(z - \frac{h}{2} \right) + \left(\frac{U_{y,1} - U_{y,2}}{h} \right) \quad (3.8)$$

and

$$v = \frac{1}{2\eta} \cdot \frac{\partial p}{\partial y} \left(z^2 - zh \right) + \left(U_{y,1} - U_{y,2} \right) \frac{z}{h} + U_{y,2} \quad (3.9)$$

The rate of lubricant flow in the x -direction per unit width of y , q_x , is given by the integral of the velocity over the film thickness

$$q_x = \int_0^h u dz = \int_0^h \left\{ \frac{1}{2\eta} \cdot \frac{\partial p}{\partial x} \left(z^2 - zh \right) + \left(U_{x,1} - U_{x,2} \right) \frac{z}{h} + U_{x,2} \right\} dz$$

which simplifies to

$$q_x = \left(U_{x,1} + U_{x,2} \right) \frac{h}{2} - \frac{h^3}{12\eta} \frac{\partial p}{\partial x} \quad (3.10)$$

In a similar manner, the rate of lubricant of flow in the y -direction per unit width of x , q_y , can be shown to be

$$q_y = \left(U_{y,1} + U_{y,2} \right) \frac{h}{2} - \frac{h^3}{12\eta} \frac{\partial p}{\partial y} \quad (3.11)$$

The volume flow rate of lubricant into the left face of the column, in the x -direction, is therefore $q_x dy$, as q_x is lubricant flow in the x -direction per unit width and dy is the width of the column. The amount of lubricant flowing out of the right face of the column in the x -direction is

$$\left[q_x + \left(\frac{\partial q_x}{\partial x} \right) dx \right] dy$$

where $q_x + (\partial q_x / \partial x)dx$ is the rate at which lubricant flows out of the column per unit width of y. Similarly, lubricant flows into the front face of the column in the y-direction at a rate of $q_y dx$ and out of the back face of the column in the y-direction at a rate of

$$\left[q_y + \left(\frac{\partial q_y}{\partial y} \right) dy \right] dx$$

where $q_y + (\partial q_y / \partial y)dy$ is the rate at which lubricant flows out of the column per unit length of x.

The net rate of lubricant inflow in the x-direction is given by

$$q_x dy - \left[q_x + \left(\frac{\partial q_x}{\partial x} \right) dx \right] dy = - \left(\frac{\partial q_x}{\partial x} \right) dxdy \quad (3.12)$$

Similarly, the net rate of lubricant inflow in the y-direction is

$$q_y dx - \left[q_y + \left(\frac{\partial q_y}{\partial y} \right) dy \right] dx = - \left(\frac{\partial q_y}{\partial y} \right) dxdy \quad (3.13)$$

The total inflow is the sum of equations (3.12) and (3.13), which yields

$$- \left(\frac{\partial q_x}{\partial x} + \frac{\partial q_y}{\partial y} \right) dxdy \quad (3.14)$$

If the bottom surface is given a velocity w_2 in the z-direction, the volume of the column will decrease at a rate of $w_2 dxdy$. If the top surface has a velocity of w_1 in the z-direction, the volume will increase at a rate of $w_1 dxdy$. The net rate of change of volume is then $(w_1 - w_2) dxdy$. The principle of the continuity of flow requires that the

rate of fluid flow into the column must equal the rate of change of the volume of the column itself. This may be stated as

$$(w_1 - w_2)dx dy = - \left(\frac{\partial q_x}{\partial x} + \frac{\partial q_y}{\partial y} \right) dx dy$$

which, upon cancelling the arbitrary area $dx dy$, becomes

$$\frac{\partial q_x}{\partial x} + \frac{\partial q_y}{\partial y} + (w_1 - w_2) = 0 \quad (3.15)$$

Substituting equations (3.10) and (3.11) into equation (3.15) for q_x and q_y yields

$$\frac{\partial}{\partial x} \left\{ (U_{x,1} + U_{x,2}) \frac{h}{2} - \frac{h^3}{12\eta} \cdot \frac{\partial p}{\partial x} \right\} + \frac{\partial}{\partial y} \left\{ (U_{y,1} + U_{y,2}) \frac{h}{2} - \frac{h^3}{12\eta} \cdot \frac{\partial p}{\partial y} \right\} + (w_1 - w_2) = 0$$

which on rearrangement becomes

$$\frac{\partial}{\partial x} \left(\frac{h^3}{\eta} \cdot \frac{\partial p}{\partial x} \right) + \frac{\partial}{\partial y} \left(\frac{h^3}{\eta} \cdot \frac{\partial p}{\partial y} \right) = 6 \left\{ \frac{\partial}{\partial x} (U_{x,1} + U_{x,2}) h + \frac{\partial}{\partial y} (U_{y,1} + U_{y,2}) h + 2(w_1 - w_2) \right\}$$

If the velocities and the viscosity are constant with respect to x and y , this can be rewritten

$$\frac{\partial}{\partial x} \left(h^3 \frac{\partial p}{\partial x} \right) + \frac{\partial}{\partial y} \left(h^3 \frac{\partial p}{\partial y} \right) = 6\eta \left\{ (U_{x,1} + U_{x,2}) \frac{\partial h}{\partial x} + (U_{y,1} + U_{y,2}) \frac{\partial h}{\partial y} + 2(w_1 - w_2) \right\} \quad (3.16)$$

This is the form of the Reynolds equation usually quoted. However, further modification is required considering the situation where the upper bounding surface (i.e. the impeller blade) is inclined, because of the bearing taper, and the lower bounding surface (i.e. the pump housing) is flat.

If the top surface is inclined and moves at a velocity $U_{x,1}$ in the x -direction, $U_{y,1}$ in the y -direction, and where w_h is an externally applied vertical velocity of the top surface,

then the total velocity of the top surface in the z-direction, w_1 , consists of three terms and is given by [22]

$$w_1 = w_h - \left(U_{x,1} \frac{\partial h}{\partial x} + U_{y,1} \frac{\partial h}{\partial y} \right) \quad (3.17)$$

If the bottom surface is flat with externally applied vertical velocity w_0 , then

$$w_2 = w_0 \quad (3.18)$$

Upon substitution of equations (3.17) and (3.18), the right hand side of equation (3.16) becomes

$$6\eta \left[\left(U_{x,1} + U_{x,2} \right) \frac{\partial h}{\partial x} + \left(U_{y,1} + U_{y,2} \right) \frac{\partial h}{\partial y} + 2 \left\{ w_h - \left(U_{x,1} \frac{\partial h}{\partial x} + U_{y,1} \frac{\partial h}{\partial y} \right) - w_0 \right\} \right]$$

which on simplification becomes

$$6\eta \left\{ \left(U_{x,2} - U_{x,1} \right) \frac{\partial h}{\partial x} + \left(U_{y,2} - U_{y,1} \right) \frac{\partial h}{\partial y} + 2(w_h - w_0) \right\} \quad (3.19)$$

From equation (3.19) it is clear that for a system with an inclined upper surface and flat lower surface, the *difference* of velocities rather than the *sum* of the velocities is considered. The same result can be obtained if the inclined surface is brought to rest by putting an overall velocity of $-U_{x,1}$ and $-U_{y,1}$ on the whole system, indicating that the pressure distribution is simply the result of the *relative* velocity between the two bounding surfaces.

If the surfaces are non-porous then $(w_h - w_0) = \partial h / \partial t$, and equation (3.16) can be written

$$\frac{\partial}{\partial x} \left(h^3 \frac{\partial p}{\partial x} \right) + \frac{\partial}{\partial y} \left(h^3 \frac{\partial p}{\partial y} \right) = 6\eta \left(U_x \frac{\partial h}{\partial x} + U_y \frac{\partial h}{\partial y} \right) + 12\eta \frac{\partial h}{\partial t} \quad (3.20)$$

where $U_x = (U_{x,2} - U_{x,1})$ and $U_y = (U_{y,2} - U_{y,1})$. This is Reynolds equation in Cartesian coordinates.

3.1.3. Reynolds equation in Cartesian coordinates

The Reynolds equation in Cartesian coordinates is given by equation (3.20). To facilitate transformation into coordinate systems other than Cartesian coordinates, equation (3.20) can be written in vector form as

$$\operatorname{div}(h^3 \operatorname{grad}(p)) = 6\eta \mathbf{U} \cdot \operatorname{grad}(h) + 12\eta \frac{\partial h}{\partial t} \quad (3.21)$$

where $\mathbf{U} = U_x \hat{\mathbf{i}} + U_y \hat{\mathbf{j}}$ is the velocity vector and $\hat{\mathbf{i}}, \hat{\mathbf{j}}$ are unit vectors in the x- and y-directions respectively. Additionally, it can be shown that [24]:

$$\operatorname{grad}(f) = \nabla f = \frac{\partial f}{\partial x} \hat{\mathbf{i}} + \frac{\partial f}{\partial y} \hat{\mathbf{j}}$$

where $f = f(x, y)$ is a scalar (i.e. p or h), and that [24]:

$$\operatorname{div}(\mathbf{F}) = \nabla \cdot \mathbf{F} = \frac{\partial F_1}{\partial x} + \frac{\partial F_2}{\partial y}$$

where $\mathbf{F} = F_1 \hat{\mathbf{i}} + F_2 \hat{\mathbf{j}}$ is a vector (i.e. $h^3 \operatorname{grad}(p)$).

3.1.4. Reynolds equation in cylindrical coordinates

The cylindrical coordinate system is convenient for describing the thrust bearing geometry of the VentrAssist impeller.

Equation (3.21) can be transformed into cylindrical coordinates r, θ, z using vector analysis. It can be shown that [24]:

$$\text{grad}(f) = \nabla f = \frac{\partial f}{\partial r} \hat{\mathbf{e}}_r + \frac{1}{r} \frac{\partial f}{\partial \theta} \hat{\mathbf{e}}_\theta \quad (3.22)$$

where f is a scalar, and $\hat{\mathbf{e}}_r, \hat{\mathbf{e}}_\theta$ are unit vectors in the r and θ coordinate directions respectively. Additionally it can be shown that, where $\mathbf{F} = F_1 \hat{\mathbf{e}}_r + F_2 \hat{\mathbf{e}}_\theta$,

$$\text{div}(\mathbf{F}) = \nabla \cdot \mathbf{F} = \frac{1}{r} \frac{\partial}{\partial r} (r F_1) + \frac{1}{r} \frac{\partial}{\partial \theta} (F_2) \quad (3.23)$$

Applying equation (3.22), then

$$\begin{aligned} h^3 \text{grad}(p) &= h^3 \nabla p \\ &= \left(h^3 \frac{\partial p}{\partial r} \right) \hat{\mathbf{e}}_r + \left(\frac{h^3}{r} \frac{\partial p}{\partial \theta} \right) \hat{\mathbf{e}}_\theta \end{aligned}$$

and subsequently, using equation (3.23),

$$\begin{aligned} \text{div}\left(h^3 \text{grad}(p)\right) &= \nabla \cdot \left(h^3 \nabla p\right) \\ &= \frac{1}{r} \frac{\partial}{\partial r} \left(r h^3 \frac{\partial p}{\partial r}\right) + \frac{1}{r} \frac{\partial}{\partial \theta} \left(\frac{h^3}{r} \frac{\partial p}{\partial \theta}\right) \\ &= \frac{1}{r} \frac{\partial}{\partial r} \left(r h^3 \frac{\partial p}{\partial r}\right) + \frac{1}{r^2} \frac{\partial}{\partial \theta} \left(h^3 \frac{\partial p}{\partial \theta}\right) \end{aligned} \quad (3.24)$$

Additionally, from equation (3.22),

$$\text{grad}(h) = \nabla h = \frac{\partial h}{\partial r} \hat{\mathbf{e}}_r + \frac{1}{r} \frac{\partial h}{\partial \theta} \hat{\mathbf{e}}_\theta$$

and subsequently, where $\mathbf{U} = U_r \hat{\mathbf{e}}_r + U_\theta \hat{\mathbf{e}}_\theta$, it can be written

$$\mathbf{U} \cdot \text{grad}(h) = \mathbf{U} \cdot \nabla h = U_r \frac{\partial h}{\partial r} + \frac{U_\theta}{r} \frac{\partial h}{\partial \theta} \quad (3.25)$$

where U_r and U_θ are the radial and tangential velocities respectively. Upon substitution of equations (3.24) and (3.25) into equation (3.21), Reynolds equation in cylindrical coordinates can be written

$$\frac{\partial}{\partial r} \left(rh^3 \frac{\partial p}{\partial r} \right) + \frac{1}{r} \frac{\partial}{\partial \theta} \left(h^3 \frac{\partial p}{\partial \theta} \right) = 6\eta \left\{ U_r r \frac{\partial h}{\partial r} + U_\theta \frac{\partial h}{\partial \theta} \right\} + 12\eta r \frac{\partial h}{\partial t} \quad (3.26)$$

If the upper surface is inclined and the lower surface is flat, then $U_r = U_{r,2} - U_{r,1}$ and $U_\theta = U_{\theta,2} - U_{\theta,1}$, where subscripts 1 and 2 again refer to the upper and lower bounding surfaces respectively. If the bottom surface is fixed then $U_{r,2} = U_{\theta,2} = 0$ and therefore

$$U_r = -U_{r,1} \text{ and } U_\theta = -U_{\theta,1} \quad (3.27)$$

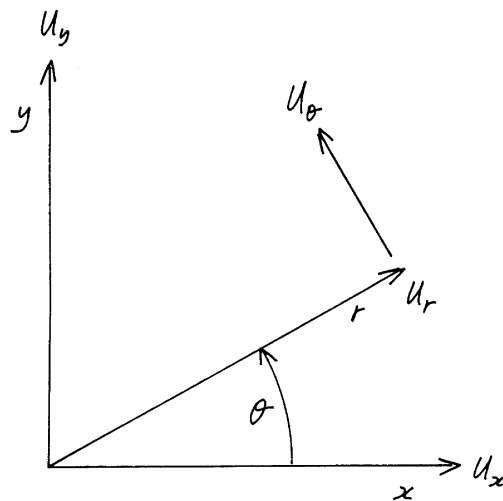


Figure 3.3. Cartesian x-y-z and cylindrical r-θ-z coordinate systems (z-axis out of page)

With the aid of Figure 3.3, the translational velocities U_x and U_y can be resolved into the radial velocity component,

$$U_{r,1} = U_x \cos \theta + U_y \sin \theta \quad (3.28)$$

and the tangential velocity component,

$$U_{\theta,1} = -U_x \sin \theta + U_y \cos \theta \quad (3.29)$$

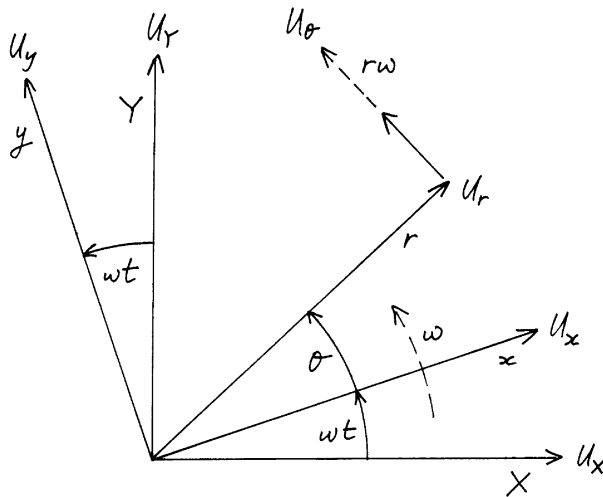


Figure 3.4. Coordinate systems X-Y-Z, x-y-z, and r-θ-z (“z” is common and directed out of the page)

However, if the upper bounding surface is both undergoing translation and spinning with angular velocity ω radians/second, then equations (3.28) and (3.29) require further modification. The most convenient method is to define a fixed coordinate system X-Y, and let coordinate system x-y rotate with angular velocity ω with respect to X-Y (i.e. x-y is fixed relative to the upper surface). This is discussed further in section 3.3. With reference to Figure 3.4, equation (3.28) may be rewritten as

$$U_{r,1} = U_x \cos(\theta + \omega t) + U_y \sin(\theta + \omega t) \quad (3.30)$$

and equation (3.29) may be rewritten as

$$U_{\theta,1} = -U_x \sin(\theta + \omega t) + U_y \cos(\theta + \omega t) + r\omega \quad (3.31)$$

where $U_{x,1}$ and $U_{y,1}$ are the translational velocities of the top surface in the X- and Y-directions respectively. The convenience lies in the fact that $U_{x,1}$ and $U_{y,1}$ are the

time derivatives of the eccentricity of the impeller in the X- and Y-directions, \dot{e}_x and \dot{e}_y respectively. Therefore, equation (3.30) can be written

$$U_{r,1} = \dot{e}_x \cos(\theta + \omega t) + \dot{e}_y \sin(\theta + \omega t)$$

and equation (3.31) can be written

$$U_{\theta,1} = -\dot{e}_x \sin(\theta + \omega t) + \dot{e}_y \cos(\theta + \omega t) + r\omega$$

However, assuming that the translational velocities are small in comparison to the rotational velocity ($r\omega \gg \dot{e}_x, \dot{e}_y$ - assumption 9), the radial and tangential velocity of the top surface become

$$U_{r,1} = 0 \text{ and } U_{\theta,1} = r\omega$$

Therefore, from equation (3.27),

$$U_r = -U_{r,1} = 0 \text{ and } U_\theta = -U_{\theta,1} = -r\omega$$

and subsequently, equation (3.26) can be written

$$\frac{\partial}{\partial r} \left(rh^3 \frac{\partial p}{\partial r} \right) + \frac{1}{r} \frac{\partial}{\partial \theta} \left(h^3 \frac{\partial p}{\partial \theta} \right) = -6\eta r\omega \frac{\partial h}{\partial \theta} + 12\eta r \frac{\partial h}{\partial t} \quad (3.32)$$

Substituting the following dimensionless terms

$$r^* = \frac{r}{r_2}, \quad h_{TB}^* = \frac{h_{TB}}{h_{0,TB}}, \quad p^* = \frac{p}{6\eta\omega} \left(\frac{h_{0,TB}}{L} \right)^2, \text{ and } t^* = \omega t$$

where $h_{0,TB}$ is the minimum film thickness and the subscript TB is used to refer to the thrust bearing on the back face of the VentrAssist impeller, equation (3.32) can be written in non-dimensional form as

$$\frac{\partial}{\partial r^*} \left(r^* h_{TB}^{*3} \frac{\partial p^*}{\partial r^*} \right) + \frac{1}{r^*} \frac{\partial}{\partial \theta} \left(h_{TB}^{*3} \frac{\partial p^*}{\partial \theta} \right) = 2R^* r^* \frac{\partial h_{TB}^*}{\partial t^*} - R^* r^* \frac{\partial h_{TB}^*}{\partial \theta} \quad (3.33)$$

where $R^* = (r_2/L)^2$ and $L = r_2 - r_1$. Equation (3.33) governs the dimensionless pressure distribution over the thrust bearing surfaces of the impeller.

3.1.5. Reynolds equation in spherical coordinates

Equation (3.21) can be similarly transformed into spherical coordinates ρ, θ, α using vector analysis and with the aid of Figure 3.5. Spherical coordinates are very convenient for conical bearings because one of the coordinates, α , the half-cone angle, is constant for the bearing. It can be shown that [24], taking α as constant,

$$\begin{aligned} \text{grad}(f) &= \nabla f \\ &= \frac{\partial f}{\partial \rho} \hat{\mathbf{e}}_\rho + \frac{1}{\rho \sin \alpha} \frac{\partial f}{\partial \theta} \hat{\mathbf{e}}_\theta + \frac{1}{\rho} \frac{\partial f}{\partial \alpha} \hat{\mathbf{e}}_\alpha \\ &= \frac{\partial f}{\partial \rho} \hat{\mathbf{e}}_\rho + \frac{1}{\rho \sin \alpha} \frac{\partial f}{\partial \theta} \hat{\mathbf{e}}_\theta \end{aligned} \quad (3.34)$$

where f is a scalar and $\hat{\mathbf{e}}_\rho$, $\hat{\mathbf{e}}_\theta$ and $\hat{\mathbf{e}}_\alpha$ are unit vectors in the ρ , θ and α coordinate directions respectively.

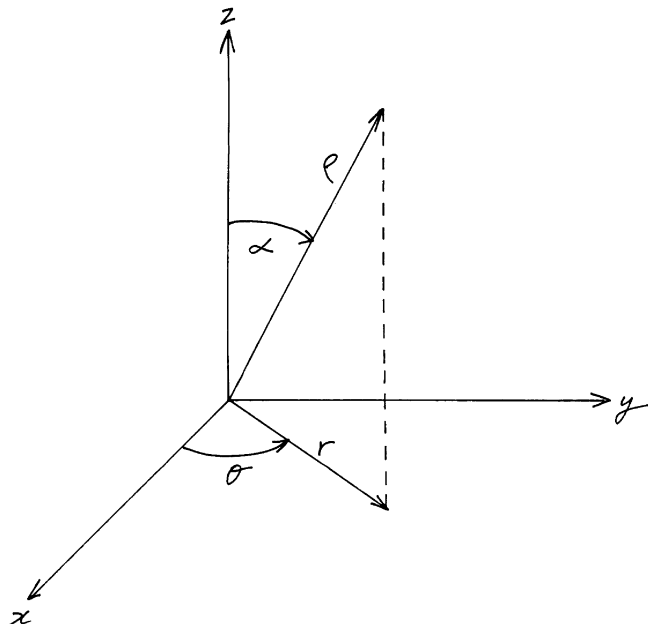


Figure 3.5. Cartesian x-y-z, cylindrical r-θ-z, and spherical ρ-θ-α coordinate systems

Additionally, where $\mathbf{F} = F_1 \hat{\mathbf{e}}_\rho + F_2 \hat{\mathbf{e}}_\theta + F_3 \hat{\mathbf{e}}_\alpha$,

$$\begin{aligned} \operatorname{div}(\mathbf{F}) &= \nabla \cdot \mathbf{F} \\ &= \frac{1}{\rho} \frac{\partial}{\partial \rho} (\rho F_1) + \frac{1}{\rho \sin \alpha} \frac{\partial}{\partial \theta} (F_2) + \frac{1}{\rho \sin \alpha} \frac{\partial}{\partial \alpha} (\sin \alpha F_3) \\ &= \frac{1}{\rho} \frac{\partial}{\partial \rho} (\rho F_1) + \frac{1}{\rho \sin \alpha} \frac{\partial}{\partial \theta} (F_2) \end{aligned} \quad (3.35)$$

Hence, using equation (3.34), it can be written

$$\begin{aligned} h^3 \operatorname{grad}(p) &= h^3 \nabla p \\ &= \left(h^3 \frac{\partial p}{\partial \rho} \right) \hat{\mathbf{e}}_\rho + \left(\frac{h^3}{\rho \sin \alpha} \frac{\partial p}{\partial \theta} \right) \hat{\mathbf{e}}_\theta \end{aligned}$$

and subsequently, making use of equation (3.35), then [25]:

$$\begin{aligned} \operatorname{div}(h^3 \operatorname{grad}(p)) &= \frac{1}{\rho} \frac{\partial}{\partial \rho} \left(\rho h^3 \frac{\partial p}{\partial \rho} \right) + \frac{1}{\rho \sin \alpha} \frac{\partial}{\partial \theta} \left(\frac{h^3}{\rho \sin \alpha} \frac{\partial p}{\partial \theta} \right) \\ &= \frac{1}{\rho} \frac{\partial}{\partial \rho} \left(\rho h^3 \frac{\partial p}{\partial \rho} \right) + \frac{1}{\rho^2 \sin^2 \alpha} \frac{\partial}{\partial \theta} \left(h^3 \frac{\partial p}{\partial \theta} \right) \end{aligned} \quad (3.36)$$

Additionally, using equation (3.34), it can be written

$$\operatorname{grad}(h) = \nabla h = \left(\frac{\partial h}{\partial \rho} \right) \hat{\mathbf{e}}_\rho + \left(\frac{1}{\rho \sin \alpha} \frac{\partial h}{\partial \theta} \right) \hat{\mathbf{e}}_\theta$$

and subsequently, where $\mathbf{U} = U_\rho \hat{\mathbf{e}}_\rho + U_\theta \hat{\mathbf{e}}_\theta$, it can be written

$$\mathbf{U} \cdot \operatorname{grad}(h) = \mathbf{U} \cdot \nabla h = U_\rho \frac{\partial h}{\partial \rho} + \frac{U_\theta}{\rho \sin \alpha} \frac{\partial h}{\partial \theta} \quad (3.37)$$

where U_ρ is the velocity in the ρ -direction and U_θ is the tangential velocity. Reynolds equation in spherical coordinates can therefore be stated as

$$\frac{1}{\rho} \frac{\partial}{\partial \rho} \left(\rho h^3 \frac{\partial p}{\partial \rho} \right) + \frac{1}{\rho^2 \sin^2 \alpha} \frac{\partial}{\partial \theta} \left(h^3 \frac{\partial p}{\partial \theta} \right) = 6\eta \left\{ U_\rho \frac{\partial h}{\partial \rho} + \frac{U_\theta}{\rho \sin \alpha} \frac{\partial h}{\partial \theta} \right\} + 12\eta \frac{\partial h}{\partial t} \quad (3.38)$$

If the upper surface is inclined (eg. because of the bearing taper) and the lower is flat, then $U_\rho = U_{\rho,2} - U_{\rho,1}$ and $U_\theta = U_{\theta,2} - U_{\theta,1}$. If the lower surface is fixed then $U_{\rho,2} = U_{\theta,2} = 0$, and therefore

$$U_\rho = -U_{\rho,1} \text{ and } U_\theta = -U_{\theta,1} \quad (3.39)$$

Similar to cylindrical coordinates, it can be shown that the velocity of the upper surface in the ρ -direction is

$$\begin{aligned} U_{\rho,1} &= -\dot{e}_z \cos \alpha + U_{r,1} \sin \alpha \\ &= -\dot{e}_z \cos \alpha + \dot{e}_x \sin \alpha \cos(\theta + \omega t) + \dot{e}_y \sin \alpha \sin(\theta + \omega t) \end{aligned} \quad (3.40)$$

where \dot{e}_z is the time derivative of the eccentricity of the impeller in the Z-direction.

Similarly, the tangential velocity of the upper surface can be shown to be

$$U_{\theta,1} = -\dot{e}_x \sin(\theta + \omega t) + \dot{e}_y \cos(\theta + \omega t) + \omega \rho \sin \alpha \quad (3.41)$$

However, assuming that the effects of translation of the bearing are negligible in comparison to bearing rotation in the same manner as for the derivation of cylindrical coordinates ($\omega \rho \sin \alpha \gg \dot{e}_x, \dot{e}_y, \dot{e}_z$ - assumption 9), then equations (3.40) and (3.41) reduce to

$$U_{\rho,1} = 0 \text{ and } U_{\theta,1} = \omega \rho \sin \alpha$$

From equation (3.39), it can now be stated that

$$U_\rho = 0 \text{ and } U_\theta = -\omega \rho \sin \alpha$$

Subsequently, equation (3.38) can be written as

$$\frac{1}{\rho} \frac{\partial}{\partial \rho} \left(\rho h^3 \frac{\partial p}{\partial \rho} \right) + \frac{1}{\rho^2 \sin^2 \alpha} \frac{\partial}{\partial \theta} \left(h^3 \frac{\partial p}{\partial \theta} \right) = -6\eta \omega \frac{\partial h}{\partial \theta} + 12\eta \frac{\partial h}{\partial t} \quad (3.42)$$

Substituting the following dimensionless terms

$$\rho^* = \frac{\rho}{\rho_2 \sin \alpha} = \frac{\rho}{r_2}, \quad h_{CJB}^* = \frac{h_{CJB}}{h_{vc}}, \quad p^* = \frac{p}{6\eta\omega} \left(\frac{h_{vc}}{L_p \sin \alpha} \right)^2 = \frac{p}{6\eta\omega} \left(\frac{h_{vc}}{L} \right)^2,$$

$$t^* = \omega t, \text{ and } R^* = \left(\frac{\rho_2 \sin \alpha}{L_p \sin \alpha} \right)^2 = \left(\frac{r_2}{L} \right)^2 = \left(\frac{\rho_2}{L_p} \right)^2$$

where $L_p = \rho_2 - \rho_1$, h_{vc} is the vertical (axial) clearance (i.e. the clearance in the z-direction) of the conical journal bearing and the subscript *CJB* is used to refer to the conical journal bearing on the front face of the VentrAssist impeller, equation (3.42) may be written in non-dimensional form as

$$\frac{1}{\rho^*} \frac{\partial}{\partial \rho^*} \left(\rho^* h_{CJB}^{*3} \frac{\partial p^*}{\partial \rho^*} \right) + \frac{1}{\rho^{*2} \sin^2 \alpha} \frac{\partial}{\partial \theta} \left(h_{CJB}^{*3} \frac{\partial p^*}{\partial \theta} \right) = 2R^* \frac{\partial h_{CJB}^*}{\partial t^*} - R^* \frac{\partial h_{CJB}^*}{\partial \theta} \quad (3.43)$$

which is the equation governing the dimensionless pressure distribution over the conical journal bearing surfaces on each of the four impeller blades. Note that, for the conical journal bearing, the vertical clearance and the minimum film thickness are related by the expression $h_{0,CJB} = h_{vc} \sin \alpha$.

3.2. Bearing geometry and properties

A simplified impeller geometry has been employed in this study, mainly to facilitate construction of the numerical grid over the bearing surfaces. The modified geometry consists of four “sector-shaped” impeller blades, each with an angular span of $\theta_0 = 45^\circ$. The cone angle was right-angled, i.e. $2\alpha = 90^\circ$ where α is the half-cone angle. The simplified geometry is pictured in Figure 3.6. Note that program *Orbit3D* allows for the variation in θ_0 , α , and the number of impeller blades N_p .

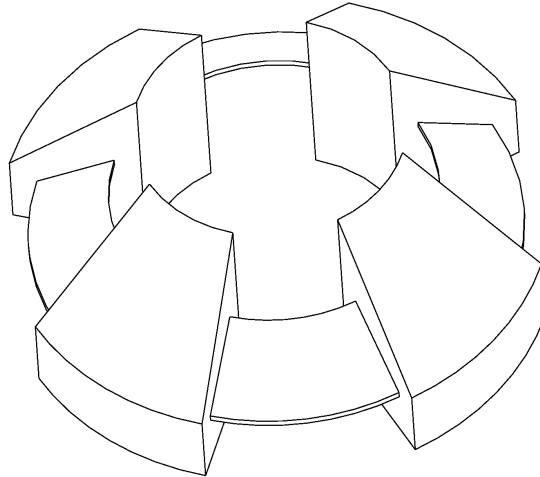


Figure 3.6. Simplified impeller geometry with sector shaped blades. Note the similarity to rotor 2.2 pictured in Figure 2.2.

The lubricated surfaces of the thrust bearing and conical journal bearing of the VentrAssist impeller have a tapered land configuration. That is, the bearing surfaces consist of two sections, a linear taper that diverges in the direction of sliding of the impeller and an untapered ‘land’, as pictured in Figure 3.7. As shown in this figure, the inner and outer radii of the thrust bearing are r_1 and r_2 respectively, the inner and outer edges of the conical journal bearing are ρ_1 and ρ_2 respectively (see Figure

3.12(a)), and the angular span of the untapered land and the tapered section is θ_{0a} and θ_{0b} respectively. Given that $\theta_0 = \theta_{0a} + \theta_{0b}$, the ratio θ_{0a}/θ_0 is the fraction of the land section of the bearing.

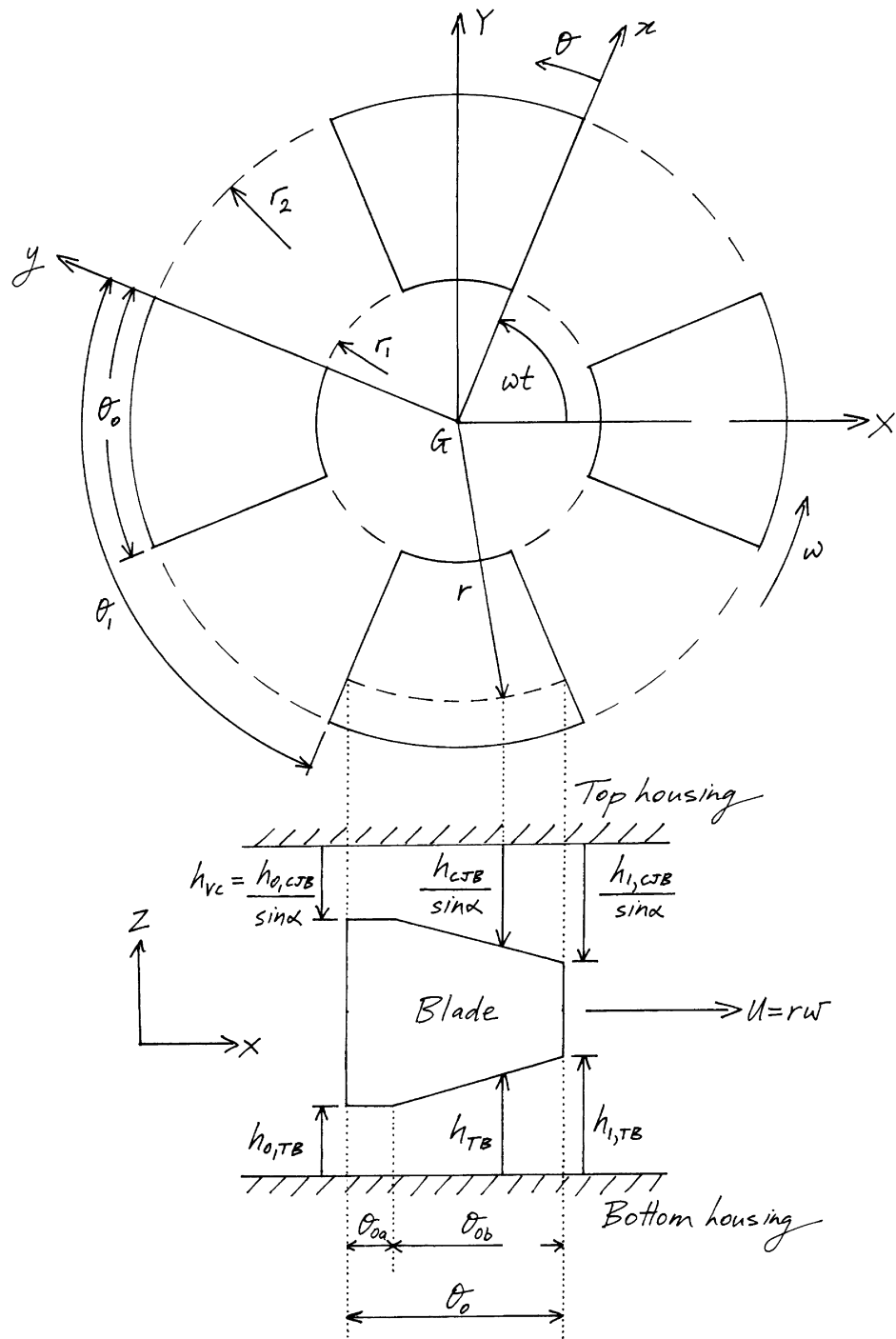


Figure 3.7. (a) Top view and (b) side view of single blade, picturing the impeller geometry

The advantage of the tapered land configuration is a increased load capacity over a completely tapered bearing and the land design which anticipates the wear that may occur on a completely tapered bearing on acceleration from rest or deceleration to a stop [16].

The film thickness h of such a configuration can be mathematically expressed for a single impeller blade as

$$h = h_0 \quad (3.44)$$

for the untapered land where $0 \leq \theta \leq \theta_{0a}$, and

$$h = h_0 + (h_1 - h_0) \left(\frac{\theta - \theta_{0a}}{\theta_{0b}} \right) \quad (3.45)$$

for the tapered section where $\theta_{0a} \leq \theta \leq \theta_0$ and h_0 , h_1 are the nominal film thicknesses at the trailing edge and leading edge, respectively, of either the thrust bearing or conical journal bearing. That is $h_0 \equiv h_{0,TB} \equiv h_{0,CJB}$ and $h_1 \equiv h_{1,TB} \equiv h_{1,CJB}$.

Expanding the expressions for the film thickness for that over each blade m where $m = 1, 2, \dots, N_p$ is the index of impeller blades, θ is replaced by $\theta - \xi$ in the equations (3.44) and (3.45), yielding the new expressions

$$h = h_0 \quad (3.46)$$

for the untapered land where $0 \leq \theta - \xi \leq \theta_{0a}$ (or alternatively $\xi \leq \theta \leq \xi + \theta_{0a}$), and

$$h = h_0 + (h_1 - h_0) \left[\frac{\theta - (\theta_{0a} + \xi)}{\theta_{0b}} \right] \quad (3.47)$$

for the tapered section where $\theta_{0a} \leq \theta - \xi \leq \theta_0$ (or alternatively $\xi + \theta_{0a} \leq \theta \leq \xi + \theta_0$), $\xi = (m-1)\theta_1$ for $m = 1, 2, \dots, N_p$ and $\theta_1 = 2\pi/N_p$ is the angular distance between the

trailing edge of consecutive blades. For the VentrAssist impeller, $N_P = 4$ and thus $\theta_1 = \pi/2$ radians.

The optimal configuration of a tapered land bearing is when $h_1/h_0 = 2.25$ (for a bearing of infinite width) corresponding to $K = 1.25$, and $\theta_{0a}/\theta_0 = 0.2$ corresponding to a 80 / 20 taper land configuration [13, 16]. The bearing surfaces of the VentrAssist impeller typically have a 50 μm taper (i.e. $h_1 - h_0 = 50\mu\text{m}$) and, given a total vertical travel of 100 μm , have $K_{TB} = 1.0$ and $K_{CJB} = 1.41$ when sitting in its nominal position. It should be noted, however, that due to forces on the impeller (i.e. gravitational, inertial, magnetic etc.) and the corresponding motion, the clearance h_0 (and thus the ratio h_1/h_0 and variable K) self-adjusts until equilibrium with the net force resulting from the hydrodynamic pressure distribution over the bearing surfaces has been reached.

The dimensions and properties of the tested impeller are summarised as follows:

Impeller dimensions	$\alpha = 45^\circ$, $N_P = 4$, $r_1 = 12.5\text{mm}$, $r_2 = 25.0\text{mm}$, $\rho_1 = 17.678\text{mm}$, $\rho_2 = 35.355\text{mm}$, $\theta_0 = 45^\circ$, $\theta_{0a}/\theta_0 = 0.2$, $h_1 - h_0 = 50\mu\text{m}$
Impeller properties	$M = 36.0\text{g}$, $I_{xx} = I_{yy} = 4.2\text{g.mm}^2$, $I_{zz} = 7.5\text{g.mm}^2$, $z_G = 5.6\text{mm}$, $\rho_G = 1.05 \rho_2 = 37.123\text{mm}$

3.3. Film thickness

The impeller rotates with angular velocity ω radians per second with respect to the pump housing. It is convenient to mathematically represent the translational and rotational displacements of the impeller and also to mathematically describe the impeller geometry with respect to a frame of reference that spins with the same velocity as the impeller (i.e. that is fixed relative to the impeller) and has its origin through the centre of mass of the impeller. This coordinate frame is designated x-y-z and is pictured in Figure 3.8.

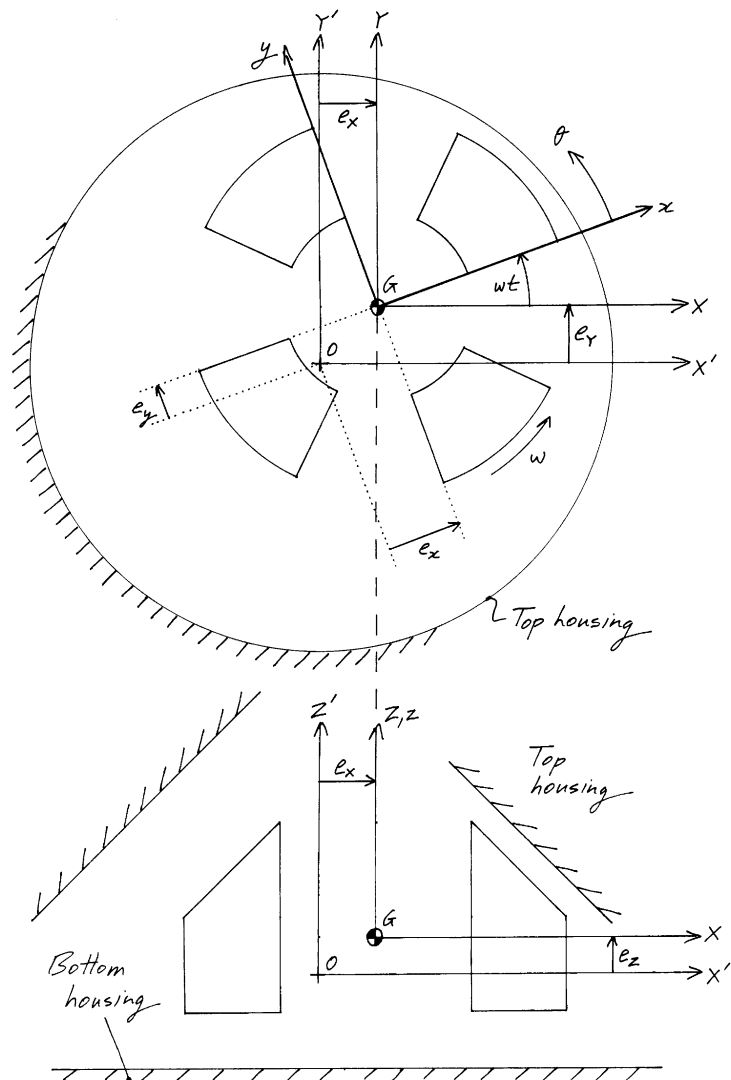


Figure 3.8. Coordinate systems x-y-z, X-Y-Z and X'-Y'-Z'.

On the other hand, it is convenient to visualise the motions of the centre of mass of the impeller with respect to coordinate system X-Y-Z, also pictured in Figure 3.8, which does not spin with the impeller although shares the same origin (and therefore is able to translate with respect to the pump housing). For these reasons, the change in local film thickness from the nominal film thickness (determined by the bearing geometry) due to displacements of the impeller are first derived with respect to the rotating x-y-z coordinate system and subsequently transformed into X-Y-Z coordinates using the following relationship for the displacements

$$\begin{bmatrix} \lambda_x \\ \lambda_y \\ \lambda_z \end{bmatrix} = \begin{bmatrix} \cos \omega t & \sin \omega t & 0 \\ -\sin \omega t & \cos \omega t & 0 \\ 0 & 0 & 1 \end{bmatrix} \begin{bmatrix} \lambda_x \\ \lambda_y \\ \lambda_z \end{bmatrix} \quad (3.48)$$

where λ represents either the eccentricity e or rotation γ of the impeller. For example, the eccentricity of the impeller in the x-direction e_x , is related to e_x and e_y , the eccentricity of the impeller in the X- and Y- directions respectively, by

$$e_x = e_X \cos \omega t + e_Y \sin \omega t$$

Note that the z-axis is identical to the Z-axis as indicated by the bottom right entry of '1' in the transformation matrix of equation (3.48), thus $e_z \equiv e_Z$.

Coordinate system X'-Y'-Z' is also pictured in Figure 3.8, which is fixed relative to the pump housing (i.e. does not translate or rotate with respect to the pump housing) with origin through the geometric centre of the pump housing, the location of which coincides with the centre of mass of the impeller running at its nominal position i.e. when $e_x = e_y = e_z = \gamma_x = \gamma_y = 0$.

3.3.1. Thrust bearing

The change in the local film thickness at any point (r, θ) (for $r_1 \leq r \leq r_2$ and $\xi \leq \theta \leq \xi + \theta_0$ where $\xi = (m-1)\theta_1$ for $m = 1, 2, \dots, N_p$) on the lubricated surfaces of the thrust bearing of the impeller due to a:

- a) small eccentricity in the x-direction e_x is given by (see Figure 3.9)

$$\Delta h_{e_x} = 0 \quad (3.49)$$

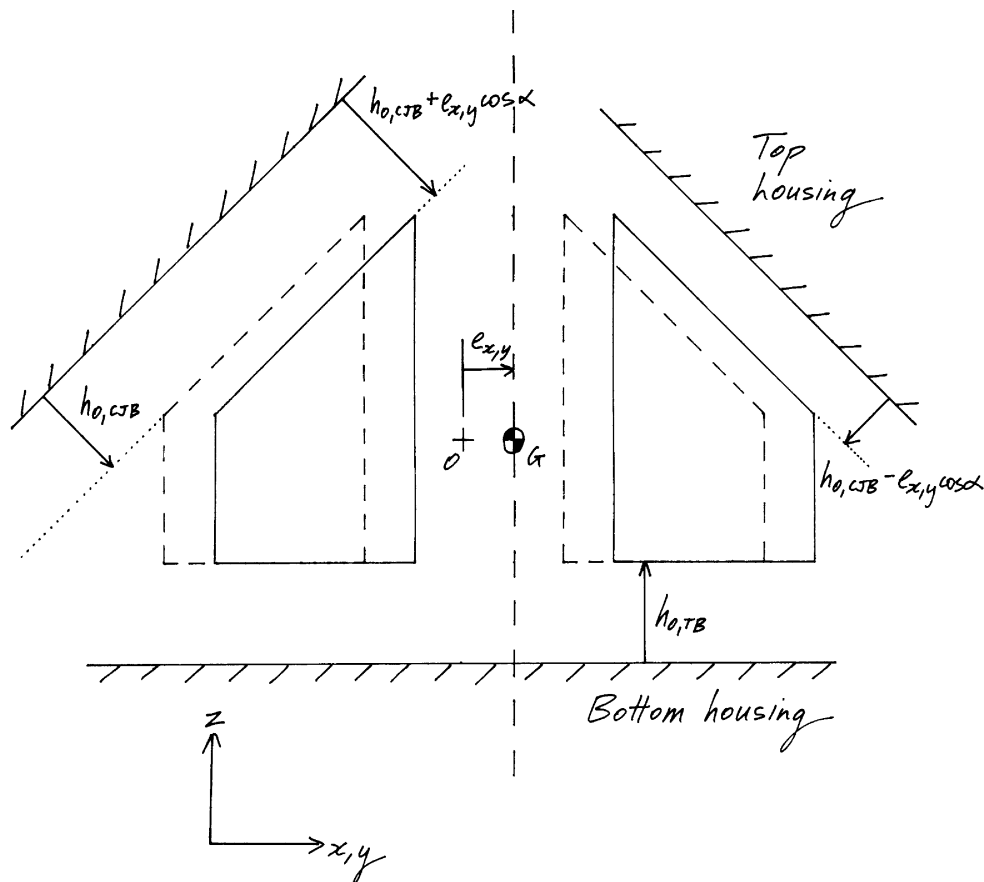


Figure 3.9. Change in film thickness of both the conical journal bearing and thrust bearing for a given eccentricity in the x or y direction.

- b) small eccentricity in the y-direction e_y is given by (see Figure 3.9)

$$\Delta h_{e_y} = 0 \quad (3.50)$$

- c) small eccentricity in the z-direction e_z is given by (see Figure 3.10)

$$\Delta h_{e_z} = e_z \quad (3.51)$$

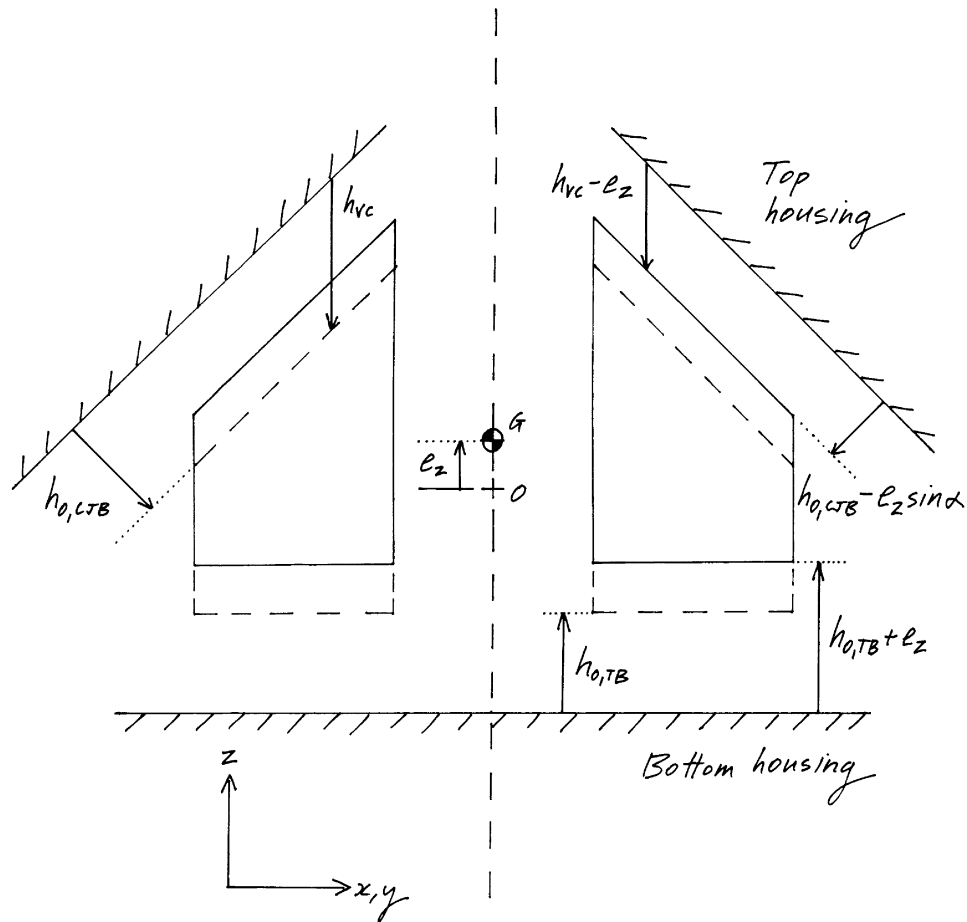


Figure 3.10. Change in film thickness of both the conical journal bearing and thrust bearing
for a given eccentricity in the z-direction

- d) small rotation about the positive y-axis γ_y is given by (see Figure 3.11)

$$\Delta h_{\gamma_y} = [R \cos \phi - R \cos(\phi + \gamma_y)](-\cos \theta) \quad (3.52)$$

for $\xi \leq \theta \leq \xi + \theta_0$, such that when $\theta = 0$ and $\theta = \pi/2$ then

$$\Delta h_{\gamma_y} = -[R \cos \phi - R \cos(\phi + \gamma_y)] \text{ and } \Delta h_{\gamma_y} = 0 \text{ respectively etc., where } \theta \text{ is}$$

taken CCW from the positive x-axis. Variable R is the perpendicular distance from the centre of mass of the impeller to the specified point (r, θ) on the thrust bearing, and angles ϕ and γ_y are as shown in Figure 3.11.

Using the following trigonometric identity [25]

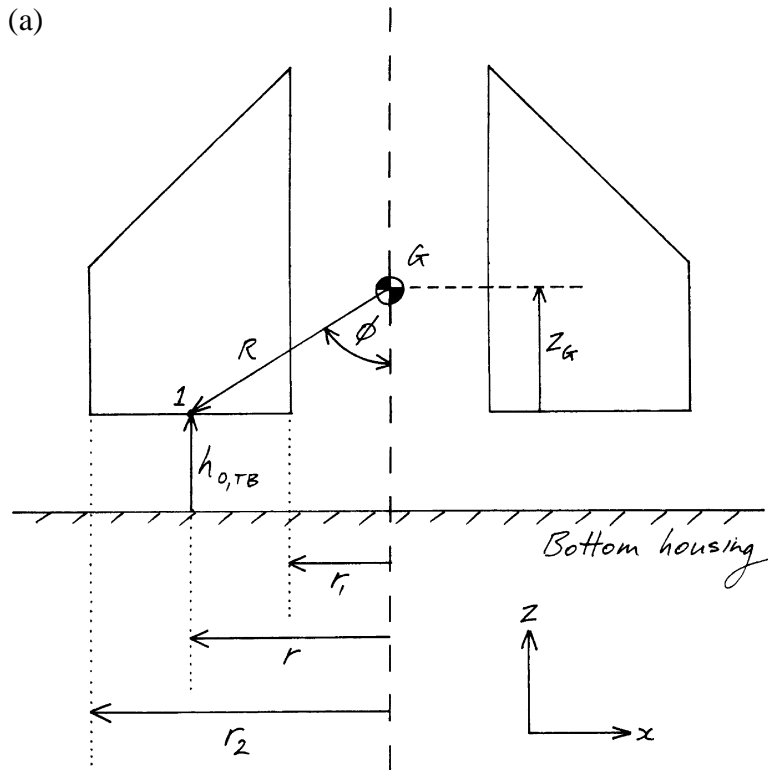
$$\cos(A + B) = \cos A \cos B - \sin A \sin B \quad (3.53)$$

equation (3.52) may be rewritten as

$$\Delta h_{\gamma_y} = [R \cos \phi - R(\cos \phi \cos \gamma_y - \sin \phi \sin \gamma_y)](-\cos \theta)$$

which simplifies to

$$\Delta h_{\gamma_y} = [R \cos \phi(1 - \cos \gamma_y) + R \sin \phi \sin \gamma_y](-\cos \theta) \quad (3.54)$$



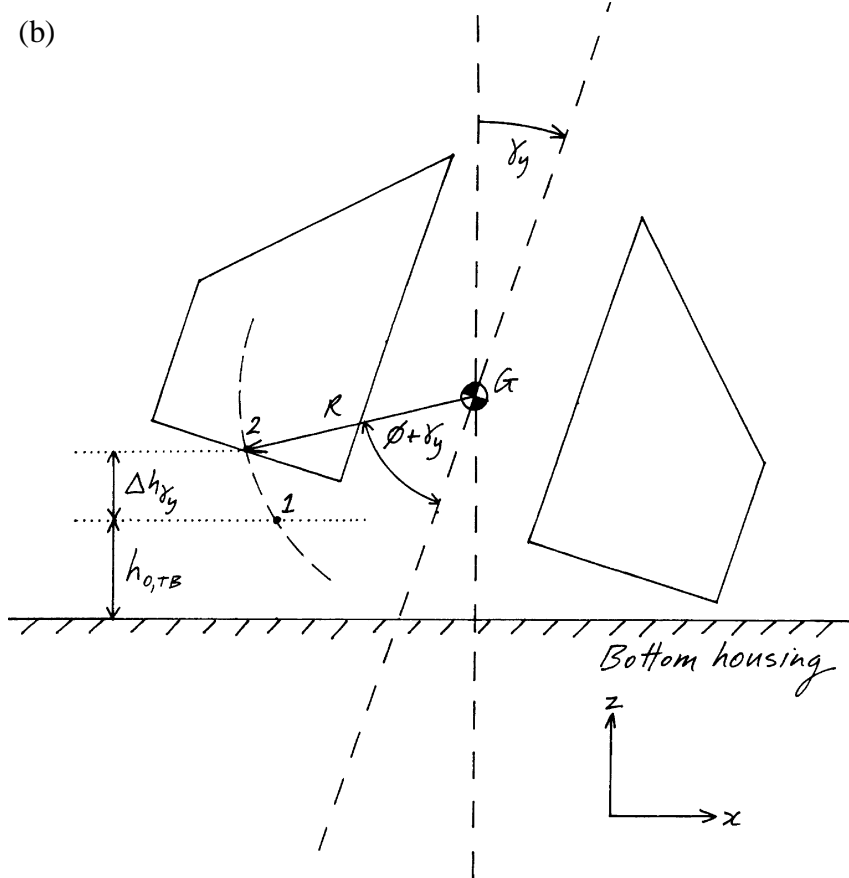


Figure 3.11. (a), (b) Change in film thickness of the thrust bearing
for a given rotation about the y-axis

Using a small angle approximation, $\cos \gamma_y \approx 1$ and $\sin \gamma_y \approx \gamma_y$ (where γ_y is in radians) and noting from Figure 3.11(a) that $r = R \sin \phi$, equation (3.54) becomes

$$\Delta h_{\gamma_y} \approx -r \gamma_y \cos \theta \quad (3.55)$$

for $\xi \leq \theta \leq \xi + \theta_0$ where $\xi = (m-1)\theta_1$ for $m = 1, 2, \dots, N_p$ and $r_1 \leq r \leq r_2$.

e) small rotation about the positive x-axis γ_x is given by

$$\Delta h_{\gamma_x} = [R \cos \phi - R \cos(\phi + \gamma_x)] (\sin \theta) \quad (3.56)$$

for $\xi \leq \theta \leq \xi + \theta_0$ where R and ϕ are as previously defined in (d).

In a similar manner to the small rotation about the positive y-axis, the change in film thickness over the lubricating surface of each blade due to small rotation γ_x can be shown to be

$$\Delta h_{\gamma_x} \approx r\gamma_x \sin \theta \quad (3.57)$$

for $\xi \leq \theta \leq \xi + \theta_0$ where $\xi = (m-1)\theta_1$ for $m = 1, 2, \dots, N_p$, $r_1 \leq r \leq r_2$ and where angle θ is taken CCW from the positive x-axis.

- f) simultaneous small eccentricities in the x-, y- and z-directions and small rotations about the positive x- and y-axes is given by the addition of equations (3.49) – (3.51) and equations (3.55) and (3.57)

$$\begin{aligned} \Delta h_{TB} &= \Delta h_{e_x} + \Delta h_{e_y} + \Delta h_{e_z} + \Delta h_{\gamma_x} + \Delta h_{\gamma_y} \\ &\approx e_z + r\gamma_x \sin \theta - r\gamma_y \cos \theta \end{aligned} \quad (3.58)$$

Using the relationship given by equation (3.48), the change in film thickness due to all possible translational and rotational displacements given by equation (3.58) can be transformed with respect to the X-Y-Z coordinate frame of reference. That is, equation (3.58) becomes

$$\begin{aligned} \Delta h_{TB} &\approx r(\gamma_x \cos \omega t + \gamma_y \sin \omega t) \sin \theta - \\ &r(-\gamma_x \sin \omega t + \gamma_y \cos \omega t) \cos \theta + e_z \end{aligned}$$

which simplifies to

$$\begin{aligned} \Delta h_{TB} &\approx r\gamma_x (\sin \theta \cos \omega t + \cos \theta \sin \omega t) - \\ &r\gamma_y (\cos \theta \cos \omega t - \sin \theta \sin \omega t) + e_z \end{aligned} \quad (3.59)$$

Using equation (3.53) and the additional trigonometric identity [25]

$$\sin(A + B) = \sin A \cos B + \cos A \sin B \quad (3.60)$$

then equation (3.59) can be rewritten as

$$\Delta h_{TB} \approx e_Z + r\gamma_X \sin(\theta + \omega t) - r\gamma_Y \cos(\theta + \omega t) \quad (3.61)$$

Now that expressions for both the bearing geometry and the change in film thickness have been derived, the film thickness over the thrust bearing can be expressed as

$$h_{TB} \approx h_{0,TB} + e_Z + r\gamma_X \sin(\theta + \omega t) - r\gamma_Y \cos(\theta + \omega t) \quad (3.62)$$

for the land section, and

$$h_{TB} \approx h_{0,TB} + (h_{1,TB} - h_{0,TB}) \left[\frac{\theta - (\theta_{0a} + \xi)}{\theta_{0b}} \right] + e_Z + r\gamma_X \sin(\theta + \omega t) - r\gamma_Y \cos(\theta + \omega t) \quad (3.63)$$

for the tapered section of the bearing.

Substituting the following non-dimensional terms

$$\begin{aligned} h_{TB}^* &= \frac{h_{TB}}{h_{0,TB}}, \quad K_{TB} = \frac{h_{1,TB} - h_{0,TB}}{h_{0,TB}}, \quad \varepsilon_Z = \frac{e_Z}{h_{0,TB}}, \quad \gamma_X^* = \frac{\gamma_X r_2}{h_{0,TB}}, \\ \gamma_Y^* &= \frac{\gamma_Y r_2}{h_{0,TB}}, \quad t^* = \omega t \text{ and } r^* = \frac{r}{r_2} \end{aligned}$$

equation (3.62) can be rewritten as an expression for the dimensionless film thickness over the land section

$$h_{TB}^* \approx 1 + \varepsilon_Z + r^* \gamma_X^* \sin(\theta + t^*) - r^* \gamma_Y^* \cos(\theta + t^*) \quad (3.64)$$

and similarly equation (3.63) can be rewritten as an expression for the dimensionless film thickness over the tapered section

$$h_{TB}^* \approx 1 + K_{TB} \left[\frac{\theta - (\theta_{0a} + \xi)}{\theta_{0b}} \right] + \varepsilon_Z + r^* \gamma_X^* \sin(\theta + t^*) - r^* \gamma_Y^* \cos(\theta + t^*) \quad (3.65)$$

3.3.1.1. Spatial and temporal derivatives of the film thickness

In regards to the thrust bearing surfaces of the VentrAssist impeller, the spatial derivative of the dimensionless film thickness with respect to r^* is

$$\frac{\partial h_{TB}^*}{\partial r^*} \approx \gamma_x^* \sin(\theta + t^*) - \gamma_y^* \cos(\theta + t^*) \quad (3.66)$$

For the land section, the spatial derivative with respect to θ is

$$\frac{\partial h_{TB}^*}{\partial \theta} \approx r^* \gamma_x^* \cos(\theta + t^*) + r^* \gamma_y^* \sin(\theta + t^*) \quad (3.67)$$

and for the tapered section, the θ derivative is

$$\frac{\partial h_{TB}^*}{\partial \theta} \approx \frac{K}{\theta_{0b}} + r^* \gamma_x^* \cos(\theta + t^*) + r^* \gamma_y^* \sin(\theta + t^*) \quad (3.68)$$

The temporal derivative of the dimensionless film thickness is

$$\frac{\partial h_{TB}^*}{\partial t^*} \approx \dot{\varepsilon}_z + (\dot{\gamma}_x^* + \dot{\gamma}_y^*) r^* \sin(\theta + t^*) + (\gamma_x^* - \dot{\gamma}_y^*) r^* \cos(\theta + t^*) \quad (3.69)$$

where $\dot{\varepsilon}_z = \frac{d\varepsilon_z}{dt^*}$, $\dot{\gamma}_x^* = \frac{d\gamma_x^*}{dt^*}$ and $\dot{\gamma}_y^* = \frac{d\gamma_y^*}{dt^*}$.

3.3.2. Conical journal bearing

The change in the local film thickness at any point (ρ, θ) (for $\rho_1 \leq \rho \leq \rho_2$ and $\xi \leq \theta \leq \xi + \theta_0$ where $\xi = (m-1)\theta_1$ for $m = 1, 2, \dots, N_p$) on the lubricated surfaces of the conical journal bearing of the impeller due to a:

- a) small eccentricity in the x-direction e_x is given by (see Figure 3.9)

$$\Delta h_{e_x} = -e_x \cos \alpha \cos \theta \quad (3.70)$$

- b) small eccentricity in the y-direction e_y is given by (see Figure 3.9)

$$\Delta h_{e_y} = -e_y \cos \alpha \sin \theta \quad (3.71)$$

c) small eccentricity in the z-direction e_z is given by (see Figure 3.10)

$$\Delta h_{e_z} = -e_z \sin \alpha \quad (3.72)$$

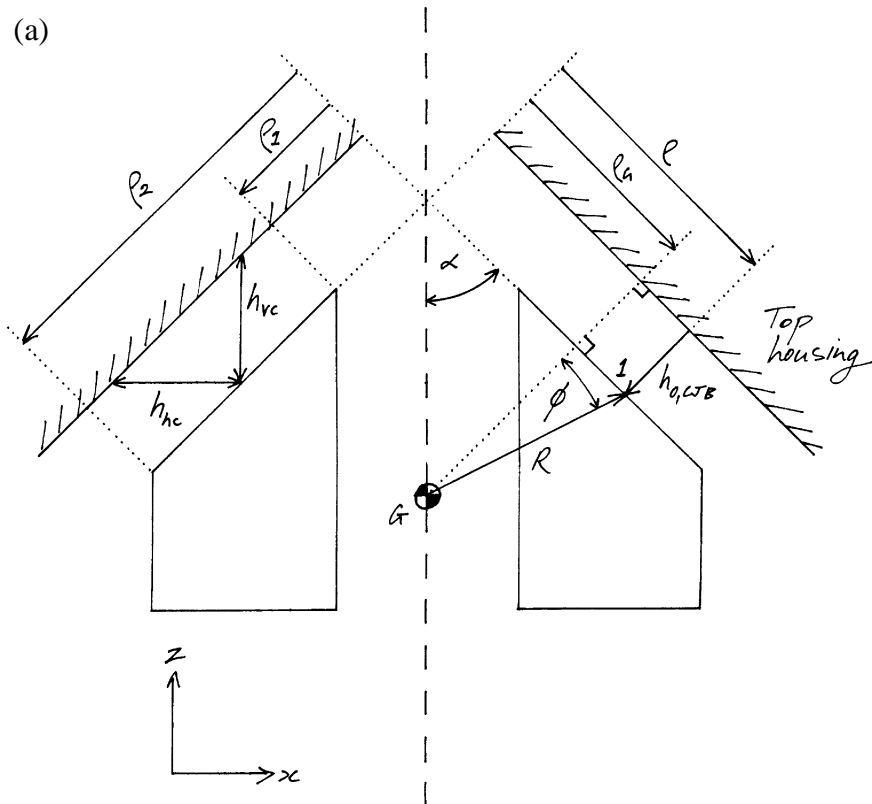
d) small rotation about the positive y-axis γ_y is given by (see Figure 3.12)

$$\Delta h_{\gamma_y} = [R \cos \phi - R \cos(\phi + \gamma_y)] (\cos \theta) \quad (3.73)$$

for $\xi \leq \theta \leq \xi + \theta_0$, such that when $\theta = 0$ and $\theta = \pi/2$ then

$\Delta h_{\gamma_y} = R \cos \phi - R \cos(\phi + \gamma_y)$ and $\Delta h_{\gamma_y} = 0$ respectively etc., where θ is taken

CCW from the positive x-axis. Variable R is the perpendicular distance from the centre of the impeller to the specified point (ρ, θ) on the surface of the conical journal bearing, and angles ϕ and γ_y are as shown in Figure 3.12.



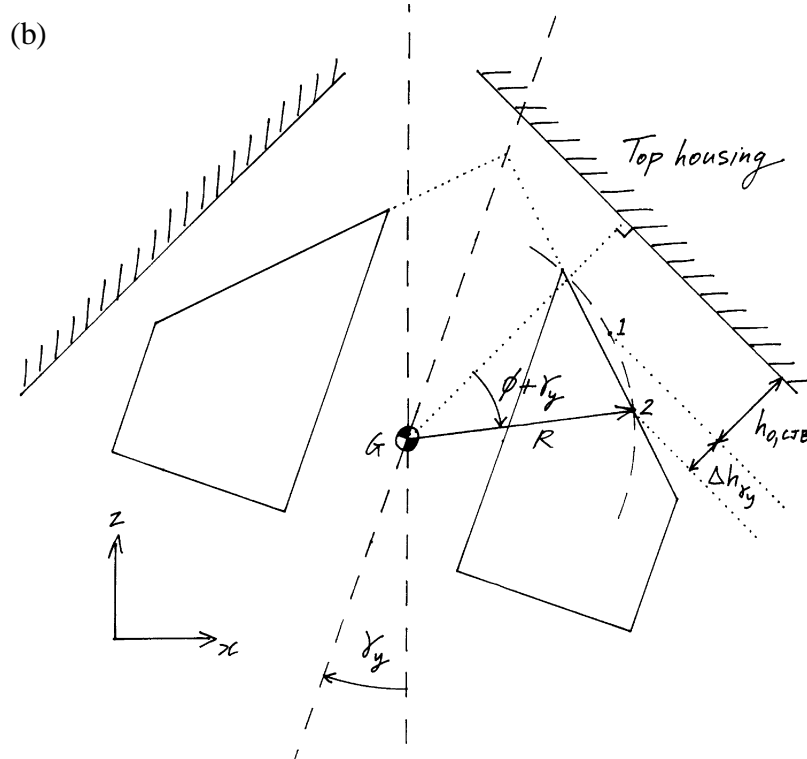


Figure 3.12. (a), (b) Change in the film thickness of the conical journal bearing for a given rotation about the y-axis

Using the trigonometric identity of equation (3.53), equation (3.73) can be written

$$\Delta h_{\gamma_y} = [R \cos \phi - R(\cos \phi \cos \gamma_y - \sin \phi \sin \gamma_y)] / (\cos \theta)$$

which simplifies to

$$\Delta h_{\gamma_y} = [R \cos \phi(1 - \cos \gamma_y) + R \sin \phi \sin \gamma_y] / (\cos \theta) \quad (3.74)$$

Using a small angle approximation, $\cos \gamma_y \approx 1$ and $\sin \gamma_y \approx \gamma_y$ (where γ_y is in radians), and noting from Figure 3.12 (a) that $R \sin \phi = \rho - \rho_G$ where ρ_G is as shown, equation (3.74) can be rewritten as

$$\Delta h_{\gamma_y} \approx (\rho - \rho_G) \gamma_y \cos \theta \quad (3.75)$$

for $\xi \leq \theta \leq \xi + \theta_0$ where $\xi = (m-1)\theta_1$ for $m = 1, 2, \dots, N_p$ and $\rho_1 \leq \rho \leq \rho_2$.

e) small rotation about the positive x-axis γ_x is given by

$$\Delta h_{\gamma_x} = [R \cos \phi - R \cos(\phi + \gamma_x)](-\sin \theta) \quad (3.76)$$

for $\xi \leq \theta \leq \xi + \theta_0$, where R and ϕ are as previously defined in (d).

In a similar manner to the small rotation about the positive y-axis, the local change in film thickness due to small rotation γ_x can be shown to be

$$\Delta h_{\gamma_x} \approx -(\rho - \rho_G) \gamma_x \sin \theta \quad (3.77)$$

for $\xi \leq \theta \leq \xi + \theta_0$ where $\xi = (m-1)\theta_1$ for $m = 1, 2, \dots, N_p$, $\rho_1 \leq \rho \leq \rho_2$ and

where angle θ is taken CCW from the positive x-axis.

f) simultaneous small eccentricities in the x-, y- and z- directions and small rotations about the positive x- and y- axes is given by the addition of equations (3.70) – (3.72) and equations (3.75) and (3.77)

$$\begin{aligned} \Delta h_{CJB} &= \Delta h_{e_x} + \Delta h_{e_y} + \Delta h_{e_z} + \Delta h_{\gamma_x} + \Delta h_{\gamma_y} \\ &\approx -e_x \cos \alpha \cos \theta - e_y \cos \alpha \sin \theta - e_z \sin \alpha \\ &\quad - (\rho - \rho_G) \gamma_x \sin \theta + (\rho - \rho_G) \gamma_y \cos \theta \end{aligned} \quad (3.78)$$

Using the relationship given by equation (3.48), the change in film thickness due to all possible translational and rotational displacements given by equation (3.78) can be transformed with respect to the X-Y-Z coordinate frame of reference. That is, equation (3.78) becomes

$$\begin{aligned} \Delta h_{CJB} &\approx -(e_x \cos \omega t + e_y \sin \omega t) \cos \alpha \cos \theta \\ &\quad - (-e_x \sin \omega t + e_y \cos \omega t) \cos \alpha \sin \theta - e_z \sin \alpha \\ &\quad - (\rho - \rho_G) (\gamma_x \cos \omega t + \gamma_y \sin \omega t) \sin \theta \\ &\quad + (\rho - \rho_G) (-\gamma_x \sin \omega t + \gamma_y \cos \omega t) \cos \theta \end{aligned}$$

which, with the aid of equations (3.53) and (3.60), simplifies to

$$\Delta h_{CJB} \approx -e_x \cos \alpha \cos(\theta + \omega t) - e_y \cos \alpha \sin(\theta + \omega t) - e_z \sin \alpha \\ - \gamma_x (\rho - \rho_G) \sin(\theta + \omega t) + \gamma_y (\rho - \rho_G) \cos(\theta + \omega t) \quad (3.79)$$

The film thickness at any point on the conical journal bearing can now be expressed as

$$h_{CJB} \approx h_{0,CJB} - e_z \sin \alpha \\ - e_x \cos \alpha \cos(\theta + \omega t) - e_y \cos \alpha \sin(\theta + \omega t) \\ - \gamma_x (\rho - \rho_G) \sin(\theta + \omega t) + \gamma_y (\rho - \rho_G) \cos(\theta + \omega t) \quad (3.80)$$

for the untapered land section and

$$h_{CJB} \approx h_{0,CJB} + (h_{1,CJB} - h_{0,CJB}) \left[\frac{\theta - (\theta_{0a} + \xi)}{\theta_{0b}} \right] - e_z \sin \alpha \\ - e_x \cos \alpha \cos(\theta + \omega t) - e_y \cos \alpha \sin(\theta + \omega t) \\ - \gamma_x (\rho - \rho_G) \sin(\theta + \omega t) + \gamma_y (\rho - \rho_G) \cos(\theta + \omega t) \quad (3.81)$$

for the tapered section.

Substituting the following non-dimensional terms

$$h_{CJB}^* = \frac{h_{CJB}}{h_{vc}}, \quad K_{CJB} = \frac{h_{1,CJB} - h_{0,CJB}}{h_{0,CJB}}, \quad \varepsilon_x = \frac{e_x}{h_{hc}}, \quad \varepsilon_y = \frac{e_y}{h_{hc}}, \quad \varepsilon_z = \frac{e_z}{h_{vc}},$$

$$\gamma_x^* = \frac{\gamma_x r_2}{h_{vc}}, \quad \gamma_y^* = \frac{\gamma_y r_2}{h_{vc}}, \quad t^* = \omega t, \quad \rho^* = \frac{\rho}{\rho_2 \sin \alpha} = \frac{\rho}{r_2} \text{ and } \rho_G^* = \frac{\rho_G}{r_2}$$

where h_{hc} is the horizontal (radial) clearance of the conical journal bearing (i.e. in the X-Y plane) and is related to the vertical clearance and minimum film thickness by $h_{hc} = h_{vc} \tan \alpha = h_{0,CJB} / \cos \alpha$, equation (3.80) can be rewritten as an expression for the dimensionless film thickness over the land section

$$h_{CJB}^* \approx \sin \alpha - \frac{e_x}{h_{vc}} \left(\frac{\sin \alpha}{\tan \alpha} \right) \cos(\theta + t^*) - \frac{e_y}{h_{vc}} \left(\frac{\sin \alpha}{\tan \alpha} \right) \sin(\theta + t^*) - \varepsilon_z \sin \alpha \\ - \frac{\gamma_x r_2}{h_{vc}} (\rho^* - \rho_G^*) \sin(\theta + t^*) + \frac{\gamma_y r_2}{h_{vc}} (\rho^* - \rho_G^*) \cos(\theta + t^*)$$

which simplifies to

$$h_{CJB}^* \approx \sin \alpha \left[1 - \varepsilon_X \cos(\theta + t^*) - \varepsilon_Y \sin(\theta + t^*) - \varepsilon_Z \right] \\ - \gamma_X^* (\rho^* - \rho_G^*) \sin(\theta + t^*) + \gamma_Y^* (\rho^* - \rho_G^*) \cos(\theta + t^*) \quad (3.82)$$

Likewise, equation (3.81) can be rewritten as an expression for the dimensionless film thickness over the tapered section

$$h_{CJB}^* \approx \sin \alpha \left[1 + K_{CJB} \left(\frac{\theta - (\theta_{0a} + \xi)}{\theta_{0b}} \right) - \varepsilon_X \cos(\theta + t^*) - \varepsilon_Y \sin(\theta + t^*) - \varepsilon_Z \right] \\ - \gamma_X^* (\rho^* - \rho_G^*) \sin(\theta + t^*) + \gamma_Y^* (\rho^* - \rho_G^*) \cos(\theta + t^*) \quad (3.83)$$

The vertical clearance of the conical journal bearing h_{vc} has been made equal to the minimum film thickness of the thrust bearing $h_{0,TB}$. That is, h_{vc} and $h_{0,TB}$ are each equal to half the total axial impeller travel i.e. $h_{vc} = h_{0,TB} = \frac{1}{2}(h_{vc} + h_{0,TB})$. This was done such that $-1 \leq \varepsilon_Z \leq 1$ and that several variables with respect to the thrust bearing and conical journal bearing were equivalent following the non-dimensionalisation process

$$\text{i.e. } \gamma_X^* = \frac{\gamma_X r_2}{h_{0,TB}} = \frac{\gamma_X r_2}{h_{vc}}.$$

3.3.2.1. Spatial and temporal derivatives of the film thickness

In regards to the conical journal bearing surfaces of the VentrAssist impeller, the spatial derivative of the dimensionless film thickness with respect to ρ^* is

$$\frac{\partial h_{CJB}^*}{\partial \rho^*} \approx -\gamma_X^* \sin(\theta + t^*) + \gamma_Y^* \cos(\theta + t^*) \quad (3.84)$$

For the untapered land, the spatial derivative with respect to θ is

$$\frac{\partial h_{CJB}^*}{\partial \theta} \approx \sin \alpha \left[\varepsilon_x \sin(\theta + t^*) - \varepsilon_y \cos(\theta + t^*) \right] \\ - \gamma_x^* (\rho^* - \rho_G^*) \cos(\theta + t^*) - \gamma_y^* (\rho^* - \rho_G^*) \sin(\theta + t^*) \quad (3.85)$$

and for the tapered section, the θ derivative is

$$\frac{\partial h_{CJB}^*}{\partial \theta} \approx \sin \alpha \left[\frac{K_{CJB}}{\theta_{0b}} + \varepsilon_x \sin(\theta + t^*) - \varepsilon_y \cos(\theta + t^*) \right] \\ - \gamma_x^* (\rho^* - \rho_G^*) \cos(\theta + t^*) - \gamma_y^* (\rho^* - \rho_G^*) \sin(\theta + t^*) \quad (3.86)$$

The temporal derivative of the dimensionless film thickness is

$$\frac{\partial h_{CJB}^*}{\partial t^*} \approx \sin \alpha \left[(\varepsilon_x - \dot{\varepsilon}_y) \sin(\theta + t^*) - (\dot{\varepsilon}_x + \varepsilon_y) \cos(\theta + t^*) - \dot{\varepsilon}_z \right] \\ - (\dot{\gamma}_x^* + \gamma_y^*) (\rho^* - \rho_G^*) \sin(\theta + t^*) - (\gamma_x^* - \dot{\gamma}_y^*) (\rho^* - \rho_G^*) \cos(\theta + t^*) \quad (3.87)$$

where $\dot{\varepsilon}_x = \frac{d\varepsilon_x}{dt^*}$, $\dot{\varepsilon}_y = \frac{d\varepsilon_y}{dt^*}$, $\dot{\varepsilon}_z = \frac{d\varepsilon_z}{dt^*}$, $\dot{\gamma}_x^* = \frac{d\gamma_x^*}{dt^*}$ and $\dot{\gamma}_y^* = \frac{d\gamma_y^*}{dt^*}$.

3.4. Solution of Reynolds equation

In order to obtain the pressure field over the thrust bearing and conical journal bearing surfaces of each blade of the VentrAssist impeller, the equations governing this pressure distribution, namely equations (3.33) and (3.43), must be solved. A direct analytical solution is possible only if the pressure gradient in the circumferential (θ) or radial directions (r or ρ) is neglected, commonly known as the infinitely short bearing and infinitely long bearing approximations respectively [13, 16]. However, if both pressure gradients are to be considered then numerical methods must be employed, which entails replacing the problem of finding the exact and continuous analytical solution with finding a number of discrete values on a finite mesh. More specifically, it involves both the discretisation and solving processes.

3.4.1. Discretisation

Discretisation was achieved by employing the method of finite differences. That is, each individual differential term in the governing equations was replaced by its equivalent finite difference approximation, resulting in a system of algebraic equations connecting nodal values of pressure. These equations could then be solved for the pressures at the discrete grid points only.

3.4.1.1. Thrust bearing

A structured numerical grid was established over the thrust bearing surfaces of each impeller blade where the spacing of grid points in the θ and r directions was uniform and given by $\Delta\theta$ and Δr respectively. The grid points are identified by index $i = 1, 2, \dots, I$ in the θ direction and $j = 1, 2, \dots, J$ in the r direction. Dropping the

asterisk notation but noting that all terms remain dimensionless, equation (3.33), which governs the dimensionless pressure field over the thrust bearing surfaces, was expanded to give

$$rh^3 \frac{\partial^2 p}{\partial r^2} + 3rh^2 \frac{\partial h}{\partial r} \frac{\partial p}{\partial r} + h^3 \frac{\partial p}{\partial r} + \frac{h^3}{r} \frac{\partial^2 p}{\partial \theta^2} + \frac{3h^2}{r} \frac{\partial h}{\partial \theta} \frac{\partial p}{\partial \theta} = 2Rr \frac{\partial h}{\partial t} - Rr \frac{\partial h}{\partial \theta} \quad (3.88)$$

Each individual pressure differential term was then replaced by its equivalent finite difference approximation. More specifically, the following central difference formulae [26] were used

$$\begin{aligned} \left. \frac{\partial p}{\partial \theta} \right|_{i,j,m} &= \frac{p_{i+1,j,m} - p_{i-1,j,m}}{2\Delta\theta} + O(\Delta\theta)^2 \approx \frac{p_{i+1,j,m} - p_{i-1,j,m}}{2\Delta\theta} \\ \left. \frac{\partial p}{\partial r} \right|_{i,j,m} &= \frac{p_{i,j+1,m} - p_{i,j-1,m}}{2\Delta r} + O(\Delta r)^2 \approx \frac{p_{i,j+1,m} - p_{i,j-1,m}}{2\Delta r} \\ \left. \frac{\partial^2 p}{\partial \theta^2} \right|_{i,j,m} &= \frac{p_{i-1,j,m} - 2p_{i,j,m} + p_{i+1,j,m}}{\Delta\theta^2} + O(\Delta\theta)^2 \approx \frac{p_{i-1,j,m} - 2p_{i,j,m} + p_{i+1,j,m}}{\Delta\theta^2} \\ \left. \frac{\partial^2 p}{\partial r^2} \right|_{i,j,m} &= \frac{p_{i,j-1,m} - 2p_{i,j,m} + p_{i,j+1,m}}{\Delta r^2} + O(\Delta r)^2 \approx \frac{p_{i,j-1,m} - 2p_{i,j,m} + p_{i,j+1,m}}{\Delta r^2} \end{aligned} \quad (3.89)$$

where $\partial p / \partial \theta|_{i,j,m}$ is the value of the gradient $\partial p / \partial \theta$ at grid point (i, j) on impeller blade m , $p_{i,j,m}$ is the value of pressure p at grid point (i, j) on impeller blade m , and where the symbols $O(\Delta\theta)^2$ and $O(\Delta r)^2$ indicate the order of magnitude of the truncation error. In this case the lowest-order terms in the truncation error contain either $\Delta\theta^2$ or Δr^2 , meaning that the approximations given by equation set (3.89) are second-order accurate. Mathematically, this means that if the grid size $\Delta\theta$ or Δr is decreased in size by half, the truncation error will be reduced to a quarter of its previous value. Note that the derivatives of the dimensionless film thickness were not replaced by finite differences as they are given by equations (3.66) – (3.69).

After the substitution of equation set (3.89), equation (3.88) can be written

$$\begin{aligned} & r_j h_{i,j,m}^3 \left(\frac{P_{i,j-1,m} - 2p_{i,j,m} + p_{i,j+1,m}}{\Delta r^2} \right) + 3r_j h_{i,j,m}^2 \frac{\partial h}{\partial r} \Big|_{i,j,m} \left(\frac{P_{i,j+1,m} - P_{i,j-1,m}}{2\Delta r} \right) \\ & + h_{i,j,m}^3 \left(\frac{P_{i,j+1,m} - P_{i,j-1,m}}{2\Delta r} \right) + \frac{h_{i,j,m}^3}{r_j} \left(\frac{p_{i-1,j,m} - 2p_{i,j,m} + p_{i+1,j,m}}{\Delta \theta^2} \right) \\ & + \frac{3h_{i,j,m}^2}{r_j} \frac{\partial h}{\partial \theta} \Big|_{i,j,m} \left(\frac{p_{i+1,j,m} - p_{i-1,j,m}}{2\Delta \theta} \right) = 2Rr_j \frac{\partial h}{\partial t} \Big|_{i,j,m} - Rr_j \frac{\partial h}{\partial \theta} \Big|_{i,j,m} \end{aligned} \quad (3.90)$$

This can be rewritten in terms of nodal values as

$$\begin{aligned} & \left(\frac{1}{r_j \Delta \theta^2} - \frac{1.5}{r_j h_{i,j,m} \Delta \theta} \cdot \frac{\partial h}{\partial \theta} \Big|_{i,j,m} \right) p_{i-1,j,m} - 2 \left(\frac{r_j}{\Delta r^2} + \frac{1}{r_j \Delta \theta^2} \right) p_{i,j,m} + \\ & \left(\frac{1}{r_j \Delta \theta^2} + \frac{1.5}{r_j h_{i,j,m} \Delta \theta} \cdot \frac{\partial h}{\partial \theta} \Big|_{i,j,m} \right) p_{i+1,j,m} + \left(\frac{r_j}{\Delta r^2} - \frac{1.5r_j}{h_{i,j,m} \Delta r} \cdot \frac{\partial h}{\partial r} \Big|_{i,j,m} - \frac{0.5}{\Delta r} \right) p_{i,j-1,m} + \\ & \left(\frac{r_j}{\Delta r^2} + \frac{1.5r_j}{h_{i,j,m} \Delta r} \cdot \frac{\partial h}{\partial r} \Big|_{i,j,m} + \frac{0.5}{\Delta r} \right) p_{i,j+1,m} = 2R \frac{r_j}{h_{i,j,m}^3} \frac{\partial h}{\partial t} \Big|_{i,j,m} - R \frac{r_j}{h_{i,j,m}^3} \frac{\partial h}{\partial \theta} \Big|_{i,j,m} \end{aligned} \quad (3.91)$$

3.4.1.2. Conical journal bearing

In a similar manner for the thrust bearing, a structured computational grid was established over the conical journal bearing surfaces of each impeller blade where the spacing of grid points in the θ and ρ directions was uniform and given by $\Delta\theta$ and $\Delta\rho$ respectively. The grid points are identified by index $i = 1, 2, \dots, I$ in the θ direction and $j = 1, 2, \dots, J$ in the ρ direction. Dropping the asterisk notation but noting that all terms remain dimensionless, equation (3.43), which governs the dimensionless pressure field over the conical journal bearing surfaces, was expanded to yield

$$h^3 \frac{\partial^2 p}{\partial \rho^2} + 3h^2 \frac{\partial h}{\partial \rho} \frac{\partial p}{\partial \rho} + \frac{h^3}{\rho} \frac{\partial p}{\partial \rho} + \frac{h^3}{\rho^2 \sin^2 \alpha} \frac{\partial^2 \theta}{\partial \theta^2} + \frac{3h^2}{\rho^2 \sin^2 \alpha} \frac{\partial h}{\partial \theta} \frac{\partial p}{\partial \theta} = 2R \frac{\partial h}{\partial t} - R \frac{\partial h}{\partial \theta} \quad (3.92)$$

Each individual pressure differential term was then replaced by its equivalent finite difference approximation. The following second-order central difference formulae were used

$$\begin{aligned}
 \left. \frac{\partial p}{\partial \theta} \right|_{i,j,m} &= \frac{p_{i+1,j,m} - p_{i-1,j,m}}{2\Delta\theta} + O(\Delta\theta)^2 \approx \frac{p_{i+1,j,m} - p_{i-1,j,m}}{2\Delta\theta} \\
 \left. \frac{\partial p}{\partial \rho} \right|_{i,j,m} &= \frac{p_{i,j+1,m} - p_{i,j-1,m}}{2\Delta\rho} + O(\Delta\rho)^2 \approx \frac{p_{i,j+1,m} - p_{i,j-1,m}}{2\Delta\rho} \\
 \left. \frac{\partial^2 p}{\partial \theta^2} \right|_{i,j,m} &= \frac{p_{i-1,j,m} - 2p_{i,j,m} + p_{i+1,j,m}}{\Delta\theta^2} + O(\Delta\theta)^2 \approx \frac{p_{i-1,j,m} - 2p_{i,j,m} + p_{i+1,j,m}}{\Delta\theta^2} \\
 \left. \frac{\partial^2 p}{\partial \rho^2} \right|_{i,j,m} &= \frac{p_{i,j-1,m} - 2p_{i,j,m} + p_{i,j+1,m}}{\Delta\rho^2} + O(\Delta\rho)^2 \approx \frac{p_{i,j-1,m} - 2p_{i,j,m} + p_{i,j+1,m}}{\Delta\rho^2}
 \end{aligned} \tag{3.93}$$

Following the substitution of equation set (3.93), equation (3.92) can be written

$$\begin{aligned}
 h_{i,j,m}^3 \left(\frac{p_{i,j-1,m} - 2p_{i,j,m} + p_{i,j+1,m}}{\Delta\rho^2} \right) + 3h_{i,j,m}^2 \left. \frac{\partial h}{\partial \rho} \right|_{i,j,m} \left(\frac{p_{i,j+1,m} - p_{i,j-1,m}}{2\Delta\rho} \right) + \\
 \frac{h_{i,j,m}^3}{\rho_j} \left(\frac{p_{i,j+1,m} - p_{i,j-1,m}}{2\Delta\rho} \right) + \frac{h_{i,j,m}^3}{\rho_j^2 \sin^2 \alpha} \left(\frac{p_{i-1,j,m} - 2p_{i,j,m} + p_{i+1,j,m}}{\Delta\theta^2} \right) + \\
 \frac{3h_{i,j,m}^2}{\rho_j^2 \sin^2 \alpha} \left. \frac{\partial h}{\partial \theta} \right|_{i,j,m} \left(\frac{p_{i+1,j,m} - p_{i-1,j,m}}{2\Delta\theta} \right) = 2R \left. \frac{\partial h}{\partial t} \right|_{i,j,m} - R \left. \frac{\partial h}{\partial \theta} \right|_{i,j,m}
 \end{aligned} \tag{3.94}$$

This can be further written in terms of nodal values as

$$\begin{aligned}
 & \left(\frac{1}{\rho_j \sin \alpha} \right)^2 \left(\frac{1}{\Delta \theta^2} - \frac{1.5}{h_{i,j,m} \Delta \theta} \cdot \frac{\partial h}{\partial \theta} \Big|_{i,j,m} \right) p_{i-1,j,m} - 2 \left[\frac{1}{\Delta \rho^2} + \left(\frac{1}{\Delta \theta \rho_j \sin \alpha} \right)^2 \right] p_{i,j,m} \\
 & + \left(\frac{1}{\rho_j \sin \alpha} \right)^2 \left(\frac{1}{\Delta \theta^2} + \frac{1.5}{h_{i,j,m} \Delta \theta} \cdot \frac{\partial h}{\partial \theta} \Big|_{i,j,m} \right) p_{i+1,j,m} \\
 & + \left(\frac{1}{\Delta \rho^2} - \frac{1.5}{h_{i,j,m} \Delta \rho} \cdot \frac{\partial h}{\partial \rho} \Big|_{i,j,m} - \frac{0.5}{\rho_j \Delta \rho} \right) p_{i,j-1,m} \\
 & + \left(\frac{1}{\Delta \rho^2} + \frac{1.5}{h_{i,j,m} \Delta \rho} \cdot \frac{\partial h}{\partial \rho} \Big|_{i,j,m} + \frac{0.5}{\rho_j \Delta \rho} \right) p_{i,j+1,m} = \frac{2R}{h_{i,j,m}^3} \cdot \frac{\partial h}{\partial t} \Big|_{i,j,m} - \frac{R}{h_{i,j,m}^3} \cdot \frac{\partial h}{\partial \theta} \Big|_{i,j,m}
 \end{aligned} \tag{3.95}$$

3.4.2. Solving of discretised equations

The systems of discretised equations were rewritten in tridiagonal form and subsequently solved using a tridiagonal solver known as the Thomas algorithm. In one-dimension, the Thomas algorithm is a direct solver. See *Appendix A – The Thomas Algorithm* for details. Additionally FORTRAN subroutine THOMAS, based on the Thomas algorithm, is given in Appendix B.

For two-dimensional problems, however, the Thomas algorithm may be classified as a multi-block indirect solver, where the algorithm is applied iteratively, in a line-by-line fashion, in which values of pressure along a selected grid line are computed. The calculation is moved to the next line and subsequently swept through the whole plane until all unknown values on each line have been calculated. The sequence in which lines are chosen is known as the sweep direction.

3.4.2.1. The Thomas algorithm in 2D

Using a five-point differencing scheme, the value of $p_{i,j,m}$ can be written in terms of the neighbouring nodal values $p_{i-1,j,m}$, $p_{i+1,j,m}$, $p_{i,j-1,m}$, and $p_{i,j+1,m}$ by means of the relationship

$$A_{i-1,j,m}p_{i-1,j,m} + A_{i,j,m}p_{i,j,m} + A_{i+1,j,m}p_{i+1,j,m} + A_{i,j-1,m}p_{i,j-1,m} + A_{i,j+1,m}p_{i,j+1,m} = B_{i,j,m} \quad (3.96)$$

which is the general form of equations (3.91) and (3.95). To enable the application of the Thomas algorithm, equation (3.96) must be arranged in the following tridiagonal form

$$A_{i-1,j,m}p_{i-1,j,m} + A_{i,j,m}p_{i,j,m} + A_{i+1,j,m}p_{i+1,j,m} = B_{i,j,m} - A_{i,j-1,m}p_{i,j-1,m} - A_{i,j+1,m}p_{i,j+1,m} \quad (3.97)$$

to sweep all $j = 2, 3, \dots, J-1$ rows of grid points, or alternatively

$$A_{i,j-1,m}p_{i,j-1,m} + A_{i,j,m}p_{i,j,m} + A_{i,j+1,m}p_{i,j+1,m} = B_{i,j,m} - A_{i-1,j,m}p_{i-1,j,m} - A_{i+1,j,m}p_{i+1,j,m} \quad (3.98)$$

to sweep all $i = 2, 3, \dots, I-1$ columns.

Further, performing iterative sweeps by rows, for example, involves rewriting equation (3.97) in the form

$$A_{i-1,j,m}p_{i-1,j,m}^{n+1} + A_{i,j,m}p_{i,j,m}^{n+1} + A_{i+1,j,m}p_{i+1,j,m}^{n+1} = B_{i,j,m} - A_{i,j-1,m}p_{i,j-1,m}^{n+1} - A_{i,j+1,m}p_{i,j+1,m}^{n+1} \quad (3.99)$$

where n denotes the iteration level and $p_{i,j,m}^{n+1}$ is the most recent value of $p_{i,j,m}$. When sweeping from $j = 2, 3, \dots, J-1$, then the values of $p_{i,j-1,m}$ are known either from the lower boundary conditions, in which case $p_{i,j-1,m} \equiv p_{i,1,m}$, or from the solution already obtained at the $n+1$ level from the row below, in which case $p_{i,j-1,m} \equiv p_{i,j-1,m}^{n+1}$.

However, values of $p_{i,j+1,m}$ are unknown so the process must be iterative. At each iteration $p_{i,j+1,m}$ is taken to have its value at the end of the previous iteration $p_{i,j+1,m}^n$, or a given initial value eg. $p_{i,j+1,m}^0 = 0$. One iterative cycle is completed when the

tridiagonal inversion has been applied to all rows. The process is continued until convergence has been achieved.

Similarly, performing sweeps by i columns from $i = 2, 3, \dots, I - 1$ involves rewriting equation (3.98) as

$$A_{i,j-1,m}P_{i,j-1,m}^{n+1} + A_{i,j,m}P_{i,j,m}^{n+1} + A_{i,j+1,m}P_{i,j+1,m}^{n+1} = B_{i,j,m} - A_{i-1,j,m}P_{i-1,j,m}^{n+1} - A_{i+1,j,m}P_{i+1,j,m}^{n+1} \quad (3.100)$$

Convergence can often be accelerated by alternating the sweep direction [27, 28], such that a complete iteration cycle consists of two half-steps eg. a sweep of all rows following which all values are at the $n + \frac{1}{2}$ iteration level, followed by a sweep of all columns after which all values are at the $n + 1$ iteration level. This involves rewriting equation (3.99) in the form

$$A_{i-1,j,m}P_{i-1,j,m}^{n+\frac{1}{2}} + A_{i,j,m}P_{i,j,m}^{n+\frac{1}{2}} + A_{i+1,j,m}P_{i+1,j,m}^{n+\frac{1}{2}} = B_{i,j,m} - A_{i,j-1,m}P_{i,j-1,m}^{n+\frac{1}{2}} - A_{i,j+1,m}P_{i,j+1,m}^n \quad (3.101)$$

to sweep over all $j = 2, 3, \dots, J - 1$ rows of grid points, and equation (3.100) as

$$A_{i,j-1,m}P_{i,j-1,m}^{n+1} + A_{i,j,m}P_{i,j,m}^{n+1} + A_{i,j+1,m}P_{i,j+1,m}^{n+1} = B_{i,j,m} - A_{i-1,j,m}P_{i-1,j,m}^{n+1} - A_{i+1,j,m}P_{i+1,j,m}^{n+\frac{1}{2}} \quad (3.102)$$

to subsequently sweep over all $i = 2, 3, \dots, I - 1$ columns.

For use with the Thomas algorithm as outlined in Appendix A, equation (3.101) is rewritten as

$$a_{i-1}P_{i-1,j,m}^{n+\frac{1}{2}} + b_{i-1}P_{i,j,m}^{n+\frac{1}{2}} + c_{i-1}P_{i+1,j,m}^{n+\frac{1}{2}} = d_{i-1} \quad (3.103)$$

for $i = 2, 3, \dots, I - 1$ where

$$a_{i-1} = A_{i-1,j,m}$$

$$b_{i-1} = A_{i,j,m}$$

$$c_{i-1} = A_{i+1,j,m}$$

$$d_{i-1} = B_{i,j,m} - A_{i,j-1,m}P_{i,j-1,m}^{n+\frac{1}{2}} - A_{i,j+1,m}P_{i,j+1,m}^n$$

Equation (3.102) must also be rewritten for use with the Thomas algorithm as

$$a_{j-1} p_{i,j-1,m}^{n+1} + b_{j-1} p_{i,j,m}^{n+1} + c_{j-1} p_{i,j+1,m}^{n+1} = d_{i-1} \quad (3.104)$$

for $j = 2,3,\dots,J-1$ where

$$a_{j-1} = A_{i,j-1,m}$$

$$b_{j-1} = A_{i,j,m}$$

$$c_{j-1} = A_{i,j+1,m}$$

$$d_{j-1} = B_{i,j,m} - A_{i-1,j,m} p_{i-1,j,m}^{n+1} - A_{i+1,j,m} p_{i+1,j,m}^{n+1}$$

3.4.2.2. Thrust bearing

To solve equation (3.91) using the Thomas algorithm by first performing sweeps by j rows for $j = 2,3,\dots,J-1$ followed by sweeps by i columns for $i = 2,3,\dots,I-1$ over the thrust bearing surfaces of each impeller blade $m = 1,2,\dots,N_p$ involved rearranging equation (3.91) in the form of equation (3.103)

$$a_{i-1} p_{i-1,j,m}^{n+1} + b_{i-1} p_{i,j,m}^{n+1} + c_{i-1} p_{i+1,j,m}^{n+1} = d_{i-1} \quad (3.105)$$

for $i = 2,3,\dots,I-1$ where

$$a_{i-1} = \left(\frac{1}{r_j \Delta \theta} \right) \left(\frac{1}{\Delta \theta} - \frac{1.5}{h_{i,j,m}} \cdot \frac{\partial h}{\partial \theta} \Big|_{i,j,m} \right)$$

$$b_{i-1} = -2 \left(\frac{r_j}{\Delta r^2} + \frac{1}{r_j \Delta \theta^2} \right)$$

$$c_{i-1} = \left(\frac{1}{r_j \Delta \theta} \right) \left(\frac{1}{\Delta \theta} + \frac{1.5}{h_{i,j,m}} \cdot \frac{\partial h}{\partial \theta} \Big|_{i,j,m} \right)$$

$$d_{i-1} = 2R \frac{r_j}{h_{i,j,m}^3} \cdot \frac{\partial h}{\partial t} \Big|_{i,j,m} - R \frac{r_j}{h_{i,j,m}^3} \cdot \frac{\partial h}{\partial \theta} \Big|_{i,j,m} \\ - \left(\frac{1}{\Delta r} \right) \left(\frac{r_j}{\Delta r} - \frac{1.5r_j}{h_{i,j,m}} \cdot \frac{\partial h}{\partial r} \Big|_{i,j,m} - 0.5 \right) p_{i,j-1,m}^{n+\frac{1}{2}} \\ - \left(\frac{1}{\Delta r} \right) \left(\frac{r_j}{\Delta r} + \frac{1.5r_j}{h_{i,j,m}} \cdot \frac{\partial h}{\partial r} \Big|_{i,j,m} + 0.5 \right) p_{i,j+1,m}^n$$

and in the form of equation (3.104)

$$a_{j-1} p_{i,j-1,m}^{n+1} + b_{j-1} p_{i,j,m}^{n+1} + c_{j-1} p_{i,j+1,m}^{n+1} = d_{i-1} \quad (3.106)$$

for $j = 2, 3, \dots, J-1$ where

$$a_{j-1} = \left(\frac{1}{\Delta r} \right) \left(\frac{r_j}{\Delta r} - \frac{1.5r_j}{h_{i,j,m}} \cdot \frac{\partial h}{\partial r} \Big|_{i,j,m} - 0.5 \right) \\ b_{j-1} = -2 \left(\frac{r_j}{\Delta r^2} + \frac{1}{r_j \Delta \theta^2} \right) \\ c_{j-1} = \left(\frac{1}{\Delta r} \right) \left(\frac{r_j}{\Delta r} + \frac{1.5r_j}{h_{i,j,m}} \cdot \frac{\partial h}{\partial r} \Big|_{i,j,m} + 0.5 \right) \\ d_{j-1} = 2R \frac{r_j}{h_{i,j,m}^3} \cdot \frac{\partial h}{\partial t} \Big|_{i,j,m} - R \frac{r_j}{h_{i,j,m}^3} \cdot \frac{\partial h}{\partial \theta} \Big|_{i,j,m} \\ - \left(\frac{1}{r_j \Delta \theta} \right) \left(\frac{1}{\Delta \theta} - \frac{1.5}{h_{i,j,m}} \cdot \frac{\partial h}{\partial \theta} \Big|_{i,j,m} \right) p_{i-1,j,m}^{n+1} \\ - \left(\frac{1}{r_j \Delta \theta} \right) \left(\frac{1}{\Delta \theta} + \frac{1.5}{h_{i,j,m}} \cdot \frac{\partial h}{\partial \theta} \Big|_{i,j,m} \right) p_{i+1,j,m}^{n+\frac{1}{2}}$$

3.4.2.3. Conical journal bearing

To solve equation (3.95) using the Thomas algorithm by first performing sweeps by j rows for $j = 2, 3, \dots, J-1$ followed by sweeps by i rows for $i = 2, 3, \dots, I-1$ over the

conical journal bearing surfaces of each impeller blade $m=1,2,\dots,N_p$ involved rearranging equation (3.95) in the form of equation (3.103)

$$a_{i-1} p_{i-1,j,m}^{n+\frac{1}{2}} + b_{i-1} p_{i,j,m}^{n+\frac{1}{2}} + c_{i-1} p_{i+1,j,m}^{n+\frac{1}{2}} = d_{i-1} \quad (3.107)$$

for $i = 2,3,\dots,I-1$ where

$$a_{i-1} = \left(\frac{1}{\Delta\theta} \right) \left(\frac{1}{\rho_j \sin \alpha} \right)^2 \left(\frac{1}{\Delta\theta} - \frac{1.5}{h_{i,j,m}} \cdot \frac{\partial h}{\partial \theta} \Big|_{i,j,m} \right)$$

$$b_{i-1} = -2 \left[\frac{1}{\Delta\rho^2} + \left(\frac{1}{\Delta\theta \rho_j \sin \alpha} \right)^2 \right]$$

$$c_{i-1} = \left(\frac{1}{\Delta\theta} \right) \left(\frac{1}{\rho_j \sin \alpha} \right)^2 \left(\frac{1}{\Delta\theta} + \frac{1.5}{h_{i,j,m}} \cdot \frac{\partial h}{\partial \theta} \Big|_{i,j,m} \right)$$

$$\begin{aligned} d_{i-1} = & \frac{2R}{h_{i,j,m}^3} \cdot \frac{\partial h}{\partial t} \Big|_{i,j,m} - \frac{R}{h_{i,j,m}^3} \cdot \frac{\partial h}{\partial \theta} \Big|_{i,j,m} \\ & - \left(\frac{1}{\Delta\rho} \right) \left(\frac{1}{\Delta\rho} - \frac{1.5}{h_{i,j,m}} \cdot \frac{\partial h}{\partial \rho} \Big|_{i,j,m} - \frac{0.5}{\rho_j} \right) p_{i,j-1,m}^{n+\frac{1}{2}} \\ & - \left(\frac{1}{\Delta\rho} \right) \left(\frac{1}{\Delta\rho} + \frac{1.5}{h_{i,j,m}} \cdot \frac{\partial h}{\partial \rho} \Big|_{i,j,m} + \frac{0.5}{\rho_j} \right) p_{i,j+1,m}^n \end{aligned}$$

and in the form of equation (3.104)

$$a_{j-1} p_{i,j-1,m}^{n+1} + b_{j-1} p_{i,j,m}^{n+1} + c_{j-1} p_{i,j+1,m}^{n+1} = d_{j-1} \quad (3.108)$$

for $j = 2,3,\dots,J-1$ where

$$a_{j-1} = \left(\frac{1}{\Delta\rho} \right) \left(\frac{1}{\Delta\rho} - \frac{1.5}{h_{i,j,m}} \cdot \frac{\partial h}{\partial \rho} \Big|_{i,j,m} - \frac{0.5}{\rho_j} \right)$$

$$b_{j-1} = -2 \left[\frac{1}{\Delta\rho^2} + \left(\frac{1}{\Delta\theta \rho_j \sin \alpha} \right)^2 \right]$$

$$c_{j-1} = \left(\frac{1}{\Delta\rho} \right) \left(\frac{1}{\Delta\rho} + \frac{1.5}{h_{i,j,m}} \cdot \frac{\partial h}{\partial \rho} \Big|_{i,j,m} + \frac{0.5}{\rho_j} \right)$$

$$\begin{aligned}
 d_{j-1} = & \frac{2R}{h_{i,j,m}^3} \cdot \frac{\partial h}{\partial t} \Big|_{i,j,m} - \frac{R}{h_{i,j,m}^3} \cdot \frac{\partial h}{\partial \theta} \Big|_{i,j,m} \\
 & - \left(\frac{1}{\Delta \theta} \right) \left(\frac{1}{\rho_j \sin \alpha} \right)^2 \left(\frac{1}{\Delta \theta} - \frac{1.5}{h_{i,j,m}} \cdot \frac{\partial h}{\partial \theta} \Big|_{i,j,m} \right) p_{i-1,j,m}^{n+1} \\
 & - \left(\frac{1}{\Delta \theta} \right) \left(\frac{1}{\rho_j \sin \alpha} \right)^2 \left(\frac{1}{\Delta \theta} + \frac{1.5}{h_{i,j,m}} \cdot \frac{\partial h}{\partial \theta} \Big|_{i,j,m} \right) p_{i+1,j,m}^{n+\frac{1}{2}}
 \end{aligned}$$

3.4.2.4. Iterative procedure

The computational procedure to calculate the pressure distribution over the lubricated surfaces of the VentrAssist impeller at a specific point in time was as follows:

- 1) The boundary conditions were established by allocating a value of zero to the grid points along the boundaries of the numerical grids on both the thrust bearing and conical journal bearing surfaces of each impeller blade. These values remained unaltered during the iterative process. That is,

$$p_{1,j,m}^k = p_{I,j,m}^k = 0 \text{ for } j = 1, 2, \dots, J, m = 1, 2, \dots, N_p \text{ and } k = 0, 1, \dots, K-1$$

$$p_{i,1,m}^k = p_{i,J,m}^k = 0 \text{ for } i = 1, 2, \dots, I, m = 1, 2, \dots, N_p \text{ and } k = 0, 1, \dots, K-1$$

- 2) An initial value was allocated to all interior grid points at the start of the iterative process at each time step as an initial “guess”. For the first time step, i.e. when $k = 0$, a value of zero was allocated. That is,

$$p_{i,j,m}^0 = 0 \text{ for } i = 2, 3, \dots, I-1, j = 2, 3, \dots, J-1, \text{ and } m = 1, 2, \dots, N_p$$

where the superscript ‘0’ refers to the time step index. However, for subsequent time steps, i.e. when $k = 1, 2, \dots, K-1$, the pressure distribution over each impeller blade at the previous time step, i.e. corresponding to

$k-1=1,2,\dots,K-1$, was used as the initial guess for the pressure values. See also section 3.6.4. for details.

- 3) Using the Thomas algorithm to perform a sweep of all $j=2,3,\dots,J-1$ rows followed by a sweep of all $i=2,3,\dots,I-1$ columns as outlined in sections 3.4.2.1. – 3.4.2.3., new pressure values were calculated for all interior grid points.
- 4) If the most recently computed pressure at grid point (i,j) on impeller blade m , denoted $p_{i,j,m}^{n+1}$ where n is the iteration level (not the time step index as referred to in step (2)), was found to be within the specified accuracy 10^{-6} of the previous value $p_{i,j,m}^{n'}$, i.e.

$$\left| p_{i,j,m}^{n+1} - p_{i,j,m}^n \right| \leq 10^{-6} \quad (3.109)$$

then the solution at this grid point was assumed to be converged (i.e. $p_{i,j,m}^{n+1} \rightarrow p_{i,j,m}^n$) and was not further altered during the iterative procedure. At this point, the converged solution is taken as the pressure value at that time step i.e. $p_{i,j,m}^{k+1} = p_{i,j,m}^{n+1}$. However, if this accuracy was not achieved, then the pressure allocated to this node was calculated as [27]

$$p_{i,j,m}^{n+1'} = p_{i,j,m}^{n'} + \omega(p_{i,j,m}^{n+1} - p_{i,j,m}^{n'}) \quad (3.110)$$

where it is expected that $p_{i,j,m}^{n+1'}$ will be closer to the final solution than the unaltered value $p_{i,j,m}^{n+1}$. Equation (3.110) is known as successive over-relaxation (SOR) and is commonly used to accelerate the iterative process. Typically, the over-relaxation factor ω has the value of $1 < \omega < 2$ as required for convergence [29], the most appropriate value of which is dependent on grid size. In the

absence of an analytical value of ω , the “optimum value” ω_0 may be determined experimentally. In this study, $\omega=1.5$ was used as it was determined during a brief investigation that this value resulted in the least number of iterative steps for a grid of size $I \times J = 31 \times 31$.

- 5) Steps (3) and (4) were repeated until the pressure values at all grid points were below the desired accuracy specified in (4).

3.4.3. Verification of solution method

The solution method outlined in section 3.4.2. was verified by the employment of this same method to analyse a rectangular shaped pad with a linear taper as outlined in Cameron [22]. Cameron gives results to several quantities derived from the pressure distribution over the pad, including the side leakage flow, end leakage flow, centre of pressure, friction force etc.. The details of the study are given in Appendix C. FORTRAN program “tb2d.f” was used to perform the numerical calculations and is listed in Appendix E.

3.4.4. Refinement of the numerical grid

The numerical grid was progressively refined in an extension of the study detailed in Appendix C. This was done to show that the solution is independent on the size of the grid. The results and details of this extended study are given in Appendix D. Program “tb2d.f” was used to carry out the calculations and again can be found in Appendix E.

This study indicated that a grid size of $I \times J = 31 \times 31$ yielded a grid independent solution. This size is small enough such that the solution time remains economical without compromising accuracy and was therefore used throughout this work.

3.5. Calculation of fluid film forces

Having established the hydrodynamic pressure distribution over the lubricating surfaces of both the conical journal bearing and thrust bearing of the impeller, it is possible to compute the resulting forces and moments exerted on the impeller. The net forces and moments on the impeller are calculated by the summation of the individual contributions of the thrust bearing and conical journal bearing. For this reason, the forces on the thrust bearing and conical journal bearing are considered separately, the results of which are subsequently combined to give the total forces and moments on the impeller.

3.5.1. Thrust bearing

Consider a small element of area $dA = rd\theta dr$ on the surface of the thrust bearing located at position $(r, \theta + \omega t)$ for $\xi \leq \theta \leq \xi + \theta_0$ where angle $\theta + \omega t$ is measured counter-clockwise from the positive X-axis. At the point under examination the pressure is p and the hydrodynamic force on the element is $prd\theta dr$, which acts perpendicular to the blade surface. Over the tapered section of the bearing, this elemental force will have a component that contributes to the lift force F_L and a much smaller component that contributes to the drag force F_D . Both F_L and F_D are pictured in Figure 3.13. Additionally, there exists a force $\tau rd\theta dr$ resulting from the viscous fluid shear τ , which acts on this same element tangentially to the blade surface. Due to the bearing taper, this force will have a component contributing to F_D and a much smaller component that contributes to F_L . Makdissi [17] indicated that the effects of the viscous fluid drag forces on both the steady running and dynamic performance of a 360° journal bearing are negligible. The contribution of the viscous

drag force $\tau r d\theta dr$ to F_L and F_D , and the contribution of force $pr d\theta dr$ to F_D were consequently not included in this study. That is, the effects of the taper were neglected in all calculations such that the lift force (and resulting moments) consisted of the force due to the pressure distribution over the bearing surfaces only, and such that the drag force F_D was neglected altogether. However, it should be noted that Bertram *et al.* [30] indicated that effects due to the taper, although small, are in fact non-negligible. Crosby [19] noted that previous investigators have found the inclusion of the friction force to have a stabilising effect. Therefore it is recommended that such effects be included in a more detailed future study.

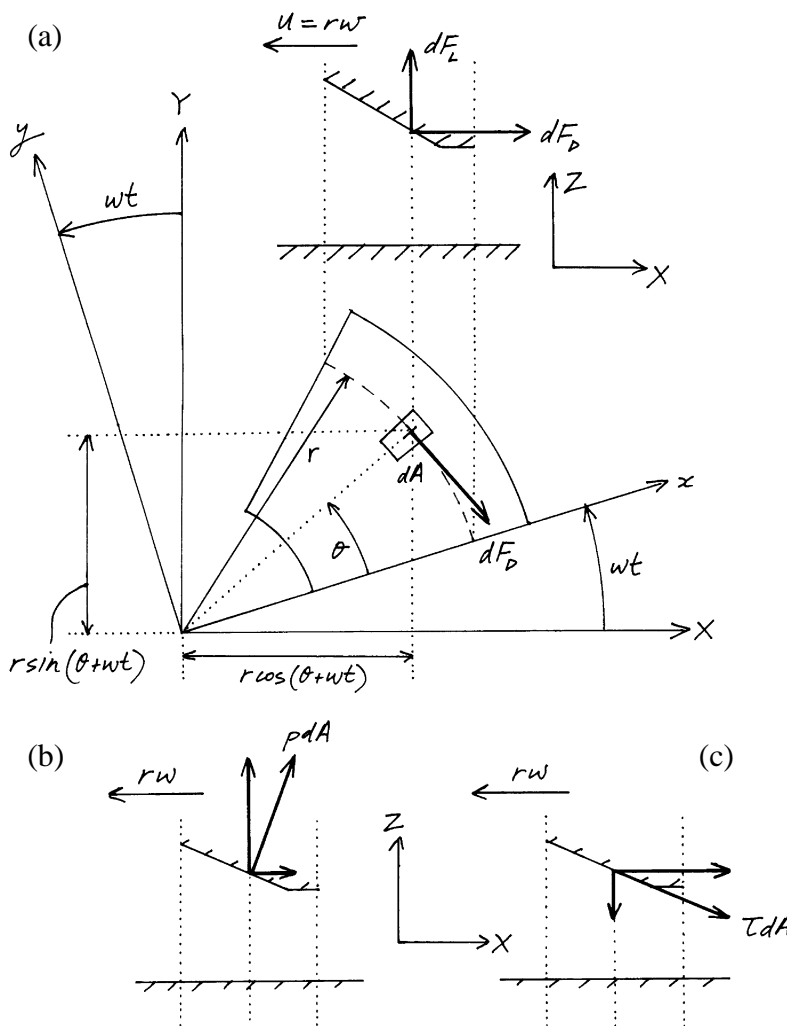


Figure 3.13. Effects of bearing taper; (a) lift and drag forces on rotating impeller, (b) components of the pressure force, and (c) components of the shear force that constitute the lift and drag forces

Neglecting the effects of the taper, this force $prd\theta dr$ acts in the Z-direction only. The total force on the impeller in the Z-direction, resulting from the pressure distribution over the thrust bearing alone, is the sum of the individual contributions from each impeller blade. That is, the total force on the thrust bearing in the Z-direction at time t is given by the sum of the integrals of elemental force $prd\theta dr$ over each blade $m = 1, 2, \dots, N_p$

$$F_{Z,TB} = \sum_{m=1}^{N_p} \int_{r_1}^{r_2} \int_{\xi}^{\xi+\theta_0} prd\theta dr \quad (3.111)$$

where N_p is the total number of blades.

Upon substitution of non-dimensional variables, equation (3.111) may be rewritten as

$$F_{Z,TB} = \sum_{m=1}^{N_p} \int_{r_1}^{r_2} \int_{\xi}^{\xi+\theta_0} \left(\frac{6\eta\omega L^2}{h_{0,TB}^2} p^* \right) (r_2 r^*) d\theta d(r_2 r^*)$$

which simplifies to

$$F_{Z,TB}^* = \sum_{m=1}^{N_p} \int_{r_1^*}^{r_2^*} \int_{\xi}^{\xi+\theta_0} p^* r^* d\theta dr^* \quad (3.112)$$

where $F_{Z,TB}^* = \frac{h_{0,TB}^2}{6\eta\omega L^2 r_2^2} F_{Z,TB}$ is the non-dimensional force on the thrust bearing in the

Z-direction.

Considering the same small element of area $dA = rd\theta dr$, the turning moment about the centre of mass of the impeller due to the force $prd\theta dr$ acting on this area will have a component about the X-axis of magnitude $yprd\theta dr$ where $y = r \sin(\theta + \omega t)$ is the perpendicular distance from the X-axis, and a component about the Y-axis given by $-xprd\theta dr$ where $x = r \cos(\theta + \omega t)$ is the perpendicular distance from the Y-axis. See Figure 3.13(a). The total moment on the impeller about coordinate axes X and Y, resulting from the pressure distribution over the thrust bearing alone, is the sum of the

contributions from each blade of the thrust bearing. That is, the total moment on the thrust bearing about the X-axis at time t is given by the sum of the integrals of the X-component over each blade $m = 1, 2, \dots, N_p$

$$M_{X,TB} = \sum_{m=1}^{N_p} \int_{r_1}^{r_2} \int_{\xi}^{\xi+\theta_0} pr^2 \sin(\theta + \omega t) d\theta dr \quad (3.113)$$

Similarly, the total moment on the thrust bearing about the Y-axis at time t is given by

$$M_{Y,TB} = - \sum_{m=1}^{N_p} \int_{r_1}^{r_2} \int_{\xi}^{\xi+\theta_0} pr^2 \cos(\theta + \omega t) d\theta dr \quad (3.114)$$

Upon substitution of non-dimensional variables equation (3.113) may be rewritten as

$$M_{X,TB} = \sum_{m=1}^{N_p} \int_{r_1}^{r_2} \int_{\xi}^{\xi+\theta_0} \left(\frac{6\eta\omega L^2}{h_{0,TB}^2} p^* \right) (r_2 r^*)^2 \sin\left(\theta + \omega \left[\frac{t^*}{\omega} \right]\right) d\theta d(r_2 r^*)$$

which simplifies to

$$M_{X,TB}^* = \sum_{m=1}^{N_p} \int_{r_1^*}^{r_2^*} \int_{\xi}^{\xi+\theta_0} p^* r^{*2} \sin(\theta + t^*) d\theta dr^* \quad (3.115)$$

where $M_{X,TB}^* = \frac{h_{0,TB}^2}{6\eta\omega L^2 r_2^3} M_{X,TB}$ is the non-dimensional turning moment on the thrust

bearing about the X-axis at the non-dimensional time t^* . Similarly, the non-dimensional moment on the thrust bearing about the Y-axis at time t^* is

$$M_{Y,TB}^* = - \sum_{m=1}^{N_p} \int_{r_1^*}^{r_2^*} \int_{\xi}^{\xi+\theta_0} p^* r^{*2} \cos(\theta + t^*) d\theta dr^* \quad (3.116)$$

where $M_{Y,TB}^* = \frac{h_{0,TB}^2}{6\eta\omega L^2 r_2^3} M_{Y,TB}$.

The computational method utilised the trapezoidal rule of integration to integrate the discrete pressure field, consisting of pressure values at cell vertices of the

computational grid, which is second-order accurate [31] and proved to be very economical for the grid size of $I \times J = 31 \times 31$. Dropping the asterisk (*) notation, but noting that all following terms are non-dimensional, equations (3.112), (3.115) and (3.116) may be rewritten in discrete form. That is, the total non-dimensional force on the thrust bearing in the Z-direction at time step k (eg. at time t_k) is

$$F_{Z,TB}^k \approx \frac{\Delta\theta}{2} \cdot \frac{\Delta r}{2} \cdot \sum_{m=1}^{N_p} \sum_{j=1}^{J-1} \sum_{i=1}^{I-1} \left[p_{i,j,m}^k r_j + p_{i,j+1,m}^k r_{j+1} + p_{i+1,j,m}^k r_j + p_{i+1,j+1,m}^k r_{j+1} \right] \quad (3.117)$$

for $k = 1, 2, \dots, K$ where $\Delta\theta$ and Δr are the cell sizes in the circumferential and radial direction respectively. From equation (3.117), it can be observed that each cell gives rise to a force which is the product of the cell area and the average of four cell vertex pressures. The total force in the Z-direction is the sum of these forces over all cells of the numerical grids on each impeller blade.

Similarly, the total non-dimensional moments on the thrust bearing about the X- and Y-axes at time step k in discrete form are

$$M_{X,TB}^k \approx \frac{\Delta\theta}{2} \cdot \frac{\Delta r}{2} \cdot \sum_{m=1}^{N_p} \sum_{j=1}^{J-1} \sum_{i=1}^{I-1} \left[p_{i,j,m}^k r_j^2 \sin(\theta_{i,m} + t_k) + p_{i,j+1,m}^k r_{j+1}^2 \sin(\theta_{i,m} + t_k) + p_{i+1,j,m}^k r_j^2 \sin(\theta_{i+1,m} + t_k) + p_{i+1,j+1,m}^k r_{j+1}^2 \sin(\theta_{i+1,m} + t_k) \right] \quad (3.118)$$

and

$$M_{Y,TB}^k \approx -\frac{\Delta\theta}{2} \cdot \frac{\Delta r}{2} \cdot \sum_{m=1}^{N_p} \sum_{j=1}^{J-1} \sum_{i=1}^{I-1} \left[p_{i,j,m}^k r_j^2 \cos(\theta_{i,m} + t_k) + p_{i,j+1,m}^k r_{j+1}^2 \cos(\theta_{i,m} + t_k) + p_{i+1,j,m}^k r_j^2 \cos(\theta_{i+1,m} + t_k) + p_{i+1,j+1,m}^k r_{j+1}^2 \cos(\theta_{i+1,m} + t_k) \right] \quad (3.119)$$

respectively. The trapezoidal rule is described further in Appendix F.

3.5.2. Conical journal bearing

Consider a small element of area $dA = \rho \sin \alpha d\theta dp$ on the surface of the conical journal bearing located at position $(p, \theta + \omega t)$ for $\xi \leq \theta \leq \xi + \theta_0$ where angle $\theta + \omega t$ is measured counter-clockwise from the positive X-axis. See Figure 3.14 below.

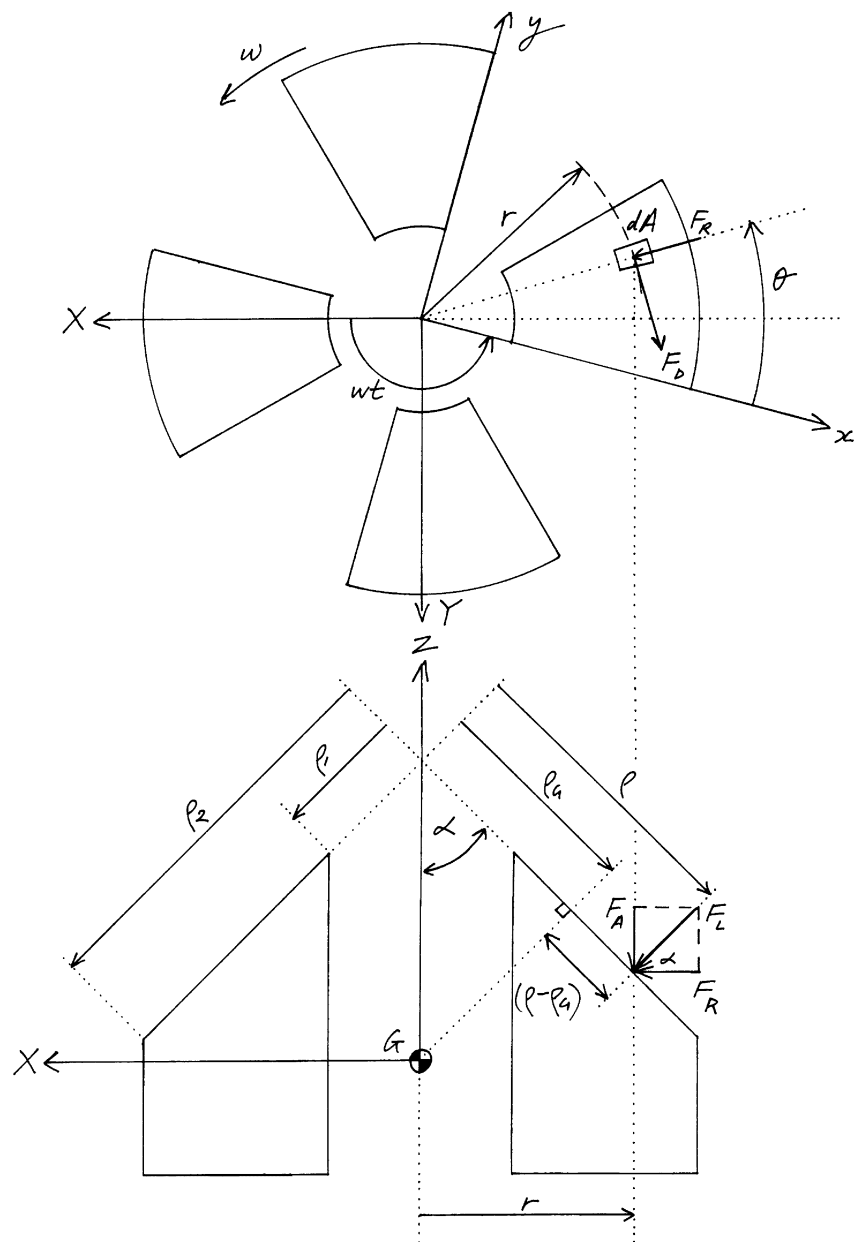


Figure 3.14. Lift and drag forces on the conical journal bearing. Note that the lift force has both an axial and radial component

At the point under examination the pressure is p and the force exerted by the hydrodynamic pressure on the element is $p \rho \sin \alpha d\theta dp$. Neglecting the effects of the bearing taper, this force may be resolved into a component in the X-direction $-p \cos \alpha \cos(\theta + \omega t) \rho \sin \alpha d\theta dp$, component $-p \cos \alpha \sin(\theta + \omega t) \rho \sin \alpha d\theta dp$ in the Y-direction, and component $-p \sin \alpha \rho \sin \alpha d\theta dp$ in the Z-direction. The total force on the impeller in each of the coordinate directions, resulting from the pressure distribution over the conical journal bearing alone, is the sum of the contributing forces from each blade of the conical journal bearing. That is, the total force on the conical journal bearing in the X-direction at time t is given by the sum of the integrals of the X-component over each blade $m = 1, 2, \dots, N_p$

$$F_{X,CJB} = -\sin \alpha \cos \alpha \sum_{m=1}^{N_p} \int_{\rho_1}^{\rho_2} \int_{\xi}^{\xi+\theta_0} p \rho \cos(\theta + \omega t) d\theta dp \quad (3.120)$$

Similarly, the total forces on the conical journal bearing in the Y-and Z-directions at time t are given by

$$F_{Y,CJB} = -\sin \cos \alpha \sum_{m=1}^{N_p} \int_{\rho_1}^{\rho_2} \int_{\xi}^{\xi+\theta_0} p \rho \sin(\theta + \omega t) d\theta dp \quad (3.121)$$

and

$$F_{Z,CJB} = -\sin^2 \alpha \sum_{m=1}^{N_p} \int_{\rho_1}^{\rho_2} \int_{\xi}^{\xi+\theta_0} p \rho d\theta dp \quad (3.122)$$

respectively.

Substituting non-dimensional variables, equation (3.120) becomes

$$F_{X,CJB} = -\sin \alpha \cos \alpha \sum_{m=1}^{N_p} \int_{\rho_1}^{\rho_2} \int_{\xi}^{\xi+\theta_0} \left(\frac{6\eta\omega L^2}{h_{vc}^2} p^* \right) (r_2 \rho^*) \cos \left(\theta + \omega \left[\frac{t^*}{\omega} \right] \right) d\theta d(r_2 \rho^*)$$

which simplifies to

$$F_{X,CJB}^* = -\sin \alpha \cos \alpha \sum_{m=1}^{N_p} \int_{\rho_1^*}^{\rho_2^*} \int_{\xi}^{\xi+\theta_0} p^* \rho^* \cos(\theta + t^*) d\theta d\rho^* \quad (3.123)$$

where $F_{X,CJB}^* = \frac{h_{vc}^2}{6\eta\omega L^2 r_2^2} F_{X,CJB}$ is the non-dimensional force on the conical journal bearing in the X-direction at non-dimensional time t^* . In a similar fashion, the non-dimensional forces on the conical journal bearing in the Y- and Z-directions at time t^* may be written

$$F_{Y,CJB}^* = -\sin \alpha \cos \alpha \sum_{m=1}^{N_p} \int_{\rho_1^*}^{\rho_2^*} \int_{\xi}^{\xi+\theta_0} p^* \rho^* \sin(\theta + t^*) d\theta d\rho^* \quad (3.124)$$

and

$$F_{Z,CJB}^* = -\sin^2 \alpha \sum_{m=1}^{N_p} \int_{\rho_1^*}^{\rho_2^*} \int_{\xi}^{\xi+\theta_0} p^* \rho^* d\theta d\rho^* \quad (3.125)$$

respectively, where $F_{Y,CJB}^* = \frac{h_{vc}^2}{6\eta\omega L^2 r_2^2} F_{Y,CJB}$ and $F_{Z,CJB}^* = \frac{h_{vc}^2}{6\eta\omega L^2 r_2^2} F_{Z,CJB}$.

Considering the same small element of area $dA = \rho \sin \alpha d\theta d\rho$, the turning moment about the centre of mass of the impeller due to the force $p \rho \sin \alpha d\theta d\rho$ acting on this area will have magnitude $|p - p_G| p \rho \sin \alpha d\theta d\rho$ (valid for $\rho_1 \leq \rho \leq \rho_2$), where $(p - p_G)$ is the perpendicular moment arm of the small area with respect to the centre of mass of the impeller. See Figure 3.14. This moment may be resolved into a component about the X-axis $-(p - p_G) p \sin(\theta + \omega t) \rho \sin \alpha d\theta d\rho$, and a component about the Y-axis given by $(p - p_G) p \cos(\theta + \omega t) \rho \sin \alpha d\theta d\rho$. The total moment on the impeller about coordinate axes X and Y, resulting from the pressure distribution over the conical journal bearing alone, is the sum of the contributions from each blade of the conical journal bearing. That is, the total moment on the conical journal bearing about the X-axis at time t is given by the sum of the integrals of the X-component over each blade $m = 1, 2, \dots, N_p$

$$M_{X,CJB} = -\sin \alpha \sum_{m=1}^{N_p} \int_{\rho_1}^{\rho_2} \int_{\xi}^{\xi+\theta_0} \rho (\rho - \rho_G) p \sin(\theta + \omega t) d\theta d\rho \quad (3.126)$$

Similarly the moment on the conical journal bearing about the Y-axis at time t is given by the expression

$$M_{Y,CJB} = \sin \alpha \sum_{m=1}^{N_p} \int_{\rho_1}^{\rho_2} \int_{\xi}^{\xi+\theta_0} \rho (\rho - \rho_G) p \cos(\theta + \omega t) d\theta d\rho \quad (3.127)$$

Upon substitution of non-dimensional variables, equation (3.126) becomes

$$M_{X,CJB} = -\sin \alpha \sum_{m=1}^{N_p} \int_{\rho_1}^{\rho_2} \int_{\xi}^{\xi+\theta_0} (r_2 \rho^*) [(r_2 \rho^*) - (r_2 \rho_G^*)] \left(\frac{6\eta\omega L^2}{h_{vc}^2} p^* \right) \sin \left(\theta + \omega \left[\frac{t^*}{\omega} \right] \right) d\theta d(r_2 \rho^*)$$

which simplifies to

$$M_{X,CJB}^* = -\sin \alpha \sum_{m=1}^{N_p} \int_{\rho_1^*}^{\rho_2^*} \int_{\xi}^{\xi+\theta_0} \rho^* (\rho^* - \rho_G^*) p^* \sin(\theta + t^*) d\theta d\rho^* \quad (3.128)$$

where $M_{X,CJB}^* = \frac{h_{vc}^2}{6\eta\omega L^2 r_2^3} M_{X,CJB}$ is the non-dimensional turning moment on the conical

journal bearing about the X-axis at non-dimensional time t^* . Similarly, the non-dimensional moment on the conical journal bearing about the Y-axis at time t^* is

$$M_{Y,CJB}^* = \sin \alpha \sum_{m=1}^{N_p} \int_{\rho_1^*}^{\rho_2^*} \int_{\xi}^{\xi+\theta_0} \rho^* (\rho^* - \rho_G^*) p^* \cos(\theta + t^*) d\theta d\rho^* \quad (3.129)$$

where $M_{Y,CJB}^* = \frac{h_{vc}^2}{6\eta\omega L^2 r_2^3} M_{Y,CJB}$.

Equations (3.123) – (3.125), (3.128), and (3.129) may be approximated in the discrete form of the trapezoidal rule. Dropping the asterisk (*) notation, but noting that all terms are non-dimensional, the total non-dimensional force on the conical journal bearing in the X-direction at time step k (eg. at time t_k) is

$$F_{X,CJB}^k \approx -\sin \alpha \cos \alpha \cdot \frac{\Delta \theta}{2} \cdot \frac{\Delta \rho}{2} \cdot \sum_{m=1}^{N_p} \sum_{j=1}^{J-1} \sum_{i=1}^{I-1} \left[\begin{array}{l} p_{i,j,m}^k \rho_j \cos(\theta_{i,m} + t_k) + \\ p_{i,j+1,m}^k \rho_{j+1} \cos(\theta_{i,m} + t_k) + \\ p_{i+1,j,m}^k \rho_j \cos(\theta_{i+1,m} + t_k) + \\ p_{i+1,j+1,m}^k \rho_{j+1} \cos(\theta_{i+1,m} + t_k) \end{array} \right] \quad (3.130)$$

Similarly, the total non-dimensional forces on the conical journal bearing at time step k in the Y- and Z-directions are

$$F_{Y,CJB}^k \approx -\sin \alpha \cos \alpha \cdot \frac{\Delta \theta}{2} \cdot \frac{\Delta \rho}{2} \cdot \sum_{m=1}^{N_p} \sum_{j=1}^{J-1} \sum_{i=1}^{I-1} \left[\begin{array}{l} p_{i,j,m}^k \rho_j \sin(\theta_{i,m} + t_k) + \\ p_{i,j+1,m}^k \rho_{j+1} \sin(\theta_{i,m} + t_k) + \\ p_{i+1,j,m}^k \rho_j \sin(\theta_{i+1,m} + t_k) + \\ p_{i+1,j+1,m}^k \rho_{j+1} \sin(\theta_{i+1,m} + t_k) \end{array} \right] \quad (3.131)$$

and

$$F_{Z,CJB}^k \approx -\sin^2 \alpha \cdot \frac{\Delta \theta}{2} \cdot \frac{\Delta \rho}{2} \cdot \sum_{m=1}^{N_p} \sum_{j=1}^{J-1} \sum_{i=1}^{I-1} \left[\begin{array}{l} p_{i,j,m}^k \rho_j + p_{i,j+1,m}^k \rho_{j+1} + \\ p_{i+1,j,m}^k \rho_j + p_{i+1,j+1,m}^k \rho_{j+1} \end{array} \right] \quad (3.132)$$

respectively. Furthermore, the non-dimensional moments on the conical journal bearing at time step k about the X- and Y- axes are

$$M_{X,CJB}^k \approx -\sin \alpha \cdot \frac{\Delta \theta}{2} \cdot \frac{\Delta \rho}{2} \cdot \sum_{m=1}^{N_p} \sum_{j=1}^{J-1} \sum_{i=1}^{I-1} \left[\begin{array}{l} \rho_j (\rho_j - \rho_G) p_{i,j,m}^k \sin(\theta_{i,m} + t_k) + \\ \rho_{j+1} (\rho_{j+1} - \rho_G) p_{i,j+1,m}^k \sin(\theta_{i,m} + t_k) + \\ \rho_j (\rho_j - \rho_G) p_{i+1,j,m}^k \sin(\theta_{i+1,m} + t_k) + \\ \rho_{j+1} (\rho_{j+1} - \rho_G) p_{i+1,j+1,m}^k \sin(\theta_{i+1,m} + t_k) \end{array} \right] \quad (3.133)$$

and

$$M_{Y,CJB}^k \approx \sin \alpha \frac{\Delta \theta}{2} \cdot \frac{\Delta \rho}{2} \cdot \sum_{m=1}^{N_p} \sum_{j=1}^{J-1} \sum_{i=1}^{I-1} \left[\begin{array}{l} \rho_j (\rho_j - \rho_G) p_{i,j,m}^k \cos(\theta_{i,m} + t_k) + \\ \rho_{j+1} (\rho_{j+1} - \rho_G) p_{i,j+1,m}^k \cos(\theta_{i,m} + t_k) + \\ \rho_j (\rho_j - \rho_G) p_{i+1,j,m}^k \cos(\theta_{i+1,m} + t_k) + \\ \rho_{j+1} (\rho_{j+1} - \rho_G) p_{i+1,j+1,m}^k \cos(\theta_{i+1,m} + t_k) \end{array} \right] \quad (3.134)$$

respectively. See Appendix F for details on double integration with the trapezoidal rule.

3.5.3. Total forces and moments on the impeller

The total non-dimensional force on the impeller at time t_k in each of the coordinate directions resulting from the hydrodynamic pressure field over the lubricated surfaces of the impeller is a sum of the contributions from the thrust bearing and the conical journal bearing and is given by

$$\begin{aligned} F_X^k &= F_{X,CJB}^k \\ F_Y^k &= F_{Y,CJB}^k \\ F_Z^k &= F_{Z,TB}^k + F_{Z,CJB}^k \end{aligned} \quad (3.135)$$

where $F_{X,CJB}^k$, $F_{Y,CJB}^k$, $F_{Z,TB}^k$, and $F_{Z,CJB}^k$ are given by equations (3.130), (3.131), (3.117) and (3.132) respectively. Note that only the conical journal bearing can support a radial load (i.e. a load in the X-Y plane), thus the contribution of the thrust bearing to the force in the X- and Y- directions is zero.

Similarly, the total non-dimensional turning moment on the impeller about the X- and Y-axes is the sum of the moments about the centre of mass of the impeller resulting from the pressure distribution over the surfaces of both the thrust and conical journal bearing and is given by

$$\begin{aligned} M_X^k &= M_{X,TB}^k + M_{X,CJB}^k \\ M_Y^k &= M_{Y,TB}^k + M_{Y,CJB}^k \end{aligned} \quad (3.136)$$

where $M_{X,TB}^k$, $M_{X,CJB}^k$, $M_{Y,TB}^k$ and $M_{Y,CJB}^k$ are given by equations (3.118), (3.133), (3.119) and (3.134) respectively.

3.6. Dynamic motion of the impeller

By means of Newtons second law, the translational and rotational motion of the impeller can be determined if all forces which act on the impeller to produce this motion are known. The loading conditions must include all possible load combinations and orientations such that the stability of the impeller in response to these conditions may be properly assessed.

3.6.1. Forces and moments in the impeller

In addition to the forces (F_x , F_y , F_z) and moments (M_x , M_y) resulting from hydrodynamic suspension of the impeller as described in section 3.5., the forces acting on the impeller, possibly in a destabilising manner, that were considered in this study include

- 1) Gravitational force (constant load)

The direction of the gravitational force which acts through the centre of mass of the impeller, i.e. the impeller weight, is dependent on the orientation of the pump. That is, the pump axis may lie in any number of positions depending on the particular body position of the patient. To account for this, the direction of the gravitational force was established by the specification of two angles, ψ_1

and ψ_2 , as defined in Figure 3.15. Given that the magnitude of the weight is

$W = Mg$, where M is the mass of the impeller and $g = 9.81 m/s^2$ is the gravitational constant, the component of the weight in the X-direction is given by

$$W_x = Mg \sin \psi_1 \cos \psi_2 \quad (3.137)$$

for $0 \leq \psi_1 \leq \pi$ and $0 \leq \psi_2 \leq 2\pi$. Similarly, the component in the Y-direction is

$$W_Y = Mg \sin \psi_1 \sin \psi_2 \quad (3.138)$$

and the component in the Z-direction is given by

$$W_Z = Mg \cos \psi_1 \quad (3.139)$$

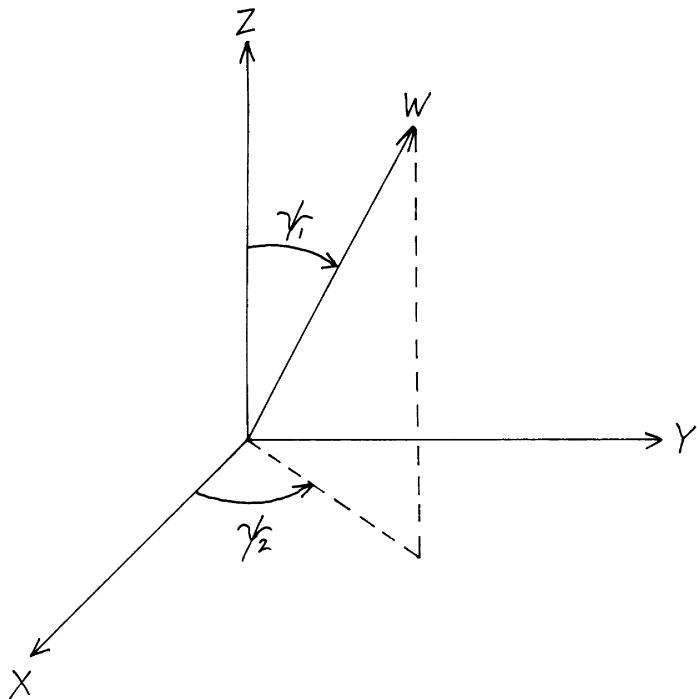


Figure 3.15. Definition of angles used in the specification of the direction of the weight (gravity vector)

2) Unbalance force

Unbalance in rotating machines is a common source of vibration excitation. In regards to the VentrAssist impeller, the unbalance force may be a result of any number of factors, for example unequal strengths of the permanent magnets, impeller blades of differing mass, small particles in the fluid that adhere to the surface of the impeller resulting in an uneven distribution of mass (mainly confined to laboratory experiments) etc..

The unbalance is represented by an eccentric mass m with eccentricity r that is rotating with angular velocity Ω_2 . With reference to Figure 3.16, the X-component of this force is given by

$$F_{X,unbalance} = -mr\Omega_2^2 \cos \Omega_2 t \quad (3.140)$$

and the Y-component is given by

$$F_{Y,unbalance} = -mr\Omega_2^2 \sin \Omega_2 t \quad (3.141)$$

where angle $\Omega_2 t$ is taken from the positive X-axis as shown.

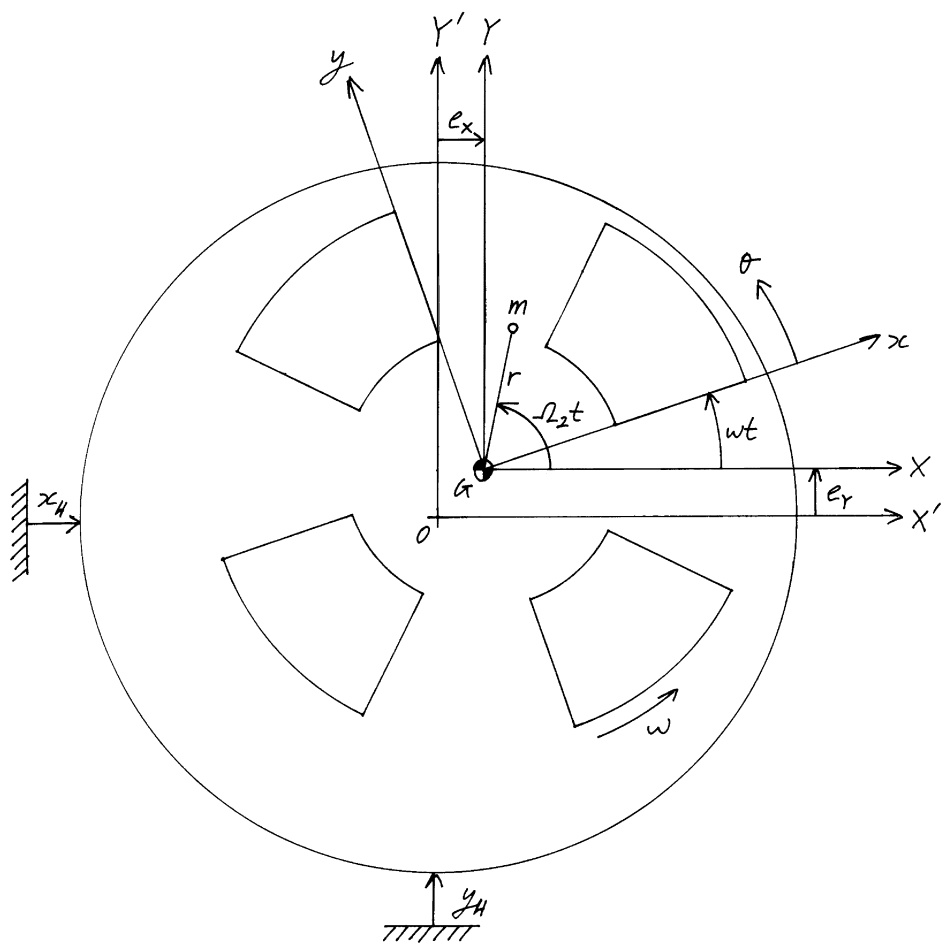


Figure 3.16. Impeller unbalance is represented by a rotating eccentric mass. The impeller also experiences a force due to “shaking” of the pump housing, which is given simple harmonic motion in the X-, Y-, and Z- coordinate directions (only X- and Y- are pictured).

In view of the fact that the magnetic force rotates at twice the rotational frequency of the impeller, the frequency $\Omega_2 = 2\omega$ is of particular interest, as is $\Omega_2 = \omega$, which simulates a mass unbalance.

3) Force due to excitation (“shaking”) of the pump housing

The pump housing is given simple harmonic motion in each of the three coordinate directions. That is, the motion of the pump housing in the X-direction is

$$x_H = X_H \sin(\Omega_1 t + \beta_1) \quad (3.142)$$

where X_H is the amplitude, Ω_1 the frequency of motion and β_1 the phase lead.

Similarly, the motion of the pump housing in the Y-direction is given by

$$y_H = Y_H \sin(\Omega_1 t + \beta_1) \quad (3.143)$$

and in the Z-direction is given by

$$z_H = Z_H \sin(\Omega_1 t + \beta_1) \quad (3.144)$$

where Y_H and Z_H are the amplitudes of motion in each direction respectively.

The excitation of the pump housing in the X-Y plane is pictured in Figure 3.16.

Suggestion for future studies include allowing for the individual specification of frequency in each of the three coordinate directions, in addition to amplitude in equations (3.142) – (3.144). Additionally, it would be interesting to allow for the motion of the pump housing to be specified using any desired function such as that to simulate typical motion of the patient (i.e. walking, jogging, falling etc), noting that most complex waveforms may be expressed as a combination of simple harmonic motion components using the appropriate Fourier series [23].

4) Gyroscopic effects

A constant precession of the impeller about the positive Y-axis, $\dot{\gamma}_Y$, results in a positive moment on the impeller about the positive X-axis. That is, the moment about the X-axis on the impeller due to precession $\dot{\gamma}_Y$ is given by [32]

$$M_{X,gyro} = I_P \omega \dot{\gamma}_Y \quad (3.145)$$

where I_P is the moment of inertia of the impeller about the spin axis, i.e.

$$I_P = I_{zz}.$$

Likewise, a constant precession of the impeller about the positive X-axis, $\dot{\gamma}_X$, results in a negative moment on the impeller about the Y-axis, given by

$$M_{Y,gyro} = -I_P \omega \dot{\gamma}_X \quad (3.146)$$

Forces that were not included in this study, although should be considered in a more detailed future study, comprised of (1) the magnetic force on the permanent magnets contained within the impeller blades and (2) the force on the impeller due to expansion of the blood within the pump volute. Most probably, the magnetic force would be assumed to vary linearly with the local film thickness and require specification of both the magnitude of the magnetic force when the impeller is in its nominal position and the gradient of this force in each of the three coordinate directions. On the other hand, the volute force is similar to the gravitational force in that its direction could be described by the specification of two angles.

3.6.2. Equations of motion

In accordance with Newton's second law which states that the sum of the forces acting on the impeller of mass M is equal to the product of this mass and the absolute acceleration $\bar{\mathbf{a}}$ of the centre of mass of the impeller, i.e. $M\bar{\mathbf{a}} = \sum \mathbf{F}$ [32], the equations governing the translational and rotational motion of the impeller can be written as

$$\begin{aligned} M(\ddot{e}_x + \ddot{x}_H) &= F_x + F_{x,\text{unbalance}} + W_x \\ &= F_x - mr\Omega_2^2 \cos \Omega_2 t + Mg \sin \psi_1 \cos \psi_2 \end{aligned} \quad (3.147)$$

$$\begin{aligned} M(\ddot{e}_y + \ddot{y}_H) &= F_y + F_{y,\text{unbalance}} + W_y \\ &= F_y - mr\Omega_2^2 \sin \Omega_2 t + Mg \sin \psi_1 \sin \psi_2 \end{aligned} \quad (3.148)$$

$$M(\ddot{e}_z + \ddot{z}_H) = F_z + W_z = F_z + Mg \cos \psi_1 \quad (3.149)$$

$$I_T \ddot{\gamma}_x = M_{x,\text{gyro}} + M_x = I_p \omega \dot{\gamma}_y + M_x \quad (3.150)$$

$$I_T \ddot{\gamma}_y = M_{y,\text{gyro}} + M_y = -I_p \omega \dot{\gamma}_x + M_y \quad (3.151)$$

where

I_T is the moment of inertia about the X- and Y-axes. That

is, $I_T = I_{xx} = I_{yy}$;

\ddot{e}_x , \ddot{e}_y , \ddot{e}_z are the relative translational accelerations of the impeller with respect to the pump housing;

\ddot{x}_H , \ddot{y}_H , \ddot{z}_H are the absolute translational accelerations of the pump housing where, for simple harmonic motion,

$$\ddot{x}_H = -\Omega_1^2 x_H, \quad \ddot{y}_H = -\Omega_1^2 y_H, \quad \text{and} \quad \ddot{z}_H = -\Omega_1^2 z_H;$$

$\ddot{e}_x + \ddot{x}_H$, $\ddot{e}_y + \ddot{y}_H$, $\ddot{e}_z + \ddot{z}_H$ are the absolute translational accelerations of the impeller;

$\ddot{\gamma}_x$, $\ddot{\gamma}_y$ are the absolute rotational accelerations of the impeller.

Equation (3.147) may be rearranged as follows

$$M\ddot{e}_x = F_x + M\Omega_1^2 X_H \sin(\Omega_1 t + \beta_1) - mr\Omega_2^2 \cos \Omega_2 t + Mg \sin \psi_1 \cos \psi_2 \quad (3.152)$$

On substitution of the following non-dimensional variables

$$M^* = \frac{c\omega^2}{F} M, \quad m^* = \frac{r\omega^2}{F} m, \quad F_x^* = \frac{c^2}{6\eta\omega L^2 r_2^2} F_x = \frac{F_x}{F\Lambda},$$

$$X_H^* = \frac{X_H}{c} \text{ and } g^* = \frac{g}{c\omega^2}$$

where F is the applied load, $\Lambda = \frac{6\eta\omega L^2}{F} \left(\frac{r_2}{c} \right)^2$ is the load parameter and

$c = h_{0,TB} = h_{vc}$, equation (3.152) can be written in non-dimensional form as

$$\begin{aligned} \left(\frac{F}{c\omega^2} M^* \right) \frac{\partial^2 (c\varepsilon_x)}{\partial (t^*/\omega)^2} &= \left(F\Lambda F_x^* \right) + \left(\frac{F}{c\omega^2} M^* \right) \Omega_1^2 \left(cX_H^* \right) \sin \left(\Omega_1 \left(\frac{t^*}{\omega} \right) + \beta_1 \right) \\ &\quad - \left(\frac{F}{r\omega^2} m^* \right) r\Omega_2^2 \cos \left(\Omega_2 \left(\frac{t^*}{\omega} \right) \right) \\ &\quad + \left(\frac{F}{c\omega^2} M^* \right) (c\omega^2 g^*) \sin \psi_1 \cos \psi_2 \end{aligned}$$

which simplifies to

$$\begin{aligned} M^* \ddot{\varepsilon}_x &= \Lambda F_x^* + M^* \left(\frac{\Omega_1}{\omega} \right)^2 X_H^* \sin \left(\frac{\Omega_1}{\omega} t^* + \beta_1 \right) \\ &\quad - m^* \left(\frac{\Omega_2}{\omega} \right)^2 \cos \left(\frac{\Omega_2}{\omega} t^* \right) + M^* g^* \sin \psi_1 \cos \psi_2 \end{aligned} \quad (3.153)$$

Note that the inverse of the non-dimensional mass M^* is a form of the stability parameter, i.e. $S_0 \equiv 1/M^* = F/Mc\omega^2$. In the case of the VentrAssist impeller $F = W = Mg$ and the stability parameter simplifies to $S_0 = 1/M^* = g/c\omega^2 = g^*$.

Additionally, the load parameter Λ may be considered a modified form of the inverse of the Sommerfeld number which is used to relate the speed and geometry of a journal

bearing and lubricant properties to the running eccentricity of the bearing. The Sommerfeld number is usually written as $\Delta \equiv \frac{W/L}{U\eta} \cdot \frac{c^2}{R^2}$ [13] where U is often replaced by $U = \omega R$.

Introducing the following non-dimensional terms,

$$V_1^* = \frac{\Omega_1}{\omega} \text{ and } V_2^* = \frac{\Omega_2}{\omega}$$

equation (3.153) may be rewritten to yield

$$\ddot{\varepsilon}_x = \left(\frac{\Lambda}{M^*} \right) F_x^* + V_1^{*2} X_H^* \sin(V_1^* t^* + \beta_1) - \left(\frac{m^*}{M^*} \right) V_2^{*2} \cos V_2^* t^* + \left(\frac{1}{M^*} \right) \sin \psi_1 \cos \psi_2 \quad (3.154)$$

In a similar manner, when $F = Mg$, equation (3.148) may be written in non-dimensional form as

$$\ddot{\varepsilon}_y = \left(\frac{\Lambda}{M^*} \right) F_y^* + V_1^{*2} Y_H^* \sin(V_1^* t^* + \beta_1) - \left(\frac{m^*}{M^*} \right) V_2^{*2} \sin V_2^* t^* + \left(\frac{1}{M^*} \right) \sin \psi_1 \sin \psi_2 \quad (3.155)$$

where $Y_H^* = Y_H/c$, as may equation (3.149) which becomes

$$\ddot{\varepsilon}_z = \left(\frac{\Lambda}{M^*} \right) F_z^* + V_1^{*2} Z_H^* \sin(V_1^* t^* + \beta_1) + \left(\frac{1}{M^*} \right) \cos \psi_1 \quad (3.156)$$

where $Z_H^* = Z_H/c$.

Again, introducing the following non-dimensional terms

$$I_T^* = \frac{c^2 \omega}{6\eta L^2 r_2^3} I_T, \quad J_P^* = \frac{I_P}{I_T} \text{ and } M_x^* = \frac{c^2}{6\eta L^2 r_2^3 \omega} M_x$$

where again $c = h_{0,TB} = h_{vc}$, equation (3.150) may be written in non-dimensional form as

$$\begin{aligned} \left(\frac{6\eta L^2 r_2^3}{c^2 \omega} I_T^* \right) \frac{\partial^2}{\partial(t^*/\omega)^2} \left(\frac{c}{r_2} \gamma_X^* \right) = & \left(\frac{6\eta L^2 r_2^3}{c^2 \omega} J_P^* I_T^* \right) \omega \frac{\partial}{\partial(t^*/\omega)} \left(\frac{c}{r_2} \gamma_Y^* \right) \\ & + \left(\frac{6\eta L^2 r_2^3 \omega}{c^2} M_X^* \right) \end{aligned}$$

which simplifies to give

$$\ddot{\gamma}_X^* = J_P^* \dot{\gamma}_Y^* + \left(\frac{r_2}{c} \right) \left(\frac{M_X^*}{I_T^*} \right) \quad (3.157)$$

Similarly, equation (3.151) can be written in the following non-dimensional form

$$\ddot{\gamma}_Y^* = -J_P^* \dot{\gamma}_X^* + \left(\frac{r_2}{c} \right) \left(\frac{M_Y^*}{I_T^*} \right) \quad (3.158)$$

In summary, the non-dimensional equations governing the motion of the impeller are

$$\ddot{\xi}_X = \left(\frac{\Lambda}{M^*} \right) F_X^* + V_1^{*2} X_H^* \sin(V_1^* t^* + \beta_1) - \left(\frac{m^*}{M^*} \right) V_2^{*2} \cos V_2^* t^* + \left(\frac{1}{M^*} \right) \sin \psi_1 \cos \psi_2 \quad (3.154)$$

$$\ddot{\xi}_Y = \left(\frac{\Lambda}{M^*} \right) F_Y^* + V_1^{*2} Y_H^* \sin(V_1^* t^* + \beta_1) - \left(\frac{m^*}{M^*} \right) V_2^{*2} \sin V_2^* t^* + \left(\frac{1}{M^*} \right) \sin \psi_1 \sin \psi_2 \quad (3.155)$$

$$\ddot{\xi}_Z = \left(\frac{\Lambda}{M^*} \right) F_Z^* + V_1^{*2} Z_H^* \sin(V_1^* t^* + \beta_1) + \left(\frac{1}{M^*} \right) \cos \psi_1 \quad (3.156)$$

$$\ddot{\gamma}_X^* = J_P^* \dot{\gamma}_Y^* + \left(\frac{r_2}{c} \right) \left(\frac{M_X^*}{I_T^*} \right) \quad (3.157)$$

$$\ddot{\gamma}_Y^* = -J_P^* \dot{\gamma}_X^* + \left(\frac{r_2}{c} \right) \left(\frac{M_Y^*}{I_T^*} \right) \quad (3.158)$$

3.6.3. Solution of the equations of motion

Equations (3.154) – (3.158) consist of five non-linear second-order differential equations. Due to lack of a direct analytical solution, a numerical time marching technique based on the classical fourth-order Runge-Kutta method was employed to solve these equations. The basic outline of this method, modified from Schwarz *et al.* [33], is as follows.

Consider the initial value problem with the following second-order differential equation

$$\ddot{y}(t) = f(t, y(t), \dot{y}(t)) \quad (3.159)$$

with initial conditions

$$y(t_0) = y^0 \text{ and } \dot{y}(t_0) = \dot{y}^0 \quad (3.160)$$

where $\dot{y}(t) = \frac{dy}{dt}$, $\ddot{y}(t) = \frac{d^2y}{dt^2}$. Equation (3.159) is first reduced to a system of simultaneous first-order differential equations by defining the first derivative as a second function. That is, we define

$$y_1(t) = y(t) \text{ and } y_2 = \dot{y}(t) \quad (3.161)$$

which upon substitution into equations (3.159) and (3.160) yields the equivalent set of equations

$$\begin{aligned} \dot{y}_1(t) &= y_2(t) \\ \dot{y}_2(t) &= f(t, y_1(t), y_2(t)) \end{aligned} \quad (3.162)$$

subject to the initial conditions

$$y_1(t_0) = y^0 \text{ and } y_2(t_0) = \dot{y}^0 \quad (3.163)$$

Introducing the following vector functions and vector,

$$\mathbf{y}(t) = \begin{pmatrix} y_1(t) \\ y_2(t) \end{pmatrix}, \mathbf{f}(t, \mathbf{y}) = \begin{pmatrix} y_2(t) \\ f(t, y_1(t), y_2(t)) \end{pmatrix}, \text{ and } \mathbf{y}^0 = \begin{pmatrix} y^0 \\ \dot{y}^0 \end{pmatrix} \quad (3.164)$$

equation set (3.162) and equation (3.163) may be written in the following vector form

$$\dot{\mathbf{y}}(t) = \mathbf{f}(t, \mathbf{y}(t)) \text{ and } \mathbf{y}(t_0) = \mathbf{y}^0 \quad (3.165)$$

The components of $\mathbf{y}(t)$, namely $y_1(t)$ and $y_2(t)$, can be obtained at each discrete time step by application of the expression

$$\mathbf{y}^{k+1} = \mathbf{y}^k + \frac{1}{6} \Delta t (\mathbf{k}_1 + 2\mathbf{k}_2 + 2\mathbf{k}_3 + \mathbf{k}_4) \quad (3.166)$$

for $k = 0, 1, \dots, K-1$ where $\Delta t = t_{k+1} - t_k$ is the time increment and

$$\begin{aligned} \mathbf{k}_1 &= \mathbf{f}(t_k, \mathbf{y}^k) \\ \mathbf{k}_2 &= \mathbf{f}\left(t_k + \frac{1}{2}\Delta t, \mathbf{y}^k + \frac{1}{2}\Delta t \mathbf{k}_1\right) \\ \mathbf{k}_3 &= \mathbf{f}\left(t_k + \frac{1}{2}\Delta t, \mathbf{y}^k + \frac{1}{2}\Delta t \mathbf{k}_2\right) \\ \mathbf{k}_4 &= \mathbf{f}(t_k + \Delta t, \mathbf{y}^k + \Delta t \mathbf{k}_3) \end{aligned} \quad (3.167)$$

Equations (3.154) – (3.158) must be solved simultaneously because the hydrodynamic fluid film forces and moments are functions of the instantaneous position and velocity of the centre of mass of the impeller in each coordinate direction, i.e. $F_X^*, F_Y^*, F_Z^*, M_X^*, M_Y^* = f(t^*, \varepsilon_X, \dot{\varepsilon}_X, \varepsilon_Y, \dot{\varepsilon}_Y, \varepsilon_Z, \dot{\varepsilon}_Z, \gamma_X^*, \dot{\gamma}_X^*, \gamma_Y^*, \dot{\gamma}_Y^*)$. Following the above procedure, each of the five governing equations was reduced to two equivalent simultaneous first-order equations, bringing the total number of simultaneous equations to ten. This involved defining the following vector functions and vector as

$$\mathbf{y}(t^*) = \begin{pmatrix} y_1(t^*) \\ y_2(t^*) \\ y_3(t^*) \\ y_4(t^*) \\ y_5(t^*) \\ y_6(t^*) \\ y_7(t^*) \\ y_8(t^*) \\ y_9(t^*) \\ y_{10}(t^*) \end{pmatrix} \quad \text{and} \quad \mathbf{y}^0 = \begin{pmatrix} y_1^0 \\ y_2^0 \\ y_3^0 \\ y_4^0 \\ y_5^0 \\ y_6^0 \\ y_7^0 \\ y_8^0 \\ y_9^0 \\ y_{10}^0 \end{pmatrix} = \begin{pmatrix} \varepsilon_X(t_0^*) \\ \dot{\varepsilon}_X(t_0^*) \\ \varepsilon_Y(t_0^*) \\ \dot{\varepsilon}_Y(t_0^*) \\ \varepsilon_Z(t_0^*) \\ \dot{\varepsilon}_Z(t_0^*) \\ \gamma_X^*(t_0^*) \\ \dot{\gamma}_X^*(t_0^*) \\ \gamma_Y^*(t_0^*) \\ \dot{\gamma}_Y^*(t_0^*) \end{pmatrix} \quad (3.168)$$

and

$$\mathbf{f}(t^*, \mathbf{y}) = \begin{cases} y_2(t^*) \\ \left(\frac{\Lambda}{M^*} \right) F_X^* + V_1^{*2} X_H^* \sin(V_1^* t^* + \beta_1) - \left(\frac{m^*}{M^*} \right) V_2^{*2} \cos V_2^* t^* + \left(\frac{1}{M^*} \right) \sin \psi_1 \cos \psi_2 \\ y_4(t^*) \\ \left(\frac{\Lambda}{M^*} \right) F_Y^* + V_1^{*2} Y_H^* \sin(V_1^* t^* + \beta_1) - \left(\frac{m^*}{M^*} \right) V_2^{*2} \sin V_2^* t^* + \left(\frac{1}{M^*} \right) \sin \psi_1 \sin \psi_2 \\ y_6(t^*) \\ \left(\frac{\Lambda}{M^*} \right) F_Z^* + V_1^{*2} Z_H^* \sin(V_1^* t^* + \beta_1) + \left(\frac{1}{M^*} \right) \cos \psi_1 \\ y_8(t^*) \\ J_P^* y_{10}(t^*) + \left(\frac{r_2}{c} \right) \left(\frac{M_X^*}{I_T^*} \right) \\ y_{10}(t^*) \\ - J_P^* y_8(t^*) + \left(\frac{r_2}{c} \right) \left(\frac{M_Y^*}{I_T^*} \right) \end{cases} \quad (3.169)$$

where $F_X^*, F_Y^*, F_Z^*, M_X^*, M_Y^* = f(t^*, \mathbf{y}(t^*))$. The displacements and velocity of the centre of mass of the impeller, i.e. each component of $\mathbf{y}(t^*)$ as defined in equation (3.168), may be calculated at each time step by the application of equation (3.166) and equation set (3.167) for $k = 0, 1, \dots, K-1$ with t and Δt replaced by non-dimensional variables t^* and $\Delta t^* = t_{k+1}^* - t_k^*$ respectively.

Note that the forces and moments due to the hydrodynamic suspension and the moment due to constant precession of the impeller were considered to be constant during each time step Δt^* . Additionally, from equation set (3.167) it can be seen that the fluid film forces are calculated four times for each computed step of the centre of

mass of the impeller, i.e. for each of \mathbf{k}_1 , \mathbf{k}_2 , \mathbf{k}_3 , and \mathbf{k}_4 . Although this method may appear computationally expensive, Gerald *et al.* [31] argue that although four evaluations are required per step as opposed to the one and two evaluations per step for the Euler and modified Euler methods respectively, Runge-Kutta methods are computationally more efficient because the size of the time increment may be several times larger for the same accuracy. That is, this particular Runge-Kutta method is fourth-order accurate, i.e. has a global error of $O(\Delta t^*)^4$, in comparison to the Euler and modified Euler methods which have global errors of $O(\Delta t^*)$ and $O(\Delta t^*)^2$ respectively.

3.6.4. Computational procedure

The computational procedure used to solve the equations of motion involved the following steps:

- 1) Initial values were assigned to ε_x , ε_y , and ε_z to define the starting position of the impeller. Variables γ_x^* and γ_y^* were set to zero, i.e. $\gamma_x^* = \gamma_y^* = 0$, such that the impeller had no initial rotation (although need not be). Additionally, all velocities $\dot{\varepsilon}_x$, $\dot{\varepsilon}_y$, $\dot{\varepsilon}_z$, $\dot{\gamma}_x^*$ and $\dot{\gamma}_y^*$ were set to zero, i.e. $\dot{\varepsilon}_x = \dot{\varepsilon}_y = \dot{\varepsilon}_z = \dot{\gamma}_x^* = \dot{\gamma}_y^* = 0$, such that the impeller was initially at rest.
- 2) The values defined in step (1) were used to calculate the pressure field over the thrust bearing and conical journal bearing surfaces of each impeller blade using a grid size of $I \times J = 31 \times 31$ on each blade surface.

As described in section 3.4.2.4., for the first time step all pressure values at each node were assigned an initial value of zero as an initial “guess” in the

iterative process. However, for subsequent time steps the pressure distribution over each impeller blade at the previous time step was used as the initial guess for the pressure values in the iterative process. That is, $p_{i,j,m}^n = p_{i,j,m}^k$. This acted to hasten convergence, more so if Δt^* or the change in the pressure value at each grid point was small.

- 3) The total forces and moments on the impeller due to hydrodynamic suspension were calculated using equation sets (3.135) and (3.136).
- 4) Equations (3.154) – (3.158) were solved for constant values of I_T^* and J_P^* using the Runge-Kutta method described in section 3.6.3. to obtain ε_X , $\dot{\varepsilon}_X$, ε_Y , $\dot{\varepsilon}_Y$, ε_Z , $\dot{\varepsilon}_Z$, γ_X^* , $\dot{\gamma}_X^*$, γ_Y^* , and $\dot{\gamma}_Y^*$ for the next time step, starting from the position defined in step (1).
- 5) Steps (2) – (4) were repeated until the values of ε_X , $\dot{\varepsilon}_X$, ε_Y , $\dot{\varepsilon}_Y$, ε_Z , $\dot{\varepsilon}_Z$, γ_X^* , $\dot{\gamma}_X^*$, γ_Y^* , and $\dot{\gamma}_Y^*$ had been determined for each time step $k = 0, 1, \dots, K - 1$.
- 6) The values of ε_X , ε_Y , and ε_Z were plotted showing the locus of the centre of mass of the impeller to help ascertain the system stability. Values of γ_X^* and γ_Y^* were also plotted with a similar intent.

3.7. Test cases

The aim of this study was to firstly develop a numerical tool in order to assess the stability of the VentrAssist IRBP and secondly to use this tool to optimise the design of the impeller. Consequently, only a select number of operating conditions were examined, testing all aspects of *Orbit3D* to show the value and capability of such a tool. Many more test cases would be necessary in order to create a stability map. In all, there are 18 test cases which can be categorised into four parts:

1) Altering the non-dimensional mass $M^* = c\omega^2/g$ and observing the trajectory in response to “shaking” of the pump housing. This involved:

(a) Varying the clearance over the values $c = 50, 100$ and $200\mu\text{m}$ at a constant rotational frequency of $\omega = 2500\text{rpm}$ (261.8rad/s), corresponding to $M^* = 0.34933, 0.69867$, and 1.39733 respectively. In each case, the true amplitude of the pump motion X_H was kept constant, corresponding to the non-dimensional amplitudes of $X_H^* = 20, 10$ and 5 respectively. The non-dimensional excitation frequency was $V_1^* = 1.0$ in all cases. The corresponding test case names are TC1, TC2, and TC3 respectively;

(b) Varying the rotational frequency over the values $\omega = 500, 1500, 2500, 3500$ and 4500 rpm (i.e. $52.36, 157.08, 261.80, 366.52$ and 471.24rad/s respectively) at a constant clearance of $c = 100\mu\text{m}$, corresponding to $M^* = 0.02795, 0.25152, 0.69867, 1.36939$, and 2.26368 respectively.

In all cases $X_H^* = 10$. Additionally, the true excitation frequency Ω_1

was kept constant in each case such that $V_1^* = 5.0, 5 / 3, 1.0, 5 / 7$, and $5 / 9$ respectively. The corresponding test case names are TC4, TC5, TC2, TC6, and TC7 respectively.

2) Altering the unbalance force. This was done by:

(a) Varying the magnitude of the unbalance mass over the values $m^* = 0.682, 2.729$, and 10.917 (which correspond to $m/M = 1/18, 1/64$ and $1/256$ respectively) at a constant non-dimensional (synchronous) frequency of $V_2^* = 1.0$. The corresponding test case names are TC8, TC9, and TC10 respectively;

(b) Varying the excitation frequency over the values $V_2^* = 0.5, 1.0$ and 2.0 with a constant unbalance mass of $m^* = 2.729$. The corresponding test case names are TC11, TC9, and TC12 respectively.

3) Altering the “shaking” motion of the pump housing. This involved varying the non-dimensional frequency of excitation over the values $V_1^* = 0.5, 1.0$ and 2.0 with a constant amplitude of motion of the value $X_H^* = 10$. For each case $M^* = 0.69867$, $\Lambda = 152.03$, and $c = 100\mu\text{m}$. The corresponding test case names are TC13, TC14, and TC15 respectively.

4) Altering the orientation of the pump and observing the trajectory in response to an initial disturbance. The orientations tested were:

- i. Conical apex pointing downwards i.e. $\psi_1 = \psi_2 = 0$;
- ii. Conical apex pointing upwards i.e. $\psi_1 = \pi, \psi_2 = 0$;

iii. Pump axis horizontal i.e. $\psi_1 = \pi/2$, $\psi_2 = 0$.

In each case the starting position was at $\varepsilon_x = 0.8$ with all other eccentricity ratios and velocities zero. Additionally, $M^* = 0.69867$, $\Lambda = 152.03$, and $c = 100\mu\text{m}$. The corresponding test case names are TC16, TC17, and TC18 respectively.

For all cases the cone apex was pointing upwards (i.e. $\psi_1 = \pi$, $\psi_2 = 0$) unless otherwise specified. The exact details for each test case are given below in Table 3.1. Note that all parameters corresponding to a particular case (other than ψ_1 and ψ_2) not specified in Table 3.1 were assigned a value of zero.

The dimensions of the simplified form of the VentrAssist impeller were listed in section 3.2. The dynamic viscosity and density of blood at body temperature were taken as $\eta = 3.5\text{mPa.s}$ and $\rho = 1050\text{kg.m}^{-3}$.

PART	Test case name	Details
1(a)	TC1	$c = 50\mu\text{m}$, $\omega = 261.80 \text{ rad/s}$, $M^* = 0.34933$, $\Lambda = 608.10$, $I_T^* = 0.053524$, $J_P^* = 1.78578$, $X_H^* = 20.0$, $V_1^* = 1.0$
	TC2	$c = 100\mu\text{m}$, $\omega = 261.80 \text{ rad/s}$, $M^* = 0.69867$, $\Lambda = 152.03$, $I_T^* = 0.214097$, $J_P^* = 1.78578$, $X_H^* = 10.0$, $V_1^* = 1.0$
	TC3	$c = 200\mu\text{m}$, $\omega = 261.80 \text{ rad/s}$, $M^* = 1.39733$, $\Lambda = 38.01$, $I_T^* = 0.856389$, $J_P^* = 1.78578$, $X_H^* = 5.0$, $V_1^* = 1.0$
1(b)	TC4	$c = 100\mu\text{m}$, $\omega = 52.36 \text{ rad/s}$, $M^* = 0.02795$, $\Lambda = 30.41$, $I_T^* = 0.042820$, $J_P^* = 1.78578$, $X_H^* = 10$, $V_1^* = 5.0$
	TC5	$c = 100\mu\text{m}$, $\omega = 157.08 \text{ rad/s}$, $M^* = 0.25152$, $\Lambda = 91.22$, $I_T^* = 0.128458$, $J_P^* = 1.78578$, $X_H^* = 10$, $V_1^* = 5 / 3$
	TC6	$c = 100\mu\text{m}$, $\omega = 366.52 \text{ rad/s}$, $M^* = 1.36939$, $\Lambda = 212.84$, $I_T^* = 0.299736$, $J_P^* = 1.78578$, $X_H^* = 10$, $V_1^* = 5 / 7$
	TC7	$c = 100\mu\text{m}$, $\omega = 471.24 \text{ rad/s}$, $M^* = 2.263681$, $\Lambda = 273.65$, $I_T^* = 0.385375$, $J_P^* = 1.78578$, $X_H^* = 10$, $V_1^* = 5 / 9$
2(a)	TC8	$c = 100\mu\text{m}$, $\omega = 261.80 \text{ rad/s}$, $M^* = 0.69867$, $\Lambda = 152.03$, $I_T^* = 0.214097$, $J_P^* = 1.78578$, $V_2^* = 1.0$, $m^* = 0.682$
	TC9	$c = 100\mu\text{m}$, $\omega = 261.80 \text{ rad/s}$, $M^* = 0.69867$, $\Lambda = 152.03$, $I_T^* = 0.214097$, $J_P^* = 1.78578$, $V_2^* = 1.0$, $m^* = 2.729$
	TC10	$c = 100\mu\text{m}$, $\omega = 261.80 \text{ rad/s}$, $M^* = 0.69867$, $\Lambda = 152.03$, $I_T^* = 0.214097$, $J_P^* = 1.78578$, $V_2^* = 1.0$, $m^* = 10.917$
2(b)	TC11	$c = 100\mu\text{m}$, $\omega = 261.80 \text{ rad/s}$, $M^* = 0.69867$, $\Lambda = 152.03$, $I_T^* = 0.214097$, $J_P^* = 1.78578$, $V_2^* = 0.5$, $m^* = 2.729$
	TC12	$c = 100\mu\text{m}$, $\omega = 261.80 \text{ rad/s}$, $M^* = 0.69867$, $\Lambda = 152.03$, $I_T^* = 0.214097$, $J_P^* = 1.78578$, $V_2^* = 2.0$, $m^* = 2.729$
3	TC13	$c = 100\mu\text{m}$, $\omega = 261.80 \text{ rad/s}$, $M^* = 0.69867$, $\Lambda = 152.03$, $I_T^* = 0.214097$, $J_P^* = 1.78578$, $X_H^* = 10.0$, $V_1^* = 0.5$
	TC14	$c = 100\mu\text{m}$, $\omega = 261.80 \text{ rad/s}$, $M^* = 0.69867$, $\Lambda = 152.03$, $I_T^* = 0.214097$, $J_P^* = 1.78578$, $X_H^* = 10.0$, $V_1^* = 1.0$
	TC15	$c = 100\mu\text{m}$, $\omega = 261.80 \text{ rad/s}$, $M^* = 0.69867$, $\Lambda = 152.03$, $I_T^* = 0.214097$, $J_P^* = 1.78578$, $X_H^* = 10.0$, $V_1^* = 2.0$
4	TC16	$c = 100\mu\text{m}$, $\omega = 261.80 \text{ rad/s}$, $M^* = 0.69867$, $\Lambda = 152.03$, $I_T^* = 0.214097$, $J_P^* = 1.78578$, $\varepsilon_X = 0.8$, $\psi_1 = 0$, $\psi_2 = 0$
	TC17	$c = 100\mu\text{m}$, $\omega = 261.80 \text{ rad/s}$, $M^* = 0.69867$, $\Lambda = 152.03$, $I_T^* = 0.214097$, $J_P^* = 1.78578$, $\varepsilon_X = 0.8$, $\psi_1 = \pi$, $\psi_2 = 0$
	TC18	$c = 100\mu\text{m}$, $\omega = 261.80 \text{ rad/s}$, $M^* = 0.69867$, $\Lambda = 152.03$, $I_T^* = 0.214097$, $J_P^* = 1.78578$, $\varepsilon_X = 0.8$, $\psi_1 = \pi/2$, $\psi_2 = 0$

Table 3.1. Details of test cases

3.8. *Orbit3D*

The numerical tool outlined in this paper was named *Orbit3D*. A copy of this program can be found in Appendix G and on disk on the inside of the back cover.

Matlab script file “Orb3Dvis.m”, a simple user interface that automatically plots all animations in addition to performing and plotting a spectral analysis of the impeller trajectory in each of the three coordinate directions, is listed in Appendix H and given on the disk inside the back cover. Note that “Orb3Dvis.m” must be located in the same directory as the result files from *Orbit3D*, namely “plotcjb.m”, “plottb.m”, and “plottraj.m” for this to work as intended.

Chapter 4 – Results & Discussion

This section shows the output of program *Orbit3D*. The reader should note that all plots were animated in Matlab 5.3 (The Mathworks, Inc., 1984-1999) using the “comet.m” and “movie.m” routines provided. What is displayed herein is a single frame (typically the first or final frame) of each animation. The output of *Orbit3D* includes the pressure distribution over both the thrust bearing and conical journal bearing and the trajectory of the impeller. Using the Matlab routine “spectrum.m”, the frequency spectrum of the motion in each coordinate direction may be found. Unfortunately, such an analysis was not possible due to technical difficulties. However, it was possible to estimate the dominant frequencies of the motion in each direction by observation of the time signal as the number of revolutions was known.

4.1. Pressure distribution

The details of the thrust bearing are $h_{0,TB} = 100\mu\text{m}$ and $h_{1,TB} - h_{0,TB} = 50\mu\text{m}$. The details of the conical journal bearing are $h_{vc} = 100\mu\text{m}$, and $h_{1,CJB} - h_{0,CJB} = 50\mu\text{m}$, and $\alpha = 45^\circ$. Common details include $\theta_0 = 45^\circ$, $\theta_{0a} = 0.2$, and $N_p = 4$.

4.1.1. Thrust bearing

The pressure distribution over the thrust bearing is shown below in Figure 4.1 when $\varepsilon_z = -0.5$ and $\varepsilon_x = \varepsilon_y = \gamma_x^* = \gamma_y^* = 0$ (all velocities are zero).

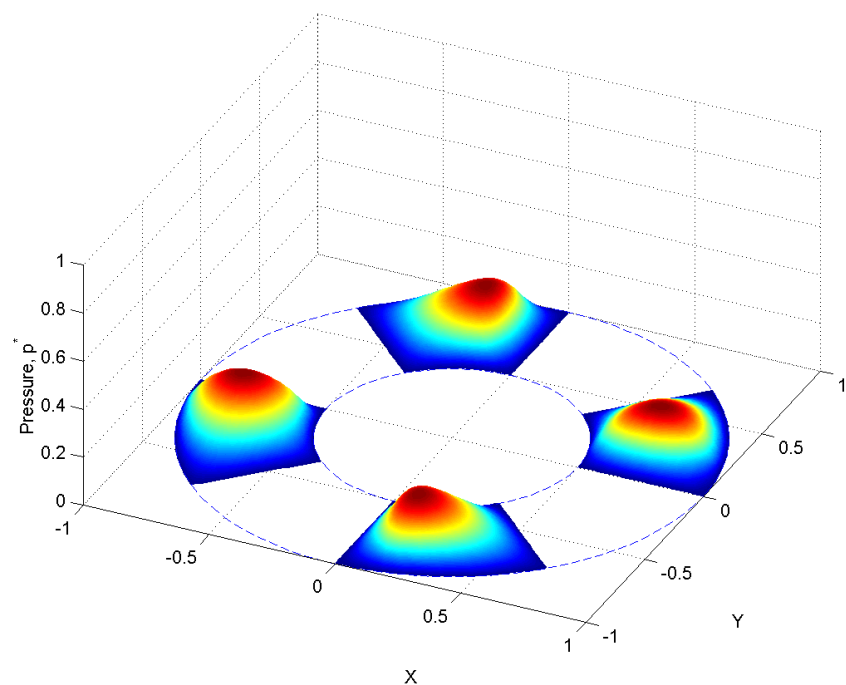


Figure 4.1. Pressure distribution over thrust bearing when $\varepsilon_z = -0.5$.

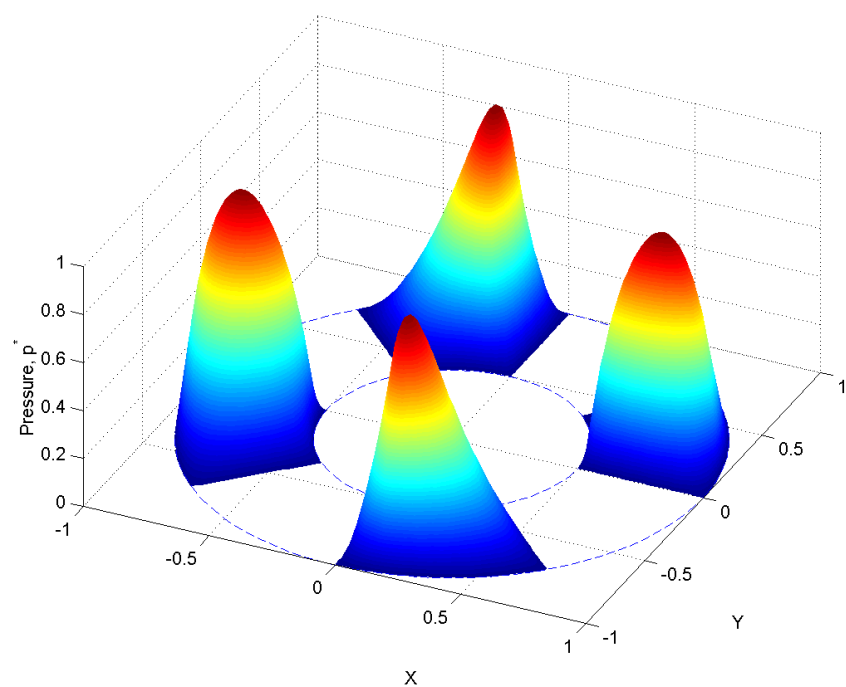


Figure 4.2. Pressure distribution over thrust bearing when $\varepsilon_z = -0.75$.

The eccentricity in the Z-direction was decreased to $\varepsilon_Z = -0.75$ to yield the distribution displayed by Figure 4.2. The results of a rotation of $\gamma_Y^* = -0.35$ when $\varepsilon_Z = -0.5$ and $\varepsilon_X = \varepsilon_Y = \gamma_X^* = 0$ are pictured in Figure 4.3. By examination of these figures it can be observed that the peak pressure over any particular blade is located very close to the trailing edge and slightly more towards the outer edge of the blade.

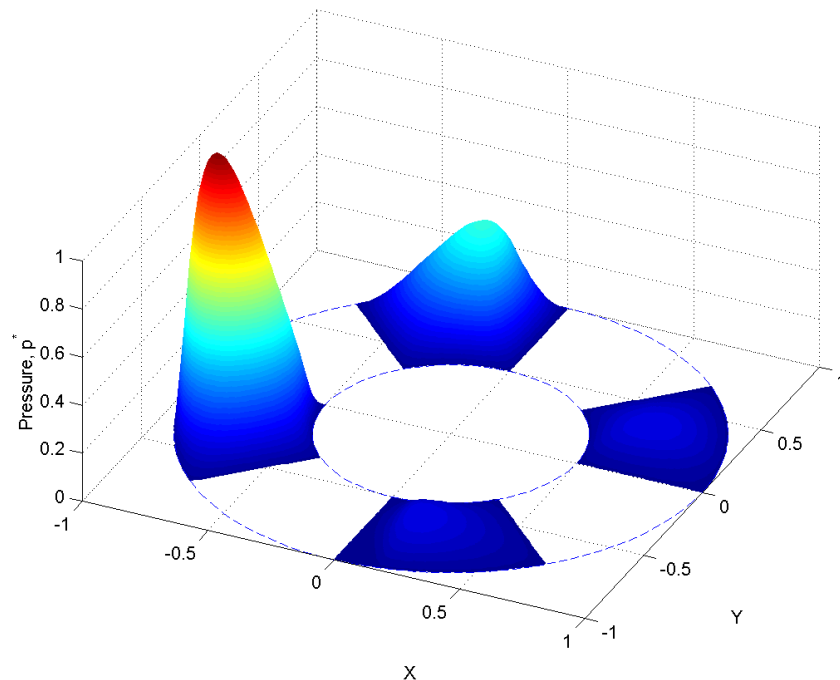


Figure 4.3. Pressure distribution over thrust bearing when $\varepsilon_Z = -0.5$ and $\gamma_Y^* = -0.35$.

4.1.2. Conical journal bearing

The pressure field over the conical journal bearing is shown below in Figure 4.4 when $\varepsilon_Z = 0.5$ and $\varepsilon_X = \varepsilon_Y = \gamma_X^* = \gamma_Y^* = 0$ (all velocities are zero). This view is like looking at the flattened cone from above.

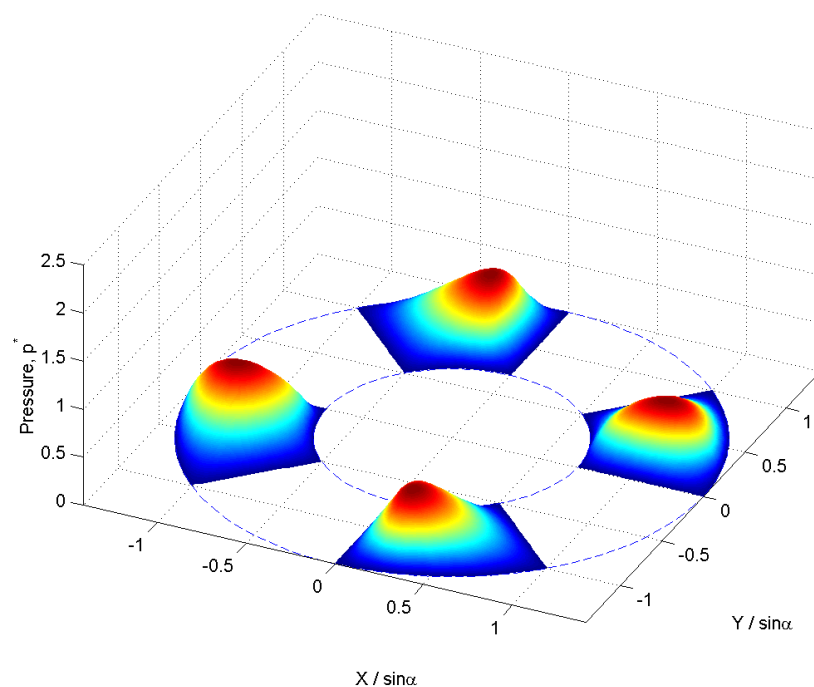


Figure 4.4. Pressure distribution over the conical journal bearing when $\varepsilon_z = 0.5$.

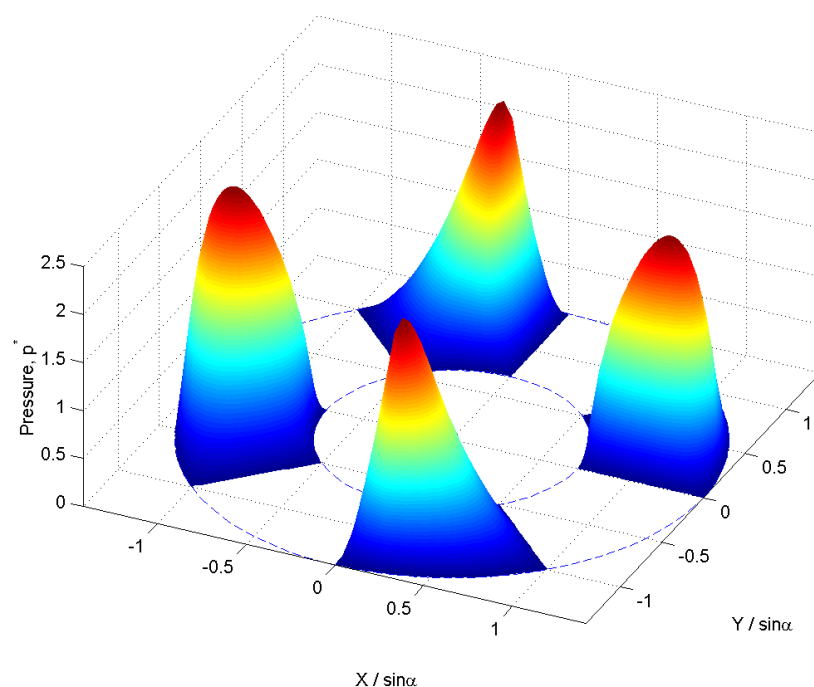


Figure 4.5. Pressure distribution over the conical journal bearing when $\varepsilon_z = 0.75$.

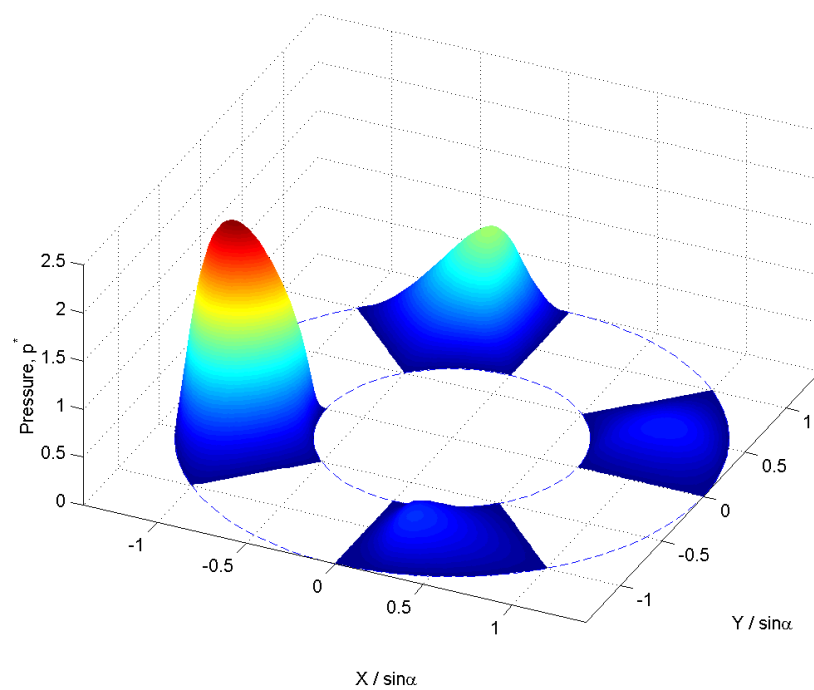


Figure 4.6. Pressure distribution over the conical journal bearing when $\varepsilon_x = -0.25$ and $\varepsilon_z = 0.5$.

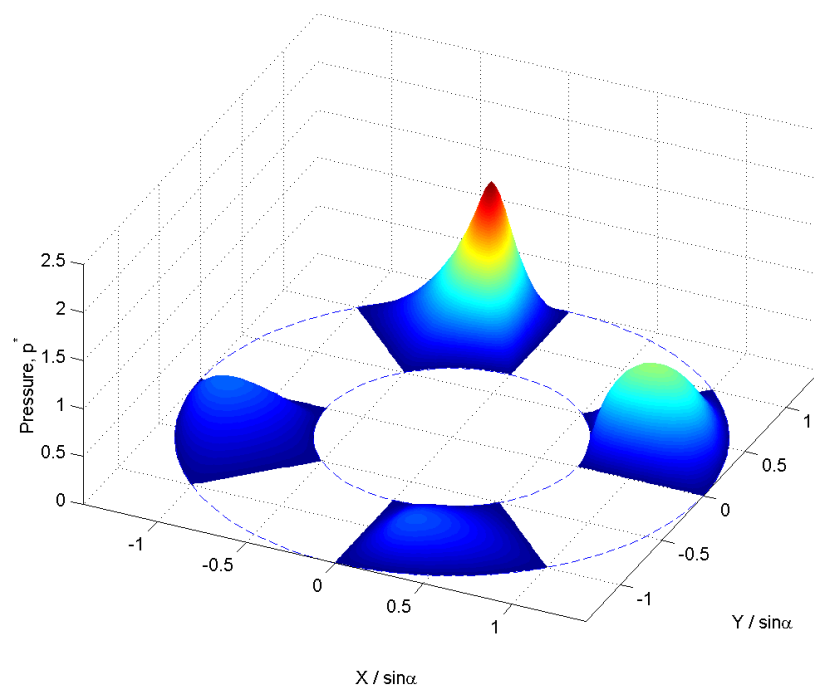


Figure 4.7. Pressure distribution over the conical journal bearing when $\varepsilon_z = 0.5$ and $\gamma_x^* = -0.35$.

Figure 4.5 pictures the case where $\varepsilon_z = 0.75$ and $\varepsilon_x = \varepsilon_y = \gamma_x^* = \gamma_y^* = 0$. Figure 4.6 shows the pressure distribution when $\varepsilon_x = -0.25$, $\varepsilon_z = 0.5$ and $\varepsilon_y = \gamma_x^* = \gamma_y^* = 0$. The results of a rotation about the X-axis of $\gamma_x^* = -0.35$ when $\varepsilon_z = 0.5$ and $\varepsilon_x = \varepsilon_y = \gamma_y^* = 0$ is shown in Figure 4.7.

The variables ε'_x and ε'_y are modified forms of the eccentricity ratios in the X- and Y-directions and are introduced here to account for the increased / decreased clearance in the X-Y plane accompanying movement of the impeller in the negative / positive Z-direction. That is, with respect to the X-direction, the horizontal clearance is equal to $h_{hc} = h_{0,CJB}/\cos\alpha$ when $\varepsilon_z = 0$, where the eccentricity ratio is defined as $\varepsilon_x = e_x/h_{hc}$. However, the true clearance over the range $-1.0 \leq \varepsilon_z \leq 1.0$ is actually $h'_{hc} = h_{hc} - e_z \tan\alpha$. Therefore, the modified eccentricity ratio is defined as $\varepsilon'_x = e_x/h'_{hc}$, which simplifies to $\varepsilon'_x = \varepsilon_x/(1-\varepsilon_z)$. Similarly, the modified eccentricity ratio in the Y-direction can be defined as $\varepsilon'_y = e_y/h'_{hc}$, which simplifies to $\varepsilon'_y = \varepsilon_y/(1-\varepsilon_z)$ where $\varepsilon_y = e_y/h_{hc}$. For example, as detailed in the previous paragraph, Figure 4.6 shows the pressure distribution when $\varepsilon_x = -0.25$ and $\varepsilon_z = 0.5$, which is equivalent to $\varepsilon'_x = -0.5$. These modified variables are particularly important in the following section. Eccentricity ratio ε_z may also be modified to correct for the increased / decreased clearance when $\varepsilon'_x \neq 0$ and / or $\varepsilon'_y \neq 0$.

4.2. Impeller trajectory

The trajectories for each test case are plotted in this section. From observation of these orbits, the stability of the system at the specified operating conditions will be assessed. For reference, the details of each test case were given in section 3.7

A grid refinement in time is not shown herein – it was found that if the Runge-Kutta procedure was unstable, the program misreported that touchdown had occurred. Halving the size of the time increment and performing the study once again remedied this. It should be noted that, in all cases, the non-dimensional time step increment was kept below $\Delta t^* = 0.5^\circ$ and in some cases, where the displacement of the impeller during a single time step was relatively large (i.e. if the non-dimensional mass was small or the magnitude of the unbalance force was large) then the time step increment was set to either $\Delta t^* = 0.125^\circ$ or 0.25° . This disadvantage of this was that 2880 and 1440 time steps were required for one revolution of the impeller, as opposed to 720 time steps when $\Delta t^* = 0.5^\circ$. However, this does not increase the solution time too significantly as the iterative process becomes quicker for each step. On an IBM Pentium III 866MHz T22 Thinkpad with 256MB RAM, the computing time was approximately 10-15 minutes for two revolutions of the impeller, depending on the time step used.

Figure 4.8 is a plot of test cases TC1 – TC3. Looking at the X-Y plane (shown in Figure 4.8(b)), the orbit of TC1 is relatively small and elliptical in shape with the major axis practically aligned with the X-axis, whereas TC2 and TC3 are progressively larger and more circular. The projection of each orbit onto the X-Z plane (shown in Figure 4.8(c)) is convex in shape, whereas the projection on the Y-Z plane (shown in Figure 4.8(d)) is concave, with the trajectory of TC1 being closer to the origin with respect to the Z-direction than both TC2 and TC3.

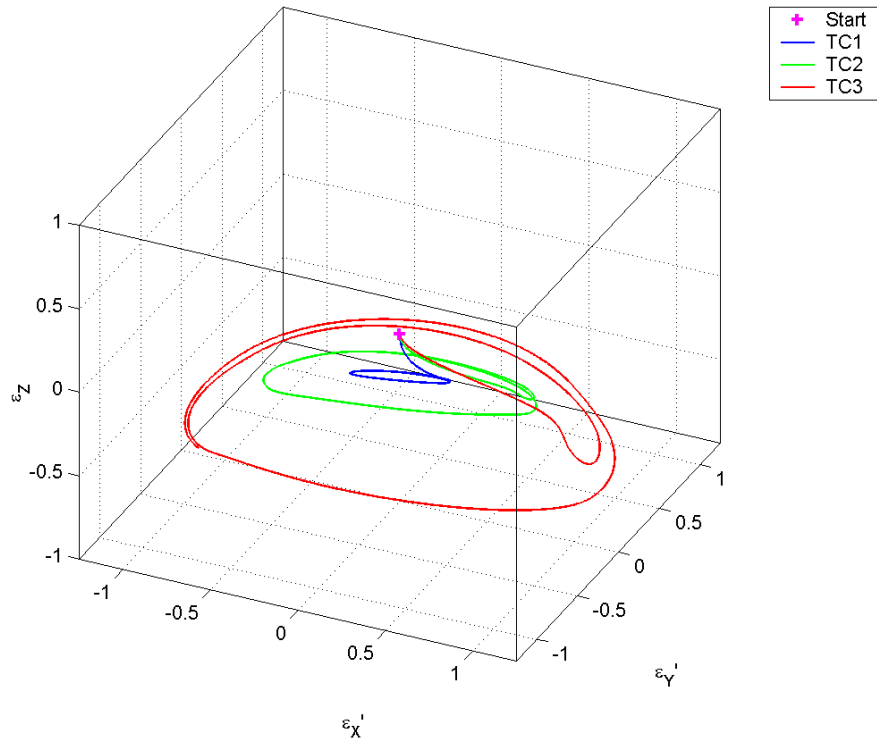


Figure 4.8(a) Impeller trajectories for test cases TC1, TC2, and TC3

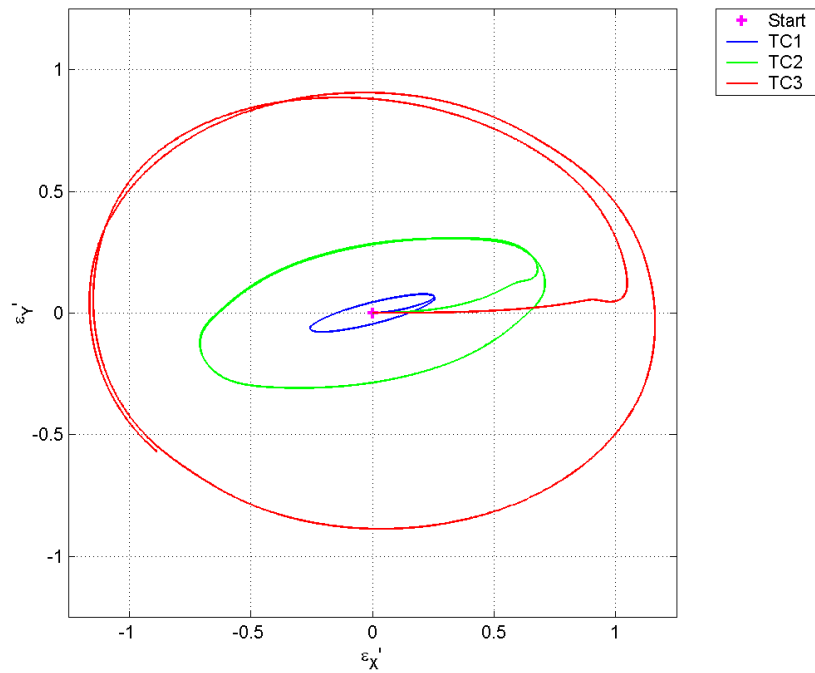


Figure 4.8(b) Projection of trajectories in (a) onto the X-Y plane

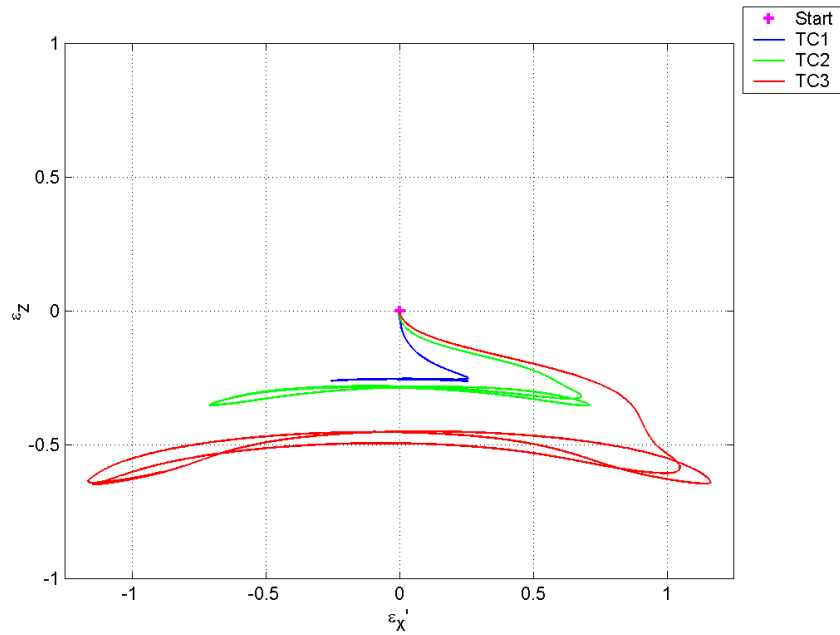


Figure 4.8(c) Projection of trajectories in (a) onto the X-Z plane

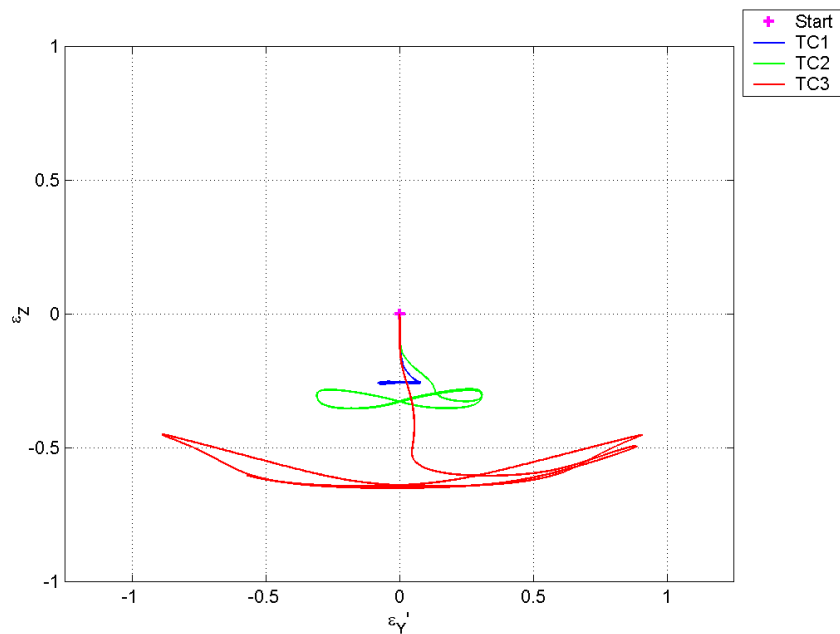


Figure 4.8(d) Projection of trajectories in (a) onto the Y-Z plane

Although each case settles into a limit cycle within 1-2 revolutions of the impeller indicating a high amount of damping, it is clear that the stiffness of the bearing is significantly decreased as the clearance is increased. Consequently, the relative movement of the impeller with respect to the pump housing is greater, resulting in a less stable impeller. Accordingly, the stability parameter decreases from $S_0 = 1/M^* = 2.86$ for $c = 50\mu\text{m}$ to 1.43 and 0.72 for $c = 100\mu\text{m}$ and $200\mu\text{m}$ respectively.

It should be noted that in Figure 4.8 and all following figures picturing the impeller trajectory, the modified eccentricities in the X- and Y- coordinate directions, ε'_X and ε'_Y (defined in section 4.1.2.), are used to give a better representation of the position of the impeller with respect to the pump housing. However, note that in Figure 4.8 (b) the modified eccentricity ratio in the X-direction exceeds the range of $-1.0 \leq \varepsilon'_X \leq 1.0$. This is because the eccentricity ratio is based on the minimum clearance $h_{0,CJB}$, that is, the clearance between the untapered land and the pump housing. However, when $|\varepsilon'_X| \geq 1.0$, the tapered section of the bearing is closest to the housing and therefore the clearance is increased and the impeller may move a greater distance before touchdown occurs. This can be remedied by determination of the true horizontal clearance, which will be a function of the non-dimensional time t^* , percentage of the taper θ_{0a} , and the angular extent of the bearing θ_0 . However, this is left for a future study.

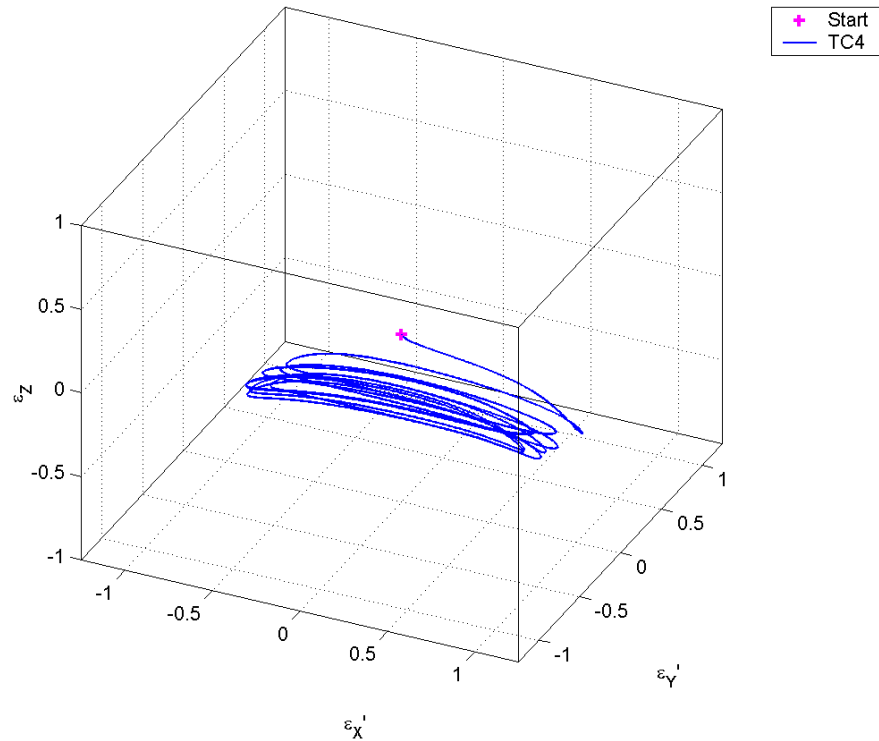


Figure 4.9(a) Impeller trajectory for test case TC4

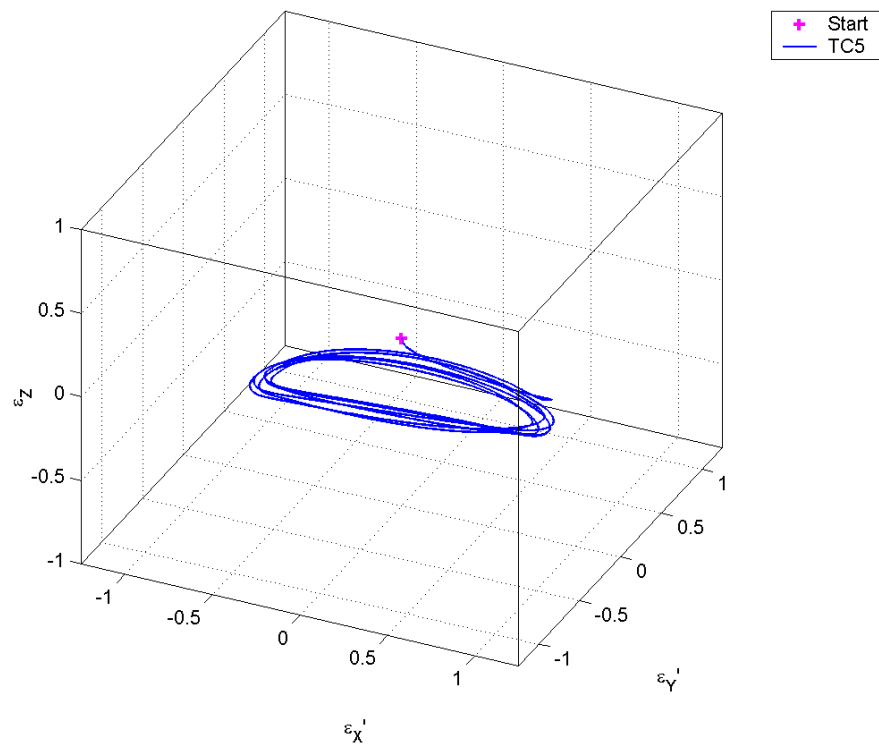


Figure 4.9(b) Impeller trajectory for test case TC5

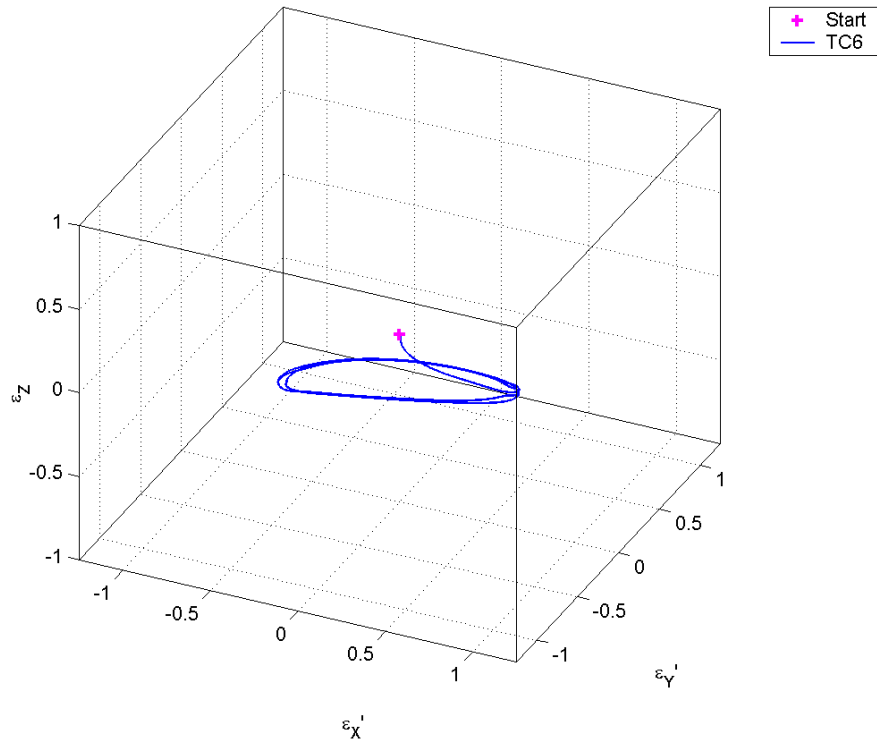


Figure 4.9(c) Impeller trajectory for test case TC6

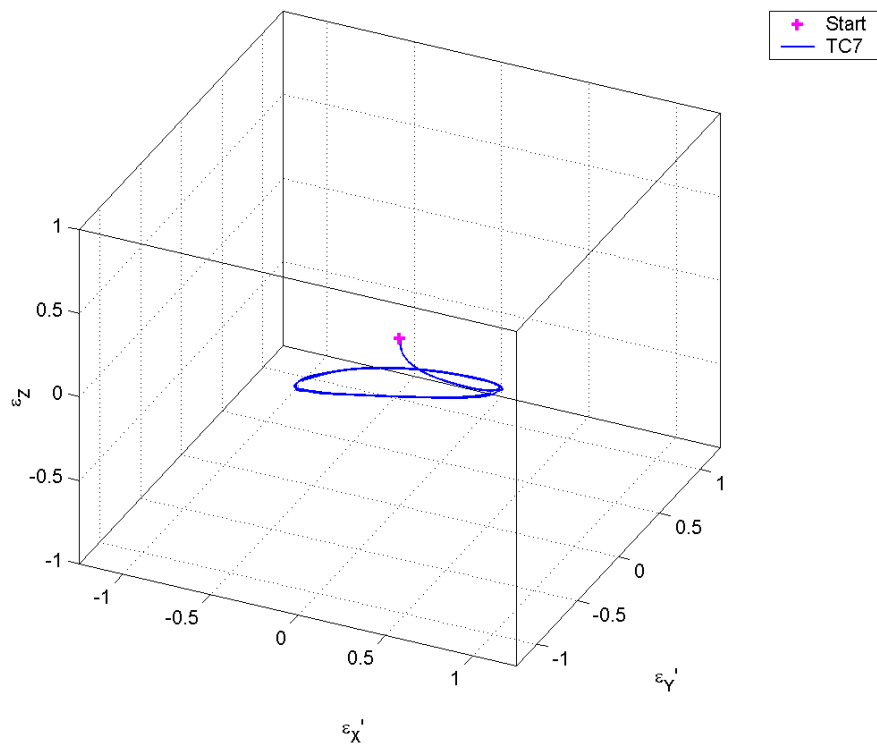


Figure 4.9(d) Impeller trajectory for test case TC7

Figure 4.9(a) – (d) is a plot of test cases TC4 – TC7 respectively. Note that test case TC2 is pictured in Figure 4.8 and so is not reprinted. From these figures, it is clear that as the rotational speed is increased while the clearance is kept constant, the stability of the impeller increases. Given that each figure in this group is a plot of four rotations of the impeller (as opposed to two rotations for all other plots), the trajectory of TC4 pictured in Figure 4.9(a) is highly directional and erratic, never settling into a stable limit cycle. However, as the rotational speed is increased, the impeller becomes stable and settles quickly into a limit cycle as pictured in Figure 4.9(d) for TC7, indicating a high stability reserve. It should be noted that, unexpectedly, the stability parameter in fact decreases from $S_0 = 1/M^* = 35.78$ to 3.98, 1.43, 0.73, and 0.44 as the rotational speed is increased from 500 RPM to 1500, 2500, 3500, and 4500 RPM respectively. This would probably be better explained once a stability map has been created.

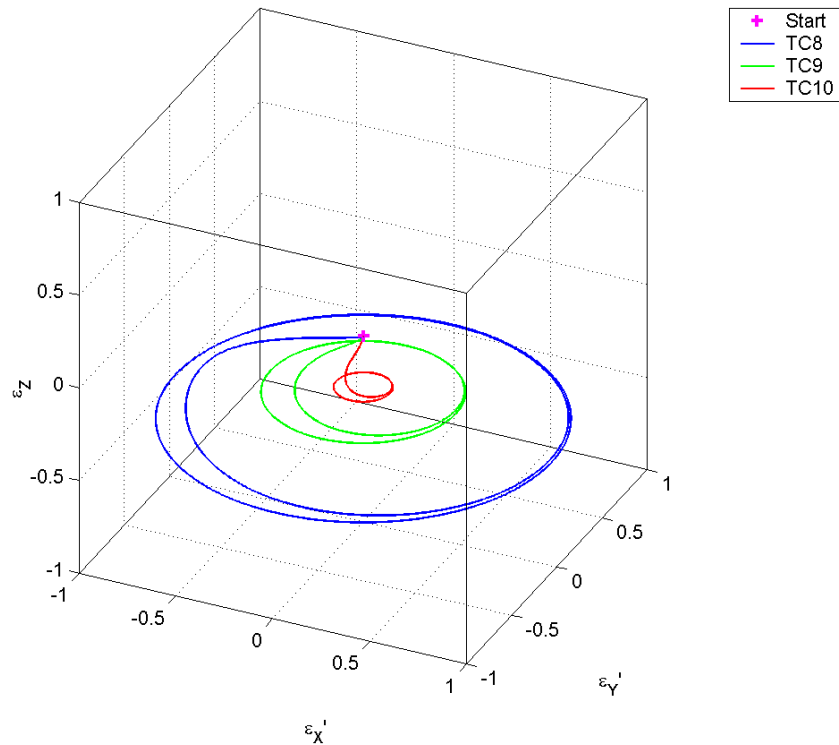


Figure 4.10(a) Impeller trajectories for test cases TC8, TC9, and TC10

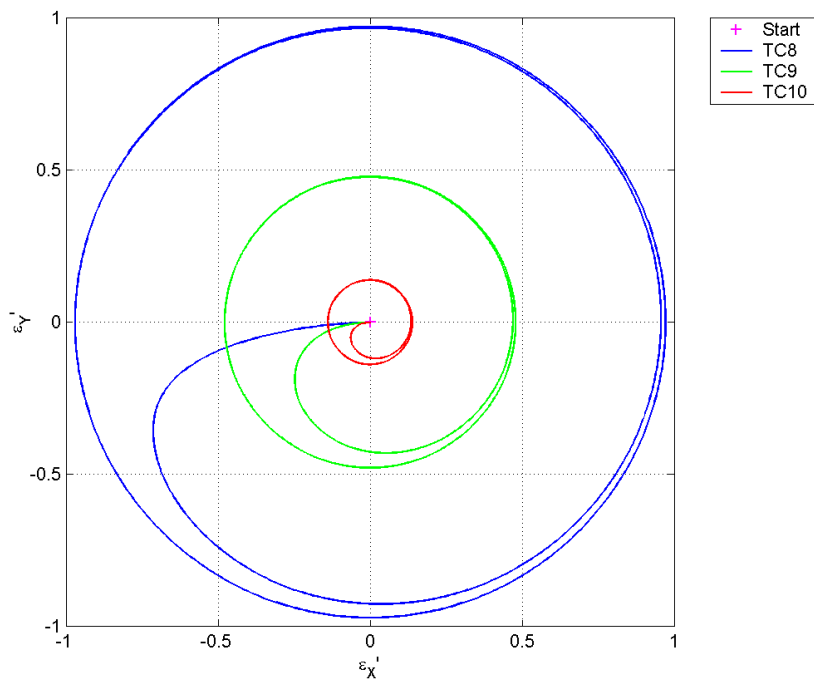


Figure 4.10(b) Projection of trajectories in (a) onto the X-Y plane

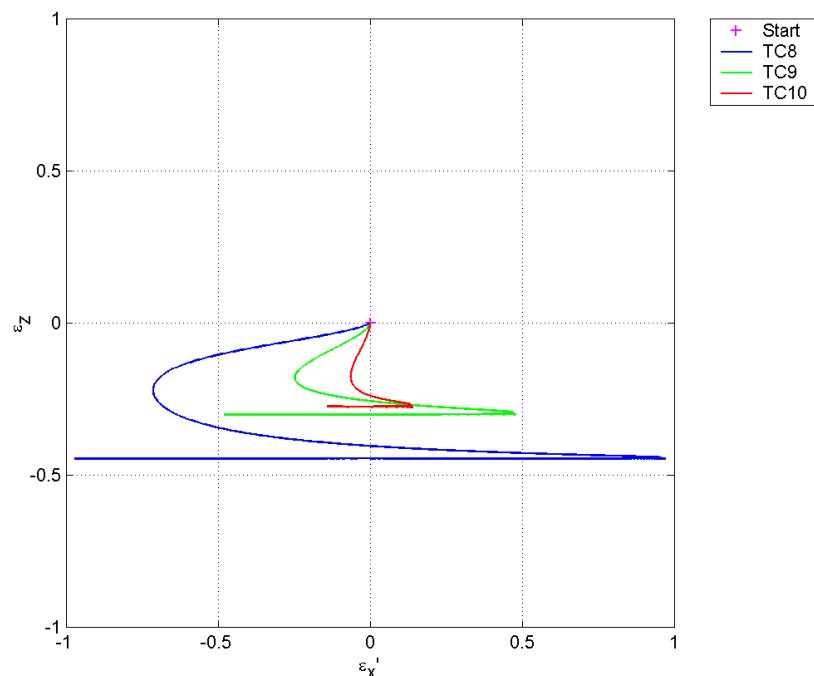


Figure 4.10(c) Projection of trajectories in (a) onto the X-Z plane

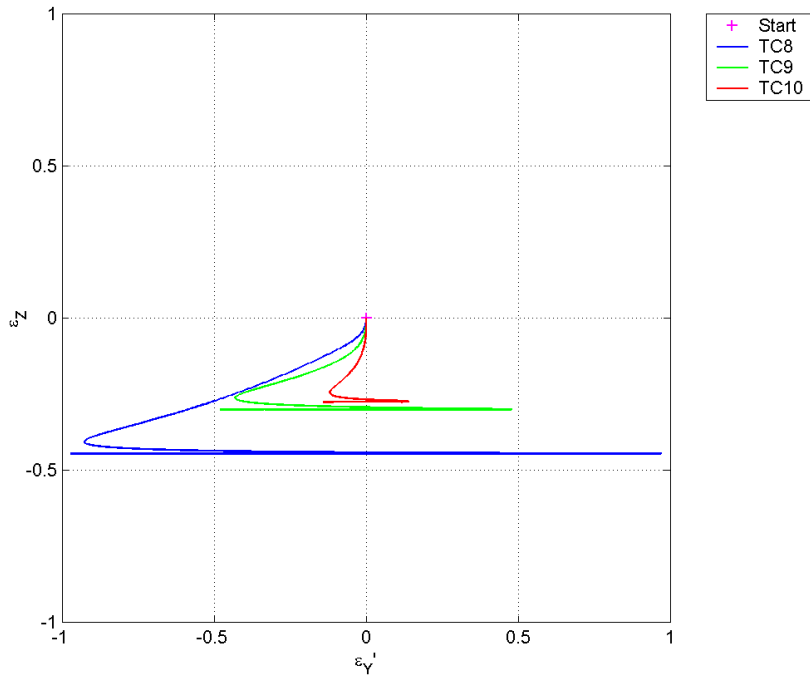


Figure 4.10(d) Projection of trajectories in (a) onto the Y-Z plane

Figure 4.10 is a plot of test cases TC8 – TC10. Note that in each case a stable limit cycle, which is circular in shape, is quickly reached. The only difference between each trajectory is the radius of the motion which, due to the increase in the magnitude of the unbalance force, was achieved by increasing the unbalance mass. Interestingly, the projection of the limit cycle onto both the X-Z and Y-Z planes is neither convex or concave, but flat. The radii of the limit cycle for each of the test cases TC8, TC9 and TC10 are approximately of length 0.97, 0.48, and 0.14 respectively.

The results of test cases TC11, TC9 and TC12 are shown in Figure 4.11. This figure indicates a high stability reserve for each case. Similar to Figure 4.10, the radius of each orbit is increased as the magnitude of the unbalance force is increased which, in this case, was achieved by increasing the frequency of the unbalance. See Figure 4.11(b). Unlike Figure 4.10, however, the outer trajectory which corresponds to TC12 appears to be slightly elliptical in shape.

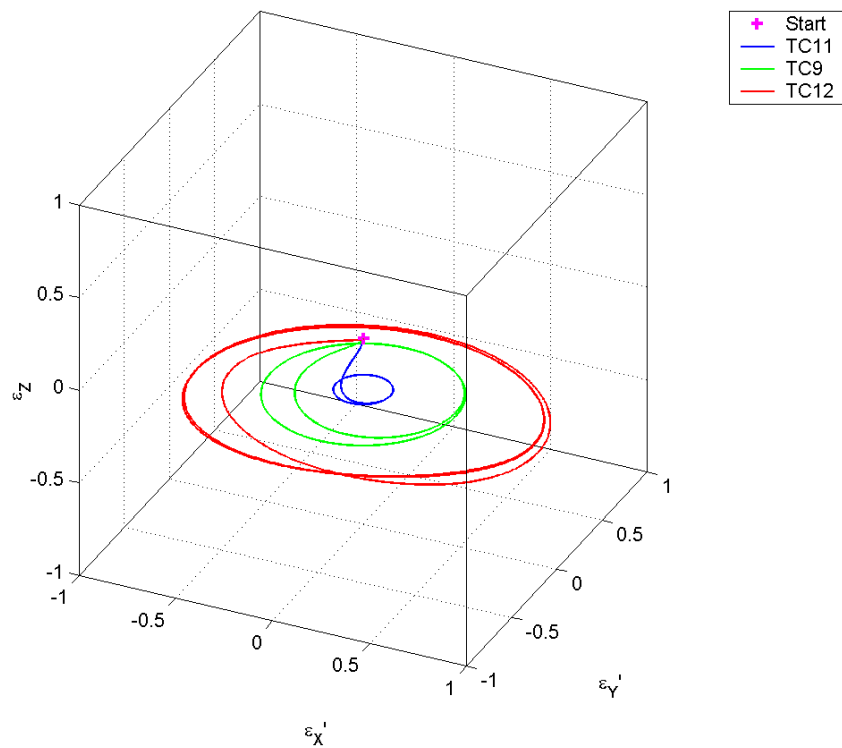


Figure 4.11(a) Impeller trajectories for test cases TC11, TC9, and TC12

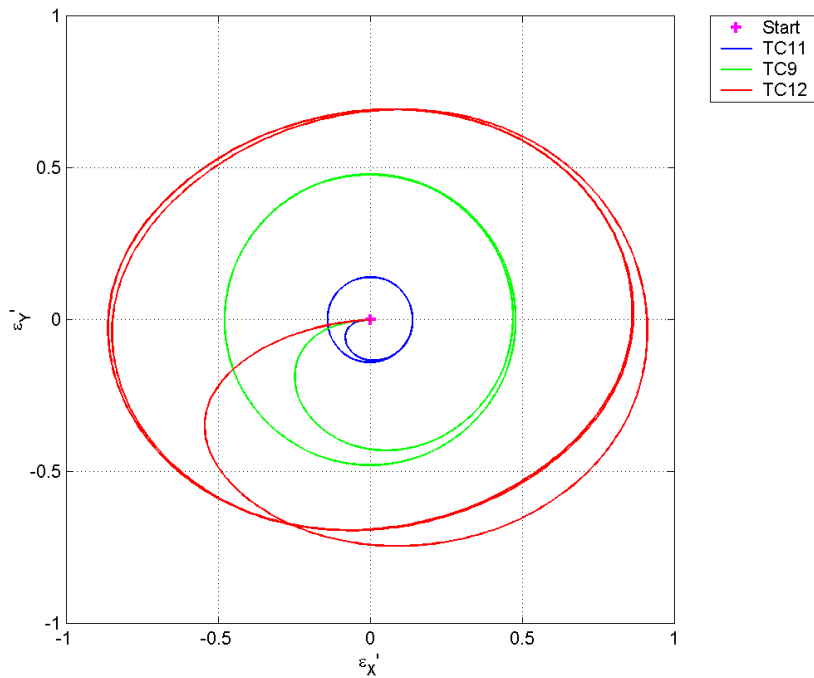


Figure 4.11(b) Projection of trajectories in (a) onto the X-Y plane

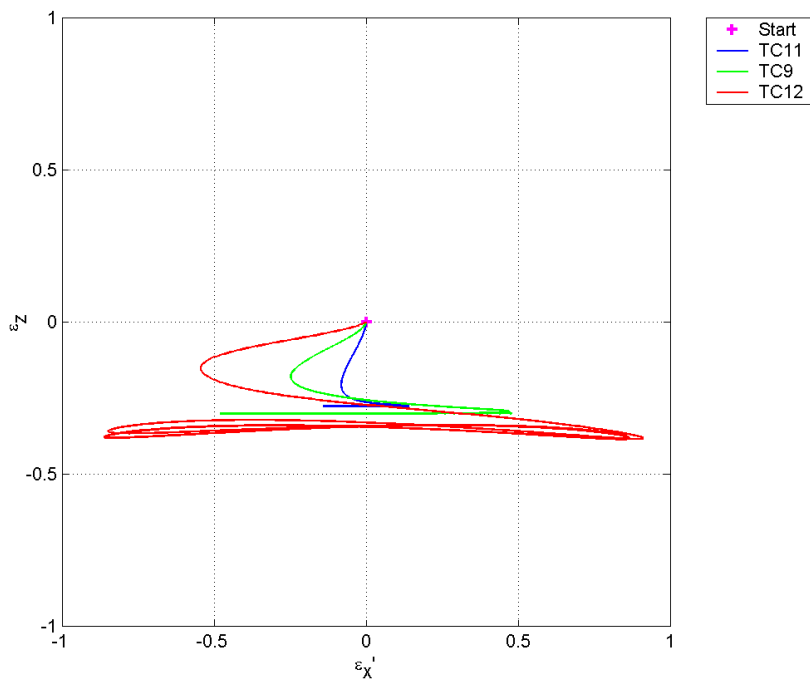


Figure 4.11(c) Projection of trajectories in (a) onto the X-Z plane

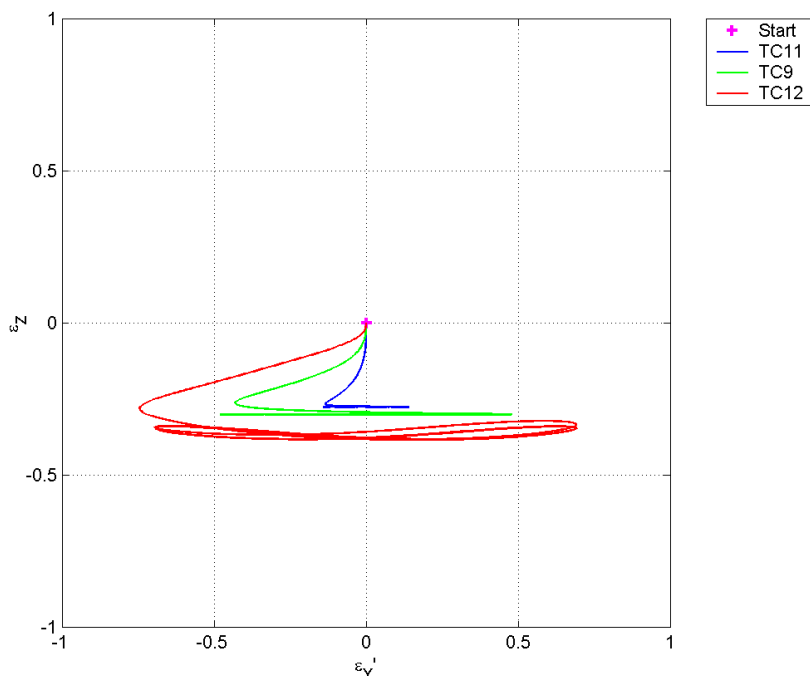


Figure 4.11(d) Projection of trajectories in (a) onto the Y-Z plane

Once again, the projection of the trajectories onto the X-Z plane (shown in Figure 4.11(c)) and the Y-Z plane (shown in Figure 4.11(d)) are practically flat, which appears to be characteristic of simultaneous excitation in both the X- and Y- directions.

Figure 4.12 is a plot of the trajectories resulting from test cases TC13 – TC15. This group of test cases is similar to the previous group consisting of TC11, TC9 and TC12, although the excitation is in the X-direction only. Interestingly, the projection of the trajectories onto the X-Z plane (shown in Figure 4.12(c)) are again convex, and in addition almost lie directly on top of each other. The projections of TC13 and TC14 onto the X-Y plane (shown in Figure 4.12(b)) are each elliptical in shape, whereas the projection of TC15 is almost “lemon” shaped.

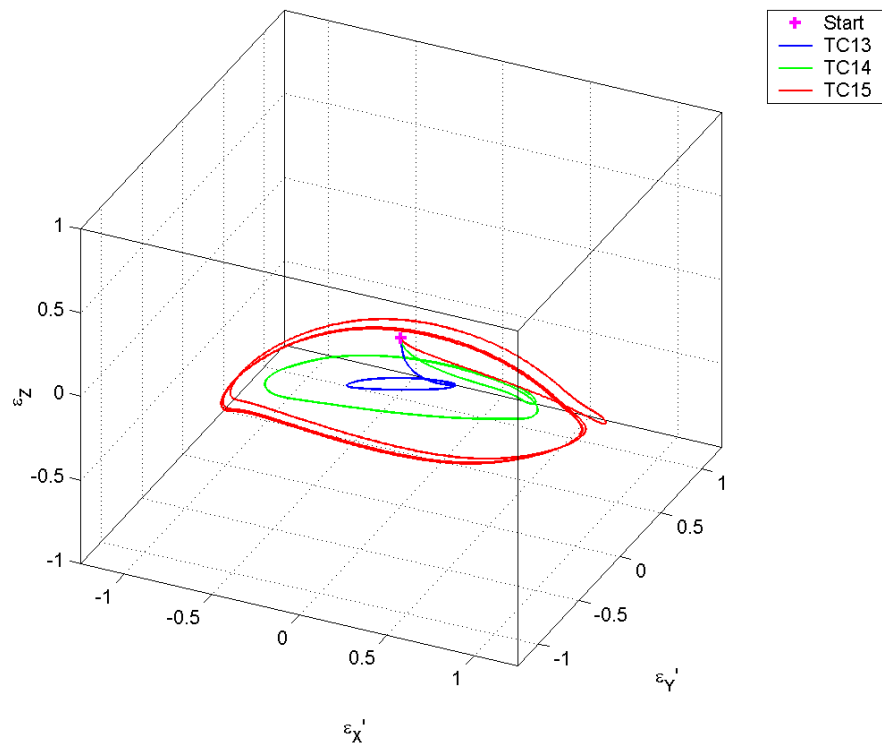


Figure 4.12(a) Impeller trajectories for test cases TC13, TC14, and TC15

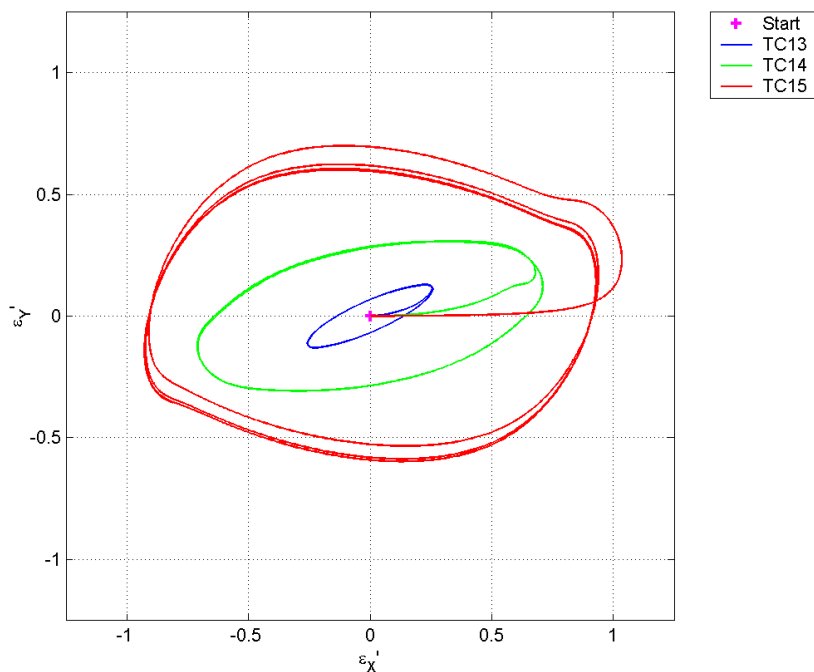


Figure 4.12(b) Projection of trajectories in (a) onto the X-Y plane

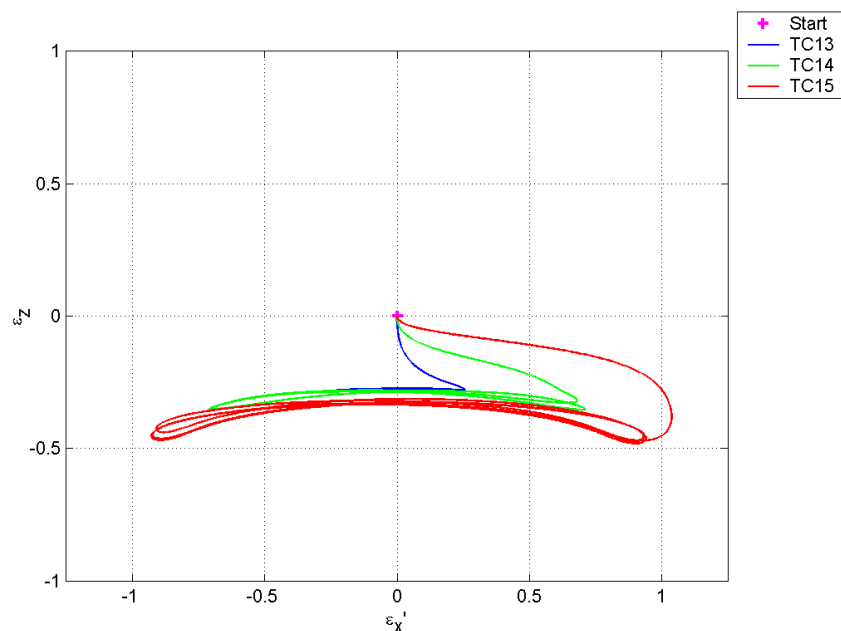


Figure 4.12(c) Projection of trajectories in (a) onto the X-Z plane

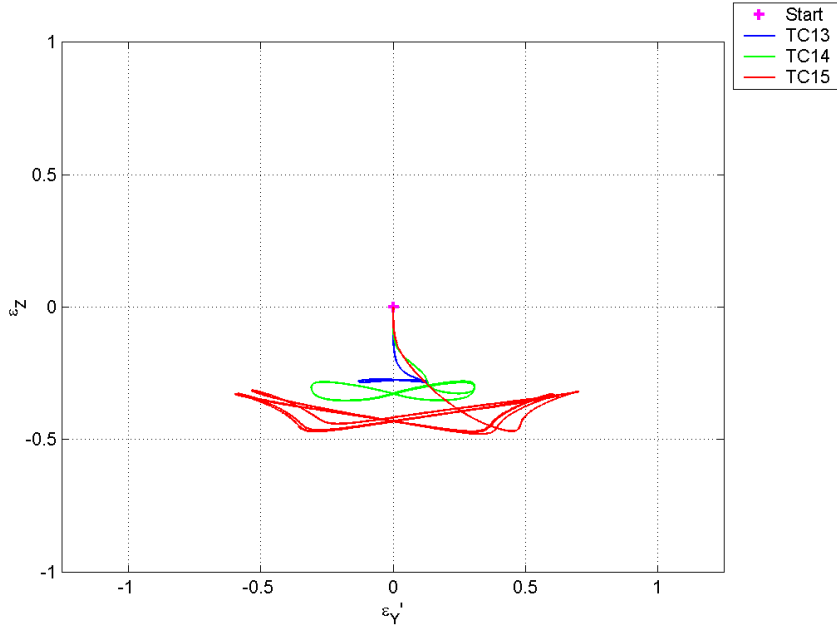


Figure 4.12(d) Projection of trajectories in (a) onto the Y-Z plane

Figure 4.13 shows the trajectories obtained from test cases TC16 – TC18. For case TC16, where the gravitational force acts in the positive Z-direction, the position of the limit point is $(\varepsilon_X, \varepsilon_Y, \varepsilon_Z) = (0.0, 0.0, -0.202)$. For case TC17, where the gravitational force acts in the negative Z-direction, the position of the limit point was found to be $(\varepsilon_X, \varepsilon_Y, \varepsilon_Z) = (0.0, 0.0, -0.272)$. Thus, with respect to the Z-direction, the impeller sits closer to the top housing when the cone apex is pointing downwards and closer to the bottom housing when the cone is pointing upwards. See Figures 4.13(c) and 4.13(d). Other than this difference, the projection of both trajectories on the X-Y plane is practically identical as pictured in Figure 4.13(b). With respect to case TC18, where the gravitational force acts in the positive X-direction, the position of the limit point was found to be $(\varepsilon_X, \varepsilon_Y, \varepsilon_Z) = (0.183, 0.101, -0.241)$. For this case, with respect to the Z-direction, the impeller lies in between the final locations of test cases TC16 and TC17, and somewhat removed from the origin in the positive X- and Y- coordinate directions.

All trajectories reach the limit point quickly and without oscillation, indicating a high level of damping and a stable system.

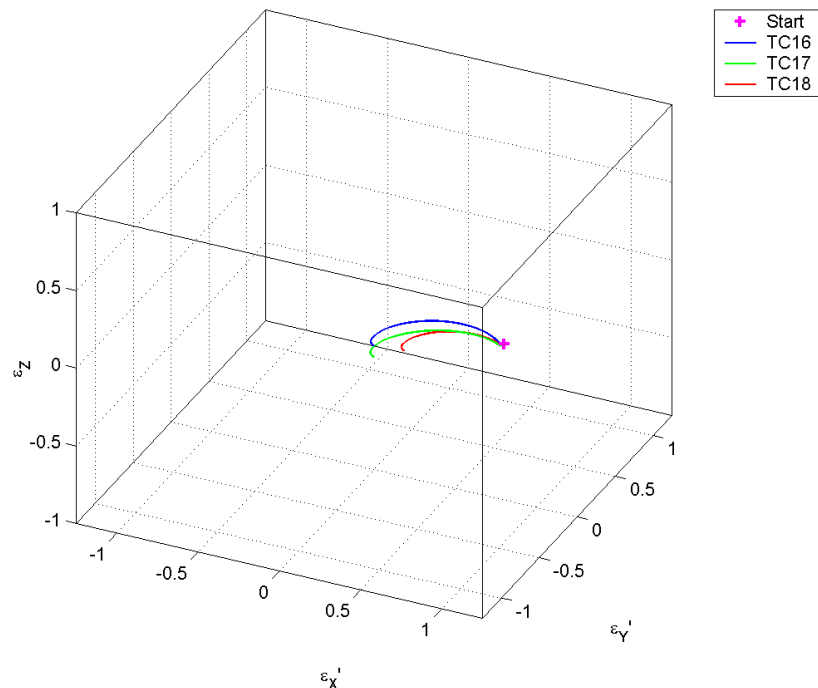


Figure 4.13(a) Impeller trajectories for test cases TC16, TC17, and TC18

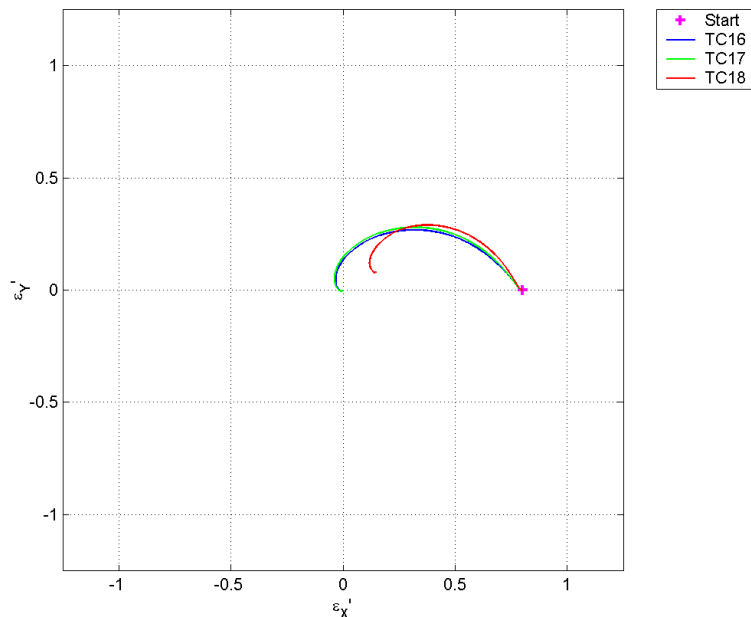


Figure 4.13(b) Projection of trajectories in (a) onto the X-Y plane

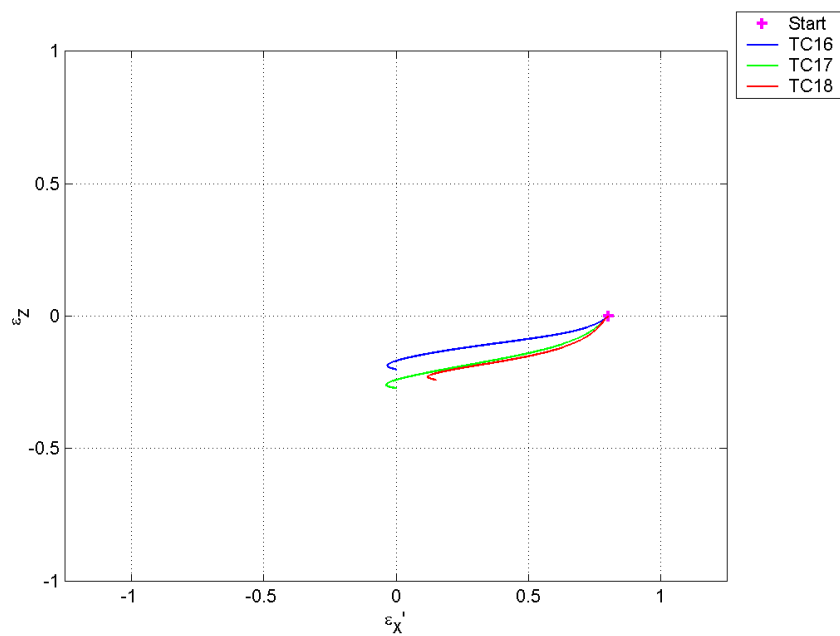


Figure 4.13(c) Projection of trajectories in (a) onto the X-Z plane

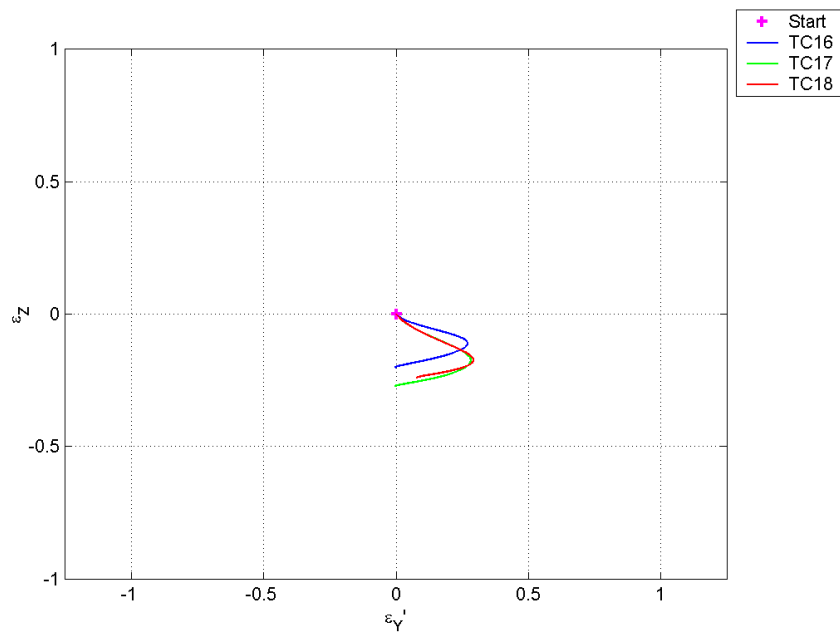


Figure 4.13(d) Projection of trajectories in (a) onto the Y-Z plane

Figures 4.14(a) – (c) show the rotational trajectory of the impeller, as opposed to the translational trajectory that has been pictured up to this point, of test cases TC4, TC5, and TC2. Such plots consist of the non-dimensional rotation about the Y-axis γ_Y^* plotted against the non-dimensional rotation about the X-axis γ_X^* . Figure 4.14(a) corresponds to test case TC4, whereas figures 4.14(b), and 4.14(c) correspond to test cases TC5 and TC2 respectively. The circular shape of the trajectory indicates that the impeller is undergoing conical whirl, although this is in response to “shaking” of the pump housing in the X-direction. Figures 4.14(a) and (b) indicate that test cases TC4 and TC5 are both bordering on the edge of instability, whereas Figure 4.14(c) indicates that TC2 is stable.

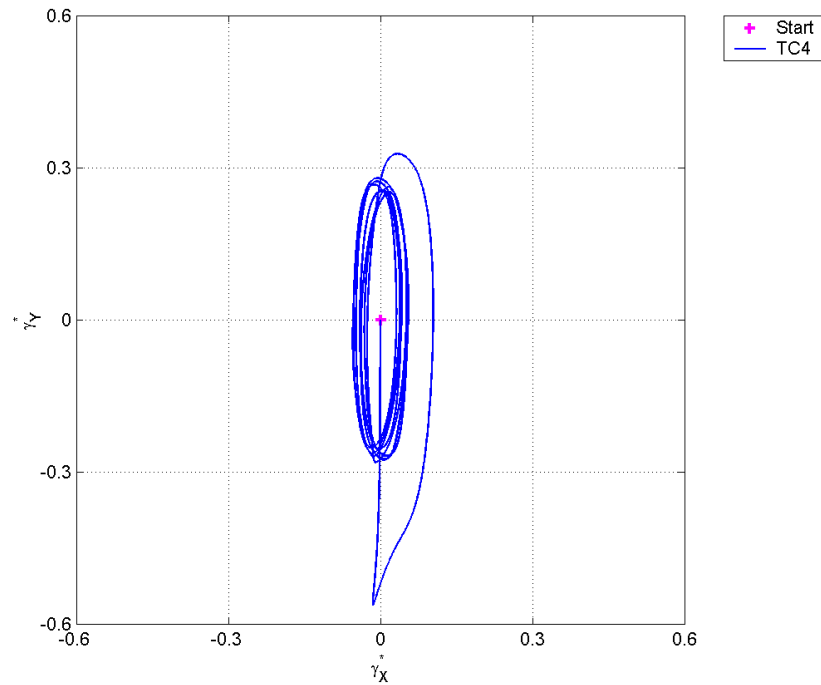


Figure 4.14(a) Rotational trajectory for test case TC4

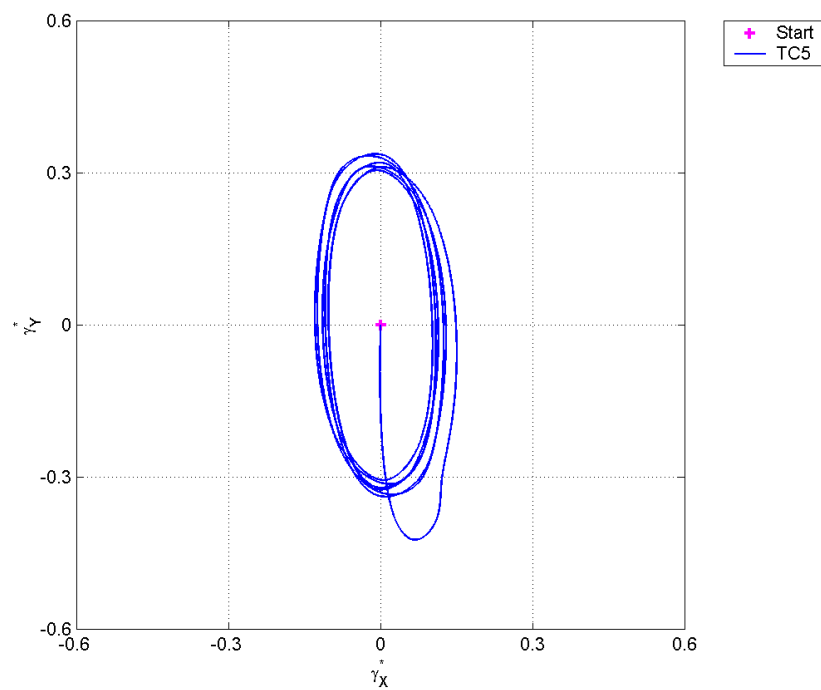


Figure 4.14(b) Rotational trajectory for test case TC5

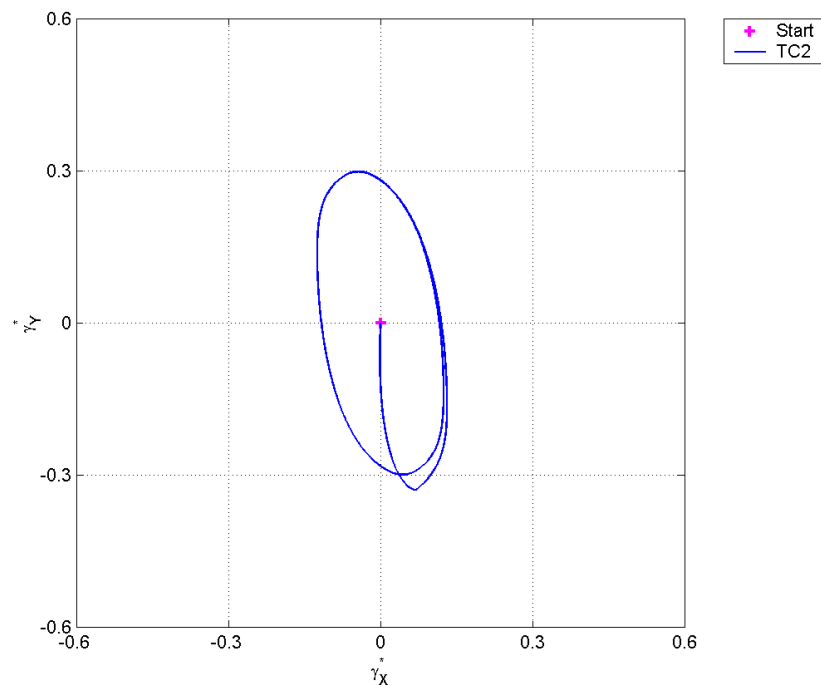


Figure 4.14(c) Rotational trajectory for test case TC2

Figures 4.15(a), 4.15(b), and 4.15(c) picture the eccentricity ratios in the X-, Y-, and Z-directions respectively against the number of impeller revolutions for test case TC4. The figures are plotted from the end of the first impeller revolution to the end of the fourth revolution (such that the immediate response is ignored). From each figure it is immediately clear that more than one discrete frequency is present in the displacement signals. From observation of Figure 4.15(a), it appears that the signal consists of a frequency component equal to the rotational frequency ω plus a more dominant frequency component equal to 5ω . This frequency of 5ω is present due to shaking of the pump housing at 5ω . These same frequencies are present in the signal pictured in Figure 4.15(b), although the frequency synchronous with ω is somewhat more dominant. Figure 4.15(c) indicates that a frequency of approximately 0.5ω is present in the signal of ε_z , as is frequency approximately 10ω , and ω although to a lesser extent. The presence of 0.5ω would indicate the occurrence of half-frequency whirl and may help to explain the unstable nature of test case TC4.

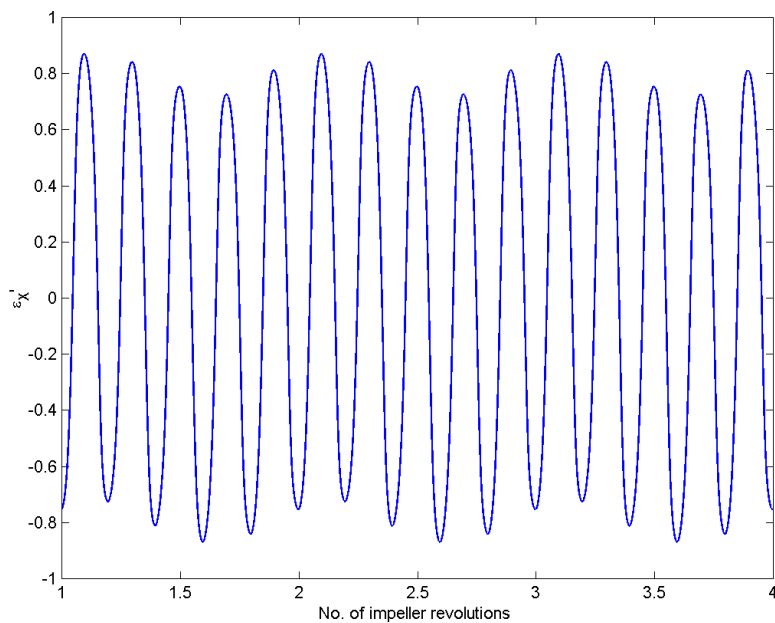


Figure 4.15(a) Eccentricity ratio in the X-direction against number of impeller revolutions

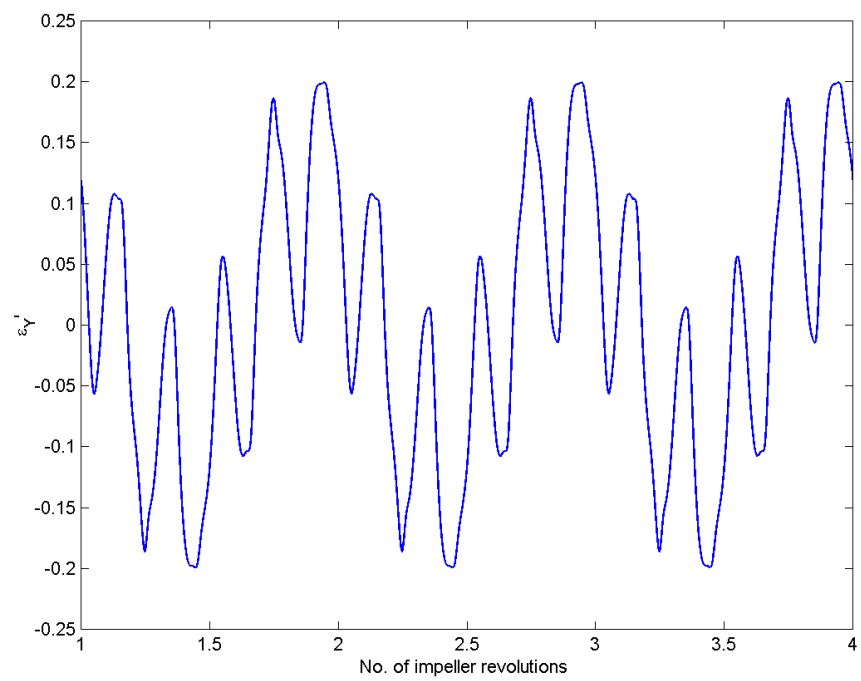


Figure 4.15(b) Eccentricity ratio in the Y-direction against number of impeller revolutions

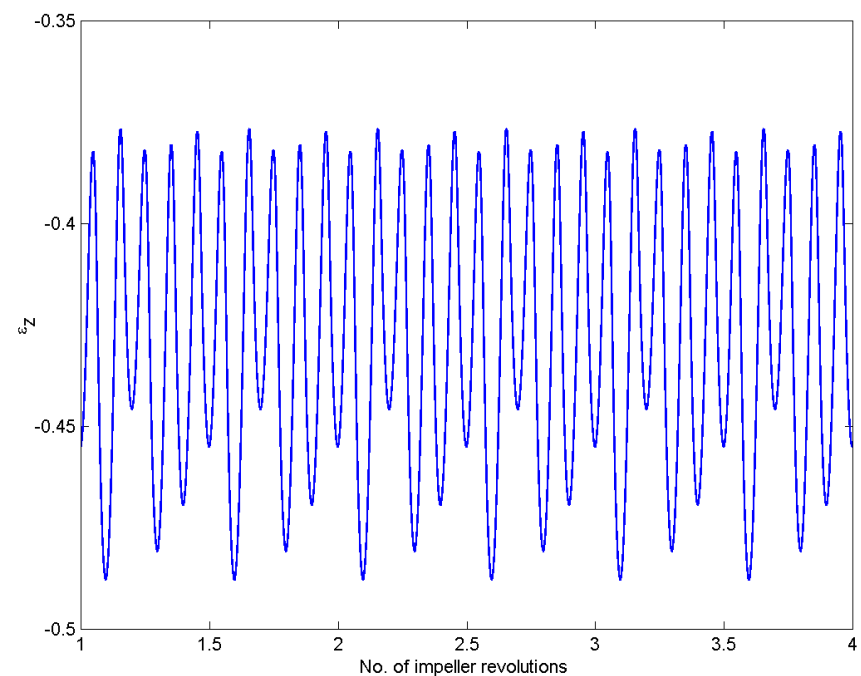


Figure 4.15(c) Eccentricity ratio in the Z-direction against number of impeller revolutions

It should be noted that the transverse moment of inertia I_T and the polar moment of inertia I_p of the impeller were assumed to be constant in this study. However, as the bearing rotates, $I_T = I_{xx} \neq I_{xx}$ and $I_T = I_{yy} \neq I_{YY}$, meaning that the transverse moment of inertia with respect to the X-Y-Z coordinate system and therefore the equations of motions, is not constant. It remains true that $I_p = I_{zz} = I_{ZZ}$. This should be investigated further.

Chapter 5 - Conclusion

From Chapter 4, it is clear that program Orbit3D is a powerful tool which, in conjunction with Matlab, can be used to both visualise the pressure distribution over the bearing surfaces of the impeller and assess the stability of the impeller at the specified operating conditions by simple observation of the impeller trajectory.

The pressure field may be viewed as a single frame with the impeller located at a position and/or velocity specified by the user, as done in Chapter 4, or in the form of an animation where each frame is a snap shot at each step of the trajectory. The former option is useful when the user wants to examine the shape of the pressure profile over a bearing surface with the impeller at a certain location, whereas the latter option can be used by the user when analysing the response of the impeller to a disturbance and subsequently correlated with the trajectory. Through visualisation of the pressure field, the shape of the bearing surfaces may be optimised such that regions of high pressure are more evenly spread over the blade and pressure gradients are minimised to lower shear rates and therefore blood damage.

Through observation of the trajectory over a range of conditions, it is possible to create a stability map which identifies the stable regions of operation. Additionally, the trajectory and determination of the dominant frequency components of the trajectory helps the designer build an understanding of the movement of the impeller in response to any number of applied disturbances such that the design can be altered to prevent any adverse outcomes that may occur as a result. To maintain accuracy and stability of the Runge-Kutta method, the non-dimensional time step should be kept below $\Delta t^* = 0.5^\circ$.

Under most tested operating conditions, a high level of damping was present and the trajectory of the impeller settled very quickly to either a point in response to an initial disturbance, or to a limit cycle in response to an unbalance force or “shaking” of the pump housing. Only for test case TC4, where the rotational speed of the impeller was 500 RPM and the impeller was subjected to shaking of the pump housing in the X-direction, did the impeller trajectory oscillate in an unstable manner and contain a frequency component of 0.5ω within the eccentricity signal.

Chapter 6 – Future directions

The most obvious next step is to perform a more detailed study using the simplified impeller geometry used in this study such that a stability map, which outlines the regions of stability and instability, can be created. This would be most useful to the design engineer.

It is recommended that *Orbit3D* be extended such that geometry files exported from commercially available CAD programs (such as Pro/Engineer etc.) may be imported into *Orbit3D* and subsequently analysed. In this way, impellers containing complex geometry, such as current models of the VentrAssist impeller, may be analysed and rated in comparison to other models.

Additional characteristics that should be analysed in the future include a radial taper as described by Kalita *et al.* [36, 37], and a power-shaped circumferential taper as described by Agrawal [25]. A radial taper on the conical journal bearing would be interesting because, in theory, it would increase stiffness at the top of the bearing. With respect to current models of the impeller, the azimuthal velocity at the inner diameter of the conical journal bearing is somewhat less than that at the outer radius of the bearing. That is, $U_\theta = \omega\rho_1 \sin\alpha$ at $\rho = \rho_1$ and $U_\theta = \omega\rho_2 \sin\alpha$ at $\rho = \rho_2$. As a consequence of this, the restoring force at the inner radius will be less than that at the outer radius for an arbitrary displacement of the impeller towards the pump housing. By employing a linear radial taper such that the nominal film thickness at the inner radius of the conical journal bearing is less than that at the outer radius, then it is possible to make the restoring forces equal, possibly making the bearing more stable.

Furthermore, a power-shaped circumferential taper to replace the taper land configuration may have a stabilising effect.

As previously recommended, the drag force on the impeller should be included in a future study such that all forces on the impeller are considered. This friction force is thought to have a stabilising effect. Other forces that should be included are the magnetic force exerted on the permanent magnets contained within the impeller blades and a force (and moment) on the impeller due to expansion of the blood within the pump volute.

Additional variables that would be of interest include the power loss, heat production, shear rate, friction factor, etc., which can all easily be incorporated into *Orbit3D*.

Reference

1. Nosé Y, Yoshikawa M, Murabayashi S, and Takano T. Development of rotary blood pump technology: past, present and future. *Artificial Organs* 2000; 24(6):412-420.
2. Rowles JR, Mortimer BJ and Olsen DB. Ventricular assist and total artificial heart devices for clinical use in 1993. *ASAIO Journal* 1993; 840-855.
3. Hart RM, Filipenco VG and Kung RTV. A magnetically suspended and hydrostatically stabilized centrifugal blood pump. *Artificial Organs* 1996; 20(6):591-596.
4. Ming Chen H, Smith WA, and Walton JF. High efficiency magnetic bearing for a rotary blood pump. *ASAIO Journal* 1998; 44:M728-M732.
5. Nosé Y. Design and development strategy for the rotary blood pump. *Artificial Organs* 1998; 22(6):438-446.
6. Yoshikawa M, Nakata K, Ohtsuka G, Takano T, Glueck J, Fujisawa A, Makinouchi K, Yokokawa M, and Nosé Y. Feasibility of a tiny gyro centrifugal pump as an implantable ventricular assist device. *Artificial Organs* 1999; 23(8):774-779.
7. Wampler R, Lancisi D, Indravudh V, Gauthier R, and Fine R. A sealless centrifugal blood pump with passive magnetic and hydrodynamic bearings. *Artificial Organs* 1999; 23(8):780-784.
8. Kung RTM, and Hart RM. Design considerations for bearingless rotary pumps. *Artificial Organs* 1997; 21(7):645-650.
9. Bearson GB, Olsen DB, Khanwilkar PS, Long JW, Sinnott M, Kumar A, Allaire PE, Baloh M, and Decker J. Implantable centrifugal pump with hybrid magnetic bearings. *ASAIO Journal* 1998; 44:M733-M736.

-
10. Watterson PA, Woodard JC, Ramsden VS, and Reizes JA. VentrAssist hydrodynamically suspended, open, centrifugal blood pump. *Artificial Organs* 2000; 24(6):475-477.
 11. Masuzawa T, Kita T, Matsuda K, and Okada Y. Magnetically suspended rotary blood pump with radial type combined motor bearing. *Artificial Organs* 2000; 24(6):468-474.
 12. Khanwilkar P, Olsen D, Bearson G, Allaire P, Maslen E, Flack R, and Long J. Using hybrid magnetic bearings to completely suspend the impeller of a ventricular assist device. *Artificial Organs* 1996; 20(6):597-604.
 13. Cameron A and Ettles CMMCC. Basic lubrication theory, 3rd Edition. Ellis Horwood Limited, 1981.
 14. Agrawal GL. Stability of rotors in compressible fluid-film bearings. *Journal of Propulsion* 1988; 4(5):437-444.
 15. Akköt M and Ettles CMMCC. The onset of whirl instability in journal bearings of various bore shapes and groove sizes. *Journal of Lubrication Technology* 1983; 105:342-352.
 16. Stachowiak GW and Batchelor AW. Engineering Tribology. Elsevier Science Publishers B.V. 1993.
 17. Makdissi J. A theoretical and experimental study into the dynamic characteristics of a hydrodynamic oil film bearing. PhD Thesis 1980.
 18. Holms R. Non-linear performance of turbine bearings. J.M.E.S. 1970; 12(6):377.
 19. Crosby WA. The stability of a rigid rotor in ruptured finite journal bearings. *Wear* 1982; 80:333-346.
 20. Pai R and Majumdar BC. Stability of submerged oil journal bearings under dynamic load. *Wear* 1991; 146:125-135.
 21. Pai R and Majumdar BC. Theoretical analysis on conical whirl instability of unloaded submerged oil journal bearings. *Wear* 1992; 52:309-316.
 22. Cameron A. The principles of lubrication. Longmans Green and Co Ltd 1966.
-

-
23. Qian Yi and Bertram CD. Computational fluid dynamics analysis of hydrodynamic bearings of the VentrAssist rotary blood pump. *Artificial Organs* 2000; 24(6):488-491.
 24. Kreyszig E. Advanced engineering mathematics, 7th Edition. John Wiley & Sons, Inc. 1993.
 25. Agrawal GL. Analysis of power-shaped multipad hydrodynamic conical gas bearings. *Tribology Transactions* 1993; 36(2):240-248.
 26. Fitzpatrick JB. New senior mathematics: three unit course for years 11 and 12. Rigby Heinemann 1995.
 27. Anderson JD. Computational fluid dynamics: the basics with applications. McGraw-Hill, Inc. 1995.
 28. Anderson DA, Tannehill JC, and Pletcher RH. Computational fluid mechanics and heat transfer. McGraw-Hill, Inc. 1984.
 29. Versteeg HK and Malalasekera W. An introduction to computational fluid dynamics: the finite volume method. Longman Group Ltd 1999.
 30. Roache PJ. Fundamentals of computational fluid dynamics. Hermosa Publishers 1998.
 31. Bertram CD, Qian Y, and Reizes JA. Computational fluid dynamics performance predication for the hydrodynamic bearings of the VentrAssist rotary blood pump. *Artificial Organs* 2001; 25(5):348-357.
 32. Gerald CF and Wheatley PO. Applied numerical analysis, 3rd Edition. Addison-Wesley Publishing Company 1985.
 33. Meriam JL and Kraige LG. Engineering mechanics (Volume 2 – Dynamics), 3rd Edition. John Wiley & Sons, Inc. 1993.
 34. Schwarz HR. Numerical analysis: a comprehensive introduction. John Wiley & Sons, Inc. 1989.
 35. Pinkus O, Lynn W. Solution of the tapered-land sector thrust bearing. *Trans. ASME* 1958; 80:1510-1516.
-

36. Kalita W, Rodkiewicz CzM, Kennedy JS. On the laminar flow characteristics of conical bearings: part I – analytical approach. *Journal of Tribology* 1986; 108:53-58.
37. Kalita W, Rodkiewicz CzM, Kennedy JS. On the laminar flow characteristics of conical bearings: part II – experimental verification. *Journal of Tribology* 1986; 108:59-64.

APPENDIX A – The Thomas Algorithm

Consider a system of equations that has the following form

$$a_1\phi_1 + b_1\phi_2 + c_1\phi_3 = d_1 \quad (\text{A.1a})$$

$$a_2\phi_2 + b_2\phi_3 + c_2\phi_4 = d_2 \quad (\text{A.1b})$$

$$a_3\phi_3 + b_3\phi_4 + c_3\phi_5 = d_3 \quad (\text{A.1c})$$

...

$$a_{I-2}\phi_{I-2} + b_{I-2}\phi_{I-1} + c_{I-2}\phi_I = d_{I-2} \quad (\text{A.1d})$$

where ϕ is any general variable (i.e. pressure p). For Dirichlet boundary conditions ϕ_1 is known at one boundary and ϕ_2 at the other. The general form of any single equation can be written as

$$a_{i-1}\phi_{i-1} + b_{i-1}\phi_i + c_{i-1}\phi_{i+1} = d_{i-1} \quad i=2,\dots,I-1 \quad (\text{A.2})$$

In order to apply the Thomas algorithm, equations (A.1a) – (A.1d) are rewritten as

$$\begin{aligned} b_1 \phi_2 &+ c_1 \phi_3 &= d_1^* \\ a_{i-1} \phi_{i-1} &+ b_{i-1} \phi_i &+ c_{i-1} \phi_{i+1} &= d_{i-1} \quad i = 3, \dots, I-2 \\ a_{I-2} \phi_{I-2} &+ b_{I-2} \phi_{I-1} &= d_{I-2}^* \end{aligned} \tag{A.3}$$

where

$$d_1^* = d_1 - a_1 \phi_1$$

$$d_{I-2}^* = d_{I-2} - c_{I-2}\phi_I$$

Equations (A.1a) – (A.1c) can be rewritten in terms of surrounding nodal values

$$\phi_2 = \frac{d_1^* - c_1 \phi_3}{b_1} \quad (\text{A.4a})$$

$$\phi_3 = -\frac{c_2}{b_2}\phi_4 - \frac{a_2}{b_2}\phi_2 + \frac{d_2}{b_2} \quad (\text{A.4b})$$

$$\phi_4 = -\frac{c_3}{b_3}\phi_5 - \frac{a_3}{b_3}\phi_3 + \frac{d_3}{b_3} \quad (\text{A.4c})$$

These equations can be solved by forward elimination and subsequent back-substitution. The forward elimination process starts with removing ϕ_2 from equation (A.4b) by substitution of equation (A.4a) and then solving in terms of ϕ_3

$$\phi_3 = -\frac{c_2}{b_2} \phi_4 - \frac{a_2}{b_2} \left(\frac{d_1^* - c_1 \phi_3}{b_1} \right) + \frac{d_2}{b_2} \quad (\text{A.5})$$

which yields

$$\phi_3 = \begin{pmatrix} -c_2 \\ b_2 - \frac{a_2}{b_1} c_1 \end{pmatrix} \phi_4 + \begin{pmatrix} d_2 - \frac{a_2}{b_1} d_1^* \\ b_2 - \frac{a_2}{b_1} c_1 \end{pmatrix} \quad (\text{A.6})$$

Adopting the notation

$$\beta_1 = b_1$$

$$\delta_1 = d_1^*$$

$$\beta_2 = b_2 - \frac{a_2}{b_1} c_1 = b_2 - \frac{a_2}{\beta_1} c_1 \quad (\text{A.7})$$

$$\delta_2 = d_2 - \frac{a_2}{b_1} d_1^* = d_2 - \frac{a_2}{\beta_1} \delta_1$$

then equation (A.4a) can be rewritten as

$$\phi_2 = \frac{\delta_1 - c_1 \phi_3}{\beta_1} \quad (\text{A.8})$$

and equation (A.6) can be rewritten in similar form as

$$\phi_3 = \begin{pmatrix} -c_2 \\ \beta_2 \end{pmatrix} \phi_4 + \begin{pmatrix} \delta_2 \\ \beta_2 \end{pmatrix} = \frac{\delta_2 - c_2 \phi_4}{\beta_2} \quad (\text{A.9})$$

Equation (A.9) is then substituted into equation (A.4c) to eliminate ϕ_3 . That is,

$$\phi_4 = -\frac{c_3}{b_3} \phi_5 - \frac{a_3}{b_3} \left(\frac{\delta_2 - c_2 \phi_4}{\beta_2} \right) + \frac{d_3}{b_3} \quad (\text{A.10})$$

which yields

$$\phi_4 = \begin{pmatrix} -c_3 \\ b_3 - \frac{a_3}{\beta_2} c_2 \end{pmatrix} \phi_5 - \begin{pmatrix} d_3 - \frac{a_3}{\beta_2} \delta_2 \\ b_3 - \frac{a_3}{\beta_2} c_2 \end{pmatrix} \quad (\text{A.11})$$

Substituting

$$\begin{aligned} \beta_3 &= b_3 - \frac{a_3}{\beta_2} c_2 \\ \delta_3 &= d_3 - \frac{a_3}{b_2} \delta_2 \end{aligned} \quad (\text{A.12})$$

equation (A.11) can then be rewritten as

$$\phi_4 = \begin{pmatrix} -c_3 \\ \beta_3 \end{pmatrix} \phi_5 - \begin{pmatrix} \delta_3 \\ \beta_3 \end{pmatrix} = \frac{\delta_3 - c_3 \phi_5}{\beta_3} \quad (\text{A.13})$$

As can be seen from equations (A.7) and (A.12), the forward-elimination process consists of, in general terms,

$$\beta_i = b_i - \frac{a_i}{\beta_{i-1}} c_{i-1} \quad i = 2, \dots, I-2 \quad (\text{A.14})$$

and

$$\delta_i = d_i - \frac{a_i}{b_{i-1}} \delta_{i-1} \quad i = 2, \dots, I-3 \quad (\text{A.15})$$

This procedure is repeated up to the last equation of the set where

$$\delta_{I-2} = d_{I-2}^* - \frac{a_{I-2}}{b_{I-3}} \delta_{I-3} \quad (\text{A.16})$$

The back-substitution procedure consists of

$$\phi_{I-1} = \frac{\delta_{I-2}}{\beta_{I-2}} \quad (\text{A.17})$$

and more generally

$$\phi_i = \frac{\delta_{i-1} - c_{i-1}\phi_{i+1}}{\beta_{i-1}} \quad i = I-2, I-3, \dots, 2 \quad (\text{A.18})$$

More formally, the Thomas algorithm consists of

- (1) Tridiagonalisation of algebraic equations (dropping the asterisk notation)

$$d_1 = d_1 - a_1\phi_1$$

$$d_{I-2} = d_{I-2} - a_{I-2}\phi_I$$

- (2) Forward elimination process

$$\beta_1 = b_1$$

$$\delta_1 = d_1$$

$$\left. \begin{aligned} \beta_i &= b_i - \frac{a_i}{\beta_{i-1}} c_{i-1} \\ \delta_i &= d_i - \frac{a_i}{b_{i-1}} \delta_{i-1} \end{aligned} \right\} \quad i = 2, \dots, I-2$$

- (3) Back-substitution process

$$\phi_{n-1} = \frac{\delta_{n-2}}{\beta_{n-2}}$$

$$\phi_i = \frac{\delta_{i-1} - c_{i-1}\phi_{i+1}}{\beta_{i-1}} \quad i = I-2, I-3, \dots, 2$$

A FORTRAN subroutine for this procedure is given in Appendix B.

APPENDIX B – The Thomas Algorithm FORTRAN subroutine

```
SUBROUTINE THOMAS (NN,A,B,C,D,MAX)
C -----
C |           *** FOR SOLVING A TRIDIAGONAL SYSTEM ***
C |
C -----
C =====
C     EXAMPLE OF USE:
C
C     *** DIRICHLET BOUNDARY CONDITION ***
C     (Where NX: => number of grid points
C      MAX:=> maximum possible array size)
C
C     NXM1=NX-1
C     NXM2=NX-2
C
C     DO 10 I=2, NXM1
C
C         A(I-1) = ....
C         B(I-1) = ....
C         C(I-1) = ....
C         D(I-1) = ....
C
C 10  CONTINUE
C
C     CALL THOMAS (NXM2,A,B,C,D,MAX)
C
C     DO 20 I=2, NXM1
C         SOLUTION(I) = D(I-1)
C 20  CONTINUE
C
C =====
C
DIMENSION A(MAX),B(MAX),C(MAX),D(MAX)
B(1)=1.0/B(1)

DO 10 I=2,NN
    B(I)=1.0/(B(I)-A(I)*B(I-1)*C(I-1))
    D(I)=D(I)-A(I)*B(I-1)*D(I-1)
10 CONTINUE

D(NN)=D(NN)*B(NN)

DO 20 I=NN-1,1,-1
    D(I)=(D(I)-D(I+1)*C(I))*B(I)
20 CONTINUE

RETURN
END
```

APPENDIX C – Analysis of a rectangular tilting thrust bearing

This Appendix verifies the solution method outlined in section 3.4. through comparison with the results listed by Cameron [22] for the solution to the hydrodynamic pressure distribution over a rectangular tilting thrust bearing and other derived quantities which include the load capacity, location of pivot point, friction force and leakage flows. The FORTRAN program “tb2d.f” used to perform the numerical calculations is listed in Appendix E.

The tilting thrust bearing considered in this study is rectangular of breadth B in the x-direction and length L in the y-direction. The bearing upper surface is tapered such that the film thickness at any point h is given by

$$h = h_1 - (h_1 - h_0) \frac{x}{B} \quad (\text{C.1})$$

where h_1 is the inlet (maximum) film thickness and h_0 is the outlet (minimum) film thickness. The x-y-z coordinate system is such that

$$\begin{aligned} z &= h = h_1 \text{ at } (x = 0, 0 \leq y \leq L) \\ z &= h = h_0 \text{ at } (x = B, 0 \leq y \leq L) \end{aligned} \quad (\text{C.2})$$

The non-dimensional film thickness at any point $h^* = h/h_0$ is given by the expression

$$h^* = 1 + K(1 - x^*) \quad (\text{C.3})$$

where $K = h_1/h_0 - 1$ and $x^* = x/B$.

The steady form of the two-dimensional Reynolds equation can be derived from equation (3.20) by the substitution of $\partial h/\partial t = 0$, yielding

$$\frac{\partial}{\partial x} \left(h^3 \frac{\partial p}{\partial x} \right) + \frac{\partial}{\partial y} \left(h^3 \frac{\partial p}{\partial y} \right) = 6\eta \left((U_{x,2} - U_{x,1}) \frac{\partial h}{\partial x} + (U_{y,2} - U_{y,1}) \frac{\partial h}{\partial y} \right) \quad (\text{C.4})$$

where $U_{x,1}$ and $U_{x,2}$ are the velocities of the upper and lower bounding surfaces in the x-direction respectively, $U_{y,1}$ and $U_{y,2}$ are the velocities of the upper and lower bounding surfaces in the y-direction respectively, and p is the hydrodynamic pressure. For this study, the lower non-tapered bounding surface moves in the x-direction with velocity U . Therefore, $U_{x,2} = U$ and $U_{x,1} = U_{y,1} = U_{y,2} = 0$ and equation (C.4) becomes

$$\frac{\partial}{\partial x} \left(h^3 \frac{\partial p}{\partial x} \right) + \frac{\partial}{\partial y} \left(h^3 \frac{\partial p}{\partial y} \right) = 6\eta U \frac{\partial h}{\partial x} \quad (\text{C.5})$$

On substitution of the following non-dimensional terms,

$$x^* = \frac{x}{B}, \quad y^* = \frac{y}{L}, \quad h^* = \frac{h}{h_0}, \quad \text{and} \quad p^* = \frac{h_0^2}{6U\eta B} p \quad (\text{C.6})$$

equation (C.5) becomes

$$\frac{\partial}{\partial x^*} \left(h^{*3} \frac{\partial p^*}{\partial x^*} \right) + \left(\frac{B}{L} \right)^2 \frac{\partial}{\partial y^*} \left(h^{*3} \frac{\partial p^*}{\partial y^*} \right) = \frac{\partial h^*}{\partial x^*} \quad (\text{C.7})$$

where $\frac{\partial h^*}{\partial x^*} = -K$. Equation (C.7) is the non-dimensional form of the two-dimensional steady Reynolds equation which governs the non-dimensional pressure distribution over the tilted thrust bearing.

A structured grid was established over the bearing surface where the spacings of grid points in the x- and y- directions was uniform and given by Δx and Δy respectively. The grid points are identified by index $i = 1, 2, \dots, I$ in the x-direction and $j = 1, 2, \dots, J$ in the y-direction. Dropping the asterisk notation, but remembering that the terms

remain non-dimensional, equation (C.7) was discretised using the following second-order central finite difference equations [26]

$$\begin{aligned} \left. \frac{\partial p}{\partial x} \right|_{i,j} &\approx \frac{p_{i+1,j} - p_{i-1,j}}{2\Delta x}, \quad \left. \frac{\partial p}{\partial y} \right|_{i,j} \approx \frac{p_{i,j+1} - p_{i,j-1}}{2\Delta y} \\ \left. \frac{\partial^2 p}{\partial x^2} \right|_{i,j} &\approx \frac{p_{i-1,j} - 2p_{i,j} + p_{i+1,j}}{\Delta x^2}, \quad \left. \frac{\partial^2 p}{\partial y^2} \right|_{i,j} \approx \frac{p_{i,j-1} - 2p_{i,j} + p_{i,j+1}}{\Delta y^2} \end{aligned} \quad (\text{C.8})$$

Upon substitution of equation set (C.8), equation (C.7) can be written in the form of equation (3.103) for sweeps by j rows for $j = 2, 3, \dots, J-1$ using the Thomas algorithm. That is,

$$a_{i-1} p_{i-1,j}^{n+\frac{1}{2}} + b_{i-1} p_{i,j}^{n+\frac{1}{2}} + c_{i-1} p_{i+1,j}^{n+\frac{1}{2}} = d_{i-1} \quad (\text{C.9})$$

for $i = 2, 3, \dots, I-1$ where

$$\begin{aligned} a_{i-1} &= \frac{1}{\Delta x} \left(\frac{1}{\Delta x} + \frac{1.5K}{h_i} \right) \\ b_{i-1} &= -2 \left(\frac{1}{\Delta x^2} + \frac{1}{\Delta y^2} \left(\frac{B}{L} \right)^2 \right) \\ c_{i-1} &= \frac{1}{\Delta x} \left(\frac{1}{\Delta x} - \frac{1.5K}{h_i} \right) \\ d_{i-1} &= \frac{-K}{h_i^3} - \frac{1}{\Delta y^2} \left(\frac{B}{L} \right)^2 p_{i,j-1}^{n+\frac{1}{2}} - \frac{1}{\Delta x^2} \left(\frac{B}{L} \right)^2 p_{i,j+1}^n \end{aligned}$$

For subsequent sweeps by i columns for $i = 2, 3, \dots, I-1$, the discretised form of equation (C.7) may be written in the form of equation (3.104) as

$$a_{j-1} p_{i,j-1}^{n+1} + b_{j-1} p_{i,j}^{n+1} + c_{j-1} p_{i,j+1}^{n+1} = d_{j-1} \quad (\text{C.10})$$

for $j = 2, 3, \dots, J-1$ where

$$a_{j-1} = \frac{1}{\Delta y^2} \left(\frac{B}{L} \right)^2$$

$$b_{j-1} = -2 \left(\frac{1}{\Delta x^2} + \frac{1}{\Delta y^2} \left(\frac{B}{L} \right)^2 \right)$$

$$c_{j-1} = \frac{1}{\Delta y^2} \left(\frac{B}{L} \right)^2$$

$$d_{j-1} = \frac{-K}{h_i^3} - \frac{1}{\Delta x} \left(\frac{1}{\Delta x} + \frac{1.5K}{h_i} \right) p_{i-1,j}^{n+1} - \frac{1}{\Delta x} \left(\frac{1}{\Delta x} - \frac{1.5K}{h_i} \right) p_{i+1,j}^{n+\frac{1}{2}}$$

(a) Load capacity

The total load that the bearing will support at a specified film geometry is obtained by integrating the pressure distribution over the bearing area. That is,

$$W = \iint_A p dA = \int_0^L \int_0^B p dx dy \quad (\text{C.11})$$

Substitution of the non-dimensional variables of equation set (C.6) yields

$$W = \int_0^L \int_0^B \left(\frac{6U\eta B}{h_0^2} p^* \right) d(Bx^*) d(Ly^*)$$

which simplifies to

$$W^* = \int_0^1 \int_0^1 p^* dx^* dy^* \quad (\text{C.12})$$

where $W^* = \frac{Wh_0^2}{6U\eta B^2 L}$ is the non-dimensional load capacity. The double integral of

equation (C.12) was solved numerically using the trapezoidal rule as outlined in Appendix F.

(b) *Location of pivot point*

The location of the pivot point (or the x coordinate of the “centre of pressure”) is given by

$$X = \frac{\int_0^L \int_0^B x p dx dy}{\int_0^L \int_0^B p dx dy} = \frac{\int_0^L \int_0^B x p dx dy}{W} \quad (\text{C.13})$$

On substitution of the non-dimensional variables this becomes

$$X^* = \frac{\int_0^1 \int_0^1 x^* p^* dx^* dy^*}{W^*} \quad (\text{C.14})$$

where $X^* = X/B$. The double integral of equation (C.14) was evaluated using the trapezoidal rule outlined in Appendix F.

(c) *Friction force*

The shear stress in the x-direction on the bounding surfaces is given by equation (3.2a) to be

$$\tau = \eta \frac{\partial u}{\partial z} \quad (\text{C.15})$$

which, upon substitution of equation (3.6) with $U_{x,1} = 0$ and $U_{x,2} = U$, becomes

$$\tau = \frac{\partial p}{\partial x} \left(z - \frac{h}{2} \right) - \frac{\eta U}{h} \quad (\text{C.16})$$

The shear on the lower surface τ_0 is given by the substitution of $z = 0$, which yields

$$\tau_0 = -\frac{\partial p}{\partial x} \frac{h}{2} - \frac{\eta U}{h} \quad (\text{C.17})$$

The shear on the upper surface τ_h is given by the substitution of $z = h$, which yields

$$\tau_h = \frac{\partial p}{\partial x} \frac{h}{2} - \frac{\eta U}{h} \quad (\text{C.18})$$

The shear stress is usually quoted as

$$\tau_{h,0} = \pm \frac{\partial p}{\partial x} \frac{h}{2} - \frac{\eta U}{h} \quad (\text{C.19})$$

where the positive sign in the $\partial p / \partial x$ term corresponds to τ_h and the negative sign corresponds to τ_0 .

The friction force on the upper and lower bounding surfaces is the integral of the shear stress over the pad area. That is,

$$F_{h,0} = \int_0^L \int_0^B \tau_{h,0} dx dy \quad (\text{C.20})$$

Substitution of equation (C.19) into equation (C.20) yields

$$F_{h,0} = \int_0^L \int_0^B \left(\pm \frac{\partial p}{\partial x} \frac{h}{2} - \frac{\eta U}{h} \right) dx dy \quad (\text{C.21})$$

Substitution of the non-dimensional terms of equation set (C.6) yields

$$F_{h,0} = \int_0^L \int_0^B \left\{ \pm \frac{\partial}{\partial(Bx^*)} \left(\frac{6UB\eta}{h_0^2} p^* \right) \frac{(h_0 h^*)}{2} - \frac{\eta U}{(h_0 h^*)} \right\} d(Bx^*) d(Ly^*)$$

which simplifies to

$$F_{h,0} = \frac{LB\eta U}{h_0} \int_0^1 \int_0^1 \left\{ \pm 3h^* \frac{\partial p^*}{\partial x^*} - \frac{1}{h^*} \right\} dx^* dy^* \quad (\text{C.22})$$

and further to

$$F_{h,0}^* = \int_0^1 \int_0^1 \left\{ \pm 3h^* \frac{\partial p^*}{\partial x^*} - \frac{1}{h^*} \right\} dx^* dy^* \quad (\text{C.23})$$

where $F_{h,0}^* = \frac{F_{h,0}h_0}{LB\eta U}$ is the non-dimensional friction force. The finite difference approximation to $\partial p^*/\partial x^*$ given in equation set (C.8) was used to represent this same pressure gradient term in equation (C.23). The double integral of equation (C.23) was subsequently solved using the trapezoidal rule outlined in Appendix F.

(d) Leakage flow

i. Side-leakage

The side-leakage is the flow leaking from the sides of the pad, where $x=0$ and $x=B$ over the range $0 \leq y \leq L$. With reference to equation (3.11) with $U_{y,1} = U_{y,2} = 0$, the side-leakage is given by the integral of the flow per unit breadth over the breadth of the pad. That is,

$$Q_s = \int_0^B q_y \Big|_{y=0}^{y=L} dx = \int_0^B \left(-\frac{h^3}{12\eta} \frac{\partial p}{\partial y} \right) \Big|_{y=0}^{y=L} dx \quad (\text{C.24})$$

Substituting the non-dimensional terms of equation set (C.6) yields

$$Q_s = \int_0^B \left\{ -\frac{(h_0 h^*)^3}{12\eta} \frac{\partial}{\partial(Ly^*)} \left(\frac{6U\eta B}{h_0^2} p^* \right) \right\} \Big|_{y=0}^{y=L} d(Bx^*)$$

which simplifies to

$$Q_s = -\frac{UB^2 h_0}{2L} \int_0^1 \left(h^{*3} \frac{\partial p^*}{\partial y^*} \right) \Big|_{y^*=0}^{y^*=1} dx^* \quad (\text{C.25})$$

The side-leakage may be non-dimensionalised by $Q_s^* = Q_s / UBh_0$ and equation (C.25) can therefore be written as

$$Q_s^* = -\frac{1}{2} \left(\frac{B}{L} \right) \int_0^1 \left(h^{*3} \frac{\partial p^*}{\partial y^*} \right)_{y^*=0}^{y^*=1} dx^* \quad (\text{C.26})$$

Alternatively, the non-dimensional side-leakage can be written as

$$Q_s^* = -\left(\frac{B}{L} \right) \int_0^1 \left(h^{*3} \frac{\partial p^*}{\partial y^*} \right)_{y^*=0,1} dx^* \quad (\text{C.27})$$

which, since the pressure profile is symmetric about $y^* = 1/2$, is twice the side-leakage at either side of the pad, where $y^* = 0$ or $y^* = 1$.

Dropping the asterisk notation, a one-sided second-order finite difference was used to represent the pressure gradient term in equation (C.27) [26].

Evaluating equation (C.27) at the side where $y^* = 0$, this finite difference is

$$\left. \frac{\partial p}{\partial y} \right|_{i,1} = \frac{-3p_{i,1} + 4p_{i,2} - p_{i,3}}{2\Delta y} + O(\Delta y)^2 \quad (\text{C.28})$$

for $i = 1, 2, \dots, I$.

The single integral of equation (C.22) was evaluated using the trapezoidal rule of integration [31].

ii. End-leakage

The end-leakage is the flow leaking from the trailing edge of the pad. With reference to equation (3.10), the end-leakage is the integral of the flow per unit length over the length of the bearing evaluated at the trailing edge. That is,

$$Q_e = \int_0^L q_x \Big|_{x=B} dy = \int_0^L \left\{ \frac{Uh}{2} - \frac{h^3}{12\eta} \frac{\partial p}{\partial x} \right\} \Big|_{x=B} dy \quad (\text{C.29})$$

Substitution of the non-dimensional terms of equation set (C.6) yields

$$Q_e = \int_0^L \left\{ \frac{U(h_0 h^*)}{2} - \frac{(h_0 h^*)^3}{12\eta} \frac{\partial}{\partial(Bx^*)} \left(\frac{6UB\eta}{h_0^2} p^* \right) \right\} \Big|_{x=B} d(Ly^*)$$

which simplifies to

$$Q_e = \frac{ULh_0}{2} \int_0^1 \left\{ h^* - h^{*3} \frac{\partial p^*}{\partial x^*} \right\} \Big|_{x^*=1} dy^* \quad (\text{C.30})$$

The end-leakage can be non-dimensionalised by $Q_e^* = Q_e / Uh_0 B$ and therefore can be written as

$$Q_e^* = \frac{1}{2} \left(\frac{L}{B} \right) \int_0^1 \left\{ h^* - h^{*3} \frac{\partial p^*}{\partial x^*} \right\} \Big|_{x^*=1} dy^* \quad (\text{C.31})$$

Similar to the side-flow, a one-sided second-order finite difference equation was used to represent the pressure gradient term in equation (C.31). That is, for $j = 1, 2, \dots, J$ [26],

$$\frac{\partial p}{\partial x} \Big|_{I,j} = \frac{3p_{I,j} - 4p_{I-1,j} + p_{I-2,j}}{2\Delta x} + O(\Delta x)^2 \quad (\text{C.32})$$

The single integral of equation (C.31) was evaluated using the trapezoidal rule of integration [31].

The load capacity, location of pivot point, friction force, side leakage and end leakage were obtained for various values of L/B using program “tb2d.f” with a grid size of

$I \times J = 31 \times 31$. The results are compared with those tabulated in Cameron [22] in Table C.1. below and clearly indicate that the solution method is accurate to within approximately 2 percent of those results given by Cameron.

L/B	Cameron					This work				
	$6W^*$	X^*	F^*	Q_s^*	Q_e^*	$6W^*$	X^*	F^*	Q_s^*	Q_e^*
2.00	0.1096	0.5730	0.7480	0.2589	1.272	0.1103	0.5734	0.7479	0.2691	1.253
1.50	0.09457	0.5756	0.7404	0.2586	0.935	0.09497	0.5759	0.7403	0.2665	0.921
1.00	0.06894	0.5818	0.7276	0.2462	0.6011	0.06912	0.5819	0.7274	0.2507	0.5922
0.75	0.05037	0.5838	0.7183	0.2229	0.4403	0.05055	0.5885	0.7181	0.2276	0.4319
0.50	0.02892	0.6005	0.7076	0.1788	0.2847	0.02908	0.6011	0.7074	0.1830	0.2775

Table C.1. Comparison of results for rectangular tilting thrust bearing

APPENDIX D – Grid independence study

This Appendix is an extension of the study performed in Appendix C. Herein the solution obtained for the pressure distribution over the tilting thrust bearing is shown to be independent of the size of the numerical grid employed. FORTRAN program “tb2d.f” employed to perform the numerical calculations is given in Appendix E.

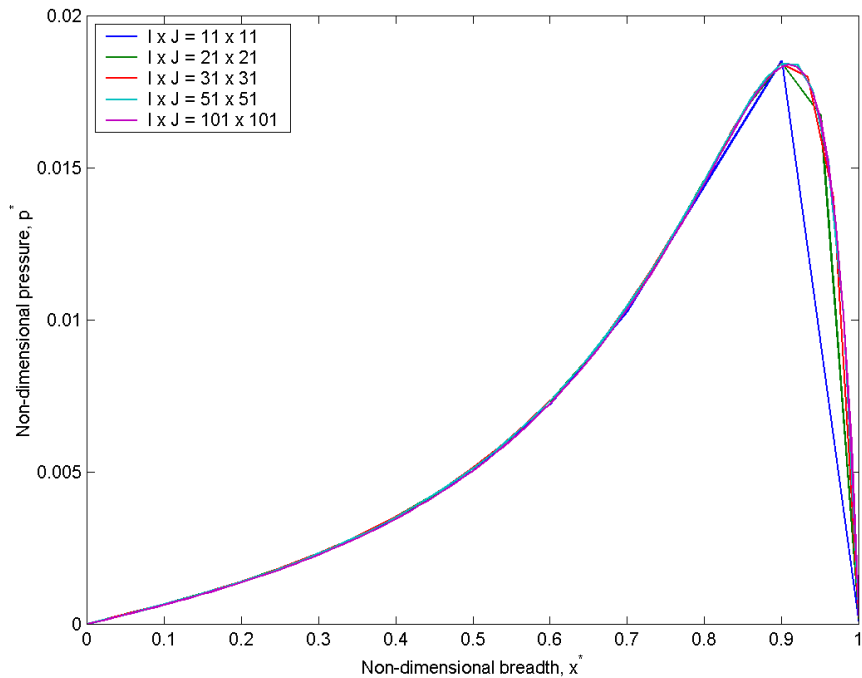


Figure D.1. Non-dimensional pressure profile along the mid-plane over the breadth of the bearing

Tests were performed using grid sizes of $I \times J = 11 \times 11$, 21×21 , 31×31 , 51×51 , and 101×101 for $L/B = 1.0$ and $K = 8$. The profiles of the non-dimensional pressure p^* and non-dimensional pressure gradient $\partial p^* / \partial x^*$ were plotted over the mid-plane along the breadth of the bearing i.e. $y^* = 0.5$ for $0.0 \leq x^* \leq 1.0$ and shown in Figures D.1 and D.2. These figures indicate that a grid size of $I \times J = 31 \times 31$ provides a grid independent solution as indicated by the fact that increasing the number of grid points

beyond this size results in approximately the same values of the plotted variables.

Thus the use of a grid size of $I \times J = 31 \times 31$ throughout this work is justified.

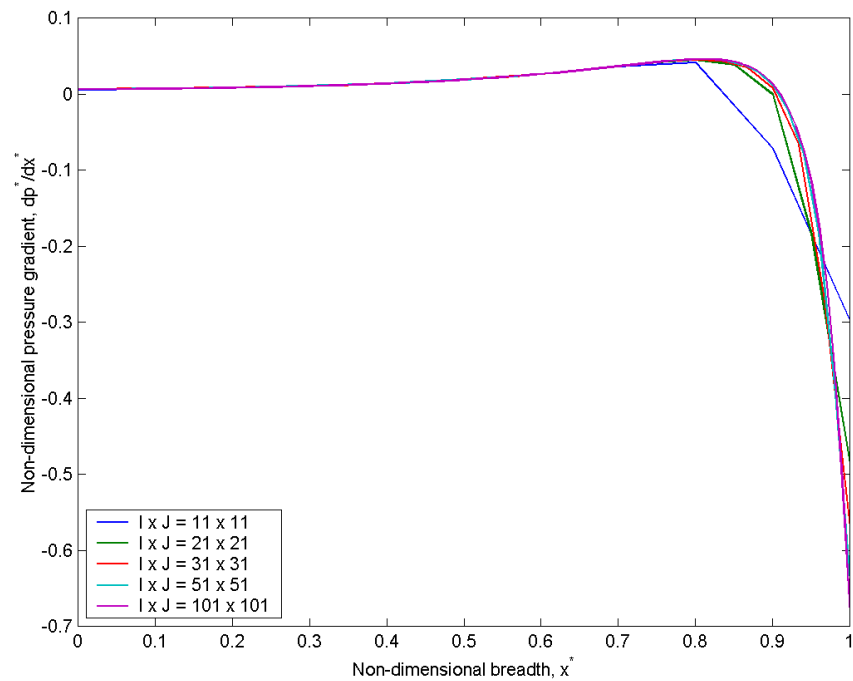


Figure D.2. The non-dimensional pressure gradient on the mid-plane over the breadth of the bearing

APPENDIX E – FORTRAN program “tb2d.f”

```

PROGRAM TB2D

C This program computes the pressure distribution and several derived
C quantities for a finite tilting thrust bearing of rectangular shape.
C Calculations can be performed for different L/B ratios.

C X(I)      = position along x-axis (ie. x coordinate)
C Y(J)      = position along y-axis (ie. y coordinate)
C NX        = number of mesh points along x-axis, I
C NY        = number of mesh points along y-axis, J
C P(I,J)    = Pressure at node i,j at latest iteration level
C PPI(I,J)  = Pressure at node i,j at the previous iteration
C H(I)      = film thickness at node i,j
C LB        = L/B ratio
C K         = H1/H0-1
C H1        = leading edge (maximum) film thickness
C H0        = trailing edge (minimum) film thickness
C NDLOAD    = Non-dimensional load capacity
C QX(J)    = Flow-rate per unit length in the x-direction at node NX,j (or I,j)
C QY(I)    = Flow-rate per unit breadth in the y-direction at node i,1
C QE        = End-leakage (evaluated at the trailing edge)
C QS        = Side-leakage (evaluated at y* = 0.0)
C DPDX(I,J) = Pressure gradient in the x-direction at node i,j
C DPDY(I,J) = Pressure gradient in the y-direction at node i,j
C TORX0(I,J) = Shear stress on the lower surface in the x-direction at node i,j
C TORXH(I,J) = Shear stress on the upper surface in the x-direction at node I,j
C FFO       = Friction force on the lower surface
C FFH       = Friction force on the upper surface
C XBAR     = Location of the pivot point
C FOR       = Successive over-relaxation factor

C Declaration of variables
PARAMETER (N = 501, NTOTAL=N*N, PI=3.141592654, FOR=1.5)
DOUBLE PRECISION K, LB, DX, DY, DX2, DY2, BL2
DOUBLE PRECISION X(N), Y(N), H(N), PPI(N,N), P(N,N)
DOUBLE PRECISION A(N), B(N), C(N), D(N)
DOUBLE PRECISION NDLOAD, SGLINT, DBLINT
DOUBLE PRECISION QX(N), QY(N), QE, QS
DOUBLE PRECISION DPDX(N,N), DPDY(N,N), TORX0(N,N), TORXH(N,N)
DOUBLE PRECISION XP(N,N), XBAR, FFO, FFH
INTEGER NX, NXM1, NXM2, NY, NYM1, NYM2, ITER
LOGICAL FLAG

C Initialise variables
DATA P /NTOTAL*0.0D0/, PPI /NTOTAL*0.0D0/
DATA FLAG /.FALSE./, ITER /1/

C Open results file
OPEN (UNIT=1, FILE='tb2d_output.dat', STATUS='UNKNOWN')
OPEN (UNIT=2, FILE='tb2d_plot.dat', STATUS='UNKNOWN')
OPEN (UNIT=3, FILE='tb2d_script.m', STATUS='UNKNOWN')

C Prompt user for input values
WRITE(*,*) 'Enter value of L/B ratio'
READ (*,*) LB
WRITE(*,*) 'Enter value of K=(h1/h0)-1'
READ (*,*) K
WRITE(*,*) 'Enter value of NX'
READ (*,*) NX
WRITE(*,*) 'Enter value of NY'
READ (*,*) NY

```

```

C      Dependent variables
NXM1 = NX-1
NXM2 = NX-2
NYM1 = NY-1
NYM2 = NY-2
DX = 1.0/NXM1
DY = 1.0/NYM1
DX2 = DX**2
DY2 = DY**2
BL2 = (1/LB)**2

C      Initialise discrete grid points in the
C      (a) x-direction
X(1)=0.0
DO 5,I=2,NX
    X(I)=X(I-1)+DX
5 CONTINUE

C      (b) y-direction
Y(1)=0.0
DO 10,J=2,NY
    Y(J)=Y(J-1)+DY
10 CONTINUE

C      Initialise film thickness
DO 15,I=1,NX
    H(I) = 1.0+K*(1-X(I))
15 CONTINUE

C ----- ITERATION PROCESS -----
C
DO WHILE(FLAGS.EQV. (.FALSE.))

C      Provide user feedback during iteration process
WRITE(*,'(10X,A12,I5)') 'Iteration = ', ITER
ITER = ITER + 1

C      Sweep all rows j=2,3,...,J-1
DO 50,J=2,NYM1
    DO 35,I=2, NXM1
        A(I-1) = (1.0/DX2)+(1.5*K)/(DX*H(I))
        B(I-1) = -2.0*((1.0/DX2)+(BL2/DY2))
        C(I-1) = (1.0/DX2)-(1.5*K)/(DX*H(I))
        D(I-1) = -K/(H(I)**3)-(BL2/DY2)*(P(I,J-1)+P(I,J+1))
35    CONTINUE

C      Use Thomas algorithm to solve tridiagonal system of algebraic equations
CALL THOMAS(NXM2,A,B,C,D,N)

C      Capture solution from Thomas and apply SOR factor, For
DO 40,I=2,NXM1
    P(I,J) = PPI(I,J)+FOR*(D(I-1)-PPI(I,J))
    PPI(I,J) = P(I,J)
40    CONTINUE

50    CONTINUE

C      Sweep all columns i=2,3,...,I-1
DO 65,I=2,NXM1
    DO 55,J=2, NYM1
        A(J-1) = (BL2/DY2)
        B(J-1) = -2.0*((1.0/DX2)+(BL2/DY2))
        C(J-1) = (BL2/DY2)
        D(J-1) = -K/(H(I)**3)
        +
        +      -((1.0/DX2)+(1.5*K)/(DX*H(I)))*P(I-1,J)
        +      -((1.0/DX2)-(1.5*K)/(DX*H(I)))*P(I+1,J)
55    CONTINUE

```

```

C      Use Thomas algorithm to solve tridiagonal system of algebraic equations
      CALL THOMAS(NYM2,A,B,C,D,N)

C      Capture solution from Thomas and apply SOR factor, For
      DO 60,J=2,NYM1
          P(I,J) = PPI(I,J)+FOR*(D(J-1)-PPI(I,J))
60      CONTINUE

65      CONTINUE

C      Convergence test
      CALL CVERGE(NX,NY,P,PPI,FLAG,N)

      END DO

C ----- END ITERATION PROCESS -------

C      Calculate the non-dimensional load
      NDLOAD = DBLINT(P,DX,DY,NXM1,NYM1,N)

C      Calculate location of the pivot point, XBAR
      DO 75,J=1,NY
          DO 70,I=1,NX
              XP(I,J)=X(I)*P(I,J)
70      CONTINUE
75      CONTINUE
      XBAR = DBLINT(XP,DX,DY,NXM1,NYM1,N)/NDLOAD

C      Calculate the pressure gradients
C      (a) in the x-direction
      DO 85,J=1,NY
          DPDX(1,J) = (-3.0*P(1,J)+4.0*P(2,J)-P(3,J))/(2.0*DX)
          DPDX(NX,J) = (3.0*P(NX,J)-4.0*P(NXM1,J)+P(NXM2,J))/(2.0*DX)
          DO 80,I=2,NXM1
              DPDX(I,J) = (P(I+1,J)-P(I-1,J))/(2.0*DX)
80      CONTINUE
85      CONTINUE

C      (b) in the y-direction
      DO 90,I=1,NX
          DPDY(I,1) = (-3.0*P(I,1)+4.0*P(I,2)-P(I,3))/(2.0*DY)
90      CONTINUE

C      Calculate the friction force by integration of the shear
C      stress over the bearing area. The friction force on the
C      lower surface is FFH, whereas that on the upper surface is FFO
      DO 100,J=1,NY
          DO 95,I=1,NX
              TORX0(I,J) = -3.0*H(I)*DPDX(I,J)-1.0/H(I)
              TORXH(I,J) = 3.0*H(I)*DPDX(I,J)-1.0/H(I)
95      CONTINUE
100     CONTINUE
      FFO = DBLINT(TORX0,DX,DY,NXM1,NYM1,N)
      FFH = DBLINT(TORXH,DX,DY,NXM1,NYM1,N)

C      Calculate the side leakage, QS
      DO 105,I=1,NX
          QY(I) = -H(I)**3/LB*DPDY(I,1)
105     CONTINUE
      QS = -SGLINT(QY,DX,NXM1,N)

C      Calculate the end leakage, QE
      DO 110,J=1,NY
          QX(J) = 0.5*LB*(H(NX)-(H(NX)**3)*DPDX(NX,J))
110     CONTINUE
      QE = SGLINT(QX,DY,NYM1,N)

```

```

C ----- PRINT RESULTS -------

C      Write results to end of existing results file
115 READ(1,* ,END=120)
      GO TO 115
120 CONTINUE
      WRITE(1,125) LB,K,6*NDLOAD,XBAR,FF0,FFH,QS,QE
125 FORMAT(2F10.2,6F10.5)

C      Write the pressure profile and pressure gradient
C      along the midplane to results file
      J=(NY+1)/2
      DO 130,I=1,NX
          WRITE(2,'(3F10.6)') X(I), P(I,J), DPDX(I,J)
130 CONTINUE

C      Create Matlab script file to plot the non-dimensional film
C      thickness and the pressure distribution over the bearing
      WRITE(3,140) 'x=['
      DO 135,J=1,NY
          WRITE(3,145) (X(I),I=1,NX)
135 CONTINUE
140 FORMAT(A3)
145 FORMAT(101F10.5)
      WRITE(3,*) ']';
      WRITE(3,*)

      WRITE(3,140) 'y=['
      DO 150,J=1,NY
          WRITE(3,145) (Y(J),I=1,NX)
150 CONTINUE
      WRITE(3,*) ']';
      WRITE(3,*)

      WRITE(3,140) 'h=['
      DO 155,J=1,NY
          WRITE(3,145) (H(I),I=1,NX)
155 CONTINUE
      WRITE(3,*) ']';
      WRITE(3,*)

      WRITE(3,140) 'p=['
      DO 160,J=1,NY
          WRITE(3,145) (P(I,J),I=1,NX)
160 CONTINUE
      WRITE(3,*) ']';
      WRITE(3,*)

C      3D plot of the film thickness
      WRITE(3,*) 'figure(1);'
      WRITE(3,*) 'hold on;'
      WRITE(3,*) 'surf(x,y,h);'
      WRITE(3,*) 'view(-30,30);'
      WRITE(3,*) 'grid on;'
      WRITE(3,*) 'box on;'
      WRITE(3,*) 'axis([-Inf Inf -Inf Inf 0 Inf]);'
      WRITE(3,*) 'xlabel('''x''');'
      WRITE(3,*) 'ylabel('''y''');'
      WRITE(3,*) 'zlabel('''h''');'

C      3D plot of the pressure distribution
      WRITE(3,*) 'figure(2);'
      WRITE(3,*) 'hold on;'
      WRITE(3,*) 'surf(x,y,p);'
      WRITE(3,*) 'view(30,30);'
      WRITE(3,*) 'grid on;'
      WRITE(3,*) 'box on;'
      WRITE(3,*) 'xlabel('''x''');'
      WRITE(3,*) 'ylabel('''y''');'
      WRITE(3,*) 'zlabel('''p''');'

```

```

C Contour plot of the pressure distribution
WRITE(3,*) 'figure(3);'
WRITE(3,*) 'hold on;'
WRITE(3,*) 'contourf(x,y,p,10,'"k");'
WRITE(3,*) 'box on;'
WRITE(3,*) 'xlabel(''x*'');'
WRITE(3,*) 'ylabel(''y*'');'

C Close results files
END FILE (UNIT=1)
END FILE (UNIT=2)
END FILE (UNIT=3)
CLOSE (UNIT=1)
CLOSE (UNIT=2)
CLOSE (UNIT=3)

STOP
END

C =====
SUBROUTINE THOMAS (NN,A,B,C,D,N)

C This subroutine uses the Thomas algorithm for solving tri-diagonal
C systems of algebraic equations with Dirichlet boundary conditions.
C It is used in iterative line-by-line sweeps to determine the pressure
C distribution over the bearing surface.

DOUBLE PRECISION A(N),B(N),C(N),D(N)
INTEGER N, NN

B(1)=1.0/B(1)

DO 5,I=2,NN
    B(I)=1.0/( B(I)-A(I)*B(I-1)*C(I-1) )
    D(I)=D(I)-A(I)*B(I-1)*D(I-1)
5 CONTINUE

D(NN)=D(NN)*B(NN)

DO 10,I=NN-1,1,-1
    D(I)=( D(I)-D(I+1)*C(I) )*B(I)
10 CONTINUE

RETURN
END

C =====
SUBROUTINE CVERGE (NX,NY,P,PPI,FLAG,N)

C This subroutine tests for convergence of the solution. If the
C residual is less than or equal to RESLIM then the solution is
C converged. If the residual is greater than RESMAX, the solution
C is diverging and the program is stopped. Otherwise, an over -
C relaxation factor is applied to speed up the iterative process

PARAMETER (RESLIM=1.0D-6, RESMAX=1.0D2)
DOUBLE PRECISION P(N,N), PPI(N,N), RESID
LOGICAL FLAG

RESID=0.0D0
DO 10,J=1,NY
    DO 5,I=1,NX
        RESID = MAX(RESID,ABS(P(I,J)-PPI(I,J)))
5 CONTINUE
10 CONTINUE

```

```

IF (RESID .LE. RESLIM) THEN
  FLAG = .TRUE.
ELSE IF (RESID .GE. RESMAX) THEN
  STOP 'Solution not converging'
ELSE
  DO 20,J=2,NY-1
    DO 15,I=2,NX-1
      PPI(I,J) = P(I,J)
15    CONTINUE
20    CONTINUE
  END IF

  RETURN
END

C =====
DOUBLE PRECISION FUNCTION SGLINT(FX,DX,NXM1,N)

C This subroutine performs a single integration using the
C trapezoidal rule of integration.

DOUBLE PRECISION SUM, DX, FX(N)
INTEGER I, NXM1, N

SUM = 0.0
DO 5,I=1,NXM1
  SUM = SUM + FX(I) + FX(I+1)
5 CONTINUE
SGLINT = 0.5*DX*SUM
END

C =====
DOUBLE PRECISION FUNCTION DBLINT(FXY,DX,DY,NXM1,NYM1,N)

C This subroutine performs a double integration using the
C trapezoidal rule of integration.

DOUBLE PRECISION SUM, DX, DY, FXY(N,N)
INTEGER NXM1, NYM1, N

SUM=0.0
DO 10,J=1,NYM1
  DO 5,I=1,NXM1
    SUM = SUM + FXY(I,J) + FXY(I,J+1) +
    +       FXY(I+1,J) + FXY(I+1,J+1)
5   CONTINUE
10 CONTINUE
DBLINT = 0.25*DX*DY*SUM
END

```

APPENDIX F – Double integration with the trapezoidal rule

The total force and moment on the impeller are obtained by the integration of the discrete pressure distribution over the lubricating surfaces of the impeller. The trapezoidal rule is used to perform the double integration, which has the following form

$$\int_a^b \int_c^d f(x, y) dy dx \quad (\text{F.1})$$

Using the trapezoidal rule of integration over the interval $[c, d]$,

$$\int_c^d f(x, y) dy \approx \sum_{j=1}^{J-1} \frac{\Delta y}{2} [f(x, y_j) + f(x, y_{j+1})]$$

where $\Delta y = \frac{d - c}{J - 1}$ and $J - 1$ is the number of subintervals of size Δy on $[c, d]$, then

equation (F.1) may be rewritten as [31]

$$\begin{aligned} \int_a^b \int_c^d f(x, y) dy dx &= \int_a^b \left[\int_c^d f(x, y) dy \right] dx \\ &\approx \int_a^b \left\{ \sum_{j=1}^{J-1} \frac{\Delta y}{2} [f(x, y_j) + f(x, y_{j+1})] \right\} dx \\ &= \frac{\Delta y}{2} \sum_{j=1}^{J-1} \int_a^b [f(x, y_j) + f(x, y_{j+1})] dx \end{aligned}$$

which yields

$$\int_a^b \int_c^d f(x, y) dy dx \approx \frac{\Delta y}{2} \sum_{j=1}^{J-1} \left[\int_a^b f(x, y_j) dx + \int_a^b f(x, y_{j+1}) dx \right] \quad (\text{F.2})$$

Once more, utilising the trapezoidal rule, the following approximations

$$\int_a^b f(x, y_j) dx \approx \sum_{i=1}^{I-1} \frac{\Delta x}{2} [f(x_i, y_j) + f(x_{i+1}, y_j)] \quad (\text{F.3})$$

and

$$\int_a^b f(x, y_{j+1}) dx \approx \sum_{i=1}^{I-1} \frac{\Delta x}{2} [f(x_i, y_{j+1}) + f(x_{i+1}, y_{j+1})] \quad (\text{F.4})$$

may be obtained, where $\Delta x = \frac{b-a}{I-1}$ and $I-1$ is the number of subintervals of size Δx over the interval $[a,b]$. Using the notation $f(x_i, y_j) = f_{i,j}$ and substituting equations (F.3) and (F.4) into equation (F.2) yields the following approximation of equation (F.1):

$$\int_a^b \int_c^d f(x, y) dy dx \approx \frac{\Delta x}{2} \cdot \frac{\Delta y}{2} \sum_{j=1}^{J-1} \sum_{i=1}^{I-1} [f_{i,j} + f_{i,j+1} + f_{i+1,j} + f_{i+1,j+1}] \quad (\text{F.5})$$

A FORTRAN function based on equation (F.5) is given below.

```

REAL FUNCTION DBLINT(FXY,DX,DY,NXM1,NYM1,N)

C      This subroutine performs a double integration using the
C      trapezoidal rule of integration.

C FXY(I,J)    = The value of the function at node i,j
C NXM1, NYM1 = Number of subintervals in the x- and y- directions
C DX, DY      = Size of subintervals in the x- and y- directions

DOUBLE PRECISION SUM, DX, DY, FXY(N,N)
INTEGER NXM1, NYM1, N

SUM=0.0
DO 10,J=1,NYM1
  DO 5,I=1,NXM1
    SUM = SUM + FXY(I,J) + FXY(I,J+1) +
    +       FXY(I+1,J) + FXY(I+1,J+1)
  5  CONTINUE
10 CONTINUE

DBLINT = 0.25*DX*DY*SUM

END

```

APPENDIX G – FORTRAN program Orbit3D

PROGRAM ORBIT3D

```

C This program was developed with the aim of determining the
C stability of the VentrAssist implantable rotary blood pump.
C Orbit3D determines the pressure distribution over the
C thrust bearing and conical journal bearing surfaces of the
C impeller, calculates the forces and moments on the impeller
C resulting from this pressure and calculates the position
C (both translational and rotational) of the impeller within
C pump housing. From observation of this 'orbit', the stability
C of the impeller can be assessed.

C Description of variables:
C
C I          = Index of grid points in the theta direction
C J          = Index of grid points in the radial (r and rho) directions
C M          = Index of impeller blades
C N          = Index of grid points in time
C NTH         = Number of grid points in the theta direction
C NR          = Number of grid points in the radial (r) direction
C NRO         = Number of grid points in the radial (rho) direction
C NP          = Number of impeller blades
C NT          = Number of temporal grid points
C DTH         = Uniform grid spacing in the theta direction (non-dim.)
C DR          = Uniform grid spacing in the radial (r) direction (non-dim.)
C DRO         = Uniform grid spacing in the radial (rho) direction (non-dim.)
C DT          = Uniform grid spacing in time (non-dim.)
C TH(,)       = Theta location of grid points on impeller m (non-dim.)
C R()         = Radial (r) location of grid points (non-dim.)
C RO()        = Radial (rho) location of grid points (non-dim.)
C T()         = Time of temporal grid points (non-dim.)
C NDT         = Time at the nth time step (non-dim.)
C REV         = Number of revolution of the impeller
C ALPHD       = Half-cone angle (degrees)
C ALP          = Half-cone angle (radians)
C TH0D         = The angular span of each impeller blade (deg.)
C TH0          = The angular span of each impeller blade (rad.)
C TH1          = Spacing of impeller blades (rad.) = 2*PI/NP
C R1           = The inner radius of the thrust bearing (m)
C R2           = The outer radius of the thrust bearing (m)
C LR           = R2 - R1 (m)
C RO1          = The inner radius of the conical journal bearing in the rho
C                 direction (m)
C RO2          = The outer radius of the conical journal bearing in the rho
C                 direction (m)
C LRO          = RO2 - RO1 (m)
C PHI1          = Angle used to specify the gravitational force (rad.)
C PHI2          = Angle used to specify the gravitational force (rad.)
C LOADP        = Load parameter (non-dim.)
C XH,YH,ZH    = Amplitude of the displacement of the pump housing (non-dim.)
C V1           = Frequency of "shaking" of the pump housing (non-dim.)
C V2           = Frequency of unbalance force (non-dim.)
C H0TB         = Minimum (outlet) film thickness of thrust bearing (m)
C H1TB         = Maximum (inlet) film thickness of thrust bearing (m)
C KTB          = H1TB/H0TB-1 (non-dim.)
C PLTB         = Fraction of thrust bearing that is untapered land
C HVC          = Vertical clearance of conical journal bearing = H0TB (m)
C H0CJB        = Minimum (outlet) film thickness of conical journal bearing (m)
C H1CJB        = Maximum (inlet) film thickness of conical journal bearing (m)
C KCJB          = H1CJB/H0CJB-1 (non-dim.)
C PLCJB        = Fraction of conical journal bearing that is untapered land
C IT           = Transverse moment of inertia (non-dim.)
C JP           = Polar moment of inertia (non-dim.)
C M1           = Mass of the impeller (non-dim.)
C M2           = Magnitude of the unbalance mass (non-dim.)
C PTB(,,)       = Pressure value at node i,j on the impeller blade m of the
C                 thrust bearing at time step N (non-dim.)
C PPITB(,,)     = Pressure value at node i,j on the impeller blade m of the
C                 thrust bearing at time step N-1 (non-dim.)
C PCJB(,,)       = Pressure value at node i,j on the impeller blade m of the
C                 conical journal bearing at time step N (non-dim.)

```

```

C PPICJB(,,) = Pressure value at node i,j on the impeller blade m of the
C           conical journal bearing at time step N-1 (non-dim.)
C FXTB      = Force in the X-direction on the impeller from the thrust
C           bearing (non-dim.)
C MXTB      = Moment about the X-axis on the impeller from the thrust
C           bearing (non-dim.)
C MYTB      = Moment about the Y-axis on the impeller from the thrust
C           bearing (non-dim.)
C FXCJB     = Force in the X-direction on the impeller from the conical
C           journal bearing (non-dim.)
C FYCJB     = Force in the Y-direction on the impeller from the conical
C           journal bearing (non-dim.)
C FZCJB     = Force in the Z-direction on the impeller from the conical
C           journal bearing (non-dim.)
C MXCJB     = Moment about the X-axis on the impeller from the conical
C           journal bearing (non-dim.)
C MYCJB     = Moment about the Y-axis on the impeller from the conical
C           journal bearing (non-dim.)
C FX(,)     = Total force in the X-direction on the impeller (non-dim.)
C FY(,)     = Total force in the Y-direction on the impeller (non-dim.)
C FZ(,)     = Total force in the Z-direction on the impeller (non-dim.)
C MX(,)     = Total moment about the X-axis on the impeller (non-dim.)
C MY(,)     = Total moment about the Y-axis on the impeller (non-dim.)
C K1()      = Variable used in the Runge-Kutta method
C K2()      = Variable used in the Runge-Kutta method
C K3()      = Variable used in the Runge-Kutta method
C K4()      = Variable used in the Runge-Kutta method
C Y1()      = Eccentricity ratio in the X-direction
C Y2()      = Instantaneous velocity in the X-direction (non-dim.)
C Y3()      = Eccentricity ratio in the Y-direction
C Y4()      = Instantaneous velocity in the Y-direction (non-dim.)
C Y5()      = Eccentricity ratio in the Z-direction
C Y6()      = Instantaneous velocity in the Z-direction (non-dim.)
C Y7()      = Rotational position of the impeller about the X-axis (non-dim.)
C Y8()      = Rotational velocity of the impeller about the X-axis (non-dim.)
C Y9()      = Rotational position of the impeller about the Y-axis (non-dim.)
C Y10()     = Rotational velocity of the impeller about the Y-axis (non-dim.)
C FLAG1     = Set to true if touchdown of the thrust bearing occurs, otherwise false
C FLAG2     = Set to true if touchdown of the conical journal bearing occurs,
C           otherwise false

C     Variable declaration
PARAMETER (N1=101, N2=4, N3=5761)
PARAMETER (NTH=21, NR=21, NRO=21, NP=4, NT=721, REV=1.0D0)
PARAMETER (ALPD=45.0, TH0D=45.0, R1=0.0125, R2=0.025)
PARAMETER (PI=3.141592654, RTOD=180.0/PI, DTOR=PI/180.0)
PARAMETER (PHI1=PI, PHI2=0.0, LOADP=152.03)
PARAMETER (XH=10.0, YH=0.0, ZH=0.0, V1=1.0, V2=0.0)
REAL H0TB, H1TB, KTB, PLTB, HVC, H0CJB, H1CJB, KCJB, PLCJB
REAL LR, RO1, RO2, LRO, IT, JP, M1, M2
REAL FZTB, MXTB, MYTB
REAL FXCJB, FYCJB, FZCJB, MXCJB, MYCJB
REAL FX(N3,4), FY(N3,4), FZ(N3,4), MX(N3,4), MY(N3,4)
DOUBLE PRECISION K1(10), K2(10), K3(10), K4(10)
DOUBLE PRECISION Y1(N3), Y2(N3), Y3(N3), Y4(N3), Y5(N3)
DOUBLE PRECISION Y6(N3), Y7(N3), Y8(N3), Y9(N3), Y10(N3)
DOUBLE PRECISION TH0, ALP, TH1, DTH, DR, DRO, DT
DOUBLE PRECISION TH(N1,N2), R(N1), RO(N1), T(N3)
DOUBLE PRECISION NDT, SA, CA
DOUBLE PRECISION PTB(N1,N1,N2), PPITB(N1,N1,N2)
DOUBLE PRECISION PCJB(N1,N1,N2), PPICJB(N1,N1,N2)
INTEGER I, J, M, N, COUNT
LOGICAL FLAG1, FLAG2
DATA FLAG1/.FALSE./, FLAG2/.FALSE./, COUNT/1/

C     Open results files
OPEN (UNIT=1, FILE='plottraj.m', STATUS='UNKNOWN')
OPEN (UNIT=2, FILE='plotcjb.m', STATUS='UNKNOWN')
OPEN (UNIT=3, FILE='plottb.m', STATUS='UNKNOWN')

C     Initialised dependent variables for the
C     (a) thrust bearing
H0TB = 100E-6
H1TB = H0TB+50E-6
KTB = H1TB/H0TB-1.0
PLTB = 0.2

```

```

C      (b) conical journal bearing
ALP    = ALPD*DTOR
SA     = DSIN(ALP)
CA     = DCOS(ALP)
R01   = R1/SA
R02   = R2/SA
ROG   = 1.05*RO2
ROG   = ROG/ (RO2*SA)
HVC   = H0TB
H0CJB = HVC*SA
H1CJB = H0CJB+50E-6
KCJB  = H1CJB/H0CJB-1.0
PLCJB = PLTB

C      Initialise the coordinates of the discrete grid points
C      in the circumferential direction for the first impeller blade
TH0=TH0*DTOR
DTH=TH0/ (NTH-1)
TH(1,1)=0.0
DO 5,I=2,NTH
    TH(I,1)=TH(I-1,1)+DTH
5 CONTINUE

C      Initialise the coordinates of the discrete grid points
C      in the circumferential direction for the remaining blades
TH1=2*PI/NP
DO 15,M=2,NP
    DO 10,I=1,NTH
        TH(I,M)=TH(I,1)+(M-1)*TH1
10    CONTINUE
15    CONTINUE

C      Initialise the coordinates of the grid points in the radial
C      direction for the thrust bearing
LR=R2-R1
DR=(LR/R2)/ (NR-1)
R(1)=R1/R2
DO 20,J=2,NR
    R(J)=R(J-1)+DR
20    CONTINUE

C      Initialise the coordinates of the grid points in the radial
C      direction for the conical journal bearing
LRO=R02-RO1
DRO=LRO/R2/ (NRO-1)
RO(1)=RO1/R2
DO 25,J=2,NRO
    RO(J)=RO(J-1)+DRO
25    CONTINUE

C      Initialise the numerical grid in time. The non-dimensional
C      time step should be in the order of 1 degree, but is typically
C      0.5 or even 0.25 degrees depending on the operating conditions.
DT=2.0*PI*REV/ (NT-1)
T(1)=0.0DO
DO 30,N=2,NT
    T(N)=T(N-1)+DT
30    CONTINUE

C      Initialise pressure to ambient (ie. zero) at t=0 for the
C      (a) thrust bearing
DO 45,M=1,NP
    DO 40,J=1,NR
        DO 35,I=1,NTH
            PTB(I,J,M) = 0.0DO
            PPITB(I,J,M) = 0.0DO
35    CONTINUE
40    CONTINUE
45    CONTINUE

C      (b) conical journal bearing
DO 60,M=1,NP
    DO 55,J=1,NRO
        DO 50,I=1,NTH
            PCJB(I,J,M) = 0.0DO
            PPICJB(I,J,M) = 0.0DO
50    CONTINUE

```

```

55    CONTINUE
60    CONTINUE

C      Set properties of the impeller
IT = 0.214097
JP = 1.78578
M1 = 0.69867
M2 = 0.0

C      Set initial conditions
Y1(1) = 0.0
Y2(1) = 0.0
Y3(1) = 0.0
Y4(1) = 0.0
Y5(1) = 0.0
Y6(1) = 0.0
Y7(1) = 0.0
Y8(1) = 0.0
Y9(1) = 0.0
Y10(1) = 0.0

C      The following DO WHILE loop uses the classical form of the fourth-order
C      Runge-Kutta method to solve the five second-order non-linear differential
C      equations that govern the translational and rotational movement of the
C      impeller. This method requires four "estimates" before giving the
C      actual position for each time step. Thus four steps are involved.

C      DO WHILE loop control:
C      If FLAG1 is becomes true during the course of the run then touchdown
C      has occurred in the thrust bearing. Furthermore, if FLAG2 becomes true
C      then touchdown has occurred in the conical journal bearing. If either
C      of these occurs then the loop is exited and the program stopped.

N=1
DO WHILE ((FLAG1 .EQV. (.FALSE.)) .AND. (FLAG2 .EQV. (.FALSE.)))
+
      .AND. (N .LE. NT))

C      *** FIRST STEP ***
NDT = T(N)

C      Call Subroutine TB (ie. Thrust Bearing) to calculate the pressure
C      distribution over the thrust bearing. This subroutine also integrates
C      this pressure to determine the forces and moments on the impeller.
CALL TB(H0TB,H1TB,KTB,PLTB,TH0,TH,DTH,NTH,R1,R2,R,DR,NR,NP,NDT,
+
      N1,N2,Y5(N),Y6(N),Y7(N),Y8(N),Y9(N),Y10(N),PTB,PPITB,
+
      FZTB,MXTB,MYTB,FLAG1)

C      Call Subroutine CJB (ie. Conical Journal Bearing) to calculate the
C      pressure distribution over the conical journal bearing. This subroutine
C      also integrates this pressure to determine the forces and moments on the
C      impeller.
CALL CJB(H0CJB,H1CJB,KCJB,PLCJB,ALP,TH0,TH,DTH,NTH,RO1,RO2,ROG,
+
      RO,DRO,NRO,NP,NDT,N1,N2,Y1(N),Y2(N),Y3(N),Y4(N),Y5(N),
+
      Y6(N),Y7(N),Y8(N),Y9(N),Y10(N),PCJB,PPICJB,FXCJB,FYCJB,
+
      FZCJB,MXCJB,MYCJB,FLAG2)

C      Calculate the net forces and moments on the impeller by summation
C      of the individual contributions of the thrust bearing and the
C      conical journal bearing
FX(N,1) = FXCJB
FY(N,1) = FYCJB
FZ(N,1) = FZTB + FZCJB
MX(N,1) = MXTB + MXCJB
MY(N,1) = MYTB + MYCJB

```

```

C   Write the pressure field at this time step to file (this is done
C   during the first step of the Runge-Kutta method only) at the first
C   time step and for every twentieth time step thereafter. If you do
C   not want to print the pressure profile to file, then set
C   (N .EQ. 1) to (N .EQ. 0) and (COUNT .EQ. 20) to (COUNT .EQ. 0)
C   in the if statement below
IF ( (N .EQ. 1) .OR. (COUNT .EQ. 20) ) THEN
    CALL PLTCJB(PCJB,N,NTH,NRO,NP,NT,SA,RO,TH,NDT,N1,N2)
    CALL PLTTB(PTB,N,NTH,NR,NP,NT,R,TH,NDT,N1,N2)
    COUNT = 1
ELSE
    COUNT = COUNT + 1
END IF

K1(1) = DT*Y2(N)
K1(2) = DT*( LOADP/M1)*FX(N,1) + (V1**2)*XH*SIN(V1*NDT)
+      - (M2/M1)*(V2**2)*COS(V2*NDT)+SIN(PHI1)*COS(PHI2)/M1 )
K1(3) = DT*Y4(N)
K1(4) = DT*( LOADP/M1)*FY(N,1) + (V1**2)*YH*SIN(V1*NDT)
+      - (M2/M1)*(V2**2)*SIN(V2*NDT)+SIN(PHI1)*SIN(PHI2)/M1 )
K1(5) = DT*Y6(N)
K1(6) = DT*( LOADP/M1)*FZ(N,1) + (V1**2)*ZH*SIN(V1*NDT)
+      + COS(PHI1)/M1 )
K1(7) = DT*Y8(N)
K1(8) = DT*( JP*Y10(N)+(R2/HOTB)*MX(N,1)/IT )
K1(9) = DT*Y10(N)
K1(10) = DT*( -JP*Y8(N)+(R2/HOTB)*MY(N,1)/IT )

C   *** SECOND STEP ***
NDT = T(N)+0.5*DT
CALL TB(HOTB,H1TB,KTB,PLTB,TH0,TH,DTH,NTH,R1,R2,R,DR,NR,NP,NDT,
+      N1,N2,Y5(N)+K1(5)/2,Y6(N)+K1(6)/2,Y7(N)+K1(7)/2,Y8(N) +
+      K1(8)/2,Y9(N)+K1(9)/2,Y10(N)+K1(10)/2,PTB,PPITB,FZTB,MXTB,
+      MYTB,FLAG1)
CALL CJB(H0CJB,H1CJB,KCJB,PLCJB,ALP,TH0,TH,DTH,NTH,RO1,RO2,ROG,
+      RO,DRO,NRO,NP,NDT,N1,N2,Y1(N)+K1(1)/2,Y2(N)+K1(2)/2,Y3(N) +
+      K1(3)/2,Y4(N)+K1(4)/2,Y5(N)+K1(5)/2,Y6(N)+K1(6)/2,Y7(N) +
+      K1(7)/2,Y8(N)+K1(8)/2,Y9(N)+K1(9)/2,Y10(N)+K1(10)/2,PCJB,
+      PPICJB,FXCJB,FYCJB,FZCJB,MXCJB,MYCJB,FLAG2)
FX(N,2) = FXCJB
FY(N,2) = FYCJB
FZ(N,2) = FZTB + FZCJB
MX(N,2) = MXTB + MXCJB
MY(N,2) = MYTB + MYCJB

K2(1) = DT*( Y2(N)+0.5*K1(2) )
K2(2) = DT*( LOADP/M1)*FX(N,2) + (V1**2)*XH*SIN(V1*NDT)
+      - (M2/M1)*(V2**2)*COS(V2*NDT)+SIN(PHI1)*COS(PHI2)/M1 )
K2(3) = DT*( Y4(N)+0.5*K1(4) )
K2(4) = DT*( LOADP/M1)*FY(N,2) + (V1**2)*YH*SIN(V1*NDT)
+      - (M2/M1)*(V2**2)*SIN(V2*NDT)+SIN(PHI1)*SIN(PHI2)/M1 )
K2(5) = DT*( Y6(N)+0.5*K1(6) )
K2(6) = DT*( LOADP/M1)*FZ(N,2) + (V1**2)*ZH*SIN(V1*NDT)
+      + COS(PHI1)/M1 )
K2(7) = DT*( Y8(N)+0.5*K1(8) )
K2(8) = DT*( JP*(Y10(N)+0.5*K1(10))+(R2/HOTB)*MX(N,2)/IT )
K2(9) = DT*( Y10(N)+0.5*K1(10) )
K2(10) = DT*( -JP*(Y8(N)+0.5*K1(8))+(R2/HOTB)*MY(N,2)/IT )

C   *** THIRD STEP ***
NDT = T(N)+0.5*DT
CALL TB(HOTB,H1TB,KTB,PLTB,TH0,TH,DTH,NTH,R1,R2,R,DR,NR,NP,NDT,
+      N1,N2,Y5(N)+K2(5)/2,Y6(N)+K2(6)/2,Y7(N)+K2(7)/2,Y8(N) +
+      K2(8)/2,Y9(N)+K2(9)/2,Y10(N)+K2(10)/2,PTB,PPITB,FZTB,MXTB,
+      MYTB,FLAG1)
CALL CJB(H0CJB,H1CJB,KCJB,PLCJB,ALP,TH0,TH,DTH,NTH,RO1,RO2,ROG,
+      RO,DRO,NRO,NP,NDT,N1,N2,Y1(N)+K2(1)/2,Y2(N)+K2(2)/2,Y3(N) +
+      K2(3)/2,Y4(N)+K2(4)/2,Y5(N)+K2(5)/2,Y6(N)+K2(6)/2,Y7(N) +
+      K2(7)/2,Y8(N)+K2(8)/2,Y9(N)+K2(9)/2,Y10(N)+K2(10)/2,PCJB,
+      PPICJB,FXCJB,FYCJB,FZCJB,MXCJB,MYCJB,FLAG2)

```

```

FX(N,3) = FXCJB
FY(N,3) = FYCJB
FZ(N,3) = FZTB + FZCJB
MX(N,3) = MXTB + MXCJB
MY(N,3) = MYTB + MYCJB

K3(1) = DT*( Y2(N)+0.5*K2(2) )
K3(2) = DT*( (LOADP/M1)*FX(N,3) + (V1**2)*XH*SIN(V1*NDT)
+ - (M2/M1)*(V2**2)*COS(V2*NDT)+SIN(PHI1)*COS(PHI2)/M1 )
K3(3) = DT*( Y4(N)+0.5*K2(4) )
K3(4) = DT*( (LOADP/M1)*FY(N,3) + (V1**2)*YH*SIN(V1*NDT)
+ - (M2/M1)*(V2**2)*SIN(V2*NDT)+SIN(PHI1)*SIN(PHI2)/M1 )
K3(5) = DT*( Y6(N)+0.5*K2(6) )
K3(6) = DT*( (LOADP/M1)*FZ(N,3) + (V1**2)*ZH*SIN(V1*NDT)
+ + COS(PHI1)/M1 )
K3(7) = DT*( Y8(N)+0.5*K2(8) )
K3(8) = DT*( JP*(Y10(N)+0.5*K2(10))+(R2/HOTB)*MX(N,3)/IT )
K3(9) = DT*( Y10(N)+0.5*K2(10) )
K3(10) = DT*( -JP*(Y8(N)+0.5*K2(8))+(R2/HOTB)*MY(N,3)/IT )

C      *** FOURTH STEP ***
NDT = T(N)+DT
CALL TB(HOTB,H1TB,KTB,PLTB,TH0,TH,DTH,NTH,R1,R2,R,DR,NR,NP,NDT,
+ N1,N2,Y5(N)+K3(5),Y6(N)+K3(6),Y7(N)+K3(7),Y8(N)+K3(8),
+ Y9(N)+K3(9),Y10(N)+K3(10),PTB,PPITB,FZTB,MXTB,MYTB,FLAG1)
CALL CJB(H0CJB,H1CJB,KCJB,PLCJB,ALP,TH0,TH,DTH,NTH,RO1,RO2,ROG,
+ RO,DRO,NRO,NDT,N1,N2,Y1(N)+K3(1),Y2(N)+K3(2),Y3(N)+
+ K1(3),Y4(N)+K3(4),Y5(N)+K3(5),Y6(N)+K3(6),Y7(N)+K3(7),
+ Y8(N)+K3(8),Y9(N)+K3(9),Y10(N)+K3(10),PCJB,PPICJB,FXCJB,
+ FYCJB,FZCJB,MXCJB,MYCJB,FLAG2)
FX(N,4) = FXCJB
FY(N,4) = FYCJB
FZ(N,4) = FZTB + FZCJB
MX(N,4) = MXTB + MXCJB
MY(N,4) = MYTB + MYCJB

K4(1) = DT*( Y2(N)+K3(2) )
K4(2) = DT*( (LOADP/M1)*FX(N,4) + (V1**2)*XH*SIN(V1*NDT)
+ - (M2/M1)*(V2**2)*COS(V2*NDT)+SIN(PHI1)*COS(PHI2)/M1 )
K4(3) = DT*( Y4(N)+K3(4) )
K4(4) = DT*( (LOADP/M1)*FY(N,4) + (V1**2)*YH*SIN(V1*NDT)
+ - (M2/M1)*(V2**2)*SIN(V2*NDT)+SIN(PHI1)*SIN(PHI2)/M1 )
K4(5) = DT*( Y6(N)+K3(6) )
K4(6) = DT*( (LOADP/M1)*FZ(N,4) + (V1**2)*ZH*SIN(V1*NDT)
+ + COS(PHI1)/M1 )
K4(7) = DT*( Y8(N)+K3(8) )
K4(8) = DT*( JP*(Y10(N)+K3(10))+(R2/HOTB)*MX(N,4)/IT )
K4(9) = DT*( Y10(N)+K3(10) )
K4(10) = DT*( -JP*(Y8(N)+K3(8))+(R2/HOTB)*MY(N,4)/IT )

C      Calculate the variables at the next time step based on the
C      results of these four steps.
Y1(N+1) = Y1(N)+(K1(1)+2.*K2(1)+2.*K3(1)+K4(1))/6.
Y2(N+1) = Y2(N)+(K1(2)+2.*K2(2)+2.*K3(2)+K4(2))/6.
Y3(N+1) = Y3(N)+(K1(3)+2.*K2(3)+2.*K3(3)+K4(3))/6.
Y4(N+1) = Y4(N)+(K1(4)+2.*K2(4)+2.*K3(4)+K4(4))/6.
Y5(N+1) = Y5(N)+(K1(5)+2.*K2(5)+2.*K3(5)+K4(5))/6.
Y6(N+1) = Y6(N)+(K1(6)+2.*K2(6)+2.*K3(6)+K4(6))/6.
Y7(N+1) = Y7(N)+(K1(7)+2.*K2(7)+2.*K3(7)+K4(7))/6.
Y8(N+1) = Y8(N)+(K1(8)+2.*K2(8)+2.*K3(8)+K4(8))/6.
Y9(N+1) = Y9(N)+(K1(9)+2.*K2(9)+2.*K3(9)+K4(9))/6.
Y10(N+1) = Y10(N)+(K1(10)+2.*K2(10)+2.*K3(10)+K4(10))/6.

C      Write results to the screen
IF (N .EQ. 1) THEN
    WRITE(*,'(A10,5A12)') 't','erx','ery','erz','xrot','yrot'
END IF
WRITE(*,65) T(N)*RTOD,Y1(N),Y3(N),Y5(N),Y7(N),Y9(N)
65 FORMAT(F10.3,5F12.6)

C      Write results of all variables to file
CALL PLTTRA(Y1,Y2,Y3,Y4,Y5,Y6,Y7,Y8,Y9,Y10,DT,T,
+ N,NT,N3,FLAG1,FLAG2)

```

```

C      If touchdown occurs, then print message to screen
IF (FLAG1 .EQV. (.TRUE.)) THEN
  WRITE(*,'(A40)') 'Touchdown reported by SUBROUTINE TB'
ELSE IF (FLAG2 .EQV. (.TRUE.)) THEN
  WRITE(*,'(A40)') 'Touchdown reported by SUBROUTINE CJB'
END IF

C      Increment time for next time step
N = N + 1

      END DO

C      End and close result files
END FILE (1)
END FILE (2)
END FILE (3)
CLOSE (1)
CLOSE (2)
CLOSE (3)

STOP
END

C =====
SUBROUTINE TB(H0,H1,K,PLAND,TH0,TH,DTH,NTH,R1,R2,R,DR,NR,NP,NDT,
+           N1,N2,ERZ,ERZDT,XROT,XROTDY,ROTDT,P,PPI,FZT,
+           MXT,MYT,FLAG2)

C      This subroutine first calculates the pressure field over the thrust
C      bearing surfaces of each impeller blade. This pressure field is then
C      integrated over the respective bearing surface to calculate the
C      forces and moments on the impeller from the thrust bearing alone.

C      Description of variables (those not already described or different
C      to those in the main program):
C
C FOR      = Successive over-relaxation factor to accelerate iterative process
C DTOR     = Converts degrees to radians
C H0       = Minimum film thickness (m)
C H1       = Maximum film thickness (m)
C K        = H1/H0-1 (non-dim.)
C PLAND    = Fraction of angular span of bearing that is untapered land
C X(,,)    = X-coordinate of grid point i,j on impeller blade m (non-dim.)
C Y(,,)    = Y-coordinate of grid point i,j on impeller blade m (non-dim.)
C FZ()     = Force on the impeller in the Z-direction due to the thrust bearing
C           surface of impeller blade m (non-dim.)
C MX()     = Moment about the X-axis on impeller due to the thrust bearing
C           surface of impeller blade m (non-dim.)
C MY()     = Moment about the Y-axis on impeller due to the thrust bearing
C           surface of impeller blade m (non-dim.)
C FZT      = Total force on impeller in the Z-direction due to the thrust
C           bearing (non-dim.)
C MXT      = Total moment on the impeller about the X-axis due to the thrust
C           bearing (non-dim.)
C MYT      = Total moment on the impeller about the Y-axis due to the thrust
C           bearing (non-dim.)
C THOA     = Angular span of the land section (rad.)
C THOB     = Angular span of the tapered section (rad.)
C ERZ      = Eccentricity of the impeller in the Z-direction (non-dim.)
C ERZDT    = Time derivative of ERZ (ie. Z-velocity) (non-dim.)
C XROT     = Rotational position of the impeller about the X-axis (non-dim.)
C XROTDY   = Time derivative of XROT (ie. X rotational velocity) (non-dim.)
C XROT     = Rotational position of the impeller about the Y-axis (non-dim.)
C XROTDY   = Time derivative of YROT (ie. Y rotational velocity) (non-dim.)
C A()-D()  = Coefficients for the Thomas algorithm subroutine
C H(,,)    = Film thickness at any point (non-dim.)
C DHDTH(,,) = Derivative of H with respect to theta (non-dim.)
C DHDR(,,)  = Derivative of H with respect to r (non-dim.)
C DHDT(,,)  = Derivative of H with respect to time (non-dim.)
C P(,,)    = Pressure at node i,j on impeller blade m at time step N (non-dim.)
C PPI(,,)   = Pressure at node i,j on impeller blade m at time step N-1 (non-dim.)
C FLAG1    = Set to true if solution converges, otherwise false
C FLAG2    = Set to true if touchdown occurs, otherwise false

```

```

C Declaration of variables
PARAMETER (PI=3.141592654, DTOR=PI/180.0, FOR=1.5)
REAL H0, H1, K, R1, R2, LR, NDR, PLAND, TH0D
REAL X(N1,N1,N2), Y(N1,N1,N2), DBLINT
REAL PR(N1,N1,N2), PRX(N1,N1,N2), PRY(N1,N1,N2)
REAL FZ(N2), MX(N2), MY(N2), FZT, MXT, MYT
DOUBLE PRECISION TH(N1,N2), TH0, TH0A, TH0B, TH1, R(N1)
DOUBLE PRECISION DTH, DTH2, DR, DR2, NDT
DOUBLE PRECISION ERZ, ERZDT, XROT, XROTD, YROT, YROTD
DOUBLE PRECISION A(N1), B(N1), C(N1), D(N1)
DOUBLE PRECISION H(N1,N1,N2), DHDT(N1,N1,N2), DHDR(N1,N1,N2)
DOUBLE PRECISION DHDT(N1,N1,N2), P(N1,N1,N2), PPI(N1,N1,N2)
INTEGER NTH, NTHM1, NTHM2, NR, NRM1, NRM2
INTEGER I, J, M, N, NP, N1, N2
LOGICAL FLAG1, FLAG2

C Initialise dependent variables
NTHM1 = NTH-1
NTHM2 = NTH-2
NRM1 = NR-1
NRM2 = NR-2
TH0A = TH0*PLAND
TH0B = TH0-TH0A
TH1 = 2*PI/NP
LR = R2-R1
NDR = (R2/LR)**2
DTH2 = DTH**2
DR2 = DR**2

C Initialise variables
FZT = 0.0
MXT = 0.0
MYT = 0.0

C Calculate the pressure distribution and subsequently the forces and moments
C on the impeller as a result of this pressure over each pad m=1,2,...,NP
DO 65,M=1,NP

C Calculate the local film thickness and spatial and temporal derivatives
DO 10,J=1,NR
    DO 5,I=1,NTH

C Film thickness for untapered land
H(I,J,M)= 1.0+ERZ
+           +XROT*R(J)*SIN(TH(I,M)+NDT)
+           -YROT*R(J)*COS(TH(I,M)+NDT)

C Derivative with respect to (w.r.t.) theta for untapered land
DHDT(I,J,M) = XROT*R(J)*COS(TH(I,M)+NDT)
+           +YROT*R(J)*SIN(TH(I,M)+NDT)

C Film thickness and derivative w.r.t. theta for taper
IF ((TH(I,M)-(M-1)*TH1) .GE. TH0A) THEN
    H(I,J,M) = H(I,J,M)+K*(TH(I,M)-(TH0A+(M-1)*TH1))/TH0B
    DHDT(I,J,M) = DHDT(I,J,M) + K/TH0B
END IF

C If the film thickness is less than or equal to zero, then
C touchdown has occurred. Set FLAG2 to true.
IF (H(I,J,M) .LE. 0.0D0) THEN
    FLAG2 = .TRUE.
    RETURN
END IF

C Radial and time derivatives
DHDR(I,J,M) = XROT*SIN(TH(I,M)+NDT)
+           -YROT*COS(TH(I,M)+NDT)
DHDT(I,J,M) = ERZDT
+           +(XROT-YROTD)*R(J)*COS(TH(I,M)+NDT)
+           +(XROTD+YROT)*R(J)*SIN(TH(I,M)+NDT)
5      CONTINUE
10     CONTINUE

C Initialise iterative process loop control variable FLAG1
FLAG1 = .FALSE.

```

```

C      Iterative process to solve for the pressure distribution
C ----- BEGIN ITERATIVE PROCESS -----
DO WHILE(FLAG1 .EQV. (.FALSE.))

C      Sweep all rows j=2,3,...,J-1
DO 25,J=2,NRM1
    DO 15,I=2,NTHM1
        A(I-1)=1./(R(J)*DTH2)-1.5*DHDTH(I,J,M)/(R(J)*H(I,J,M)*DTH)
        B(I-1)=-2.*(R(J)/DR2+1./(R(J)*DTH2))
        C(I-1)=1./(R(J)*DTH2)+1.5*DHDTH(I,J,M)/(R(J)*H(I,J,M)*DTH)
        D(I-1)=-(NDR*R(J))/(H(I,J,M)**3)*DHDTH(I,J,M)
        +
        +     +(2.*NDR*R(J))/(H(I,J,M)**3)*DHDT(I,J,M)
        +
        +     -(R(J)/DR2-(1.5*R(J))/(H(I,J,M)*DR)
        +
        +     *DHDR(I,J,M)-0.5/DR)*P(I,J-1,M)
        +
        +     -(R(J)/DR2+(1.5*R(J))/(H(I,J,M)*DR)
        +
        +     *DHDR(I,J,M)+0.5/DR)*P(I,J+1,M)
15      CONTINUE

C      Use Thomas algorithm to solve tridiagonal system of algebraic equations
CALL THOMAS(NTHM2,A,B,C,D,N1)

C      Capture solution from Thomas and apply SOR factor, For
DO 20,I=2,NTHM1
    P(I,J,M) = PPI(I,J,M)+FOR*(D(I-1)-PPI(I,J,M))
    PPI(I,J,M) = P(I,J,M)
20      CONTINUE

25      CONTINUE

C      Sweep all columns i=2,3,...,I-1
DO 40,I=2,NTHM1
    DO 30,J=2,NRM1
        A(J-1) = (R(J)/DR-(1.5*R(J)*DHDR(I,J,M))/H(I,J,M)-0.5)/DR
        B(J-1) = -2.*(R(J)/DR2+1./(R(J)*DTH2))
        C(J-1) = (R(J)/DR+(1.5*R(J)*DHDR(I,J,M))/H(I,J,M)+0.5)/DR
        D(J-1) = -(NDR*R(J))/(H(I,J,M)**3)*DHDTH(I,J,M)
        +
        +     +(2.*NDR*R(J))/(H(I,J,M)**3)*DHDT(I,J,M)
        +
        +     -(1./(R(J)*DTH2)-1.5/(R(J)*H(I,J,M)*DTH)
        +
        +     *DHDTH(I,J,M))*P(I-1,J,M)
        +
        +     -(1./(R(J)*DTH2)+1.5/(R(J)*H(I,J,M)*DTH)
        +
        +     *DHDTH(I,J,M))*P(I+1,J,M)
30      CONTINUE

C      Use Thomas algorithm to solve tridiagonal system of algebraic equations
CALL THOMAS(NRM2,A,B,C,D,N1)

C      Capture solution from Thomas and apply SOR factor, For
DO 35,J=2,NRM1
    P(I,J,M) = PPI(I,J,M)+FOR*(D(J-1)-PPI(I,J,M))
35      CONTINUE

40      CONTINUE

C      Convergence test
CALL CVERGE(NTH,NR,P,PPI,FLAG1,M,N1,N2)

END DO

C ----- END ITERATIVE PROCESS -----

C      Transform the position of each grid point on the lubricating surfaces of
C      the rotating impeller in Cartesian x-y coordinates relative to the pump
C      housing (which is fixed)
DO 50,J=1,NR
    DO 45,I=1,NTH
        X(I,J,M)=R(J)*COS(TH(I,M)+NDT)
        Y(I,J,M)=R(J)*SIN(TH(I,M)+NDT)
45      CONTINUE
50      CONTINUE

```

```

C      Calculate the force (Fz) and moments (Mx and My) on the impeller
C      due to each separate blade
DO 60,J=1,NR
  DO 55,I=1,NTH
    PR(I,J,M) = P(I,J,M)*R(J)
    PRX(I,J,M) = -P(I,J,M)*R(J)*X(I,J,M)
    PRY(I,J,M) = P(I,J,M)*R(J)*Y(I,J,M)
55  CONTINUE
60  CONTINUE
FZ(M) = DBLINT(PR,DTH,DR,NTHM1,NRM1,N1,N2,M)
MX(M) = DBLINT(PRX,DTH,DR,NTHM1,NRM1,N1,N2,M)
MY(M) = DBLINT(PRY,DTH,DR,NTHM1,NRM1,N1,N2,M)

C      Calculate the total force (Fz) and moment (Mx and My) on the centre
C      of mass of the impeller
FZT = FZ(M)
MXT = MXT + MX(M)
MYT = MYT + MY(M)

65 CONTINUE

RETURN
END

C =====
SUBROUTINE CJB(H0,H1,K,PLAND,ALP,TH0,TH,DTH,NTH,RO1,RO2,ROG,RO,
+           DRO,NRO,NP,NDT,N1,N2,ERX,ERXDT,ERY,ERYDT,ERZ,ERZDT,
+           XROT,XROTDT,YROT,YROTDT,P,PPI,FXT,FYT,FZT,MXT,MYT,
+           FLAG2)

C      This subroutine first calculates the pressure field over the conical
C      journal bearing surfaces of each impeller blade. This pressure field
C      is then integrated over the respective bearing surface to calculate
C      the forces and moments on the impeller from the conical journal bearing
C      alone.

C      Description of variables (those not already described or different
C      to those in the main program):
C
C FOR      = Successive over-relaxation factor to accelerate iterative process
C DTOR     = Converts degrees to radians
C H0       = Minimum film thickness (m)
C H1       = Maximum film thickness (m)
C K        = H1/H0-1 (non-dim.)
C PLAND   = Fraction of angular span of bearing that is untapered land
C FX()     = Force on the impeller in the X-direction due to the conical
C            journal bearing surface of impeller blade m (non-dim.)
C FY()     = Force on the impeller in the Y-direction due to the conical
C            journal bearing surface of impeller blade m (non-dim.)
C FZ()     = Force on the impeller in the Z-direction due to the conical
C            journal bearing surface of impeller blade m (non-dim.)
C MX()     = Moment about the X-axis on impeller due to the conical journal
C            bearing surface of impeller blade m (non-dim.)
C MY()     = Moment about the Y-axis on impeller due to the conical journal
C            bearing surface of impeller blade m (non-dim.)
C FXT     = Total force on impeller in the X-direction due to the conical
C            journal bearing (non-dim.)
C FYT     = Total force on impeller in the Y-direction due to the conical
C            journal bearing (non-dim.)
C FZT     = Total force on impeller in the Z-direction due to the conical
C            journal bearing (non-dim.)
C MXT     = Total moment on the impeller about the X-axis due to the conical
C            journal bearing (non-dim.)
C MYT     = Total moment on the impeller about the Y-axis due to the conical
C            journal bearing (non-dim.)
C TH0A    = Angular span of the land section (rad.)
C TH0B    = Angular span of the tapered section (rad.)
C ERX     = Eccentricity of the impeller in the X-direction (non-dim.)
C ERXDT   = Time derivative of ERX (ie. X-velocity) (non-dim.)
C ERY     = Eccentricity of the impeller in the Y-direction (non-dim.)
C ERYDT   = Time derivative of ERY (ie. Y-velocity) (non-dim.)
C ERZ     = Eccentricity of the impeller in the Z-direction (non-dim.)
C ERZDT   = Time derivative of ERZ (ie. Z-velocity) (non-dim.)
C XROT    = Rotational position of the impeller about the X-axis (non-dim.)
C XROTDT  = Time derivative of XROT (ie. X rotational velocity) (non-dim.)

```

```

C XROT      = Rotational position of the impeller about the Y-axis (non-dim.)
C XROTDT    = Time derivative of YROT (ie. Y rotational velocity) (non-dim.)
C A() -D()  = Coefficients for the Thomas algorithm subroutine
C H(,,)     = Film thickness at any point (non-dim.)
C DHDT(,,)   = Derivative of H with respect to theta (non-dim.)
C DHDR(,,)   = Derivative of H with respect to r (non-dim.)
C DHDT(,,)   = Derivative of H with respect to time (non-dim.)
C P(,,)      = Pressure at node i,j on impeller blade m at time step N (non-dim.)
C PPI(,,)    = Pressure at node i,j on impeller blade m at time step N-1 (non-dim.)
C FLAG1     = Set to true if solution converges, otherwise false
C FLAG2     = Set to true if touchdown occurs, otherwise false

C Declaration of variables
PARAMETER (PI=3.141592654, DTOR=PI/180.0, FOR = 1.5)
REAL H0, H1, K, RO1, RO2, ROG, LRO, NDR, PLAND
REAL TH0D, ALPD, DBLINT
REAL FX(N2), FY(N2), FZ(N2), MX(N2), MY(N2)
REAL FXT, FYT, FZT, MXT, MYT
REAL DFX(N1,N1,N2), DFY(N1,N1,N2), DFZ(N1,N1,N2)
REAL DMX(N1,N1,N2), DMY(N1,N1,N2)
DOUBLE PRECISION TH(N1,N2), TH0, TH0A, TH0B, TH1, RO(N1)
DOUBLE PRECISION DTH, DTH2, DRO, DRO2
DOUBLE PRECISION ERX, ERXDT, ERY, ERYDT, ERZ, ERZDT
DOUBLE PRECISION XROT, XROTDT, YROT, YROTDT
DOUBLE PRECISION A(N1), B(N1), C(N1), D(N1), NDT, ALP, SA, CA
DOUBLE PRECISION H(N1,N1,N2), DHDR(N1,N1,N2), DHDT(N1,N1,N2)
DOUBLE PRECISION DHDT(N1,N1,N2), P(N1,N1,N2), PPI(N1,N1,N2)
INTEGER NTH, NRO, NTHM1, NTHM2, NROM1, NROM2
INTEGER I, J, M, NP, N1, N2
LOGICAL FLAG1, FLAG2

C Independent variables
SA    = DSIN(ALP)
CA    = DCOS(ALP)

C Dependent variables
NTHM1 = NTH-1
NTHM2 = NTH-2
NROM1 = NRO-1
NROM2 = NRO-2
TH0A = TH0*PLAND
TH0B = TH0-TH0A
TH1  = 2*PI/NP
LRO  = RO2-RO1
NDR  = (RO2/LRO)**2
DTH2 = DTH**2
DRO2 = DRO**2

C Initialise variables
FXT = 0.0
FYT = 0.0
FZT = 0.0
MXT = 0.0
MYT = 0.0

C Calculate the pressure distribution and subsequently the forces and moments
C on the impeller as a result of this pressure over each pad m=1,2,...,Np
DO 55,M=1,NP

C Calculate local film thickness and the spatial and temporal derivatives
DO 10,J=1,NRO
  DO 5,I=1,NTH
    H(I,J,M) = ( 1.0-ERZ
    +
    +          -ERX*COS(TH(I,M)+NDT)
    +          -ERY*SIN(TH(I,M)+NDT) )*SA
    +          -XROT*(RO(J)-ROG)*SIN(TH(I,M)+NDT)
    +          +YROT*(RO(J)-ROG)*COS(TH(I,M)+NDT)
    DHDT(I,J,M) = ( ERX*SIN(TH(I,M)+NDT)
    +
    +          -ERY*COS(TH(I,M)+NDT) )*SA
    +          -XROT*(RO(J)-ROG)*COS(TH(I,M)+NDT)
    +          -YROT*(RO(J)-ROG)*SIN(TH(I,M)+NDT)
    IF ((TH(I,M)-(M-1)*TH1) .GE. TH0A) THEN
      H(I,J,M) = H(I,J,M) +
      ( K*(TH(I,M)-(TH0A+(M-1)*TH1))/TH0B )*SA
      DHDT(I,J,M) = DHDT(I,J,M) + ( K/TH0B )*SA
    END IF

```

```

      IF ( H(I,J,M) .LE. 0.0D0) THEN
        FLAG2 = .TRUE.
        RETURN
      END IF
      DHDRD(I,J,M) = -XROT*SIN(TH(I,M)+NDT)
      +           +YROT*COS(TH(I,M)+NDT)
      + DHDT(I,J,M) = ( -ERZDT
      +           +(ERX-ERYDT)*SIN(TH(I,M)+NDT)
      +           -(ERXDT+ERY)*COS(TH(I,M)+NDT) )*SA
      +           -(XROT-YROTD)* (RO(J)-ROG)*COS(TH(I,M)+NDT)
      +           -(XROTDT+YROT)* (RO(J)-ROG)*SIN(TH(I,M)+NDT)
      5   CONTINUE
10   CONTINUE

C     Initialise iterative process loop control variable FLAG1
FLAG1 = .FALSE.

C     Iterative process to solve for the pressure distribution
C ----- BEGIN ITERATIVE PROCESS -----
DO WHILE(FLAG1 .EQV. (.FALSE.))

C     Sweep all rows j=2,3,...,J-1
DO 25,J=2,NROM1
  DO 15,I=2,NTHM1
    A(I-1) = (1./DTH-1.5/H(I,J,M)*DHDT(I,J,M))
    +           /(DTH*(RO(J)*SA)**2)
    B(I-1) = -2*(1./DRO2+1./(DTH*RO(J)*SA)**2)
    C(I-1) = (1/DTH+1.5/H(I,J,M)*DHDT(I,J,M))
    +           /(DTH*(RO(J)*SA)**2)
    D(I-1) = (2.0*NDR*DHDTH(I,J,M))/H(I,J,M)**3
    +           -NDR*DHDTH(I,J,M)/H(I,J,M)**3
    +           -(1./DRO)*(1./DRO-1.5/H(I,J,M)*DHDRD(I,J,M)
    +           -0.5/RO(J))*P(I,J-1,M)
    +           -(1./DRO)*(1./DRO+1.5/H(I,J,M)*DHDRD(I,J,M)
    +           +0.5/RO(J))*P(I,J+1,M)
15   CONTINUE

C     Use Thomas algorithm to solve tridiagonal system of algebraic equations
CALL THOMAS(NTHM2,A,B,C,D,N1)

C     Capture solution from Thomas and apply SOR factor, For
DO 20,I=2,NTHM1
  P(I,J,M) = PPI(I,J,M)+FOR*(D(I-1)-PPI(I,J,M))
  PPI(I,J,M) = P(I,J,M)
20   CONTINUE

25   CONTINUE

C     Sweep all columns i=2,3,...,I-1
DO 40,I=2,NTHM1
  DO 30,J=2,NROM1
    A(J-1) = (1./DRO)*(1./DRO-1.5/H(I,J,M)
    +           *DHDRD(I,J,M)-0.5/RO(J))
    B(J-1) = -2*(1./DRO2+1./(DTH*RO(J)*SA)**2)
    C(J-1) = (1./DRO)*(1./DRO+1.5/H(I,J,M)
    +           *DHDRD(I,J,M)+0.5/RO(J))
    D(J-1) = (2.0*NDR*DHDTH(I,J,M))/H(I,J,M)**3
    +           -NDR*DHDTH(I,J,M)/H(I,J,M)**3
    +           -(1./DTH-1.5/H(I,J,M)*DHDT(I,J,M))
    +           /(DTH*(RO(J)*SA)**2)*P(I-1,J,M)
    +           -(1./DTH+1.5/H(I,J,M)*DHDT(I,J,M))
    +           /(DTH*(RO(J)*SA)**2)*P(I+1,J,M)
30   CONTINUE

C     Use Thomas algorithm to solve tridiagonal system of algebraic equations
CALL THOMAS(NROM2,A,B,C,D,N1)

C     Capture solution from Thomas and apply SOR factor, For
DO 35,J=2,NROM1
  P(I,J,M) = PPI(I,J,M)+FOR*(D(J-1)-PPI(I,J,M))
35   CONTINUE

40   CONTINUE

```

```

C           Convergence test
CALL CVERGE(NTH,NRO,P,PPI,FLAG1,M,N1,N2)

END DO

C ----- END ITERATIVE PROCESS -----

C      Calculate forces (Fx, Fy and Fz) and moments (Mx and My) on
C      the impeller due to each separate blade
DO 50,J=1,NRO
    DO 45,I=1,NTH
        DFX(I,J,M)=P(I,J,M)*RO(J)*COS(TH(I,M)+NDT)
        DFY(I,J,M)=P(I,J,M)*RO(J)*SIN(TH(I,M)+NDT)
        DFZ(I,J,M)=P(I,J,M)*RO(J)
        DMX(I,J,M)=P(I,J,M)*RO(J)*(RO(J)-ROG)*SIN(TH(I,M)+NDT)
        DMY(I,J,M)=P(I,J,M)*RO(J)*(RO(J)-ROG)*COS(TH(I,M)+NDT)
45    CONTINUE
50    CONTINUE
FX(M) = -SA*CA*DBLINT(DFX,DRO,DTH,NROM1,NTHM1,N1,N2,M)
FY(M) = -SA*CA*DBLINT(DFY,DRO,DTH,NROM1,NTHM1,N1,N2,M)
FZ(M) = -SA*SA*DBLINT(DFZ,DRO,DTH,NROM1,NTHM1,N1,N2,M)
MX(M) = -SA*DBLINT(DMX,DRO,DTH,NROM1,NTHM1,N1,N2,M)
MY(M) = SA*DBLINT(DMY,DRO,DTH,NROM1,NTHM1,N1,N2,M)

C      Calculate the total force (Fx, Fy and Fz) and moment (Mx and My)
C      on the centre of mass of the impeller
FXT = FXT + FX(M)
FYT = FYT + FY(M)
FZT = FZT + FZ(M)
MXT = MXT + MX(M)
MYT = MYT + MY(M)

55 CONTINUE

RETURN
END

C =====

SUBROUTINE THOMAS(NXM2,A,B,C,D,N1)

C This subroutine uses the Thomas algorithm for solving tri-diagonal
C systems of algebraic equations with Dirichlet boundary conditions.
C It is used in iterative line-by-line sweeps to determine the pressure
C distribution over the bearing surfaces.

DOUBLE PRECISION A(N1),B(N1),C(N1),D(N1)
INTEGER I, N1, NXM2

B(1)=1.0/B(1)

DO 5,I=2,NXM2
    B(I)=1.0/(B(I)-A(I)*B(I-1)*C(I-1))
    D(I)=D(I)-A(I)*B(I-1)*D(I-1)
5 CONTINUE

D(NXM2)=D(NXM2)*B(NXM2)

DO 10,I=NXM2-1,1,-1
    D(I)=(D(I)-D(I+1)*C(I))*B(I)
10 CONTINUE

RETURN
END

C =====

SUBROUTINE CVERGE(NX,NY,P,PPI,FLAG,M,N1,N2)

C This subroutine tests for convergence of the solution. If the
C residual is less than or equal to RESLIM then the solution is
C converged. If the residual is greater than RESMAX, the solution
C is diverging and the program is stopped. Otherwise, an over -
C relaxation factor is applied to speed up the iterative process

```

```

C   (This is performed in subroutines TB and CJB)

PARAMETER (RESLIM=1.0D-4, RESMAX=1.0D4)
DOUBLE PRECISION P(N1,N1,N2), PPI(N1,N1,N2), RESID
LOGICAL FLAG

RESID=0.0D0
DO 10,J=1,NY
  DO 5,I=1,NX
    RESID = MAX(RESID,ABS(P(I,J,M)-PPI(I,J,M)))
5 CONTINUE
10 CONTINUE
IF (RESID .LE. RESLIM) THEN
  FLAG = .TRUE.
ELSE IF (RESID .GE. RESMAX) THEN
  STOP 'Solution not converging'
ELSE
  DO 20,J=2,NY-1
    DO 15,I=2,NX-1
      PPI(I,J,M) = P(I,J,M)
15 CONTINUE
20 CONTINUE
END IF

RETURN
END

C =====
REAL FUNCTION DBLINT(FXY,DX,DY,NXM1,NYM1,N1,N2,M)

C This subroutine performs a double integration using the
C trapezoidal rule of integration.

REAL SUM, FXY(N1,N1,N2)
DOUBLE PRECISION DX, DY
INTEGER I, J, M, NXM1, NYM1

SUM = 0.0
DO 10,J=1,NYM1
  DO 5,I=1,NXM1
    SUM = SUM + FXY(I,J,M) + FXY(I,J+1,M) +
    + FXY(I+1,J,M) + FXY(I+1,J+1,M)
5 CONTINUE
10 CONTINUE

DBLINT = 0.25*DX*DY*SUM

END

C =====
SUBROUTINE PLTTRA(ERX,ERXDT,ERY,ERYDT,ERZ,ERZDT,XROT,XROTD,YROTT,
+ YROTTDT,DT,T,N,NT,N3,FLAG1,FLAG2)

C This subroutine creates a Matlab script file that plots the
C trajectory of the impeller. It doubles as a results file.

PARAMETER(PI=3.141592654, RTOD=180.0/PI)
DOUBLE PRECISION ERX(N3), ERY(N3), ERZ(N3), XROT(N3), YROT(N3)
DOUBLE PRECISION ERXDT(N3), ERYDT(N3), ERZDT(N3)
DOUBLE PRECISION XROTD(N3), YROTTDT(N3), DT, T(N3)
INTEGER N, NT, N3
LOGICAL FLAG1, FLAG2

IF (N .EQ. 1) THEN
  WRITE(1,*) '% Where C refers to the column no. of matrix data:'
  WRITE(1,*) '% C1: Non-dim. time'
  WRITE(1,*) '% C2: Eccentricity ratio in the X-direction'
  WRITE(1,*) '% C3: Translational velocity in the X-direction'
  WRITE(1,*) '% C4: Eccentricity ratio in the Y-direction'
  WRITE(1,*) '% C5: Translational velocity in the Y-direction'
  WRITE(1,*) '% C6: Eccentricity ratio in the Z-direction'
  WRITE(1,*) '% C7: Translational velocity in the X-direction'
  WRITE(1,*) '% C8: Non-dim. rotation about the X-axis'

```

```

      WRITE(1,*) '% C9: Non-dim. rotational velocity about the X-axis'
      WRITE(1,*) '% C10: Non-dim. rotation about the X-axis'
      WRITE(1,*) '% C11: Non-dim. rotational velocity about the Y-axis'
      WRITE(1,*) WRITE(1,*) 'data=['
      END IF

      WRITE(1,5) T(N)*RTOD,ERX(N),ERXDT(N),ERY(N),ERYDT(N),ERZ(N),
+           ERZDT(N),XROT(N),XROTDT(N),YROT(N),YROTDT(N)

      IF ((N .EQ. NT) .OR. (FLAG1 .EQV. (.TRUE.))
+           .OR. (FLAG2 .EQV. (.TRUE.))) THEN
        WRITE(1,*) ']';
        WRITE(1,*) WRITE(1,*) 'sf=', 2*PI/DT, ';'
        WRITE(1,*) 'K=', K, ';'
        WRITE(1,*) 'erx=data(:,2);'
        WRITE(1,*) 'ery=data(:,4);'
        WRITE(1,*) 'erz=data(:,6);'
        WRITE(1,*) 'xrot=data(:,8);'
        WRITE(1,*) 'yrot=data(:,10);'

C       A correction is made to the eccentricities in the X and Y
C       directions where the erz term below accounts for increased /
C       decreased clearance as the impeller moves down/up inside the
C       cone shaped upper pump housing.
        WRITE(1,*) 'erx=erx./(1.0-erz);'
        WRITE(1,*) 'ery=ery./(1.0-erz);'
      END IF
      5 FORMAT(F10.3,10F12.6)

      RETURN
      END

```

```

C =====
      SUBROUTINE PLTCJB(P,N,NTH,NRO,NP,NT,SA,RO,TH,NDT,N1,N2)

C       This subroutine plots the pressure distribution over the conical
C       journal bearing of the impeller at each time step. A Matlab movie
C       is created by playing these plots in the correct sequence. To run
C       this movie load and run the Matlab script file "Orbit3D.m" and
C       click the appropriate selection on the pop-up menu.

      DOUBLE PRECISION P(N1,N1,N2), TH(N1,N2), RO(N1), NDT, SA
      INTEGER I, J, M, N, NTH, NRO, NP, NT

      DO 65,M=1,NP

      IF ((N .EQ. 1) .AND. (M .EQ. 1)) THEN
        WRITE(2,*) 'dth=2*pi/100;'
        WRITE(2,*) 'theta=0:dth:2*pi;'
        WRITE(2,40) 'xro1=', RO(1), '*cos(theta);'
        WRITE(2,40) 'yro1=', RO(1), '*sin(theta);'
        WRITE(2,40) 'xro2=', RO(NRO), '*cos(theta);'
        WRITE(2,40) 'yro2=', RO(NRO), '*sin(theta);'
        WRITE(2,*) 'MOV1=moviein(', NT, ')';
        WRITE(2,*)
      END IF

      IF (N .LT. 10) THEN
        WRITE(2,10) 'xcjb', N, M, '=[ '
      ELSE IF (N .LT. 100) THEN
        WRITE(2,15) 'xcjb', N, M, '=[ '
      ELSE
        WRITE(2,20) 'xcjb', N, M, '=[ '
      END IF
      DO 5,J=1,NRO
        WRITE(2,25) ((RO(J)*COS(TH(I,M)+NDT)),I=1,NTH)
      5  CONTINUE
      10 FORMAT(A4,I1,I1,A2)
      15 FORMAT(A4,I2,I1,A2)
      20 FORMAT(A4,I3,I1,A2)
      25 FORMAT(101F10.5)
      WRITE(2,*) ']';
      WRITE(2,*)

```

```

      IF (N .LT. 10) THEN
        WRITE(2,10) 'ycjb', N, M, '=['
      ELSE IF (N .LT. 100) THEN
        WRITE(2,15) 'ycjb', N, M, '=['
      ELSE
        WRITE(2,20) 'ycjb', N, M, '=['
      END IF
      DO 30,J=1,NRO
        WRITE(2,25) (RO(J)*SIN(TH(I,M)+NDT)), I=1,NTH)
30    CONTINUE
      WRITE(2,*) '] ; '
      WRITE(2,*)

      IF (N .LT. 10) THEN
        WRITE(2,10) 'pcjb', N, M, '=['
      ELSE IF (N .LT. 100) THEN
        WRITE(2,15) 'pcjb', N, M, '=['
      ELSE
        WRITE(2,20) 'pcjb', N, M, '=['
      END IF
      DO 35,J=1,NRO
        WRITE(2,25) (P(I,J,M), I=1,NTH)
35    CONTINUE
      WRITE(2,*) '] ; '
      WRITE(2,*)

      IF (N .LT. 10) THEN
        WRITE(2,45) 'surf(xcjb',N,M,',ycjb',N,M,',pcjb',N,M,');'
      ELSE IF (N .LT. 100) THEN
        WRITE(2,50) 'surf(xcjb',N,M,',ycjb',N,M,',pcjb',N,M,');'
      ELSE
        WRITE(2,55) 'surf(xcjb',N,M,',ycjb',N,M,',pcjb',N,M,');'
      END IF
      IF (M .EQ. 1) THEN
        WRITE(2,*) 'hold on;'
        WRITE(2,60) 'axis([',-1./SA,1./SA,-1./SA,1./SA,0,0.5,']);'
        WRITE(2,*) 'set(gca,''PlotBoxAspectRatio'',[2 2 1]);'
        WRITE(2,*) 'view(25,30);'
        WRITE(2,*) 'plot(xro1,yro1,''--'');'
        WRITE(2,*) 'plot(xro2,yro2,''--'');'
        WRITE(2,*) ' xlabel(''X / sin\ alpha'');'
        WRITE(2,*) ' ylabel(''Y / sin\ alpha'');'
        WRITE(2,*) ' zlabel(''Pressure, p*'');'
        WRITE(2,*)
      ELSE IF (M .EQ. NP) THEN
        WRITE(2,*) 'shading interp;'
        WRITE(2,*) 'hold off;'
        WRITE(2,*) 'MOV1(', N ,') = getframe;'
        WRITE(2,*)
      END IF
40    FORMAT(A5,F6.4,A12)
45    FORMAT(A9,2I1,A5,2I1,A5,2I1,A2)
50    FORMAT(A9,I2,I1,A5,I2,I1,A5,I2,I1,A2)
55    FORMAT(A9,I3,I1,A5,I3,I1,A5,I3,I1,A2)
60    FORMAT(A6,6F10.6,A3)

65 CONTINUE

      RETURN
END

```

C =====

SUBROUTINE PLTTB(P,N,NTH,NR,NP,NT,R,TH,NDT,N1,N2)

C This subroutine plots the pressure distribution over the thrust
C bearing of the VentrAssist impeller at each time step. A Matlab
C movie is created by playing these plots in the correct sequence.
C To run this movie load and run the Matlab script file "Orbit3D.m"
C and click the appropriate selection on the pop-up menu.

DOUBLE PRECISION P(N1,N1,N2), TH(N1,N2), R(N1), NDT
INTEGER I, J, M, N, NTH, NR, NP, NT

```

DO 60,M=1,NP

IF ((N .EQ. 1) .AND. (M .EQ. 1)) THEN
    WRITE(3,*) 'dth=2*pi/100;'
    WRITE(3,*) 'theta=0:dth:2*pi;'
    WRITE(3,40) 'xr1=', R(1), '*cos(theta);'
    WRITE(3,40) 'yr1=', R(1), '*sin(theta);'
    WRITE(3,40) 'xr2=', R(NR), '*cos(theta);'
    WRITE(3,40) 'yr2=', R(NR), '*sin(theta);'
    WRITE(3,*) 'MOV2=moviein(', NT, ');'
    WRITE(3,*)
END IF

IF (N .LT. 10) THEN
    WRITE(3,10) 'xtb', N, M, '['
ELSE IF (N .LT. 100) THEN
    WRITE(3,15) 'xtb', N, M, '['
ELSE
    WRITE(3,20) 'xtb', N, M, '['
END IF
DO 5,J=1,NR
    WRITE(3,25) ((R(J)*COS(TH(I,M)+NDT)),I=1,NTH)
5  CONTINUE
10 FORMAT(A4,I1,I1,A2)
15 FORMAT(A4,I2,I1,A2)
20 FORMAT(A4,I3,I1,A2)
25 FORMAT(10F10.5)
    WRITE(3,*) ']';
    WRITE(3,*)

IF (N .LT. 10) THEN
    WRITE(3,10) 'ytb', N, M, '['
ELSE IF (N .LT. 100) THEN
    WRITE(3,15) 'ytb', N, M, '['
ELSE
    WRITE(3,20) 'ytb', N, M, '['
END IF
DO 30,J=1,NR
    WRITE(3,25) ((R(J)*SIN(TH(I,M)+NDT)),I=1,NTH)
30  CONTINUE
    WRITE(3,*) ']';
    WRITE(3,*)

IF (N .LT. 10) THEN
    WRITE(3,10) 'ptb', N, M, '['
ELSE IF (N .LT. 100) THEN
    WRITE(3,15) 'ptb', N, M, '['
ELSE
    WRITE(3,20) 'ptb', N, M, '['
END IF
DO 35,J=1,NR
    WRITE(3,25) (P(I,J,M),I=1,NTH)
35  CONTINUE
    WRITE(3,*) ']';
    WRITE(3,*)

IF (N .LT. 10) THEN
    WRITE(3,45) 'surf(xtb',N,M,',ytb',N,M,',ptb',N,M,');'
ELSE IF (N .LT. 100) THEN
    WRITE(3,50) 'surf(xtb',N,M,',ytb',N,M,',ptb',N,M,');'
ELSE
    WRITE(3,55) 'surf(xtb',N,M,',ytb',N,M,',ptb',N,M,');'
END IF
IF (M .EQ. 1) THEN
    WRITE(3,*) 'hold on;'
    WRITE(3,*) 'axis([-1 1 -1 1 0 0.5]);'
    WRITE(3,*) 'set(gca,''PlotBoxAspectRatio'',[2 2 1]);'
    WRITE(3,*) 'view(25,30);'
    WRITE(3,*) 'plot(xr1,yr1,''--'');'
    WRITE(3,*) 'plot(xr2,yr2,''--'');'
    WRITE(3,*) ' xlabel(''X'');'
    WRITE(3,*) ' ylabel(''Y'');'
    WRITE(3,*) ' zlabel(''Pressure, p*'');'
    WRITE(3,*)

```

```
ELSE IF (M .EQ. NP) THEN
    WRITE(3,*) 'shading interp;'
    WRITE(3,*) 'hold off;'
    WRITE(3,*) 'MOV2(' , N , ') = getframe;'
    WRITE(3,*)
END IF
40 FORMAT(A4,F6.4,A12)
45 FORMAT(A9,2I1,A5,2I1,A5,2I1,A2)
50 FORMAT(A9,I2,I1,A5,I2,I1,A5,I2,I1,A2)
55 FORMAT(A9,I3,I1,A5,I3,I1,A5,I3,I1,A2)

60 CONTINUE

RETURN
END
```

APPENDIX H – Matlab script file “Orb3Dvis.m”

```
% ***** Orb3Dvis *****
%
% This program is a Matlab script file written to visualise the
% output from Orbit3D which consists of the trajectory of the
% VentrAssist impeller, the pressure distribution over the surfaces
% of the conical journal bearing and the thrust bearing and a
% frequency analysis of the trajectory. The input files for this
% script file are "plotraj.m", "plotcjb.m", and "plottb.m", which
% all must be located in the same directory as Orb3Dvis.

flaga=1;
while flaga ~= 0,
    choice1 = menu('Select option','Bearing trajectory - Eccentricity',...
        'Bearing trajectory - Rotation','CJB pressure distribution',...
        'TB pressure distribution','FFT analysis of trajectory','Quit');

    switch choice1

        case 1
            flag1 = figflag('Bearing Trajectory - Eccentricity');
            if flag1 == 0,
                h1=figure('name','Bearing Trajectory - Eccentricity');
            end
            clf(h1); plotraj;
            plot3(erx(1),ery(1),erz(1),'b+');
            hold on;
            xlabel('\epsilon_X''');
            ylabel('\epsilon_Y''');
            zlabel('\epsilon_Z');
            axis([-1.25 1.25 -1.25 1.25 -1 1]);
            grid on;
            box on;
            set(gca,'PlotBoxAspectRatio',[1.25 1.25 1])
            view(25,30);
            comet3(erx,ery,erz);
            plot3(erx,ery,erz,'LineWidth',1);
            rotate3d on;

        case 2
            flag2 = figflag('Bearing Trajectory - Rotation');
            if flag2 == 0,
                h2=figure('name','Bearing Trajectory - Rotation');
            end
            clf(h2); plotraj;
            plot(xrot(1),yrot(1),'b+');
            hold on;
            xlabel('gamma_X**');
            ylabel('gamma_Y**');
            axis([-1 1 -1 1]);
            box on;
            comet(xrot,yrot);
            plot(xrot,yrot,'LineWidth',1);

        case 3
            flag3 = figflag('CJB Pressure Distribution');
            if flag3 == 0,
                h3=figure('name','CJB Pressure Distribution');
            end
            plotcjb;

        case 4
            flag4 = figflag('TB Pressure Distribution');
            if flag4 == 0,
                h4=figure('name','TB Pressure Distribution');
            end
            plottb;

        case 5
            flagb = 1;
            while flagb ~= 0,
                choice2 = menu('Select option','Eccentricity ratio in X-direction',...
                    'Eccentricity ratio in Y-direction','Eccentricity ratio in Z-direction',...
                    'Rotation about the X-axis','Rotation about the Y-axis','Quit');

                switch choice2
                    case 1
                        flag5a = figflag('Non-dim. freq. spectrum of eccentricity in X-direction');
                        if flag5a == 0,
                            h5a=figure('name','Non-dim. freq. spectrum of eccentricity in X-direction');
                        end
                        plotraj;
                        [P,F]=spectrum(erx,[],[],[],sf);
                        plot(F,P(:,1));
                end
            end
    end
end
```

```

xlabel('Non-dimensional frequency');
ylabel('PSD');
axis([0 16 0 Inf]);

case 2
flag5b = figflag('Non-dim. freq. spectrum of eccentricity in Y-direction');
if flag5b == 0,
    h5b=figure('name','Non-dim. freq. spectrum of eccentricity in Y-direction');
end
plottraj;
[P,F]=spectrum(ery,[],[],[],sf);
plot(F,P(:,1));
xlabel('Non-dimensional frequency');
ylabel('PSD');
axis([0 16 0 Inf]);

case 3
flag5c = figflag('Non-dim. freq. spectrum of eccentricity in Z-direction');
if flag5c == 0,
    h5c=figure('name','Non-dim. freq. spectrum of eccentricity in Z-direction');
end
plottraj;
[P,F]=spectrum(erz,[],[],[],sf);
plot(F,P(:,1));
xlabel('Non-dimensional frequency');
ylabel('PSD');
axis([0 16 0 Inf]);

case 4
flag5d = figflag('Non-dim. freq. spectrum of rotation about X-axis');
if flag5d == 0,
    h5d=figure('name','Non-dim. freq. spectrum of rotation about X-axis');
end
plottraj;
[P,F]=spectrum(xrot,[],[],[],sf);
plot(F,P(:,1));
xlabel('Non-dimensional frequency');
ylabel('PSD');
axis([0 16 0 Inf]);

case 5
flag5e = figflag('Non-dim. freq. spectrum of rotation about Y-axis');
if flag5e == 0,
    h5e=figure('name','Non-dim. freq. spectrum of rotation about Y-axis');
end
plottraj;
[P,F]=spectrum(yrot,[],[],[],sf);
plot(F,P(:,1));
xlabel('Non-dimensional frequency');
ylabel('PSD');
axis([0 16 0 Inf]);

case 6
flag5a = figflag('Non-dim. freq. spectrum of eccentricity in X-direction');
if flag5a == 1,
    close(h5a);
end
flag5b = figflag('Non-dim. freq. spectrum of eccentricity in Y-direction');
if flag5b == 1,
    close(h5b);
end
flag5c = figflag('Non-dim. freq. spectrum of eccentricity in Z-direction');
if flag5c == 1,
    close(h5c);
end
flag5d = figflag('Non-dim. freq. spectrum of rotation about X-axis');
if flag5d == 1,
    close(h5d);
end
flag5e = figflag('Non-dim. freq. spectrum of rotation about Y-axis');
if flag5e == 1,
    close(h5e);
end
flagb = 0;

end
end

case 6
flag1 = figflag('Bearing Trajectory - Eccentricity');
if flag1 == 1,
    close(h1);
end
flag2 = figflag('Bearing Trajectory - Rotation');
if flag2 == 1,
    close(h2);
end

```

```
flag3 = figflag('CJB Pressure Distribution');
if flag3 == 1,
    close(h3);
end
flag4 = figflag('TB Pressure Distribution');
if flag4 == 1,
    close(h4);
end
flaga = 0;

end

end
```